Geochemical evolution of Andean arc volcanism and the uplift of the Andes

SCOTT, ERIN,MARGARET

SCOTT, ERIN,MARGARET (2019) *Geochemical evolution of Andean arc volcanism and the uplift of the Andes*, Durham theses, Durham University. Available at Durham E-Theses Online: http://etheses.dur.ac.uk/13135/

Geochemical evolution of Andean arc volcanism and the uplift of the Andes

Erin M Scott

Durham University

A thesis submitted for the degree of

Doctor of Philosophy (PhD)

December 2018

Abstract

The Andean Plateau is the only modern-day orogenic plateau formed by subduction and not continental collision. The geodynamic mechanisms responsible for initiating crustal shortening and thickening in the Andes at ~70 Ma, after subduction had been ongoing for over 200 Ma, are still debated. The timing of Andean surface uplift is also controversial, and currently two models remain prevalent: (1) slow and steady uplift synchronous with crustal shortening from ~70-50 Ma, and (2) rapid surface uplift of up to 2 km in the last 20-16 Ma, resulting from large scale lower lithosphere removal or lower crustal flow.

We find a very strong correlation between Nazca plate age entering the trench and Andean crustal thickness ($r = 0.939$; $r^2 = 0.882$; p value < 0.01). Thrust earthquakes at the Nazca-South America plate interface occur only where the slab age at the trench is older than 30 Myr, except where oceanic ridges are colliding with the trench. Based on these observations a new hypothesis is proposed, that long-term subduction of intermediate aged oceanic lithosphere (~30-80 Myr) can provide an explanation for the initiation and distribution of crustal shortening in the Andean plate. Intermediate aged slabs have a greater mechanical strength than weak and young oceanic lithosphere (<30 Myr), but a greater positive buoyancy compared to older slabs. These slab properties combined with trench-ward overriding plate motion transmit higher compressional stress into the overriding South American plate than during other subduction zone configurations.

A new approach is used to constrain regional Andean surface uplift. Cross correlations are tested between several physical parameters relating to the Andean subduction zone and several geochemical parameters from Andean arc volcanoes. $^{87}Sr/^{86}Sr$ and $^{143}Nd/^{144}Nd$ ratios have the strongest correlations with both crustal thickness and, due to isostasy, elevation. Very strong linear correlations exist between smoothed elevation and $^{87}Sr/^{86}Sr$ (R^2=0.858, n=17) and $^{143}Nd/^{144}Nd$ (R^2=0.919, n=16) ratios of non-plateau arc lavas. $^{87}Sr/^{86}Sr$ and $^{143}Nd/^{144}Nd$ ratios of lavas erupted through the Andean Plateau are distinctly crustal (>0.705 and <0.5125, respectively) and can be used as a plateau discriminant. These relationships are used to constrain 200 Myr of surface uplift history for the Western Cordillera (present elevation 4200±516 m). Jurassic-Paleogene isotope compositions (including new Paleogene analyses) became gradually more ‘crust-like’ over time, yet the distinct isotope signatures relating to the Andean Plateau were not achieved until the Miocene (23 Ma).

Results support the slow and steady surface uplift model, synchronous with gradual crustal shortening and thickening. The isotope paleo-elevation model predicts that current elevations were attained in the Western Cordillera by 23 Ma. From 23-10 Ma, both deformation and surface uplift gradually propagated southwards by ~400 km.

Table of Contents

Declaration

I declare that this thesis, which I submit for the degree of Doctor of Philosophy at Durham University, is my own work and not substantially the same as any which has previously been submitted at this or any other university.

Where appropriate, work in this thesis which has already been published is clearly indicated.

Work for this thesis was conducted from October 2015 to December 2018 under the primary supervision of Prof. Mark Allen at Durham University.

Erin M Scott
Durham University
December 2018

Acknowledgements

First, I would like to thank my supervisors. Especially, a huge amount of thanks goes to Mark Allen, who has been a source of continual support, inspiration and light-heartedness throughout this project. Thank you for believing in me from the beginning, encouraging me, and never turning me away when I came knocking on your office door! Many thanks go to Colin Macpherson, Ken McCaffrey and Chris Saville; for all their support, encouragement and patience. A massive thank you goes to all of them for reading my chapters so quickly over the last few months! I would also like to extend my thanks and admiration to the late Jon Davidson. Jon's pioneering research in isotope geochemisty and the Andes set the foundations for this project, and I feel very lucky and humbled to have had the opportunity to have worked and learned from him.

This project has been funded by the Charles Waites Studentship, and I am extremely grateful to the Waites family for their generosity. I am also grateful to the numerous bodies which helped fund my fieldwork and geochemical analyses, including Geological Society of London 'Mike Coward' Fieldwork Grant and the International Association of Geochemistry (IAGC) Student Research Grant. Thanks to Mark for financially supporting the extra fieldwork and analytical costs. I am extremely grateful to Geoff Nowell for all his support and training in the clean lab and for allowing me to double my number of isotope analyses! Chris Ottley in Durham and Tom Knott in Leicester trained and helped me with ICP-MS and XRF, respectively. A big thanks to Cristian Tambley and his amazing team at Campoalto, for not allowing Mark, Julien and myself to get lost in the Atacama Desert while on the hunt for (sometimes non-existent) Paleogene lavas. Lucy McGee, Felipe Aguilera, and Francisco Gutierrez all gave invaluable logistical support during fieldwork in Chile. The SOTA7 workshop in San Pedro de Atacama (September 2018) was an incredible experience, I would like to thank Gerhard Wörner for inviting me and to the Santander International Collaboration Grant for funding my attendance, and to all the SOTA7 attendees for being so inspirational! Thanks to Daniel Viete for taking me along to Greece for my first research fieldtrip. Thank you to everyone in Durham's various research groups: Structural Geology and Tectonics, Volc Coffee, and GCD. Particularly, I would like to thank Jeroen van Hunen, Phil Heron, Ana Negredo and Ben Maunder, whose work helped inspire the ideas behind Chapters 2 and 3, and conversations with them since helped vastly improve the ideas from initial 'back-of-envelope' sketches!

To my family, thank you for always believing in me and for sparking my early love of science and the Earth. Last, but definitely not least, thanks to all the wonderful people I have met here in Durham, especially all the research students and post-docs in the Deptartment! The adventures, gigs, festivals, pub trips and Newcastle nights have been a blast. My old housemates, Emma, Ben, Chris (and Edward), thanks for being just as crazy as me. George and Liz, thank you for housing me over the last 4 months and looking after me while I wrote up (I wouldn't have been able to do it without you both!). Thanks to Sean for being a very chilled-out write up buddy, and for reminding me that a pint at The Vic helps solve many write up problems (even a broken computer!).

For all my family, and my Grandad, Stan Scott.

"Science is the greatest story of all"

- Dan Rather, AGU Fall Meeting 2017

Adapted 3 Minute Thesis Entry (Dept. Conference, June 2018)

Now my game is the Andean Plateau,
(I've even made it out of gateaux!)
And this all came about
When Mark found out,
He needed the Andes to complete his trio.

Over 200 million years of subduction,
Have led to vast magma production,
In three quite big zones,
Of large stratocones,
It's quite the explosive concoction!

Now the tectonic & uplift history
Of the high plateau are quite the mystery,
While one group think slow,
The others say, hell no!!
Over 30 years of debate, oh so grisly!

We found isotopes have the best correlation,
That match with volcano elevation,
And by filtering out,
Those silicics causing doubt,
Oh heck, we had quite the revelation!

Then by extrapolating back through time
(and shifting through some isotope grime)
The uplift history,
No longer a mystery,
As the geology and isotopes do chime!

So for the last 23 million years,
We think that the plateau was near,
About 4000 meters
(plus or minus a teeter)
...A fight with the haters, I fear!

But what's that? Oh crap.
Have we found a data gap?
Those Paleogene lavas,
Caused quite a palaver,
No isotopes even though they were mapped!

So then lots of money was spent
And off to the Andes we went,
We got those old lavas,
(And saw lots of llamas!)
For more isotopes we were hell-bent!

Now if you want something more scientific,
That isn't just part of a limerick,
Then the thesis is next
I hope it doesn't perplex,
To discuss it would be quite terrific!

Chapter 1: Introduction

1.1 Project rationale and thesis aims

The Andean mountain range is the only barrier to atmospheric circulation in the Southern hemisphere and hence the uplift of the Andes is thought to have had a large impact on Cenozoic climate change (Molnar and England, 1990; Hartley, 2003; McKenzie et al., 2014; Armijo et al., 2015; Lee et al., 2015). The Andean Plateau is the only orogenic plateau which has not been induced by continental collision and it currently has the thickest crust of any subduction zone on Earth. The geodynamic evolution and timing of Central Andean Plateau formation remains uncertain (Barnes and Ehlers, 2009; Capitanio et al., 2011; Maloney et al., 2013; Faccenna et al., 2017; Garzione et al., 2017; Horton, 2018b). Two end-member models of Andean Plateau uplift remain prevalent (Barnes and Ehlers, 2009; Garzione et al., 2017): (1) slow, steady uplift from at least 40 Ma primarily due to crustal thickening synchronous with crustal shortening (Mamani et al., 2010; McQuarrie et al., 2005; Carrapa et al., 2006; Carlotto, 2013; Canavan et al., 2014; Chapman et al., 2015b; Zhou et al., 2017); and (2) rapid, recent surface uplift after crustal shortening (<20-16 Ma) as a result of lower lithosphere removal and/or lower crustal flow (Garzione et al., 2006, 2008; Leier et al., 2013; Kar et al., 2016; Garzione et al., 2014; Schildgen et al., 2009; Lamb, 2011, 2016; Gerbault et al., 2005; Ouimet and Cook, 2010).

The vast magmatic record along strike and through time, combined with systematic variations in elevation, crustal thickness, stress regime and slab geometry make the Andes the perfect study area to better understand the complexities of subduction in a non-collisional orogen. In this thesis, the main aims are to quantitatively explore: (1) current relationships between Andean subduction parameters and crustal thickness in the South American Plate to give insight into the causative mechanisms related to the onset of crustal thickening; and (2) the relationships between Andean arc geochemical systematics and crustal thickness along the arc. Strong correlations between geochemical parameters and crustal thickness can then be extrapolated back through time and compared with independent geological evidence of crustal shortening, thickening and uplift in the Andes.

1.2 Geological background

1.2.1 Plate Tectonics

The theory of plate tectonics provides a unifying explanation for planet Earth's major surface features. The Earth's outer layer (called the lithosphere; Figure 1) is divided into a series of tectonic plates which act as rigid bodies and move relative to one another over geological time (Turcotte and Oxburgh, 1972). Tectonic plate motions are a result of complex feedback mechanisms between plate driving forces and mantle convection (Conrad and Lithgow-Bertelloni, 2002; Bercovici, 2003; Stadler et al., 2010). Mantle convection is the result of gravitational instabilities which arise within planetary bodies as their surfaces are colder (and therefore denser) than the hotter interior (Bercovici, 2003). Despite this, planet Earth is the only known planet where mantle-scale plate tectonics operates (Tackley, 2000). Several fundamental questions remain unanswered surrounding the onset of modern plate tectonics and the formation of continental crust (Rapp and Watson, 1995; Barth et al., 2002; Horodyskyj et al., 2007; Gazel et al., 2015; Dhuime et al., 2015; Magni, 2017), and feedbacks between tectonics and climate (Molnar and England, 1990; Molnar et al., 1993; Hartley, 2003; Lamb and Davis, 2003; Armijo et al., 2015; Lee et al., 2015).

The Earth's lithosphere is comprised of both the crust and the uppermost part of the solid mantle (Figure 1). The uppermost solid mantle is termed the lithospheric mantle. Two types of lithosphere are present on Earth, oceanic and continental, which are distinct in terms of composition, density, thickness and age (Jordan, 1978; Molnar and Atwater, 1978; McKenzie et al., 2005). Lithospheric plates behave as strong, rigid bodies due to the low temperature and pressure conditions near the surface where rocks deform in a brittle manner (Byerlee, 1978). Lithospheric plates overlie a weak layer of the mantle called the asthenosphere, which is crystalline but behaves as a highly viscous fluid over geological time due to solid-state creep processes (Turcotte and Oxburgh, 1972; Weertman and Weertman, 1975). The boundary separating lithospheric and asthenospheric mantle is temperature dependent (e.g. Jordan, 1978).

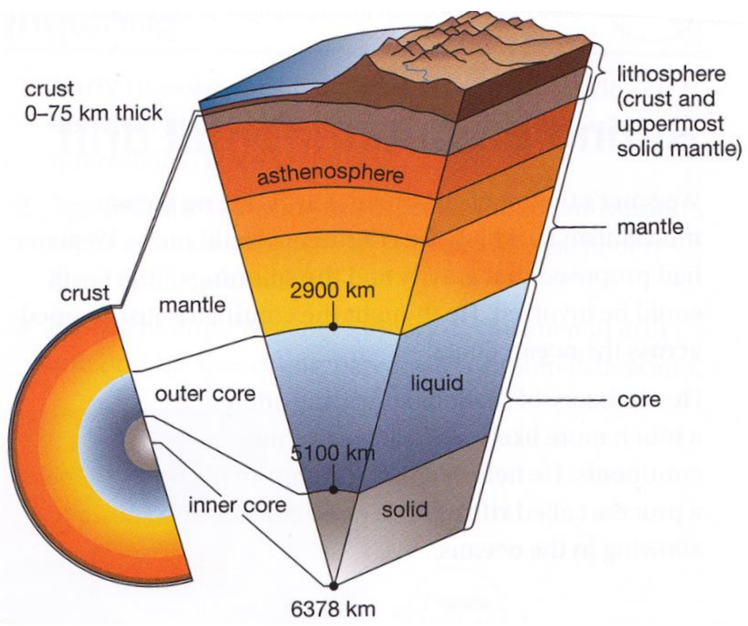

Figure 1: The compositional layering of the Earth. Earth's mantle is divided into several layers, from top to bottom: the lower mantle (base: 2900 km depth); the upper mantle (base 660 km); the asthenosphere (a layer within the upper mantle); and the rigid lithospheric mantle (ranging from ~0-100 km thick). The mantle lithosphere and crust combined make up the Earth's lithospheric plates, of which there are two types: oceanic and continental. Oceanic crust is generally ~7 km thick, whereas continents vary in crustal thickness from ~20-75 km.

Tectonic plates move apart at mid-ocean ridges (MORs), where the underlying mantle asthenosphere rises to fill the space created as the two plates move apart. Adiabatic decompression of the rising asthenosphere induces partial melting, melts rise to the surface, cool, crystallise and form oceanic crust (e.g. Kay et al., 1970). At MOR axes, the thickness of the curst and lithosphere is effectively zero (Figure 2). Oceanic lithosphere thickens and subsides with age as the plate cools and becomes denser with increasing distance from mid-ocean ridges (Figure 2; e.g. Caldwell and Turcotte, 1979; McKenzie et al., 2005).

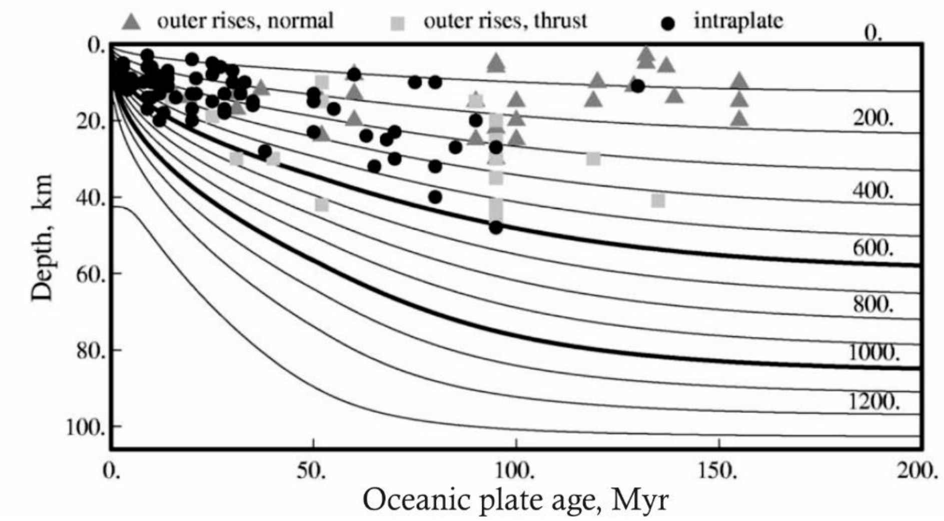

Figure 2: A model of the distribution of geotherms (in ° C) in an oceanic plate with increasing age. The base of the oceanic lithosphere is defined by a constant temperature (~1300° C) and therefore its thickness increases as a function of plate age (e.g. Caldwell and Turcotte, 1979; McKenzie et al., 2005). Depths of intraplate earthquakes generally occur at less than 600° C, roughly half the thickness of the oceanic lithosphere. Figure adapted from McKenzie et al. (2005).

1.2.2 Subduction zones

Subduction zones can cause of some of the largest natural hazards on our planet: megathrust earthquakes, tsunamis and volcanic eruptions. The 'Pacific Ring of Fire' is the common umbrella-term relating to the volcanoes and earthquakes which result from the ring of subduction zones surrounding the Pacific Ocean. Subduction zones are where two tectonic plates collide and one plate descends into the mantle underneath the overriding tectonic plate (Figure 3). The upper plate can be either an oceanic or a continental plate. The descending plate in most modern-day subduction zones is typically oceanic, however, more buoyant continental plates may partially subduct at continental collision zones (e.g. Jamieson and Beaumont, 2013). As the Andean margin is the topic of this thesis, the following discussion concentrates on subduction of oceanic plates.

As oceanic lithosphere descends into the mantle, the pressure and temperature increase and minerals within the gabbroic oceanic lithosphere become unstable and undergo a phase transition to eclogite (Yoder and Tilley, 1962; Kirby et al., 1996). Basalt and gabbro are relatively buoyant compared to the surrounding asthenospheric mantle, whereas eclogite is more dense and therefore has a negative buoyancy (e.g. Kirby et al., 1996; van Hunen et al., 2000). Subduction of dense oceanic lithosphere is thought to be the main driving force of plate tectonics, due to the negative buoyancy of either (1) 'attached' slabs generating gravitational pull forces (Figure 3; Schellart, 2004); or (2) sinking of 'detached' slabs exciting mantle flow (Conrad and Lithgow-Bertelloni, 2002).

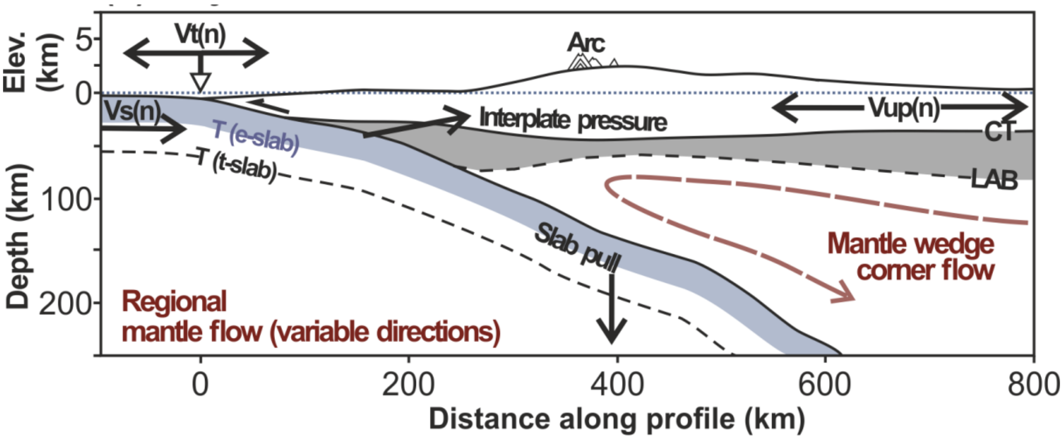

Figure 3: A schematic diagram showing the major forces and processes acting on an oceanic-continental subduction zone. Vs(n), Vt(n) and Vup(n) correspond to the trench normal components of: down-going oceanic plate velocity, trench migration velocity, and upper plate velocity, respectively. T (t-slab) relates to the thickness of the oceanic lithosphere. CT is the overriding plate crustal thickness and LAB is the upper plate lithosphere-asthenosphere boundary depth.

Shallow earthquakes at the plate interface result from friction acting between two colliding plates (Byerlee, 1978). Only when stress build-up is great enough to overcome the frictional forces do the plates move suddenly and release seismic energy in the form of an earthquake. The term 'megathrust' generally relates to very large earthquakes greater than magnitude 7 or

8. One of the largest earthquakes on record (Mw 9.5) is the 1960 Valdivia event, Central Chile (e.g. Moreno et al., 2009; Dzierma et al., 2012). High densities of megathrust events have been associated with particular subduction margins, such as Chile and Japan, where the relative overriding plate motion is directed towards the trench and causes increased seismic coupling (Conrad et al., 2004). Subduction related seismicity has meant that variations in the shape and geometry of slabs worldwide can be imaged using geophysical techniques (e.g. Hayes et al., 2012).

Complex interactions between the two colliding plates and the surrounding mantle mean that there are wide ranges of subduction zone geometries and styles observed around the globe (Heuret and Lallemand, 2005a). Broadly, oceanic-oceanic subduction zones tend to have steeper dipping slabs and back-arc spreading, whereas oceanic-continental subduction zones have shallower slabs and back-arc compression (Lallemand et al., 2005). Among global subduction zones, changes in overriding plate stress state have been attributed to: the incoming oceanic plate age (Molnar and Atwater, 1978; Capitanio et al., 2011); subducted slab dip (Lallemand et al., 2005; Sdrolias and Müller, 2006; Crameri et al., 2017); relative plate velocities (Heuret and Lallemand, 2005a; Maloney et al., 2013; Guillaume et al., 2018; Cerpa et al., 2018); and large scale mantle flow (Sdrolias and Müller, 2006). The relationships between subduction parameters and stress state along the Andean margin are explored in Chapter 2.

1.3 Arc magmatism and geochemistry

Volcanoes related to subduction zones form chains which run parallel to the subduction zone and trench. Collectively, these volcanic chains are called ‘arcs’, due to the common arcuate shape of most subduction zones (England et al., 2004). Study of the chemistry of arc magmas is important for understanding the formation and evolution of continental crust (Rudnick, 1995; Hawkesworth and Kemp, 2006; Gazel et al., 2015; Dhuime et al., 2015) and the recycling of elements and water on Earth (Plank, 2005; Chiaradia, 2014; Spinelli et al., 2016; Magni, 2017). Subduction zones are key tectonic settings related to the formation of economic mineral deposits, such as large copper porphyry systems (Mungall, 2002; Richards, 2003; Chiaradia, 2014; Jenner, 2017). Furthermore, concentration of economically important metals into the shallow crust has been associated with obliquely convergent subduction zones which have a tectonically thickened overriding plate (Richards, 2003; Chiaradia, 2014). Correlations between crustal thickness and certain geochemical parameters of arc lavas are well established, both globally and along individual arc segments, but the causative mechanisms which explain these relationships remain debated (Leeman, 1983; Feigenson and Carr, 1986; Hildreth and Moorbath, 1988; Plank and Langmuir, 1988; Turner and Langmuir, 2015b; Farner and Lee, 2017). In this study, quantifying controls of crustal thickness on Andean arc geochemical compositions and making sure the same signals have a minimal influence by any slab or other component, is a key aim (Chapter 3). Then the long record of pre-Quaternary Andean arc compositions can be used to make inferences on the crustal thickening and uplift history (Chapters 4 and 5).

Subduction zone magmas are the product of complex interactions between: (1) dehydration of the down-going slab and subducted sediments (±slab or sediment melting); (2) hydration and partial melting of the mantle wedge; and (3) differentiation of mantle melts within the overlying plate (± assimilation of crustal material). These interactions are difficult to segregate, and hence several very different mechanisms or processes can be ascribed to produce the same geochemical fingerprint observed in arc volcanic products. A brief overview to these processes is outlined in Figure 4 and described below.

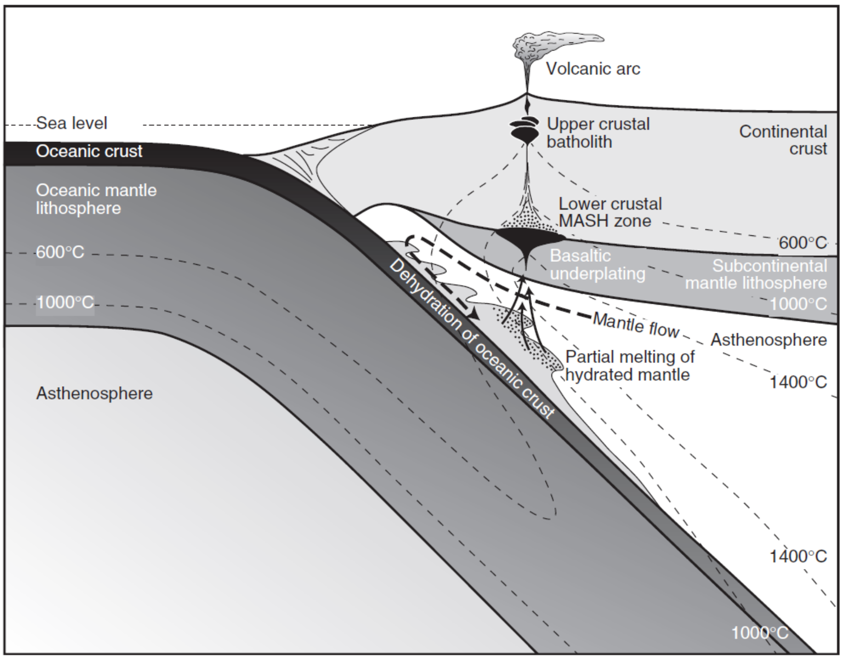

Figure 4: A schematic diagram illustrating subduction processes which result in arc magmatism. The oceanic plate can contain altered (serpentinized) fracture zones and a variable thickness of pelagic sediment. Taken from (Richards, 2003).

1.1.1.1 Slab processes

The down-going oceanic plate contains water, both bound within hydrous mineral phases (such as serpentinite) and contained within wet oceanic sediments which can accumulate on top of the basaltic crust (Ulmer and Trommsdorff, 1995; Plank and Langmuir, 1998; Dobson et al., 2002; van Keken et al., 2011; Magni et al., 2014; Spinelli et al., 2016). Fracture zones within the oceanic lithosphere, caused by displacement between MOR segments or during outer rise faulting, are highly serpentinized and contain a particularly high proportion of mineral bound water (Christensen, 2015). As the slab increases in temperature as it descends, dehydration reactions occur within the slab and the resultant fluids are released into the overlying mantle (Figure 4; van Keken et al., 2011; Magni et al., 2014). 'Slab fluids', including their dissolved element cargo, percolate into the mantle wedge and cause partial melting by lowering the solidus of mantle peridotite (Gaetani and Grove, 1998). The importance of slab dehydration and mantle wedge melting was originally noted by studying trace element systematics in arc lavas (Gill, 1981; McCulloch and Gamble, 1991; Pearce and Peate, 1995). Large Ion Lithophile Elements (LILEs; Ba, Cs, Pb, Rb and Sr) are incompatible in most rocks and are highly fluid mobile (McCulloch and Gamble, 1991). On the other hand, the high valence of High Field Strength Elements (HFSEs: Zr, Hf, Nb, Ta, ±Ti) means they are fluid immobile, and compatible in oxides and accessory phases (such as apatite, titanite, sphene and rutile). Fluid immobile HFSE elements are held onto by accessory phases in the down-going slab as it dehydrates, meanwhile fluid mobile LILEs are stripped away from the slab by the released fluids and resultant mantle melts (Pearce and Peate, 1995). Therefore, high ratios of LILE/HFSE (e.g. Ba/Zr or La/Nb) elements are often termed an 'arc' or 'subduction' signature (Pearce and Peate, 1995).

Slab dehydration reactions are pressure-temperature dependant, therefore they are related to the thermal structure of the down-going oceanic plate (Kirby et al., 1996; van Keken et al., 2011). Variations in subduction parameters control the thermal state of the down-going slab. A proxy for slab temperature, the 'slab thermal parameter', is defined as the product of the age of the subducting oceanic lithosphere and the vertical descent rate of the slab (Kirby et al., 1996; Magni et al., 2014). Calculations of slab surface temperatures (a function of the 'thermal parameter' corrected to depth to slab) have been found to correlate strongly with H_2O/Ce compositions of melt inclusions, which have consequently been termed a 'slab thermometer' (Syracuse et al., 2010; Cooper et al., 2012; Turner et al., 2016).

Slow subduction of young (<25 Myr) and relatively hot oceanic lithosphere has been associated with partial melting of eclogitized slabs, a process which is thought to result in intermediate arc magmas having unusually high Sr/Y and La/Yb ratios, termed an 'adakitic' signature (Defant and Drummond, 1990; Stern and Kilian, 1996; Mungall, 2002). High Sr/Y, Sm/Yb and La/Yb ratios are indicative of the presence of magmatic garnet in either the residual or fractionating assemblage, as heavy Rare Earth Elements (REEs) Y and Yb are preferentially incorporated into garnet over lighter REEs (Van Westrenen et al., 1999). However, the physical likelihood of slab melting, even in warm subduction zones, is in question (Garrison and Davidson, 2003; Macpherson et al., 2006; Chiaradia, 2009; Bouilhol et al., 2015; Spinelli et al., 2016).

1.1.1.2 Mantle processes

Hydration and partial melting of the mantle wedge is the main source of arc magmatism (Plank and Langmuir, 1988; Gaetani and Grove, 1998). The composition of the mantle controls the starting composition of arc magmas before any differentiation or contamination processes occur. Yet mantle compositions are not homogeneous (Pearce, 1983; Sun and McDonough, 1989; Salters and Stracke, 2004). Continental mantle lithosphere can have a relatively enriched composition compared to the depleted asthenospheric wedge (Sun and McDonough, 1989;

Salters and Stracke, 2004). Both physical and thermal erosion of the overriding plate lithosphere in subduction zones is thought to occur by: (1) subduction erosion of the forearc crust and lithosphere (Stern, 1991; Kay and Kay, 2002); (2) thermal erosion below the arc by ascending mantle wedge melts (Macpherson, 2008; Perrin et al., 2016; Rees Jones et al., 2018); and (3) regionally across the back arc by mantle wedge corner flow (Sun and McDonough, 1989; Tao and O'Connell, 1992; Turner et al., 2017). Subduction erosion is another mechanism which has been proposed to explain adakitic trace element signatures in intermediate melts, as during subduction erosion forearc crust and subducted sediments are taken to high pressures under the arc, where they would melt and contaminate mantle melts (Kay and Kay, 2002).

The degree of partial melting strongly influences geochemical arc systematics (e.g. Plank and Langmuir, 1988), and there are several physical factors which will influence the degree of mantle melting other than the starting composition. Slab surface and ambient mantle temperatures influence mantle wedge thermal structure (Syracuse et al., 2010). Mantle wedge thermal structure and thickness affect both the degree and location of partial melting (Plank and Langmuir, 1988; Turner and Langmuir, 2015b, 2015a; Turner et al., 2016; Perrin et al., 2018).

1.1.1.3 Crustal processes

The crust-mantle boundary is thought to be a density and/or temperature barrier which provides a natural stalling point for ascending basaltic magmas (Hildreth and Moorbath, 1988; Annen and Sparks, 2002; Jagoutz, 2014; Perrin et al., 2016). Current models for the genesis of arc basaltic-andesites and andesites involve repeated basaltic injection into a storage zone at the base of the crust, where processes of partial melting, assimilation and fractionation occur. Such zones have been named in the literature as either 'melting, assimilation, storage and homogenisation zones' (MASH; Hildreth and Moorbath, 1988); or 'deep crustal hot zones' (Annen and Sparks, 2002; Annen et al., 2006; Solano et al., 2012), shown in Figure 4. Slow seismic wave speeds and positive seismic tomography anomalies have been interpreted as a MASH zone under the Altiplano-Puna plateau (Delph et al., 2017). Exhumed deep arc sections in Argentina and Kohistan expose thick sections of chemically stratified cumulate layers overlain by frozen plutonic rocks, which are inferred to have formed near the crust-mantle boundary in a MASH or hot zone (Walker et al., 2015). Although, the most evolved and silicic arc products are thought to evolve in 'shallow crustal cold zones' (labelled 'upper crustal batholith' on Figure 4) and eruptions of these evolved products are likely triggered by mixing and recharge from more deeply sourced basalts and basaltic andesites (Kent et al., 2010; Adam et al., 2016). Long term mantle melt recharge, differentiation and melt segregation cause cumulate build up at and below the crust-mantle boundary. 'Cumulate roots' of arcs are thought to both build up the lithosphere and be convectively removed (Müntener and Ulmer, 2006; Kaislaniemi et al., 2014; Currie et al., 2015; Jenner, 2017). The lower crust and mantle lithosphere are generally thought to have a more refractory and depleted signature compared to the upper crust (Rudnick and Fountain, 1995; Rudnick, 1995).

Average arc compositions have been found to become increasingly evolved with increasing crustal thickness (Feigenson and Carr, 1986; Kent et al., 2010; Farner and Lee, 2017). Magmatic garnet is a high-pressure phase stable at depths ~>45 km, and even potentially as shallow as ~35km in hydrous conditions (Alonso-Perez et al., 2008). Garnet is therefore an important residual phase in hydrated mantle wedges and in the lower crust of thickened arcs (Van Westrenen et al., 1999; Macpherson et al., 2006; Alonso-Perez et al., 2008; Chiaradia, 2009). Regional and global compilations of averaged Sr/Y and La/Yb ratios from arcs and collision zones have been found to correlate strongly with crustal thickness, and are attributed to the increasing importance of garnet as a fractionating or residual phase with increasing crustal thickness (Chiaradia, 2015; Turner and Langmuir, 2015b, 2015a; Chapman et al., 2015a; Profeta et al., 2015a; Farner and Lee, 2017; Hu et al., 2017).

1.1.1.4 Crust and mantle reservoirs

Debate ensues over the relative importance of each of the above mechanisms, and especially on the interplay between mantle and crustal processes. $^{87}Sr/^{86}Sr$ and $^{143}Nd/^{144}Nd$ ratios, amongst other radiogenic isotope systems such as Pb and Hf, are useful tools which can help with interpreting sources and contaminants of igneous rocks (e.g. Zindler and Hart, 1986; Sun and McDonough, 1989; Rudnick and Fountain, 1995). The Earth's asthenospheric mantle has a 'depleted' isotope signature due to long term fractionation of parent/daughter ratios over Earth history (Sun and McDonough, 1989; Salters and Stracke, 2004; Workman and Hart, 2005). In the Rb/Sr system, Rb (parent) is more incompatible than Sr (daughter) and Rb is therefore more readily incorporated into and enriched in the continental crust. The Sm/Nd system behaves in the opposite way, as Nd (daughter) is more incompatible than Sm (parent). Therefore, the continental crust has evolved to higher $^{87}Sr/^{86}Sr$ and lower $^{143}Nd/^{144}Nd$ ratios relative to the mantle (Rudnick and Fountain, 1995; Rudnick, 1995). Different isotopic domains within the mantle and different basement terranes which make up the crust are isotopically distinct and so their relative contributions can be estimated (Sun and McDonough, 1989). The asthenosphere is the source of mid-ocean ridge basalts (MORB), MORB have a very uniform composition compared to arc basalts due to the influence of less potential contaminants (Sun and McDonough, 1989). MORB therefore act as a window to explore the composition of the asthenosphere, which is often referred to as the 'depleted mantle' (Sun and McDonough, 1989; Salters and Stracke, 2004; Workman and Hart, 2005). EM1 (Enriched Mantle 1) is the isotope composition most likely related to sub-lithospheric mantle compositions or mantle contaminated by assimilated subducted sediment or oceanic lithosphere (Sun and McDonough, 1989). Average composition of Global Subducting Sediment, "GLOSS", is similar to upper continental crust compositions (Plank and Langmuir, 1998).

1.3.1 Orogenesis and tectonic plateaux

Mountain chains (also called 'orogenic belts' or 'cordilleras') form as strain accumulates due to compressional forces acting within or between continental plates (Clark et al., 1988; Jamieson and Beaumont, 2013). Convergent margins and continental deformation are arguably the most complicated and dynamic plate boundaries and the mechanisms which accommodate overall plate convergence within plate interiors remains a fundamental question in modern geological research (Schellart and Rawlinson, 2010; Allen et al., 2017). Orogenic plateaux are characterised by having high, flat and wide intra-mountain basins with deformation mainly occurring in fold and thrust belts on the lower bordering margins (Jordan et al., 1983a; Allmendinger et al., 1997; McQuarrie, 2002b; DeCelles and Horton, 2003; Oncken et al., 2012). The Tibetan Plateau and Himalayas are the classic case studies. The Tibetan Plateau is the largest tectonic plateau and formed from the collision between India and Eurasia (Molnar and Tapponnier, 1977; Molnar et al., 1993). In contrast, the Andean Plateau (2nd largest tectonic plateau) is the only modern day tectonic plateau which has resulted from oceanic-continental subduction (Schellart and Rawlinson, 2010).

Shortening and thickening of the continental crust combined with subduction and accretion of material during collision are important factors leading to orogenesis (Jamieson and Beaumont, 2013). As the continental crust thickens it forms a relatively buoyant crustal 'root' which supports high elevations by isostasy (Allmendinger et al., 1997; Watts, 2001). As the crust shortens, the underlying continental lithosphere must also shorten and thicken, which introduces cold, dense material into the hotter asthenosphere (Houseman et al., 1981). If thickened lithosphere undergoes the gabbro-eclogite transition it will become denser and create excess mass (Sobolev and Babeyko, 2005), this would result in lower elevations than would be predicted by isostasy (Figure 5; Molnar et al., 1993). Such a cold, dense lithospheric root has been suggested to be gravitationally and convectively unstable (Molnar et al., 1993). Removal of dense lithosphere has been termed 'delamination', for which several different mechanisms have been proposed: (1) large scale, orogen wide delamination (Houseman et al., 1981; Molnar et al., 1993; Garzione et al., 2006, 2008); (2) small scale 'drip' delamination (Ducea et al., 2013; Kaislaniemi et al., 2014); and (3) continuous, ablative, thermal erosion of the lower lithosphere by mantle wedge corner flow (Tao and O'Connell, 1992). However, the negative thermal buoyancy of continental lithosphere relative to the mantle asthenosphere has suggested to be offset by a reduction in compositional density of the lithosphere caused by long-term melt extraction and residue accumulation (Jordan, 1978; Lee, 2003). This argument has been used to suggest that whole-sale mantle delamination is unlikely, as the density contrast between lithosphere and asthenosphere is not great enough (Jordan, 1978; Lee, 2003).

Removal of dense lithosphere would in turn lead to dynamic uplift at the surface and would expose the lower crust to asthenospheric temperatures (Houseman et al., 1981; Molnar et al., 1993). The processes of delamination are important for understanding the uplift of mountains and, especially, for sustaining the width of highly elevated and flat tectonic plateaux. One very large lithosphere removal event would result in very rapid uplift (up to ~2 km) over a geologically short timescale (<<10 Myr) (Garzione et al., 2006, 2008). Smaller scale 'drip' delamination would be associated with cyclic periods of uplift and shortening (DeCelles et al., 2009). Continual removal of the lithosphere would lead to elevations being supported mainly by isostasy, and uplift occurring synchronously with crustal shortening and thickening (Barnes and Ehlers, 2009). Cyclic 'drip-type' delamination below thick-crusted arcs has been associated with 'flare-up' modes in arc magmatism (Kay and Kay, 1993; Davidson and de Silva, 1995; DeCelles et al., 2009; Ducea et al., 2013; Burns et al., 2015) and has also been related to magmatic thickening, for example, the development of the large Altiplano-Puna Magma Body (APMB; e.g. Ward et al., 2014; Perkins et al., 2016).

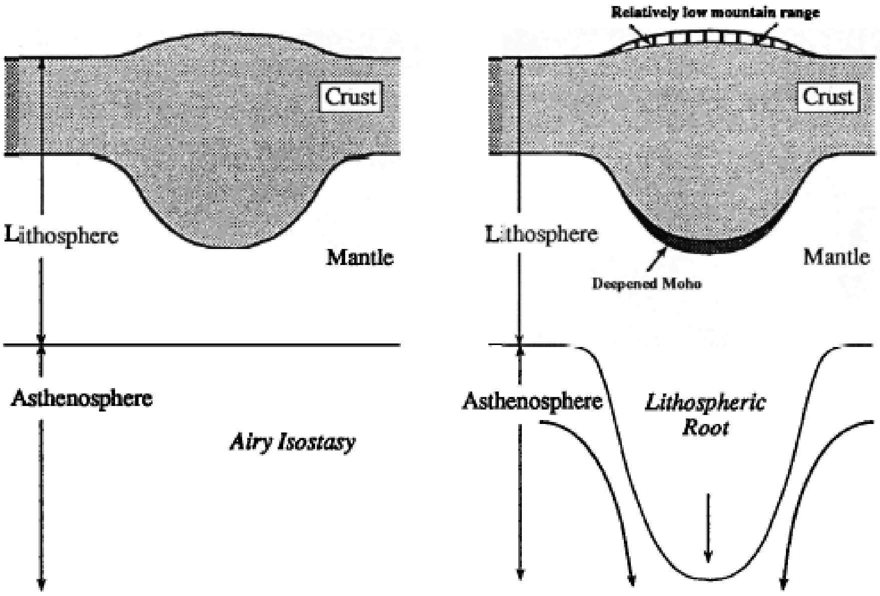

Figure 5: Two schematic diagrams of mountain belts showing the difference between elevations supported by Airy Isostasy (left), and thickening of the entire mantle lithosphere (right), taken from (Molnar et al., 1993). Lithospheric thickening has been suggested to create excess mass and result in lower elevations than the Airy model, however the compositional density of the lithosphere may offset it's negative thermal buoyancy (Jordan, 1978; Lee, 2003).

1.4 The Andean Margin

The Andean margin (Figure 6) is the text-book example of oceanic-continental subduction. The Central Andes have the highest elevations (>4 km) and thickest crust (exceeding 60 km;

(Assumpção et al., 2013) of any modern day subduction zone. Geophysical evidence requires a thin mantle lithosphere under the Andean Plateau, despite significant shortening and thickening (e.g. Tassara and Echaurren, 2012).

From west to east the Andean Plateau spans over 400 km and is divided into three tectonically distinct zones: the Western Cordillera (including the active Central Volcanic Zone, CVZ, of the Andean arc); the internally drained Altiplano and Puna plateaux; and the Eastern Cordillera and Sub-Andean fold-and-thrust belts (Figure 6). The Western and Eastern Cordilleras form drainage divides which isolate the internally-drained Altiplano and Puna basins. Both the Altiplano and Puna basins combine to form the central core of the Andean Plateau, but the two basins are morphologically distinct. The Altiplano has average elevations of ~3.7 km and has very low relief (for example the Salar de Uyuni, Bolivia, is the world's largest salt flat, >10,500 km^2), whereas the Puna has higher average elevations (~4.2 km) and has a higher relief (Barnes and Ehlers, 2009). The Eastern Cordillera is the highest relief unit of the Andean Plateau, comprised of deformed Precambrian basement, Paleozoic sediments and overlying Cenozoic volcanics (McQuarrie, 2002b). The Altiplano-Eastern Cordillera boundary consists of both thick and thin skinned deformation styles.

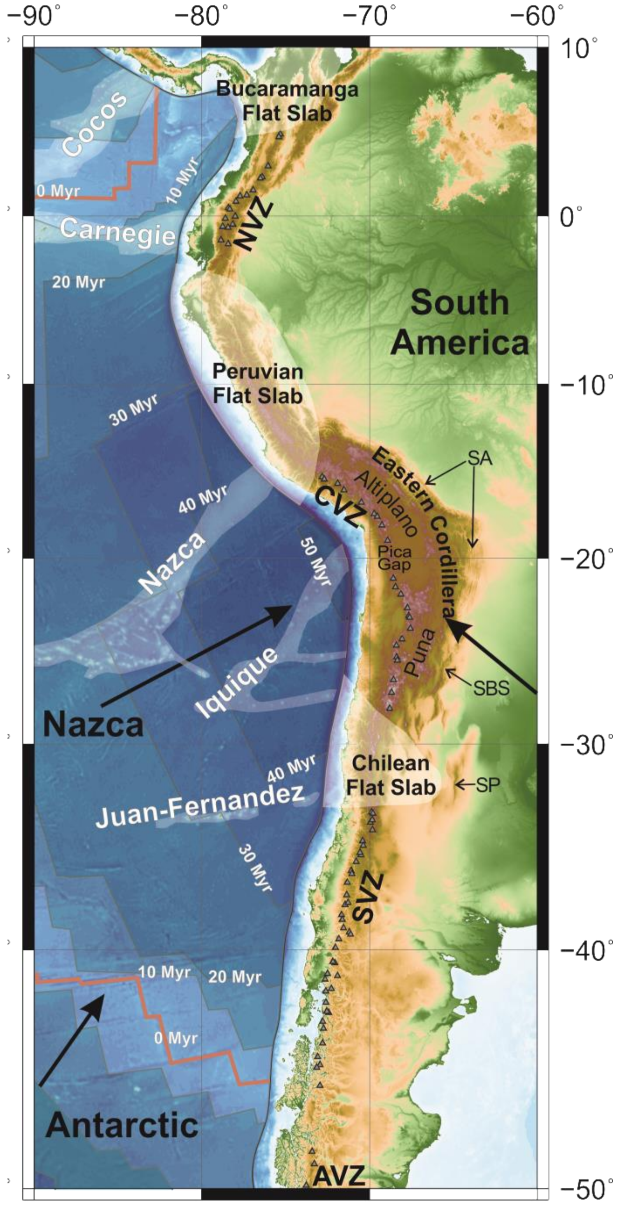

Figure 6: A topographic and bathymetric overview map of the Andean subduction system. On the incoming Nazca plate 10 Myr age contours are shown (Sdrolias & Müller, 2006) alongside the main bathymetric features entering the subduction zone. Black arrows represent the absolute plate velocities (Sdrolias and Müller, 2006). The present locations of the three South American flat slabs are highlighted and labelled. Grey triangles are locations of Quaternary frontal arc volcanoes of the Northern, Central, Southern and Austral (NVZ, CVZ, SVZ and AVZ, respectively). The Western Cordillera is located along the CVZ arc. Tectonic zones of the Andean Plateau are: SA, Sub-Andean fold and thrust belt; SBS, Santa Bárbara System; and SP, Sierras Pampeanas.

Deformation style east of the Eastern Cordillera switches from north to south between predominantly low-angle, 'thin-skinned' fold and thrust belts like the Sub-

Andean belt (bordering the Altiplano in the north), to thick-skinned deformation in the Santa Bárbara System (Southern Puna) and Sierras Pampeanas (Figure 6; Kley et al., 1999; Kley and Monaldi, 1998; Martinod et al., 2010; McQuarrie, 2002b). The Santa Bárbara System and Sierras Pampeanas are characterised by high angle reverse faults and basement uplifts (Kley et al., 1999), which have in turn been associated with an over-thickened lithosphere relating to the Chilean flat slab (Gutscher, 2002; Martinod et al., 2010).

The crust of the high Altiplano and Puna is largely aseismic, with only a few strike-slip and extensional events recorded in the Altiplano (Devlin et al., 2012). The vast majority of active compressional strain in the Central Andes is accommodated in the Eastern Cordillera and Sub-Andean belts (Oncken et al., 2012). The two most seismically active regions of the Central Andes are above the Chilean and Peruvian flat slab segments (Jordan et al., 1983a; Gutscher et al., 2000), where earthquakes can occur even within the usually aseismic lower crust (Devlin et al., 2012). North and south of the plateau Andean arc magmatism continues in the Northern and Southern Volcanic Zones (NVZ and SVZ, respectively), which are separated from the CVZ by two volcanic gaps occurring above segments of sub-horizontal subduction. So called 'flat slabs' occur at three locations in the Andes associated with no modern arc magmatism on the overriding plate (Figure 6; Jordan et al., 1983; Manea et al., 2017; Ramos and Folguera, 2009). The Nazca Plate entering the trench along the Andean margin is relatively young (<60 Myr; Figure 6) compared to the global slab age range of 0-160 Ma (Sdrolias and Müller, 2006). The Andean subduction zone is also characterised by a shallow slab dip along the entire margin, generally <30 °, compared to other subduction zones which usually have slab dips >40° and can be up to 90° (Lallemand et al., 2005).

The seaward concave bend of the South American coastline, the 'Arica Bend', and the corresponding curve of the Bolivian Orocline (Isacks, 1988; McQuarrie, 2002b), have attracted much attention as subduction zones usually have a seaward convex shape (e.g England et al., 2004). The degree of crustal shortening is greatest in the Altiplano region, inboard of the Arica bend (~420 km; McQuarrie, 2002; Schepers et al., 2017). Shortening estimates decrease systematically both to the north and south (McQuarrie, 2002a; Schepers et al., 2017). Paleo-magnetic rotation data from the Andean forearc and evidence from plate reconstructions indicate that the concave margin developed from ~70-20 Ma and can be explained by the differential degrees of shortening observed in the Eastern Cordillera and Sub-Andean belt (Arriagada et al., 2006b, 2008; Schepers et al., 2017). Minimal degrees of bending have occurred since ~20 Ma (Arriagada et al., 2008). The break-up of the Farallon oceanic plate into the Nazca and Cocos plates caused a shift in the plate convergence rate and direction during the late Oligocene to early Miocene, at around ~20 Ma (Sdrolias and Müller, 2006; Seton et al., 2012), and could be associated with the changes in deformation observed in the Andean plate at this time.

1.4.1 Pre-Andean basement

The South American continent is made up of several Pre-Cambrian to Early Paleozoic metamorphic basement terranes which were adjusted, separated and accreted during global plate reorganisations, such as the dispersal of Rodinia and the reconstruction of the Gondwana supercontinent (Figure 7; Ramos, 2008). Characterising the continental basement is important for studying and understanding the influence of the crust on ascending arc magmas (e.g. Davidson et al., 2005). The Andean basement is somewhat difficult to characterise due to the lack of basement exhumation and widespread cover of Tertiary sediments (e.g. Figure 7a). Geochemical analysis of metamorphic xenoliths and study of Pb isotope compositions of Andean arc lavas define the boundaries between exposed basement outcrops (Tilton and Barreiro, 1980; Damm et al., 1994; Davidson and de Silva, 1995; Aitcheson et al., 1995; Tosdal, 1996; Lucassen et al., 2000; Wörner et al., 2000; Mamani et al., 2008; McLeod et al., 2013; Chapman et al., 2015b).

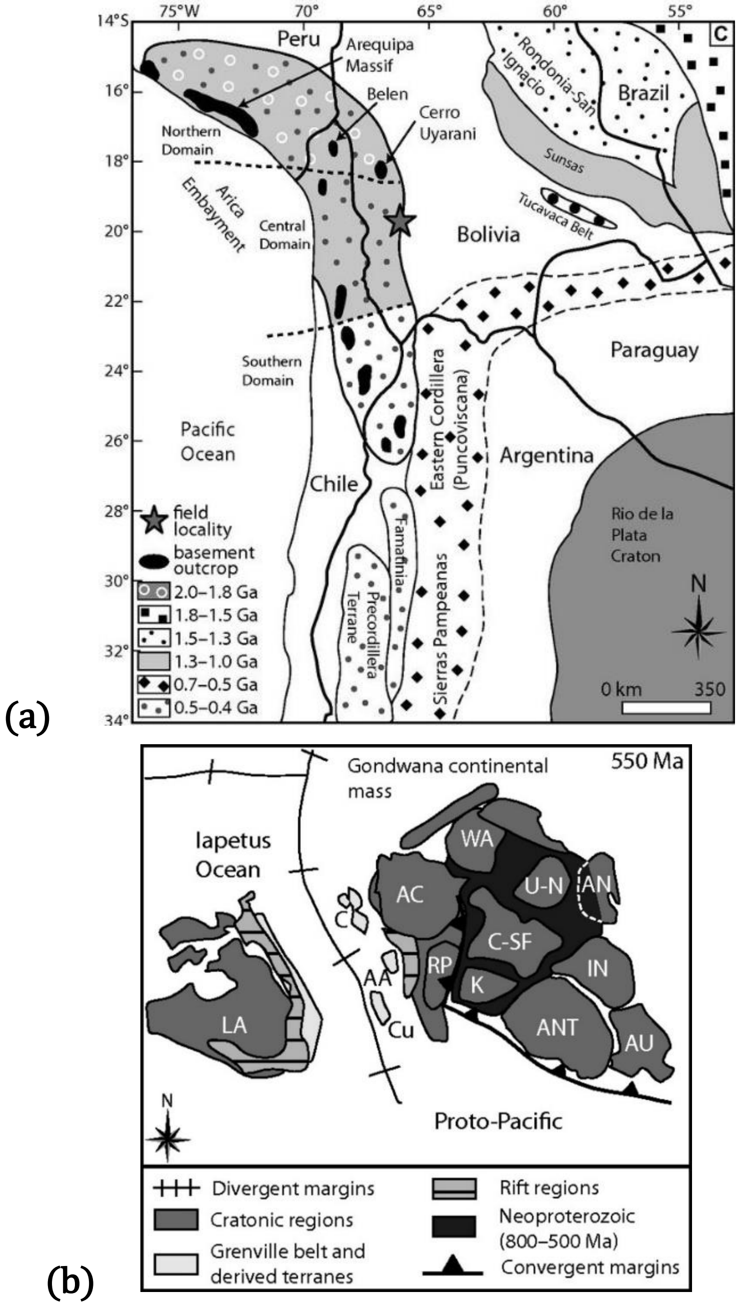

Figure 7: Taken from McLeod et al. (2013). (a) A map showing three basement domains within the Arequipa-Antofalla basement (AAB) block of the Central Andes and slightly younger Precordillera Terrane in the south-Central Andes (Loewy et al., 2004). Note that outcrops of metamorphic basement are rare. The two large continental cratons, the Brazilian and Rio de la Plata, are shown on the eastern side of the map. (b) Plate re-construction map for the beginning of the Cambrain period (Cordani et al., 2005). AA—Arequipa-Antofalla basement; AC—Amazonian Craton; AN—Arabian-Nubian Shield; ANT—Antarctica; AU—Australia; C-SF—Congo–San Francisco; C—Colombian basement; Cu—Cuyania; IN—India; K—Kalahari; LA—Laurentia; RP—Rio de la Plata; U-N—Uweinat-Nile; WA—western Africa.

Mamani et al. (2008) synthesised a large geochemical database of Andean basement and volcanic rocks ranging from Proterozoic to Recent. They argue that even though tectono-geographic arrangements changed, the crustal column under the Coastal-. Pre- and Western-Cordilleras largely remained unchanged from the Paleozoic-Neogene (Mamani et al., 2008). Lead isotopic compositions (especially $^{206}Pb/^{204}Pb$) of Central Andean volcanics have been shown to reflect the transition to the Pre-Cambrian and mafic Arequipa terrane located along the Peruvian coastal cordillera (Figure 7a; Tilton and Barreiro, 1980; Aitcheson et al., 1995; Wörner et al., 2000; Mamani et al., 2008). The Arequipa domain does not have the same affect on ^{87}Sr/^{86}Sr or ^{143}Nd/^{144}Nd ratios of volcanic rocks, as lavas erupted through both Arequipa and the more felsic Paleozoic Antofalla terrane have a similar range of radiogenic compositions (Mamani et al., 2008). A much younger buoyant oceanic plateau accreted to the Ecuadorian continental margin during the Late Cretaceous to Eocene times, and is relatively more mafic in composition than the older and more felsic Andean basement terranes and therefore has a much less radiogenic isotope signature (Cordani et al., 2005; Allibon et al., 2008).

1.4.2 A brief tectonic history of the Andean margin

Schematic diagrams representing an overview of basin development in the Central Andes are shown in Figure 8 (Horton, 2018a). Marine fossil-bearing sediments intercalated with Jurassic to Early Cretaceous Andean arc lavas, alongside large accumulations of back arc sedimentation, indicate that the early Andean arc developed in an extensional tectonic setting partly below sea level (Mamani et al., 2010; Rossel et al., 2015; Horton, 2018a). In the Early- to Mid-Cretaceous, there was a period of localised extension and crustal thinning as the Salta rift developed at the current location of the southern Eastern Cordillera and Santa Barbara System, which has been proposed to coincide with opening of the South Atlantic from ~130-120 Ma (Coira et al., 1982; Horton, 2018b). A switch from post-rift subsidence to retro-arc shortening in the Late Cretaceous is evident from the development of fold and thrust systems in the current locations of the Coastal Cordillera and Chilean Precordillera (Arriagada et al., 2006b; Horton, 2018b). The onset of compressional deformation in the Western Cordillera between 90-70 Ma is evident from angular unconformities and extensive conglomerate deposition in a developing foreland basin within the back-arc region (Haschke et al., 2002b; McQuarrie, 2002b; Oncken et al., 2006; Carlotto, 2013). Marked differences in provenance of Late Eocene-Oligocene sediments between basins east and west of the 'Proto'-Western Cordillera provide evidence for the formation of a drainage divide at this time (Wotzlaw et al., 2011). Deformation and crustal shortening then became diachronous in both the Western and Eastern cordilleras from c. 50-40 Ma (McQuarrie et al., 2005; Oncken et al., 2006), at the time that the Altiplano and Puna regions remained close to sea level in-between the two deformation belts (Lamb et al., 1997; Lamb and Hoke, 1997). Tectonic inversion of faults and lithospheric weaknesses related to the Salta Rift in the Neogene may have been key to accommodate shortening and eastward widening of the deformation belt into the Eastern Cordillera (Deeken et al., 2006). Uplift-related facies changes within forearc basins occurred at ~35 Ma (Decou et al., 2013). The Paleogene period is thought to have had a 'mixed-mode' tectonic setting, switching between phases of compression and neutral stress regimes (Horton, 2018b).

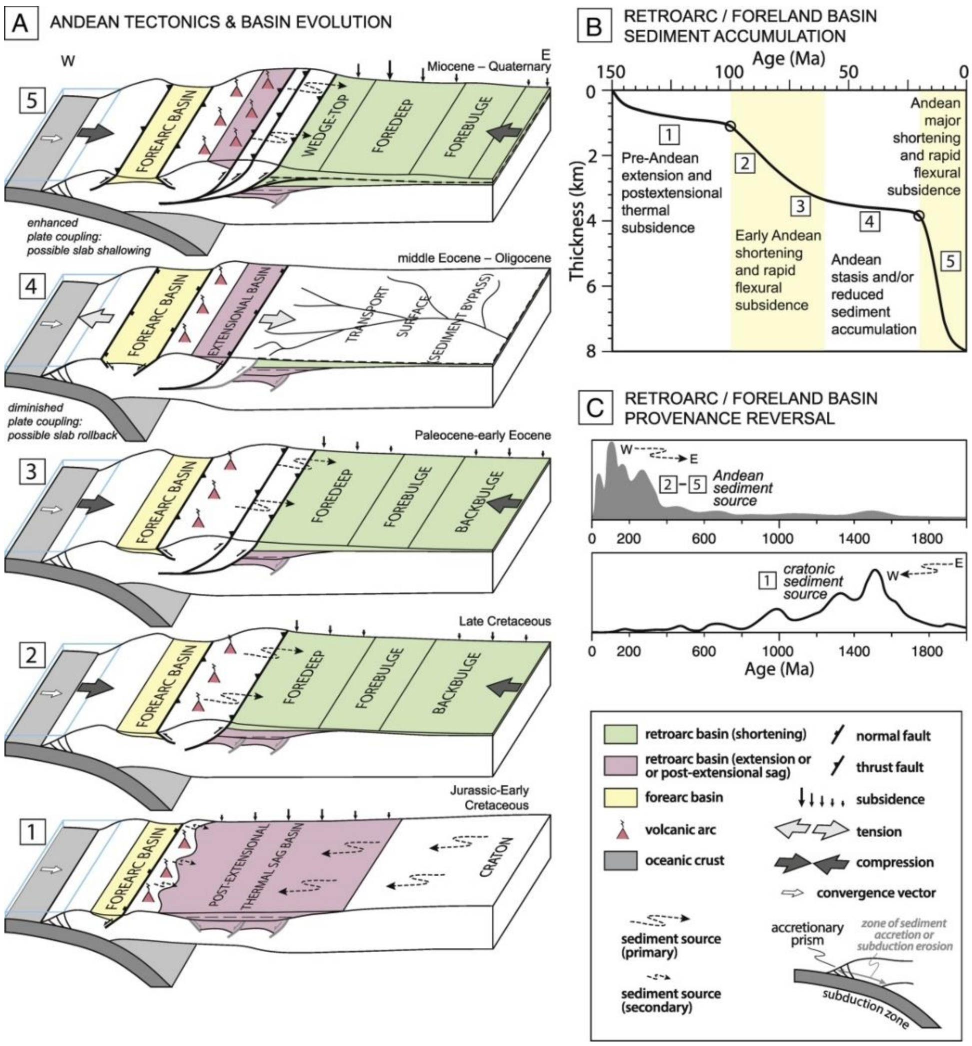

Figure 8: Schematic diagrams depicting basin development in the Central Andes, taken from Horton (2018a).

1.4.3 Andean arc magmatism

Large volumes of Andean arc magmatism have been emplaced along the South American margin since >200 Ma as result of oceanic subduction under the South American continent (Coira et al., 1982). During this time the locus of Central Andean arc magmatism has progressively shifted eastward from the modern coastline to its present location (Coira et al., 1982; Kay et al., 2006). The extensive Andean magmatic record and along strike variability in crustal thickness make the Andes the perfect study area for exploring tectono-magmatic interactions and crustal thickening through time (Trumbull et al., 1999, 2006; Haschke et al., 2002b; Kay and Coira, 2009; Mamani et al., 2010; Kay et al., 2014; Jones et al., 2015). Even though elevation has been used as a proxy for crustal thickness to explore the influence of crustal thickness on global geochemical systematics (Farner and Lee, 2017), geochemistry had not previously been used as a proxy for regional scale elevation until Scott et al. (2018), shown in Chapter 4 of this thesis.

1.5 Outstanding questions in Andean geology

1.5.1 What caused the onset of Andean shortening and thickening at ~70-50 Ma?

Although subduction along the Andean margin has been ongoing since at least the early Jurassic (~200 Ma; Haschke, et al., 2006; Ramos, 2009), compressional deformation in the overriding plate did not initiate until 70-50 Ma at the earliest (McQuarrie et al., 2005; Oncken et al., 2006; Barnes and Ehlers, 2009; Garzione et al., 2017). The particular set of subduction parameters related to the initiation of shortening in the Central Andes after over 100 Myr of subduction with a neutral to extensional tectonic regime in the overriding plate, are still enigmatic (Lamb and Davis, 2003; Schellart and Rawlinson, 2010; Capitanio et al., 2011; Maloney et al., 2013; Faccenna et al., 2017; Horton, 2018b). The characteristically shallow slab dip below the Andes has been related to the high degrees of shortening and thickening in the Andes (Jordan et al., 1983a). Flat slabs are thought to have been locally transient and migrating features under the Andean margin throughout the Cenozoic (Kay and Mpodozis, 2002; Kay et al., 2006; Ramos and Folguera, 2009; Kay and Coira, 2009; Schepers et al., 2017). The existence of both the Peruvian and Chilean flat slabs since the Pliocene (~5-10 Ma) and the potential existence of a southward migrating flat slab below the current Puna region in the Eocene-Oligocene (~50-25 Ma) have been suggested to explain both increased plate coupling, contractional deformation and the migration of the main deformation belt over 400 km into the back-arc (Gutscher, 2002; Espurt et al., 2008; Martinod et al., 2010; O'Driscoll et al., 2012). In contrast, there is not currently a relationship between increased degrees of shortening and the current flat slab segments, as the highest degrees of shortening are located around the Bolivian Orocline and decrease to the north and south (McQuarrie, 2002a). Furthermore, simulations of flat slab subduction require overriding plate crustal and lithospheric thickening to induce 'mantle-suction' forces in the mantle wedge which lead to slab shallowing (Rodríguez-González et al., 2012; Manea et al., 2017).

Results from studies using numerical models of subduction have related the onset of Andean crustal thickening with 'slab anchoring' at the mantle transition zone, which generates large scale return flow in the mantle wedge and drags the upper plate into the subduction zone (Faccenna et al., 2017). Other numerical modelling studies have suggested that slab-age dependent sinking of the slab can, in turn, increase mantle wedge corner flow and traction forces at the base of the upper plate towards the trench (Capitanio et al., 2011). Other models point to mechanisms which increase shear stresses at the Nazca-South America plate interface, for example by trench sediment starvation (Lamb and Davis, 2003; Sobolev and Babeyko, 2005).

Most previous models require the South American plate velocity to be in a direction towards the trench (e.g. Schepers et al., 2017) but, as yet, there is no agreement on what caused the initiation of deformation at the western margin of the South American plate in the Late Cretaceous to Paleogene, which takes into account known variations in subduction parameters both along strike and though time.

1.5.2 The Andean uplift debate

Another debate revolves around the timing and magnitude of surface uplift of the Andean Plateau (see also recent reviews on this topic: Garzione et al., 2017; Schildgen and Hoke, 2018). Uplift of the Andean Plateau is known to be segmented, for example the Western and Eastern Cordilleras rose earlier than either the internal Altiplano or Puna (Lamb et al., 1997; Lamb and Hoke, 1997; Wotzlaw et al., 2011; Decou et al., 2013; Schildgen and Hoke, 2018), however there are still two prevalent end-member models of Andean Plateau uplift (Barnes and Ehlers, 2009; Garzione et al., 2017): (1) slow, steady uplift from at least 40 Ma primarily due to crustal thickening and continual lithosphere removal (Mamani et al., 2010; McQuarrie et al., 2005; Carrapa et al., 2006; Carlotto, 2013; Canavan et al., 2014; Chapman et al., 2015b; Zhou et al., 2017); and (2) rapid, recent surface uplift post 16 Ma as a result of large-scale lower lithosphere removal, magmatic thickening or lower crustal flow (Garzione et al., 2006, 2008; Leier et al., 2013; Kar et al., 2016; Garzione et al., 2014; Schildgen et al., 2009; Lamb, 2011, 2016; Perkins et al., 2016). Lower crustal flow from regions of tectonically thickened crust to areas of less thick crust, is a mechanism which has been proposed to account for crustal thicknesses (mainly in the Puna region) that cannot be explained by crustal shortening estimates (Gerbault et al., 2005; Ouimet and Cook, 2010).

The recent and rapid model of uplift was originally proposed by Garzione et al. (2006, 2008) and is based on paleoelevation proxies, such as stable isotope techniques (Garzione et al., 2006, 2008; Leier et al., 2013; Canavan et al., 2014; Kar et al., 2016) and paleobotany (e.g. Gregory-Wodzicki et al., 1998; Kar et al., 2016; and references therein). Stable isotope paleoeveleation proxies rely on the assumption that parameters such as air temperature and humidity follow the same dependency on elevation in the past as they do now in the present (Garzione et al., 2017). However, regional climate change related to surface uplift (e.g. development of the Atacama rain shadow; Dunai et al., 2005) may account for some of the signals used to interpret elevation gain (Barnes and Ehlers, 2009; Insel et al., 2012; Fiorella et al., 2015; Schildgen and Hoke, 2018). These paleoclimate conditions are difficult to correct for and can hence result in large errors in paleoelevation estimates of up to a few kilometres (Insel et al., 2012; Fiorella et al., 2015). The debate on topographic evolution of the Andes (and other tectonic plateaux) remains a hot topic due to the implications of timing of uplift on Cenozoic climate change and associated evolution of fauna and flora (Hartley, 2003; McKenzie et al., 2014; Armijo et al., 2015).

1.6 Thesis outline

In this thesis, the main aims are to quantitatively and statistically explore relationships between modern physical characteristics of the down-going slab and Andean arc geochemical systematics to the distribution of crustal thickness in the South American plate. Relationships between crustal thickness and elevation are studied to determine if elevations are primarily supported by isostacy. These relationships are explored in attempt to answer fundamental questions relating both to the onset of crustal shortening and thickening and to the timing of uplift events in the Western Cordillera of the Andean Plateau.

1.6.1 Chapter 2

With the aim of studying the initiating mechanisms that caused Andean shortening and thickening, statistical techniques are employed to analyse the present-day structure and dynamics of the Andean subduction zone. A very strong correlation is found between Nazca plate age entering the trench and Andean crustal thickness ($r = 0.939$; $r^2 = 0.882$; p value < 0.01). Thrust earthquakes at the Nazca-South America plate interface occur only where the slab age at the trench is older than 30 Myr or where oceanic ridges are colliding with the trench. A new hypothesis is proposed, that the initiation and distribution of crustal shortening in the Andes can be attributed to long term subduction of intermediate aged oceanic lithosphere (~30-80 Myr) combined with trench-ward overriding plate motion. Intermediate aged lithosphere has greater mechanical strength than younger oceanic lithosphere but is relatively buoyant compared to older oceanic lithosphere.

1.6.2 Chapter 3

Correlations between crustal thickness and certain geochemical parameters of arc lavas are well established, both globally and along individual arc segments, but the causative mechanisms which explain these relationships remain debated. The young slab age in the Andes may also affect geochemical signatures at the arc. In this chapter, a dataset is compiled which combines Quaternary Andean arc geochemistry with subduction parameters (slab age, slab thermal parameter) and depths to geophysical boundaries (crustal thickness, lithosphere-asthenosphere depth and depth to slab), to explore and quantify the control of crustal thickness upon Andean geochemistry.

1.6.3 Chapter 4

Building on the results of Chapter 3, a new climate-independent approach is proposed to constrain regional Andean surface uplift in the Western Cordillera. Strong linear correlations exist between smoothed elevation and $^{87}Sr/^{86}Sr$ (R^2=0.858, n=17) and $^{143}Nd/^{144}Nd$ (R^2=0.919, n=16) ratios of non-plateau arc lavas. $^{87}Sr/^{86}Sr$ and $^{143}Nd/^{144}Nd$ ratios of the Quaternary

Central Andean arc, within the Andean Plateau, are distinct from non-plateau arc lavas (>0.705 and <0.5125, respectively), and termed as a 'plateau discriminant' signature. These relationships are used to constrain 200 Myr of surface uplift history for the Western Cordillera.

The work presented in this chapter has been published in Nature Communications (DOI: 10.1038/s41467-018-03173-4).

1.6.4 Chapter 5

The Paleogene (66-23 Ma) is a critical tectonic period of Andean Plateau thickening and uplift. Paleogene Andean arc lavas that have previously been mapped and dated were selected for major, trace element and Sr- and Nd-isotope analyses. The new data fit well with the elevation model proposed in Chapter 4. Furthermore, a 'petrological-switch' is identified near the Late Cretaceous-Paleogene boundary, which suggests deeper magma equilibration depths below the plagioclase stability field in Paleogene and younger lavas compared to Jurassic-Early Cretaceous lavas. The results support geological evidence of crustal thickening in the Western Cordillera at this time.

Chapter 2: Long term subduction of intermediate aged oceanic lithosphere can explain slow and steady Andean shortening

2.1 Chapter Summary

Synthesis and analysis of multiple geological and geodynamical datasets allows us to relate incoming slab age to the initiation of crustal thickening in the Andes. The slab age entering the Andean trench over the last 190 Myr has been consistently younger than 80 Myr. We show that the dates where slab ages become older than 40 Myr at the trench match with dates corresponding to the onset of compressional deformation in the Western Cordillera. A very strong correlation is found between slab age at the trench and overriding plate crustal thickness along the Andean margin ($r = 0.939$; $r^2 = 0.882$; p value < 0.01). Thrust earthquakes at the Nazca-South America plate interface occur only where the slab age at the trench is older than 30 Myr except where aseismic ridges are being subducted in the Northern Andes. Where the slab is younger than 30 Myr, there is a lack of any slab related seismicity either at the plate interface or at depth. These results support previous hypotheses that the elastic thickness and mechanical strength of slabs increase for slabs >30 Myr in age, yet we further suggest that slabs younger than 30 Myr are intrinsically weak. Intermediate slab ages (~30-80 Myr) have a greater mechanical strength than younger slabs,but are still relatively buoyant compared to older slabs. The strong correlation between slab age and overriding plate crustal thickness can therefore be attributed to increased plate coupling and overriding plate compression associated with trench-ward overriding plate motion and longterm subduction of intermediate aged slabs (~30-80 Myr). The southward younging of slab ages over time can provide a possible explanation for the degree of crustal shortening being greatest in the Altiplano region and decreasing systematically both to the north and south.

Where plate convergence rates are high and slab ages are between 30-80 Myr, ridge collision further enhances increased plate coupling and overriding plate thickening, and crucially, allows the overriding plate lithosphere to thicken faster than it can be thermally eroded by arc magmatism or wedge corner flow. This generates a hydrodynamic suction force in the mantle wedge which shallows the slab and shuts off arc magmatism. Flats slabs are related to changing deformation style in the overriding plate.

2.2 Introduction

Subduction is the main driving force of plate tectonics, the negative buoyancy of subducted slabs generate gravitational pull forces which drive tectonic plate motions and excite mantle flow (Conrad and Lithgow-Bertelloni, 2002; Schellart, 2004). The age of the subducting oceanic plate entering the trench is the main control on oceanic plate thickness and the temperature-dependant density of the slab (Molnar and Atwater, 1978; Caldwell and Turcotte, 1979; Carlson et al., 1983; McKenzie et al., 2005; Capitanio et al., 2011). Oceanic plate thickness and density in turn control both the resistance of the slab to bending (Faccenna et al., 2007; Hu et al., 2016; Zhang et al., 2018) and the magnitude of the slab pull force (Conrad and Lithgow-Bertelloni, 2002; Schellart, 2004). Complex interactions between incoming oceanic plate age (Molnar and Atwater, 1978; Capitanio et al., 2011), subducted slab dip (Lallemand et al., 2005; Sdrolias and Müller, 2006; Crameri et al., 2017), relative and absolute plate velocities (Heuret and Lallemand, 2005a; Maloney et al., 2013; Guillaume et al., 2018; Cerpa et al., 2018) and large scale mantle flow (Sdrolias and Müller, 2006) amongst global subduction zones have been suggested to control the tectonic regime in the overriding plate.

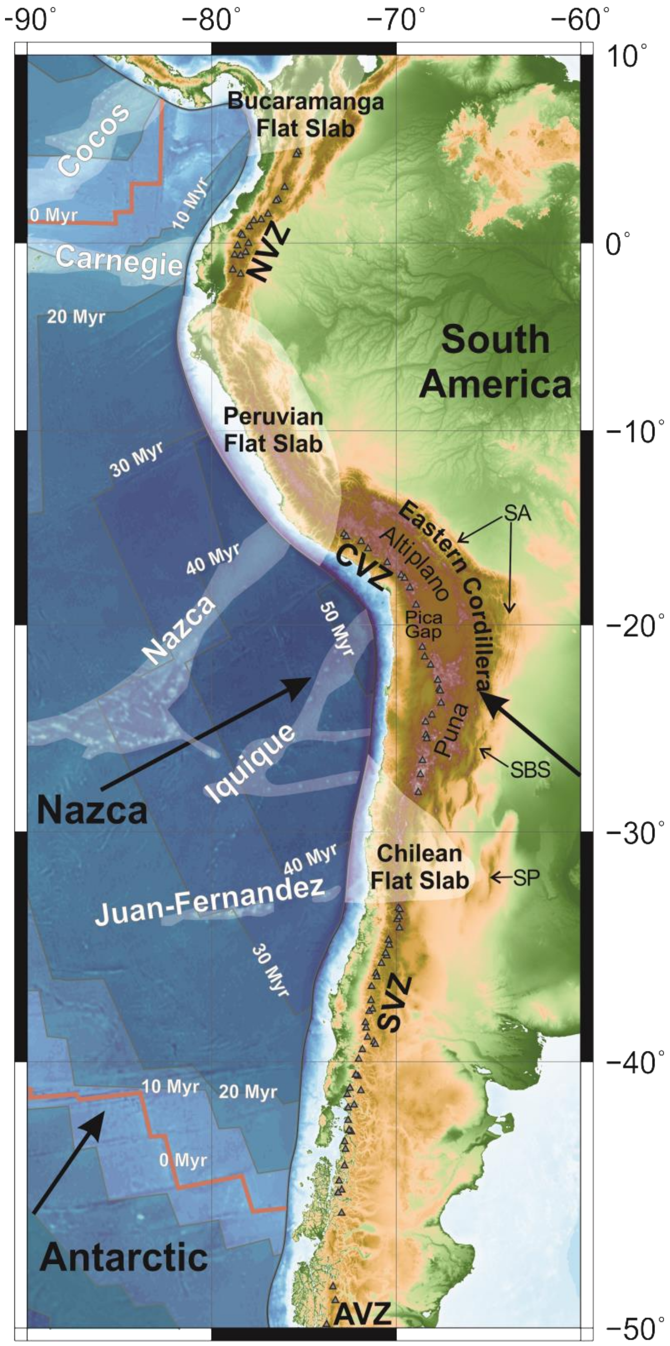

Figure 9: A topographic and bathymetric overview map of the Andean subduction system. On the incoming Nazca plate 10 Myr age contours (Sdrolias & Müller, 2006) and aseismic ridges are highlighted. Black arrows represent the absolute plate motions relative to the absolute reference frame (Sdrolias and Müller, 2006). The present locations of the three South American flat slabs are highlighted and labelled. Grey triangles are locations of Quaternary frontal arc volcanoes of the Northern, Central, Southern and Austral (NVZ, CVZ, SVZ and AVZ, respectively). Tectonic zones of the Andean Plateau are: SA, Sub-Andean fold and thrust belt; SBS, Santa Bárbara System; and SP, Sierras Pampeanas.

The Andean margin (Figure 9) is the text-book example of oceanic-continental subduction. The Central Andes have the highest elevations (>4 km) and thickest crust (exceeding 60 km; (Assumpção et al., 2013) of any modern day subduction zone. Despite this, the geodynamic evolution and timing of Central Andean Plateau formation remains uncertain (Barnes and Ehlers, 2009; Capitanio et al., 2011; Maloney et al., 2013; Faccenna et al., 2017; Garzione et al., 2017; Horton, 2018b). The Andean Plateau is the second largest tectonic plateau in the world and the only present-day tectonic plateau which has not formed due to continental collision (Jordan et al., 1983a; Gephart, 1994; Gregory-Wodzicki, 2000; Barnes and Ehlers, 2009; Garzione et al., 2017). Although subduction along the Andean margin has been ongoing since at least the early Jurassic (~200 Ma; Haschke, et al., 2006; Ramos, 2009), compressional deformation in the overriding plate did not initiate until 70-50 Ma at the earliest (McQuarrie et al., 2005; Oncken et al., 2006; Barnes and Ehlers, 2009; Garzione et al., 2017). The particular set of subduction parameters related to the initiation of shortening in the Central Andes after over 100 Myr of subduction with a neutral to extensional tectonic regime in the overriding plate, are still enigmatic (Schellart and Rawlinson, 2010; Capitanio et al., 2011; Maloney et al., 2013; Horton, 2018b). The magnitude and style of deformation in the Andes also vary along strike. The degree of crustal shortening is greatest in the Altiplano region, inboard of the Arica bend (~420 km; McQuarrie, 2002; Schepers et al., 2017). Shortening estimates decrease systematically both to the north and south (McQuarrie, 2002a; Schepers et al., 2017). Deformation style in the Central Andes switches between thin-skinned shallow fold and thrust belts like the Sub-Andean belt, to thick-skinned basement involved deformation in the Santa Bárbara System and Sierras Pampeanas (Figure 9; Kley et al., 1999; Kley and Monaldi, 1998; Martinod et al., 2010; McQuarrie, 2002b). One explanation for this variation in shortening is that climate-driven aridification of the Atacama, related to uplift of the Andean Plateau, led to sediment starvation at the trench which further focused plate boundary stresses at the subduction zone interface and enhanced compressional deformation (Lamb and Davis, 2003).

Complex relationships and feedback loops between incoming oceanic plate age, subducting sediment thickness, slab dip, plate motions and overriding plate heterogeneities make it difficult to define causal relationships between subduction parameters and overriding plate deformation. Both oceanic plate age at the trench and the slab dip have been suggested to control stress state in the overriding plate among global subduction zones. Relationships amongst global subduction parameters suggest that there is a relationship between slab dip and stress state in the overriding plate (Jarrard, 1986; Heuret and Lallemand, 2005a; Lallemand et al., 2005). Steeply dipping slabs (>50°; e.g. Mariana) are associated with back arc extension and slab roll back, whereas shallower dipping slabs (<30°; e.g. the Andes) are associated with back arc shortening (Lallemand et al., 2005; Sdrolias and Müller, 2006). Yet analysis of global sets of subduction parameters show no direct correlations between incoming oceanic plate age and slab dip at depth (Lallemand et al., 2005; Cruciani et al., 2005; Cerpa et al., 2018). The initial portion of the slab shows better correlation with slab age, as at shallow depths the slab better retains its rigidity and shape and is less influenced by mantle flow (Sdrolias and Müller, 2006).

Slab age has a twofold contrasting effect on subduction geodynamics and slab dip: (1) older slabs have a thicker lithospheric mantle, a greater mechanical strength and so are more resistant to bending (Hu et al., 2016; Crameri et al., 2017; Zhang et al., 2018); (2) older slabs are colder and denser and so have a greater negative buoyancy force (Molnar and Atwater, 1978). Global subduction zones can be grouped into classes based on the age of the subducting lithosphere (Sdrolias and Müller, 2006). Currently the entire Andean margin, along with Central America and the Cascades, have relatively young (<60 Myr) oceanic lithosphere entering the trench compared to the global slab age range of 0-160 Ma (Sdrolias and Müller, 2006). The Andes is an unusual case where the age of the subducting lithosphere has remained less than 80 Myr along the entire 5500 km margin throughout the last 66 Ma (Sdrolias and Müller, 2006; Seton et al., 2012). This distribution of ocean plate age which entered the trench was due to the oblique subduction of several ~trench-perpendicular orientated mid-ocean ridge segments (Seton et al., 2012). The propagation of one such spreading ridge led to the break up of the Farallon oceanic plate and caused a shift in the plate convergence rate and direction during the late Oligocene-Early Miocene (Sdrolias and Müller, 2006; Seton et al., 2012).

The Andean subduction zone is characterised by a shallow slab dip along the entire margin. Andean slab dip is generally <30 °, compared to other subduction zones which usually have slab dips >40° and can be up to 90° (Lallemand et al., 2005). Segments of sub-horizontal (~0 °) slab dip occur at three locations in the Andes associated with no arc magmatism on the overriding plate (Figure 9; Jordan et al., 1983; Manea et al., 2017; Ramos and Folguera, 2009). Both the Peruvian and Chilean flat slab segments descend into the mantle with a dip of ~30 ° up to ~100 km depth, and then extend out laterally for over 600 km before descending again at steeper dips (Mulcahy et al., 2014; Scire et al., 2016). Flat slabs are thought to have been locally transient and migrating features under the Andean margin throughout the Cenozoic (Kay and Mpodozis, 2002; Kay et al., 2006; Ramos and Folguera, 2009; Kay and Coira, 2009; Schepers et al., 2017). The existence of both the Peruvian and Chilean flat slabs since the Pliocene (~5-10 Ma) and the potential existence of a southward migrating flat slab below the current Puna region in the Eocene-Oligocene (~50-25 Ma) have been suggested to explain both increased plate coupling, contractional deformation and the migration of the main deformation belt over 400 km into the back-arc (Gutscher, 2002; Espurt et al., 2008; Martinod et al., 2010; O'Driscoll et al., 2012). In contrast, results of geodynamical models indicate that an already thickened overriding plate is necessary to form flat slab segments (Rodríguez-González et al., 2012; Manea et al., 2012, 2017; Hu et al., 2016).

At other subduction zones flat slab segments are very rare. Mexico, eastern Alaska and the Nankai trough (Southern Japan) are the only other margins currently with segments of sub-horizontal subduction (Gutscher, 2001; Lallemand et al., 2005; Manea et al., 2017). These flat slabs only extend out laterally for <<300 km rather than >600 km under the Andean margin and are not associated with the same degree of overriding plate deformation (Gutscher, 2001; Manea et al., 2017). Sub-horizontal subduction appears to occur locally along these arc segments with little to no along-strike variations in subduction parameters (Manea et al., 2017). To simulate flat slab subduction using numerical models the negative buoyancy of the slab must be overcome by an opposing force (van Hunen et al., 2000, 2004). Although a viable mechanism which explains all existing flat slab segments has not yet been found (Manea et al., 2017), it seems that the most important conditions which facilitate slab flattening are: (1) trench-ward overriding plate motion coupled with seaward trench migration (van Hunen et al., 2004; Schepers et al., 2017); (2) sub-slab horizontal mantle flow in a direction toward the overriding plate (van Hunen et al., 2000); (3) a young incoming oceanic plate age (<40 Myr; Hu et al., 2016; Manea et al., 2017); and (4) hydrodynamic suction in the mantle wedge caused by overriding plate heterogeneity (Rodríguez-González et al., 2012; Manea et al., 2012, 2017; Hu et al., 2016).

Incoming buoyant features on the oceanic plate have been correlated with both the Peruvian and Chilean flat slabs (Gutscher et al., 1999b; van Hunen et al., 2002b, 2002a; Martinod et al., 2010). Yet, results from recent numerical models have shown that subduction of a relatively buoyant oceanic ridge (e.g. either Nazca ridge or Juan-Fernandez ridge; Figure 9) alone is not sufficient to induce strong slab flattening (Gerya et al., 2009). Such results support observations from the Mariana arc and western Pacific subduction zones, where aseismic ridge subduction does not induce slab flattening (Rosenbaum and Mo, 2011). Instead, trench-ward motion of the overriding plate, and especially trench-ward motion of a thickened lithosphere, are thought to be twice as important at inducing slab flattening than ridge buoyancy (van Hunen et al., 2004; Manea et al., 2012; Hu et al., 2016).

Latitudinal variations in elevation, crustal thickness, stress state and slab geometry make the Andes the perfect study area to better understand the complexities of subduction in a non-collisional orogen. By building on numerical modelling and statistical studies of global subduction systems, an Andes specific study is carried out here, using compilations of high-resolution datasets for the South American convergence zone. Subduction parameters such as slab age, slab dips (both initial and deep) and convergence direction (Heuret and Lallemand, 2005a) are compared to geophysical estimates of overriding plate crustal and lithospheric thicknesses (Assumpção et al., 2013). These data are compared with focal mechanisms for both the Nazca and South American plates so the key parameters controlling variations stress regime within both plates can be determined. The aims are to study the key set of subduction criteria and dynamics along strike and through time which led to the formation of both the Andean Plateau and flat slab segments, and to find how these two unique end-member products of subduction are related.

2.3 Datasets and methods

2.3.1 Smoothed elevation

Digital Elevation Models (DEMs) were downloaded from Shuttle Radar Topography Mission (SRTM1; Farr et al., 2007). Pixel size is 90 m. Elevation data are smoothed to a horizontal radius of 37.5 km using focal statistics in ArcGIS™. A radius of 37.5 km is selected as this is half of the maximum crustal thickness in the Andes (e.g. Tassara and Echaurren, 2012). Smoothing to this degree filters out non-isostatic, short wave-length topography such as volcanic edifices and river valleys which are not supported by isostasy.

2.3.2 Focal mechanisms

Focal mechanisms (or beach ball diagrams) graphically represent the orientation and sense of slip on a fault during an earthquake event. Focal mechanism solutions include information such as the earthquake moment tensor, composed of 9 spatially orientated components which can be described in terms of three orthogonal axes. Two of these axes represent the orientation of the fault plane, and the third specifies the orientation of the slip vector. The slip vector is used to calculate the rake, which is the slip vector on the inferred hanging wall of the fault. Moment tensors for individual earthquakes vary according to the fault movement which caused the earthquake. The stress geometry of tectonically active regions can be identified by comparing the distribution of focal mechanisms on maps.

Earthquake focal mechanism solutions for the Andes were downloaded from the Global CMT catalogue (Ekström et al., 2012). The region of interest was specified between 10° to -50° latitude and -55° to -90° longitude. For crustal seismicity earthquakes with hypocentre depths of less than 50 km are selected. For slab related seismicity we select earthquakes with hypocentres greater than 50 km depth. Focal mechanisms are plotted using Generic Mapping Tools (GMT) 'psmeca' code, and colour co-ordinated by thrust, normal and strike slip events. Event types are filtered by their rake as follows:

- normal $-150 < \text{rake} \leq -30$;
- reverse $30 < \text{rake} \leq 150$;
- Strike-slip $-180 \leq \text{rake} \leq -150$, $-30 < \text{rake} \leq 30$ and $150 < \text{rake} \leq 180$

2.3.3 Geophysical boundary depths

Model surface geometries of the overriding plate (crustal thickness, CT; and lithosphere-asthenosphere boundary depth, LAB) and down-going slab are presented by Tassara and

Echaurren (2012). They calculate surface depths by integrating a compilation of independent seismic data with a new 3-D density model derived from forward modelling the Bouguer anomaly (Earth Gravitational Model; EGM2008). The main assumption of the model is that each of the bodies (i.e. the crust, lithospheric mantle, slab and asthenosphere) are assigned constant values of density based on petrophysical considerations taking into account estimated lateral variations in composition and temperature-pressure conditions (Tassara and Echaurren, 2012). Uncertainties are quoted as 10 km for both slab and lithosphere depths and 5 km for crustal thickness. Horizontal resolution parallel to the convergence direction is ~10 km and trench parallel horizontal resolution is 25 km. Supplementary Information files S1, S2 and S3 from (Tassara and Echaurren, 2012) are ASCII tables containing a grid of vertices representing the location (longitude, latitude) and depth below sea level of the slab surface, lithosphere-asthenosphere boundary (LAB) and continental Moho between 18-42° S (Tassara and Echaurren, 2012). Inverse distance squared weighted (IDW) interpolation in ArcGIS was used to generate 3-D surfaces from the grid files of crustal thickness, LAB depth and slab depth (Tassara and Echaurren, 2012). IDW predicts values for unknown locations using the surrounding measured values, with the measured values closest to the prediction location having greater influence on the predicted value than those further away. IDW uses the explicit assumption that each measured point has a local influence that diminishes with distance, which is justified for interpolating datasets with topography. Each surface was smoothed to a radius of 37.5 km following the same method as smoothing elevation datasets. A 37.5 km radius is higher than both the horizontal resolutions (10 km and 25 km) and therefore removes unresolved noise from the raster surfaces. From the smoothed interpolated raster surfaces, along-arc, trench-parallel and trench-normal profiles are created to better visualise and analyse the along-strike variations in Andean geometry. Data are also extracted at the locations of each volcanic centre from the geochemical datasets used in Chapter 3. In Chapter 3, the relative influence of each of the geophysical boundaries (Tassara and Echaurren, 2012) and slab parameters (Heuret and Lallemand, 2005a) on arc front geochemistry are explored.

2.3.4 Subduction parameters

SubMap (Heuret and Lallemand, 2005b) is an open-access online database of global physical subduction zone parameters compiled by Heuret and Lallemand (2005a). Each subduction zone segment is divided into trench-normal profiles distanced ~200 km along-strike, which for the Andes equates to ~2° latitude. Table 1 shows the data downloaded from SubMap for the Andes. Trench parameters are trench depth (Td) and sediment thickness at the trench (Tsed). Slab parameters are: slab age at the trench (A; Müller et al., 2008); the oceanic plate thickness and elastic thickness (T t-slab and T e-slab, respectively, are discussed below); shallow slab dip (α_s); deep slab dip (α_d); and the slab thermal parameter (ϕ; discussed below). Trench normal (n) components of absolute plate velocities with respect to the Pacific hot spot reference frame (HS3; Gripp and Gordon, 2002) include the velocity of the upper plate (Vup), the subducting plate (Vsub), and the trench (Vt). Positive trench and upper plate velocities represent seaward trench migration, as represented schematically in Figure 10a. The relative major plate convergence rate, Vc(n), is the sum of Vsub(n) and Vup(n) (Heuret and Lallemand, 2005a). Subduction parameters are assigned to both geophysical boundary depths and volcanic centres according to proximity to the nearest trench normal profile shown in Table 1 (Heuret and Lallemand, 2005a). Geophysical boundary data are extracted from the smoothed along-arc and trench-parallel profiles at 20 km intervals along each profile.

Data for the oceanic plate age at the trench back through time (used for comparison to Andean shortening history) were taken from the study of Maloney et al (2013). Maloney et al (2013) established the age of the subducting slab entering the trench over the last 0-190 Ma, by sampling a reconstructed age grid (at 55 defined sampling points along the Andean trench) based on the plate reconstruction model of Seton et al (2012).

2.1.1.1 Slab elastic thickness [T(e-slab), km]

The elastic thickness of the oceanic lithosphere is considered to represent the upper portion of the lithosphere where stresses do not relax on geological timescales, and hence permit tectonic plates to move as rigid bodies (Caldwell and Turcotte, 1979; McKenzie et al., 2005). In comparison, in the lower plastic lithosphere, temperatures are higher and stresses can be relaxed by creep processes. The extent of isostatic compensation or flexural bending are controlled by elastic thickness (Watts, 2001; McKenzie et al., 2005). Hence, the elastic thickness of a slab [T(e-slab), km] can be directly related as a function of the slab bend wavelength of the outer rise (also called the 'slab forebuldge', related to flexural bending of a slab before it enters the trench) (Caldwell and Turcotte, 1979). The base of the oceanic lithosphere is defined by a constant temperature (~1300° C) and therefore its thickness and elastic thickness both increase as a function of plate age (e.g. Caldwell and Turcotte, 1979; McKenzie et al., 2005).

Table 1: Compilation of Andean subduction parameters from the SubMap database (Heuret and Lallemand, 2005b, 2005a). * slab thermal parameter from the SubMap database is defined by Kirby et al. (1996). See Section 3.4.2 for further definition of the slab thermal parameter.

		Trench		***Slab parameters***						***Relative conv. (mm/yr)***	***HS3 (mm/yr)***		
Profile	**Latitude**	**Td (km)**	**Tsed (km)**	**Slab age (A; Myr)**	**T(t-slab; km)**	**T(e-slab; km)**	**α(s; °)**	**α(d; °)**	**ϕ (km)***	**Vc(n)**	**Vup(n)**	**Vt(n)**	**Vsub (n)**
SAM47	-19	7	0	53	67	31	25	41	1996	73	44	35	29
SAM48	-21	6	0	53	67	31	23	40	2191	78	48	42	30
SAM49	-23	7	0	51	66	30	18	45	2043	75	47	42	30
SAM50	-25	7	0	47	63	29	17	47	1927	77	47	41	30
SAM51	-27	7	0	46	62	29	14	49	1694	73	45	39	29
SAM52	-29	6	0	45	61	28	14			75	45	39	30
SAM53	-30.5	6	0	40	58	27	13	50	1526	77	46	40	31
SAM54	-32	6	0	39	57	26	12			77	46	39	32
SAM55	-34	5	2	36	55	25	21	35	1232	66	39	39	27
SAM56	-35.5	5	2	34	54	24	22			62	37	37	25
SAM57	-37	4	2	32	52	24	24			72	42	42	31
SAM58	-39	4	1	29	49	22	25			75	43	43	33
SAM59	-41	3	1	23	45	20	25			75	43	43	33
SAM60	-43	3	2	13	33	15				76	43	43	33
SAM61	-45	3	2	3	16	8				75	42	42	34

2.1.1.2 Re-measuring Andean slab dips

To account for the variability of slab dip with depth, standard practice is to take two different dip measurements: the shallow dip angle of the slab between 0-125 km slab depth, and the deep dip angle from 125-D_{max} km slab depth (Jarrard, 1986; Lallemand et al., 2005). D_{max} is the limit the slab can be imaged, which can usually be up to the 660 km mantle discontinuity. The two slab dip measurements from SubMap (Heuret and Lallemand, 2005b) which follow this practice do not accurately account for the 100 km deep sub-horizontal flat slab sections in the Andes. This is due to calculation of dip measurements between two ranges of slab depth. Shallow dips (from 0-125 km) take into account only a small portion of the flat slab segment. Deep dips measured by this method effectively measure the dip of the flat slab segments after they have steepened again, which can be up to 700 km horizontally inboard from the trench. A different approach is taken here to better constrain the dip of flat slab segments. Slab dips are calculated for ranges of horizontal distance perpendicular to the trench instead of slab depth, so that simple trigonometry can be used to calculate the dip for each horizontally-spaced slab segment using slab depth data (Tassara and Echaurren, 2012) taken from trench normal profiles (Figure 10b). An initial slab dip is taken for slab segments between 100-200 km perpendicular distance from the trench. Deep slab dip is calculated for each slab segment between 300-400 km from the trench (Figure 10b).

2.1.1.3 Slab thermal parameter (ϕ)

The thermal structure of any given slab depends on heating by conduction as it is subducted into the hotter mantle. A slab 'thermal parameter' (ϕ) was originally defined by Kirby et al. (1996) as a proxy for the depth-dependent temperature of slab interiors. The calculation is the slab age (Ma) times the vertical descent rate (sine of slab dip multiplied by trench-normal convergence rate km/Myr). The slab thermal parameter is given in units of length (km) and represents the maximum depth reached by a given isotherm within the slab. Lower values therefore characterize warm slabs (for example young, thin slabs with a slow descent velocity), whereas higher slab thermal parameters correspond to cold slabs (for example old, thick slabs with a fast descent velocity). Values for the slab thermal parameter from SubMap use the definition of Kirby et al. (1996) using the deep slab dip. Note the data gaps in Table 1 for the south-central Andes, which is due to the lack of seismic constraints on slab depth in the Southern Andes. The general lack of slab seismicity in the southern Andes is discussed in Section 4.4. Slab thermal parameters are re-calculated using the new initial slab dip measurements of this study to gain better data coverage, and uses rates of subduction velocity in accordance with Magni et al. (2014). Initial dips are used to better represent the thermal structure of the slab before it reaches the arc (~<300 km slab depth).

(a) major subduction forces

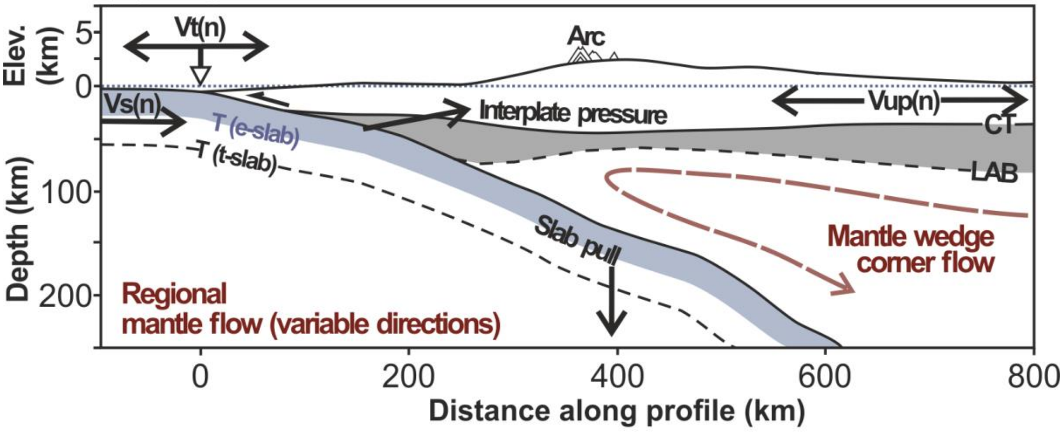

(b) re-calculating slab dips

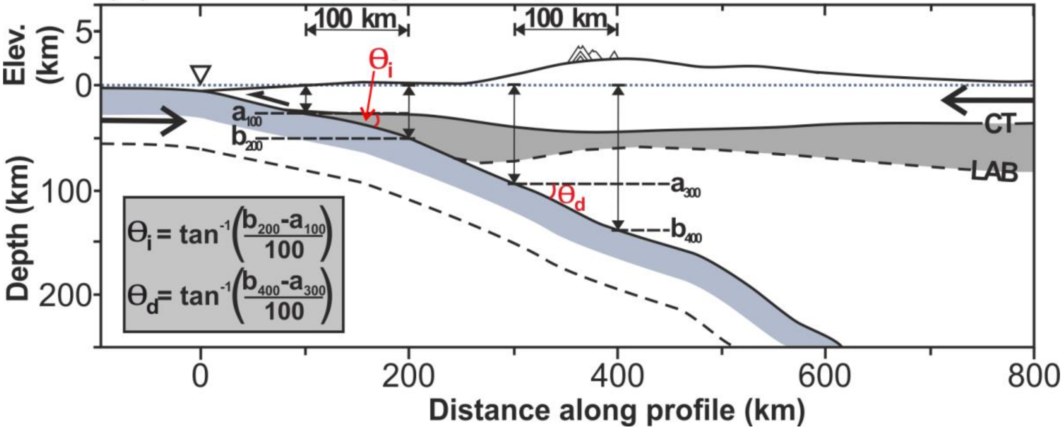

Figure 10: (a) a sketch of the major forces acting on a subduction zone (adapted from Heuret and Lallemand, 2005a). (b) Sketch illustrating the new method proposed to calculate both the initial (θ_i) and deep (θ_d) slab dips, using slab depth data from the model of Tassara and Echaurren (2012).

2.4 Results

2.4.1 Andean subduction parameters

Figure 11 shows trench-parallel variations in slab age, thickness, convergence velocities and the four measurements of slab dip described above (both this study and Heuret and Lallemand, 2005a). Slab age and the age dependent thickness of the slab (Figure 11a) have the most consistent variation across the study area compared to the other subduction parameters shown Figure 11b and c. Slab age smoothly decreases from 53 Myr to 23 Myr from north to south of the study area. All four convergence rates shown in Figure 11b are relatively consistent across the study area. Although, between 33-36° S there is a decrease in relative convergence rate (by ~10 km/Myr compared to rates north of 33° S) and both absolute trench velocity (~5 km/Myr) and upper plate velocity (~10 km/Myr). South of ~33° S, upper plate velocity is equal to the trench migration velocity, indicating that the trench is not under compression, compared to north of 33° S where the upper plate velocity is higher than the trench velocity (Figure 11b).

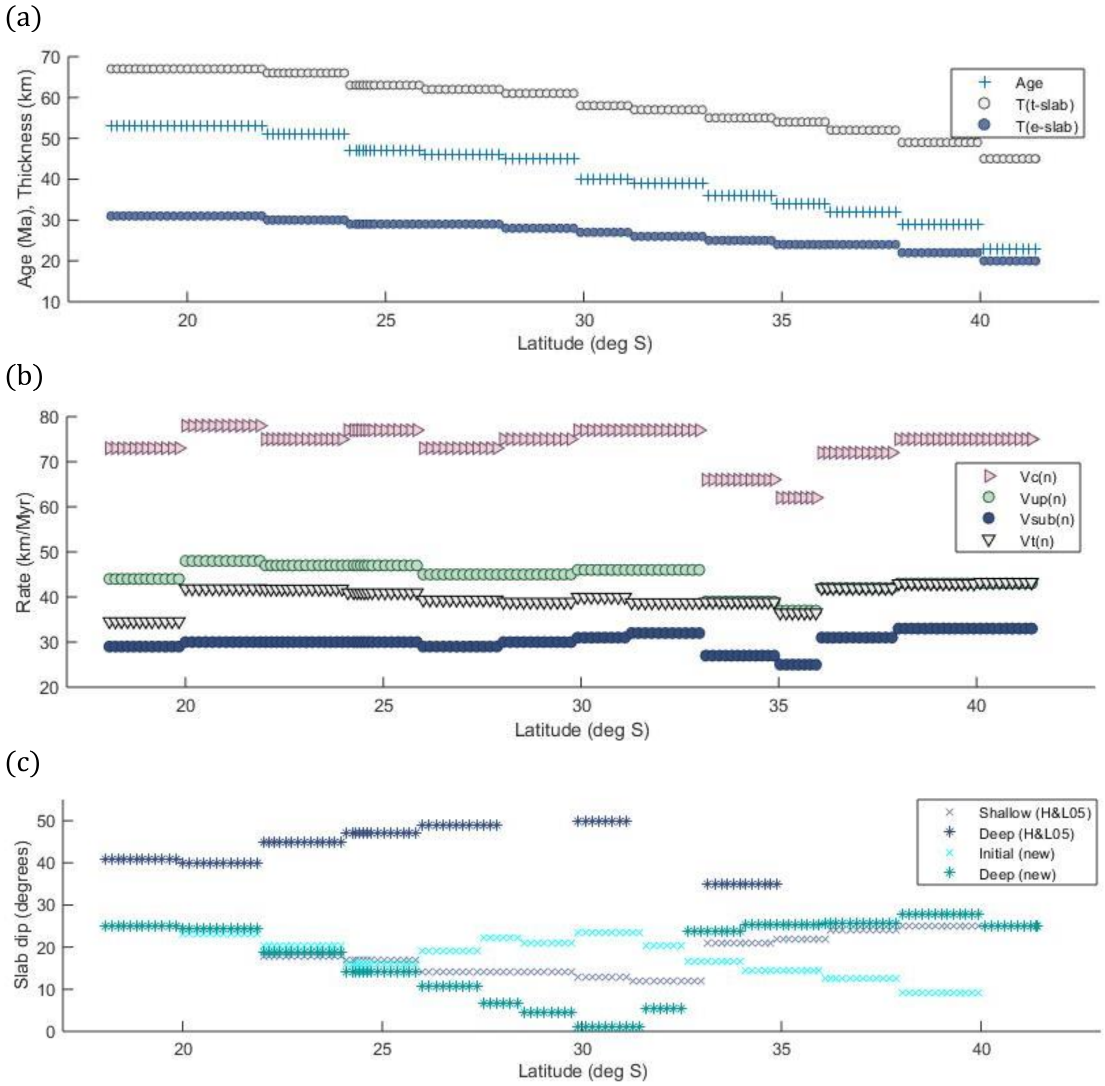

Figure 11: (a) Lithospheric and elastic thicknesses (t-slab and e-slab, respectively) of oceanic lithosphere are both functions of slab age (Caldwell and Turcotte, 1979; McKenzie et al., 2005). (b) Variations in trench normal components of both relative convergence and absolute plate velocities (HS3 reference frame; Gripp and Gordon, 2002). Positive values of Vc, Vup and Vt are all trench-ward. Note that south of 33° S, Vup(n) is equal to Vt(n). (c) Comparisons between different dip measurements which characterise the variability of slab dip with depth. All data except new slab dips from this study are from the SubMap database (Heuret and Lallemand, 2005a), and are listed in Table 1.

Figure 11c shows variability between the different methods used to measure slab dip. Slab dips below 125 km (deep dip measurements of H&L, 2005a) are thought to be largely influenced by mantle processes (Lallemand et al., 2005), and therefore are not considered further in this study. Between 18-26° S, 'shallow' dips measured between 0-125 km slab depth (Heuret and Lallemand, 2005a) correspond well to both the 'initial' and 'deep' dips of this study (measured between 100-200 km and 300-400 km horizontal distance from the trench, respectively, Figure 10b). This arc segment corresponds to the region under the southern Altiplano and northern Puna, where slab dips remain fairly consistent with depth, but the slab gradually shallows to the south. The deep dip of this study best represents the sub-horizontal nature of the Chilean flat slab (~28-33° S). Initial dips (this study) reach maxima of ~25° dip in the regions of both the northern Altiplano and Chilean flat slab segments. Initial slab dips decrease between 32-40° S.

2.4.2 Present slab and over-riding plate geometries

From south to north along the arc, crustal thickness and slab depth show a first order increase across the study area (Figure 12). Overriding plate crustal thickness increases sharply from 40° S to 30° S, before becoming relatively constant at 63±5 km north of ~32° S, under the Andean Plateau. Depth to slab below the arc is much more variable. For example, from Volcan Llullaillaco (CVZ, south of the Salar de Atacama [SdA], ~24.71° S) to Volcan Lascar (CVZ, east of SdA, ~23.37° S) slab depth increases from 100±10 km to 130±10 km due to the eastward deviation of the arc around the Salar de Atacama basin. The shallower slab north of the SdA correlates with the location of the Iquique ridge on the incoming Nazca plate and the Pica gap within the CVZ on the South American plate (shown in Figure 9). Lithosphere-asthenosphere boundary (LAB) depth under both CVZ and SVZ arc ranges between 61-86±10 km. Overlying the Chilean flat slab segment LAB depth of the overriding plate increases sharply (range of 85-102±10 km). Yet, LAB depths must be treated with caution, especially under the active volcanic arc, as unconstrained volumes of magma will both reduce seismicity and change the density structure of the overriding plate (see Discussion). LAB depths have been drawn as dashed lines for this reason.

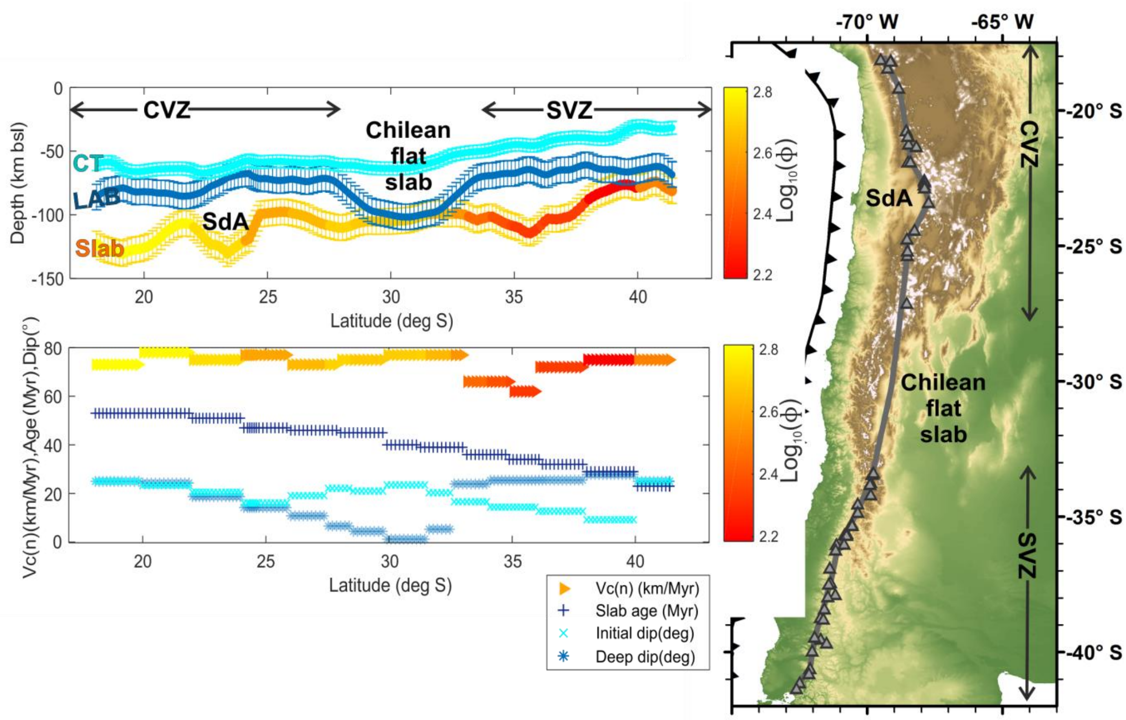

Figure 12: A topographic map of the study area, including labels for the Central Volcanic Zone (CVZ; excluding volcanoes outside the study area north of 18° S); Salar de Atacama basin (SdA); Chilean flat slab segment; and Southern Volcanic Zone (SVZ). The upper panel shows an along arc profile of crustal thickness (CT, light blue), lithosphere thickness (LAB; mid-blue) and slab depth (Slab, coloured according to $\text{Log}_{10}[\phi]$). CT, LAB and slab depth are based on models from Tassara and Echaurren, (2012). Lower panel shows along arc variations in slab age and trench normal convergence rate from the SubMap database (Heuret and Lallemand, 2005a) and the initial and deep dip measurements from this study (Methods).

Figure 13 shows variations in crustal thickness, lithosphere depth and slab depth along trench parallel profiles at fixed lateral distances of 100 km (P100), 200 km (P200), 250 km (P250) and 300 km (P300) from the trench. In P200 and P300 the depth to all three boundaries increases northwards from 40 to 30° S, and remains relatively constant within each respective error between 30 and 18° S. P300 lies closest to the arc and mostly resembles the along arc profile shown in Figure 12 with a few notable differences. The increased depth to slab below the arc bordering the SdA basin is not seen at P300 (Figure 13). Instead the depth to slab remains at 100±10 km for over 1000 km (~32.5-22.5° S), which is the current expanse of both the Puna Plateau (with active arc magmatism) and Chilean Flat Slab (with no Quaternary arc magmatism; Figure 9). Slab depth is also very shallow (~80 km bsl at P300) between 38-40° S, associated with a slight convex bend in the trench bordering the Arauco peninsula (37-38° S). Depth to slab is greatest inboard of the concave trench around the Arica Bend (north of 21° S; Figure 13).

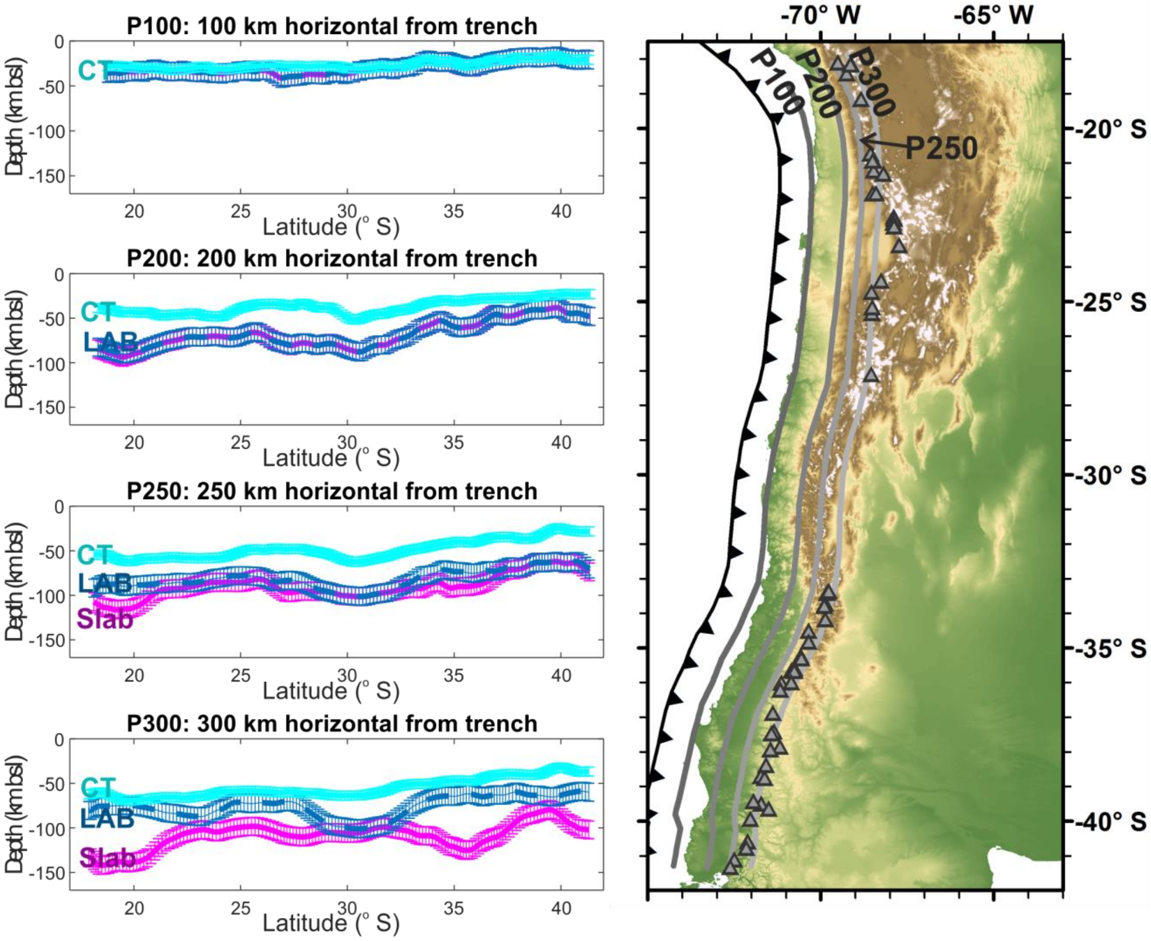

Figure 13: Trench parallel profiles of crustal thickness, LAB depth and slab depth (Tassara and Echaurren, 2012) taken at fixed horizontal distances from the trench. The majority of Andean arc front volcanoes lie between lateral distances of 250-300 km from the trench, except where the arc deviates to the east around the Salar de Atacama (SdA). Data from profiles 2 (P200) and 4 (P300) are used for linear regression analysis in the next section. P200 is taken to represent the transition from the 'locked' portion of the plate interface and initial slab dips are used for cross correlations. P300 is taken to represent the along-arc or intermediate portion of the subduction zone and deep dips are used in cross correlations.

Figure 14 shows trench normal profiles spaced every 2° latitude (~200km) along the trench which correspond to the profiles of Heuret and Lallemand (2005a) listed in Table 1, and include an extra profile on the northern margin of the flat slab (SAM52a). Profiles of smoothed elevation (37.5 km radius, see Methods) along the same profiles are shown in green (top panels; Figure 14). High elevations of the Central Andean Coastal Cordilleras (SAM48-50) create extremely steep slopes leading up to the Western Cordillera and Andean Plateau. On profile SAM49 the steep slope on the western flank of the Andean Plateau is broken by the Salar de Atacama basin (at ~2500 m elevation). South of SAM51, peak elevations decrease from over 4000 m to 1800 m. From profile SAM52a to SAM56, the peak elevation for each profile migrates landward from ~300 km east of the trench to over 400 km east of the trench.

The lower panels on Figure 14 capture trench normal variations in Andean subduction zone geometry between 21 and 39° S. Lithosphere-asthenosphere boundary depths, again, are dashed due to the uncertainties in imaging this boundary. The overall slab dip shallows gradually southward between 21 to 28° S. Initial slab dips (between 0-200 km along each profile) are steepest between 28 to 32° S, associated with the Chilean Flat Slab. Overall slab dips south of 33° S are very similar to those in the Central Andes north of 28° S, as the depth to slab reaches 250 km at ~600 km distance from the trench.

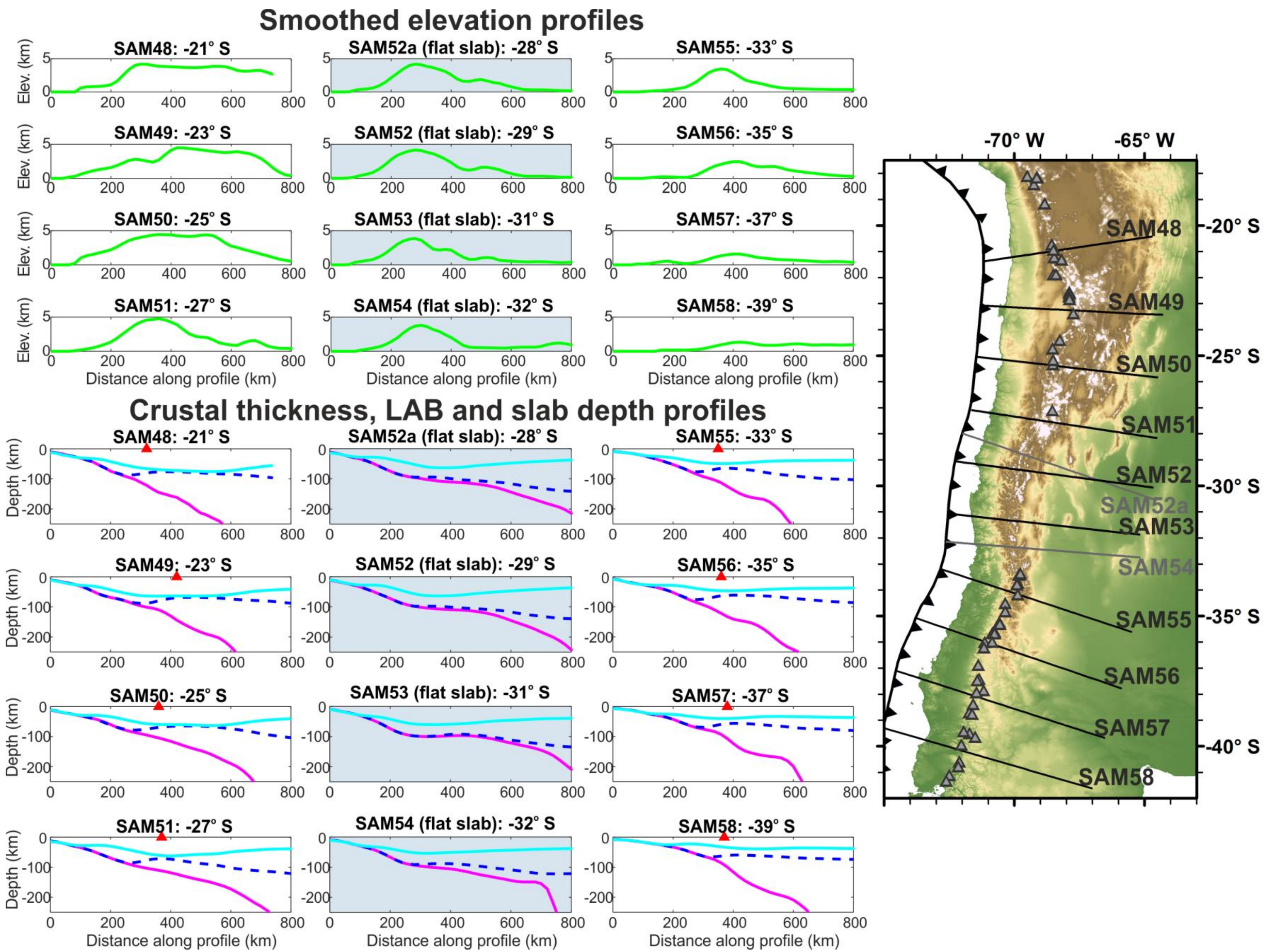
Smoothed elevation profiles
SAM48: -21° S
SAM49: -23° S
SAM50: -25° S
SAM51: -27° S
SAM52a (flat slab): -28° S
SAM52 (flat slab): -29° S
SAM53 (flat slab): -31° S
SAM54 (flat slab): -32° S
SAM55: -33° S
SAM56: -35° S
SAM57: -37° S
SAM58: -39° S
Elev. (km)
5
0
0
200
400
600
800
Distance along profile (km)
Crustal thickness, LAB and slab depth profiles
Depth (km)
0
-100
-200
-70° W
-65° W
-20° S
-25° S
-30° S
-35° S
-40° S
SAM48
SAM49
SAM50
SAM51
SAM52
SAM52a
SAM53
SAM54
SAM55
SAM56
SAM57
SAM58

Figure 14 (previous page): Geometries of the Andean subduction zone across and along strike. Trench normal profiles are taken every ~2° latitude along the trench (~200 km), including an extra profile at the northern edges of the flat slab segment (SAM52a). Red triangles represent the location of the arc front. Data are the same as Figure 12. Trench normal profiles of smoothed elevation (green; top panels), crustal thickness (cyan blue), LAB depth (dark blue) and slab depth (magenta). Elevation profiles are vertically exaggerated (x 20 compared to horizontal distance). Lower panels of geophysical boundary profiles have no vertical exaggeration compared to horizontal distance.

2.4.3 Cross correlations between slab dip and slab age

As described in the introduction, relationships amongst global subduction parameters suggest that there is a relationship between slab dip and stress state in the overriding plate (Jarrard, 1986; Heuret and Lallemand, 2005a; Lallemand et al., 2005). The dip of the shallow portion of the slab has been suggested to have a higher dependence on slab age than deeper slab sections (Sdrolias and Müller, 2006), however results of other studies have contradicted this and suggested there is no direct function between slab dip and oceanic plate age (Cruciani et al., 2005). In this section, the aim is to determine if either slab dip or slab age can be correlated with overriding plate crustal thickness, which is used as a function of long-term overriding plate compressional strain. As shown in Section 4.1, slab dip changes with depth and so it is important to consider such variations. Previous methods of measuring slab dip (Jarrard, 1986; Heuret and Lallemand, 2005a) do not account for sub-horizontal sections of subduction in the Andes but overestimate these dips by up to 14° (Figure 11c). A simple change in method when calculating the slab dip allows the flat slab sections in the Andes to be more accurately represented (Section 2.1.1.2). Initial slab dips from this study have a strong, positive correlation with slab age ($r = 0.871$, $p < 0.05$; Figure 15a). There is no statistically significant correlation between deep slab dip and slab age (Figure 15b). For slabs between 20-38 Myr in age, there is a negative relationship with deep slab dip. The relationship then switches to a positive correlation with slab dip for slab ages >38 Myr. This switch occurs between the slab segments either side of the Chilean flat slab.

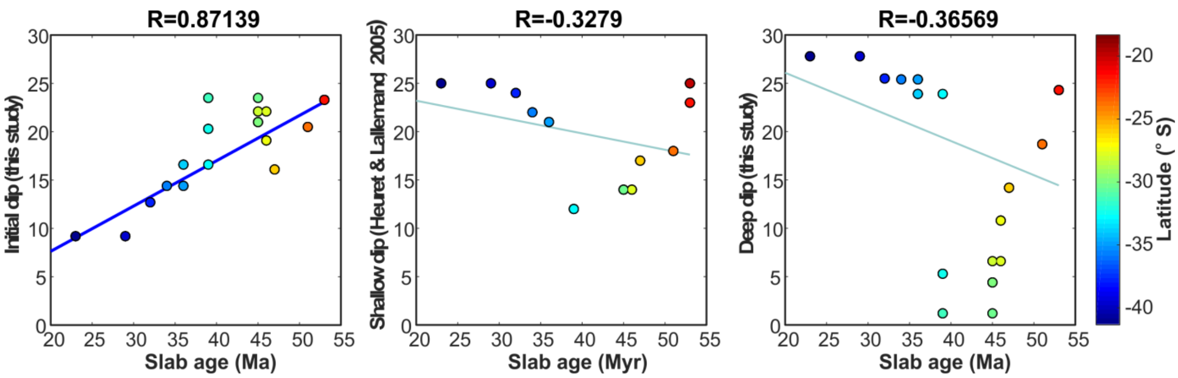

Figure 15: Linear regression analysis between initial and deep slab dips (both this study and Heuret & Lallemand, 2005a). Data points are colour coded by latitude. Correlation coefficients are printed above each panel.

Figure 16 shows the results of statistical analysis between slab age and slab dip and each of the geophysical boundary depths along trench-parallel profiles P200 and P300 (slab depth, overriding plate crustal thickness and LAB depth). P200 is selected to represent the relationships within the forearc. P300 is used as a fixed-distance proxy to the arc to remove the effect of the deviation of the arc to the east around the Salar de Atacama, which is generally agreed to be controlled by the presence of an anomalously cold and dense lithospheric block under the basin (Mpodozis et al., 2005; Reutter et al., 2006; Arriagada et al., 2006a) and not to subduction processes. Shallow slab dips are used for linear regression tests using boundary data from P200. Deep dips are used for boundary data from P300.

Geophysical boundary data (crustal thickness, lithosphere thickness, slab depth) from profile P200 show strong linear correlations between both slab age and initial slab dip ($r = 0.81\text{-}0.96$). Such a result is unsurprising as initially the slab dip is controlled by slab age, with older and denser slabs descending more steeply (Figure 15). The strongest correlations are between both slab depth, LAB depth and the initial slab dip (Figure 16), which is expected as slab depth is a function of initial slab dip in the shallow portion of the slab. LAB depth and slab depth are within error of each other at P200 (Figure 13), so both boundaries would be predicted to behave similarly. Nevertheless, data from the flat slab segment have large positive residuals from trends with slab age, indicating a thicker overriding plate and deeper slab depth than would be predicted by the incoming slab age (Figure 16). Increased coupling, deformation and overriding plate thickening during flat slab subduction could explain this observation, and are discussed later in this Chapter.

At profile P300, in the deeper portion of the subduction zone, the strongest correlation is a positive correlation between crustal thickness of the overriding plate and slab age ($r = 0.939$; $r^2 = 0.882$; p value < 0.01). The increasing elastic thickness of older slabs means they are mechanically stronger (Figure 11a), and later it is discussed that this may relate to increasing degrees of compression in the overriding plate, which in turn would manifest as crustal thickening via crustal shortening over time. A slight deviation from trends with slab age again occur in the area of the Chilean flat slab segment where crustal thicknesses and LAB depths are greater than would be predicted by the corresponding slab age at the trench. LAB and slab depth have weaker positive correlations with slab age than crustal thickness ($r < 0.6$). Both crustal thickness and lithosphere thickness at P300 have negative correlations with deep slab dip ($r = -0.545$ and $r = -0.791$, respectively). This is in contrast to the strong positive relationships with initial slab dip at P200. Interestingly, slab depth under P300 (close to the arc) is constantly ~105 km (within ±10km error) except for the region north of 20° S (near the Arica Bend) and south of 35° S (in the south-central SVZ), where depth to slab ranges between 80-140 km over a small range in deep slab dip (24-28°).

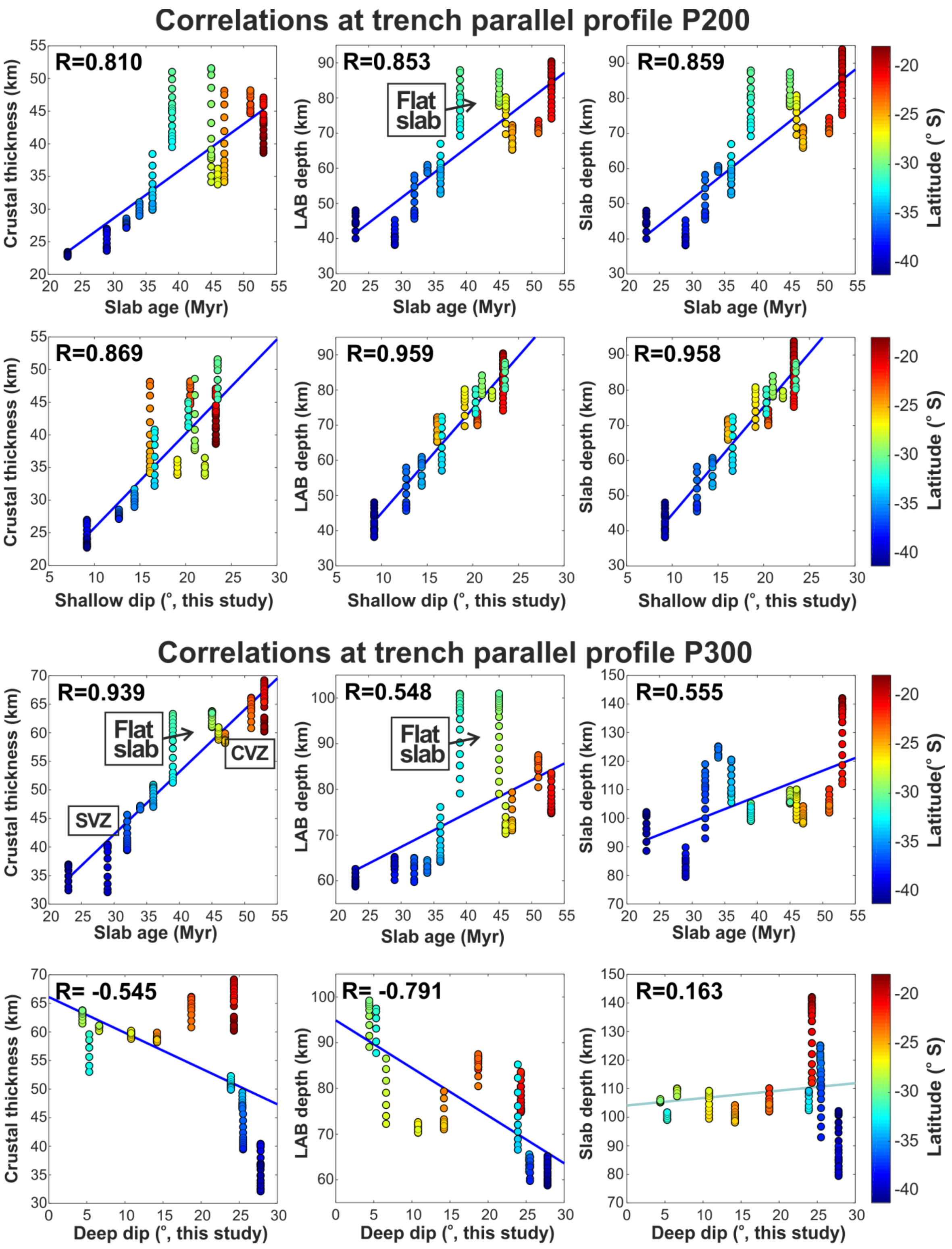

Figure 16: Linear regression analysis between geophysical estimates of over-riding plate crustal thickness, lithosphere-asthenosphere boundary (LAB) depth and depth to slab (Tassara and Echaurren, 2012), to Nazca plate age at the trench (slab age) and slab dip measurements (this study). Data points are extracted from trench-parallel profiles P200 and P300 shown in Figure 13. The initial slab dip is used for correlations with data from P200 and deep slab dip for data from profile P300. Data points are coloured by latitude so data from the each region (e.g. CVZ, flat slab and SVZ) can be identified.

2.4.4 Andean earthquake distribution

Figure 17a shows the seismicity distribution of earthquakes greater than magnitude 5 occurring at less than 50 km depth. Filtering earthquakes to this depth separates crustal seismicity within the overriding plate from the majority of slab related seismicity,except for thrust earthquakes at the trench which are less than 50 km depth and related to the locked portion of the plate interface. It is well known that active thrust earthquakes are uncommon within the high Andean Plateau (Devlin et al., 2012), but small thrust events occur at lower elevations in the fold and thrust belt of the Eastern Cordillera. There are areas of higher density of upper plate thrust focal mechanisms above both flat slab segments and in the overriding plate above segments where the Carnegie Ridge collides with Northern South America. An interesting observation is a cluster of thrust focal mechanisms at ~31-32° S, which occur on a direct projection inland from the Juan-Fernandez ridge on the Nazca plate. There are also higher densities of thrust earthquakes at the locations where aseismic ridges are entering the trench (Figure 17a). Offshore Chile, there is a change in stress regime at the trench at ~39° S. South of 39° S the slab is younger than 30 Myr, outer rise extension dominates and there is almost no thrust seismicity in the shallow portion of the plate interface. North of 39° S, outer-rise extension becomes rare, thrust seismicity at the plate interface dominates and the slab age increases above 30 Myr (Figure 17a). Note that sediment thickness at the trench increases dramatically at ~33° S (see Table 1), although it is not particularly well constrained in the dataset of Heuret and Lallemand. There are also a high density of large fracture zones entering the trench offshore southern Chile which can be seen in the ocean bathymetry maps (Figure 17a & b), associated with the Chile Rise spreading ridge. The northernmost major fracture zone (the Valdivia Fracture Zone) enters the trench at ~40° S. As discussed in the next section, both subducting sediment and the presence of fracture zones have been associated with decreased plate coupling at subduction zones. The effect of fracture zones is hard to discriminate from oceanic plate age, but the two are coupled as the density of fracture zones increases with increasing proximity to the spreading ridge. However, there is a disparity between the location of the change in stress regime at the trench and where the sediment thickness increases, indicating that sediment lubrication is not the only cause of weakening at the subduction interface. The same relationship between slab age and stress regime are not seen in Northern South America and Central America, but this may be due to the presence of multiple bathymetric features on the down-going slab, including the Carnegie and Cocos ridges and the Nazca-Cocos spreading ridge.

Slab related seismicity (>50 km depth) related to earthquakes greater than magnitude 5 are shown in Figure 17b. Earthquake depths increase eastward from the trench. Slab seismicity greater than 50 km depth is mainly extensional due to the slab pull force (see Discussion). As with seismicity less than 50 km, there seems to be spatial relationships between clusters of earthquakes and projections from incoming features on the Nazca plate (Figure 17b). The strike of the nodal planes calculated for the focal mechanisms in the slab are much more variable than the shallow seismicity, where the strikes are roughly parallel to the trench. Under Southern Chile (south of 39° S), the slab becomes predominantly aseismic corresponding to slab ages <30 Myr. The transitional behaviour seen at 30 Myr slab age in the southern Andes is not seen in the Northern Andes. The anomalous seismicity at depth under Columbia is termed the 'Bucaramanga Nest' and is discussed in the next section.

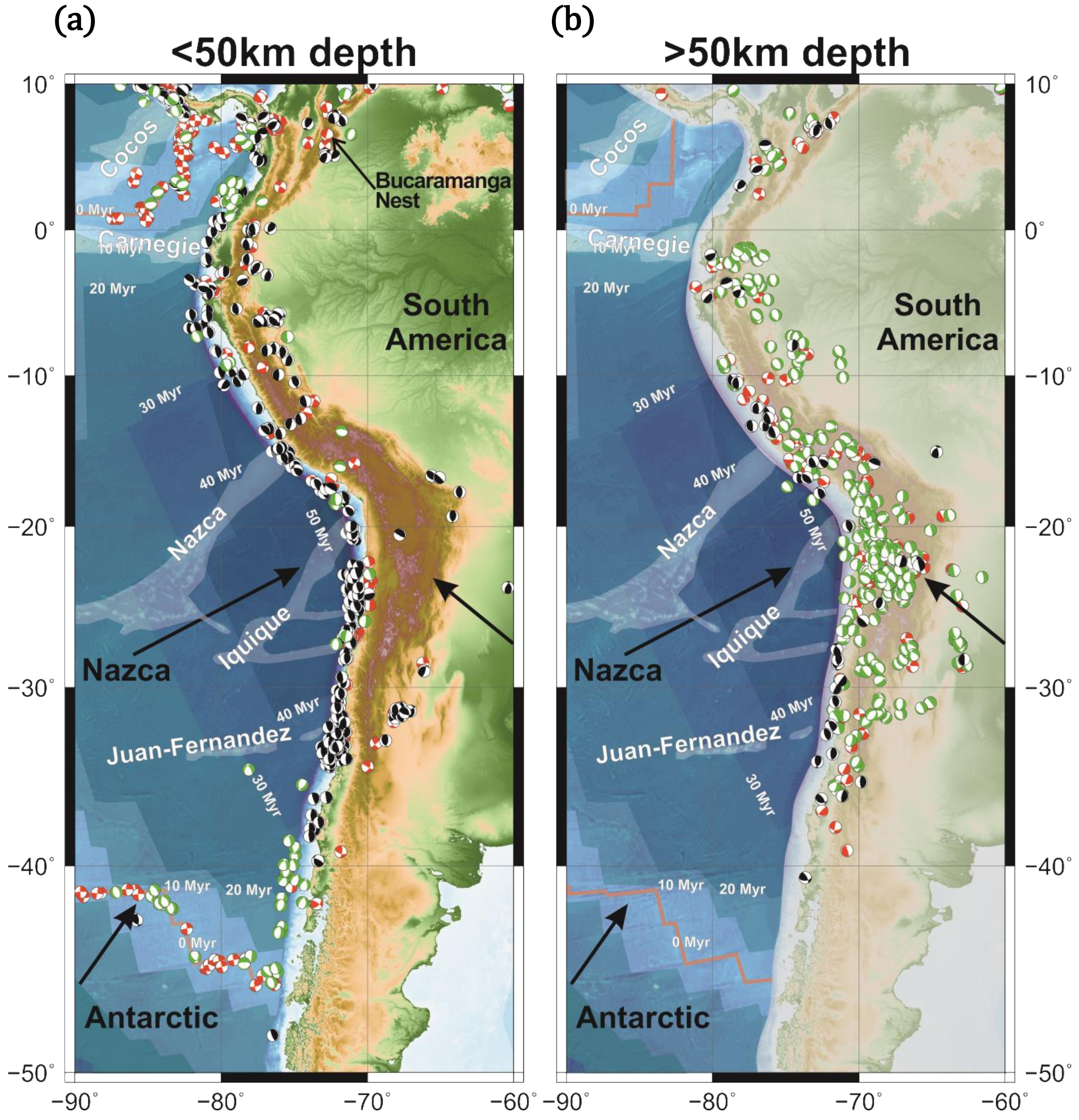

Figure 17: Base maps are the same as Figure 9. Focal mechanisms of earthquakes greater than M5 are from the Global CMT catalogue (see Methods, time period: 1976-2018). Thrust quakes are coloured black, normal are green and strike slip are red. (a) Left panel shows earthquakes with hypocentre depths of <50 km, representing crustal seismicity and thrust events in the shallow portion of the plate interface. The cluster of anomalous intermediate depth seismicity under Columbia is called the 'Bucaramanga Nest' (Syracuse et al., 2016). (b) Right panel shows earthquakes with hypocentres greater than 50 km which are related to the down-going slab. Note the switch from a dominantly compressional stress regime to an extensional regime in the slab ~100 km from the trench.

2.5 Discussion

Slab age and overriding plate crustal thickness have never before been directly quantified, even though the symmetrical distribution between Nazca plate age and corresponding degree of compressional deformation in the South American plate has been noted over the last four decades (Molnar and Atwater, 1978; Capitanio et al., 2011). Subduction of oceanic lithosphere younger than 50 Myr in age has been attributed to need an 'extra force' to overcome its relative positive buoyancy compared to older and colder oceanic plates (Molnar and Atwater, 1978). Slab age has also been attributed to induce overriding plate crustal thickening due to increasing the age dependent sinking of the slab into the mantle, which in turn is suggested to induce increased mantle wedge convection and traction at the base of the upper plate (Capitanio et al., 2011). Despite these results, it is still debated if the relationship between subducting plate age and overriding plate deformation is truly causal or not, and many studies instead relate overriding plate compression mainly to plate kinematic processes (Maloney et al., 2013; Crameri et al., 2017; Guillaume et al., 2018; Cerpa et al., 2018). It is well known that overriding plate motion towards the trench must indeed be a crucial factor in causing interplate compression (Heuret and Lallemand, 2005a; Sdrolias and Müller, 2006). Maloney et al. (2013) synthesised a dataset of Andean plate velocities and slab ages for the last ~170 Ma, using the global plate kinematic model of Seton et al. (2012). Trench normal velocities of South America have remained in a trench-ward direction along the entire Andean margin (excluding Patagonia) over the last 100 Ma (Seton et al., 2012; Maloney et al., 2013), and Maloney et al. (2013) suggest that the development of fold and thrust belts is associated with trench normal plate convergence rates >4 cm/yr. Yet, there is no significant variability in plate convergence rates between the present day central and southern Andes even though there are large variations in crustal shortening and crustal thickness (Figure 11b). Overriding plate motions towards the trench actually decreased in magnitude from ~70-50 Ma when the onset of deformation initiated (Seton et al., 2012; Maloney et al., 2013). Therefore, convergence velocities or overriding plate motion alone cannot explain the variations in Andean deformation.

A synthesis of the observations from this study are provided in four schematic cross sections (Figure 18) which are drawn to scale using data from trench-normal profiles SAM49, SAM52, SAM56 and SAM58 (data from Figure 14). The very strong correlation found between Nazca plate age and overriding South American plate crustal thickness ($r = 0.939$; $r^2 = 0.882$; p value < 0.01; Figure 16) is attributed to increased plate coupling and overriding plate compression caused by long term subduction of intermediate aged slabs (~30-80 Myr) combined with continual seaward overriding plate motion. Both the current distribution of seismicity and models of oceanic plate age entering the South American trench over the last 190 Ma support the hypothesis and are discussed below.

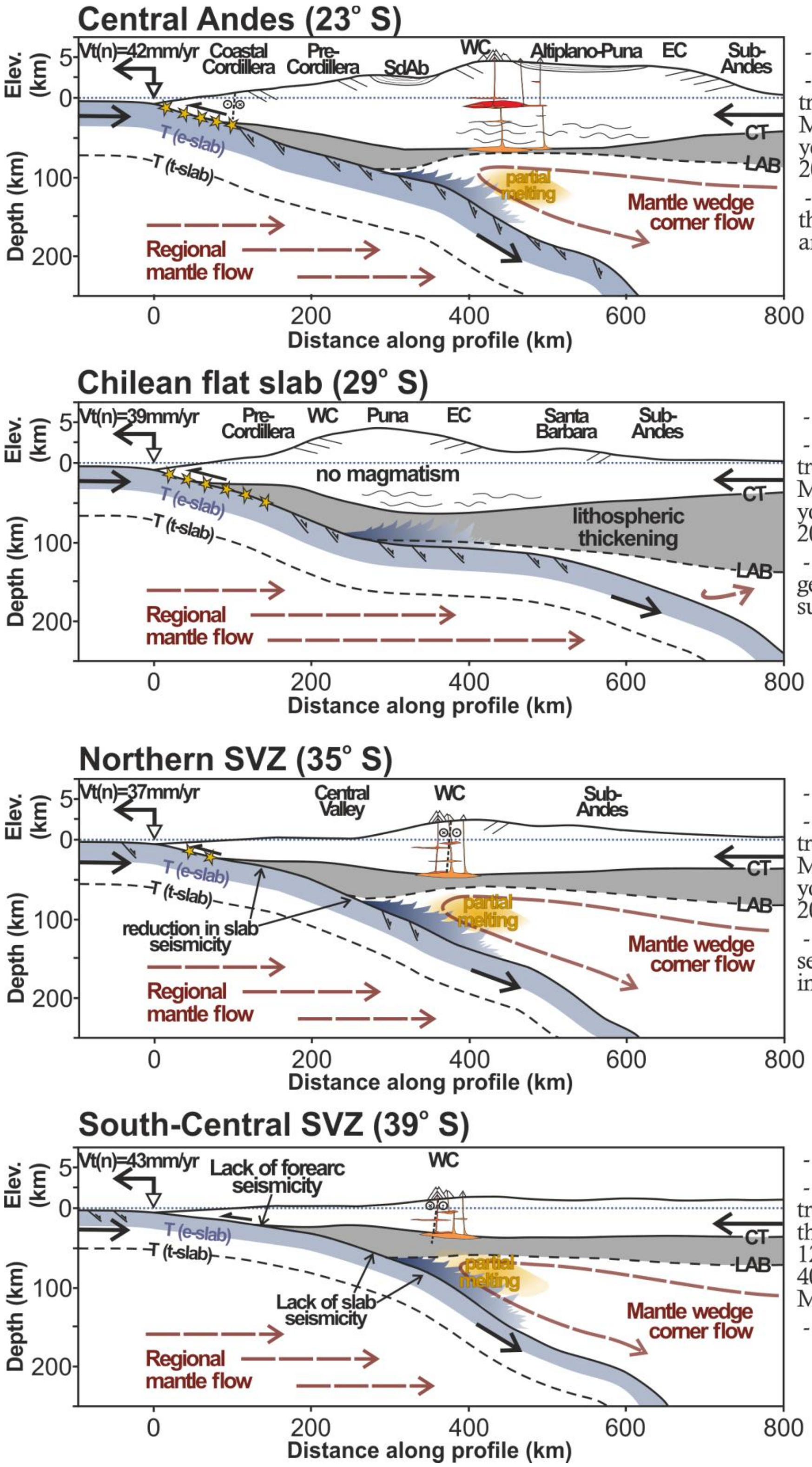

Central Andes (23° S)

- Current slab age: **51 Myr**
- Slab age entering the trench was between 40-80 Myr from 60-50 Ma, and younger than 40 Myr from 200-60 Ma
- Current high density of thrusts at the plate interface and slab extension at depth

Chilean flat slab (29° S)

- Current slab age: **45 Myr**
- Slab age entering the trench was between 40-80 Myr from 50-40 Ma, and younger than 40 Myr from 200-50 Ma
- Thickened lithosphere generates mantle wedge suction and slab shallowing

Northern SVZ (35° S)

- Current slab age: **34 Myr**
- Slab age entering the trench was between 40-60 Myr from 30-10 Ma, and younger than 40 Myr from 200-30 Ma
- Reduction in slab seismicity at the plate interface and at depth

South-Central SVZ (39° S)

- Current slab age: **29 Myr**
- Slab age entering the trench has been younger than 40 Myr for the last 120 Ma, and was between 40-50 Myr old before 120 Ma.
- Lack of slab seismicity.

Figure 18: Schematic cross sections (to scale), with a vertical exaggeration on elevation profiles of x10. Overriding plate smoothed elevation, crustal thickness (CT), lithosphere-asthenosphere boundary (LAB) depth and slab surface data are the same as Figure 14 (Farr et al., 2007; Tassara and Echaurren, 2012). Oceanic lithosphere thickness (T, t-slab) and elastic thickness (T, e-slab) are from the SubMap database (Heuret and Lallemand, 2005a; see also McKenzie et al., 2005), both thicknesses are a function of the slab age, which decreases from north to south. The normal components of trench velocity (Vt(n)) are labelled (HS3 reference frame; (Heuret and Lallemand, 2005a). Yellow stars represent the shallow thrust seismicity shown in Figure 17a, and normal faults in the lower portion of the slab north of 38° S represent the extensional seismicity within the slab shown in Figure 17b.

Along the South American (SA) margin, the Nazca plate entering the trench is relatively young compared to most global subduction zones (SA range: 0-55 Myr, global range: ~0-160 Myr; e.g. Heuret and Lallemand, 2005). Increased pressure at the plate interface, associated with overriding plate compression, is related to the dissipation of energy as the slab bends on entering the trench (Faccenna et al., 2007), for example slabs which have a greater resistance to bending cause increased compression at the plate interface. For old oceanic plates (>120 Myr), slab elastic thicknesses and bend wavelengths are systematically large (Zhang et al., 2018), but can be counteracted by the higher negative buoyancy of old slabs which increases the slab pull force (e.g. Faccenna et al., 2007). The excess weight of old slabs means they can also be more easily affected by mantle processes, such as lateral mantle flow or slab anchoring at the 660 km discontinuity (Lallemand et al., 2005; Faccenna et al., 2007). Intermediate slab ages (~30-80 Myr) are relatively buoyant compared to older slabs, and slab bend wavelengths have been found to be more variable due to differences in axial loading and the potential for a greater influence of faults reducing the effective elastic thickness (Zhang et al., 2018). Results from numerical models of subduction have shown that the importance of slab strength, resistance to bending and effective elastic thickness increase for slab ages >30 Myr (Hu et al., 2016). Slabs younger than 30 Myr have been found to have consistently thin elastic thicknesses (Zhang et al., 2018).

There are higher densities of thrust focal mechanisms at the plate interface at slab ages >30 Ma and/or where oceanic plateaus and aseismic ridges collide with the trench (Figure 17a), indicating potential relationships between intraplate pressure and the age of the slab. The updip and downdip limits on subduction zone thrust earthquake ruptures are thought to be strongly controlled by temperature in the slab, and therefore by depth and slab age (Oleskevich et al., 1999). Below the coupling depth (the down dip limit of megathrust events), generally the slab pull force dominates and the slab stress becomes extensional (Oleskevich et al., 1999; Bloch et al., 2018). Extensional slab seismicity is observed in the central Andes and even in the flat slab segments (Figure 17b). South of the Chilean flat slab (~33-40° S), there is a decrease in all seismicity at >50 km depth, and a lack of any seismicity at >50 km depth south of 40° S (Figure 17b). Between ~33-40° S the slab age at the trench decreases from ~38 to 30 Myr (Figure 17b). The oceanic plate entering the trench is <30 Myr south of 38° S. Slabs younger than 30 Myr may be too weak to deform in a brittle manner at depth (hence no extensional seismicity) or to be strongly coupled with the overriding plate (no mega-thrusts at the plate interface). The same relationships between young slab age and decreased slab seismicity are not seen in the Northern Andes (Figure 17b). Increased shallow thrust seismicity and fore arc compression in Ecuador are related to the anomalously thick oceanic plate associated with the Carnegie ridge (Gutscher et al., 1999a). Multiple plates entering the subduction zone under Columbia explain the increased seismicity there (Syracuse et al., 2016) even for young slab ages (<25 Myr). The Bucaramanga nest situated under Columbia is an anomalous small region of intense intermediate depth seismicity attributed to compression induced by the collision between the Nazca and Caribbean plates (Syracuse et al., 2016; Figure 17b).

The sharp lateral transition from strong to weak plate locking behaviour in the Southern Andes corresponds to the coastline inflection at the Arauco peninsula at 39° S. North of the peninsula is the location of the great 2010 Maule and 1960 Valdivia earthquakes (Moreno et al., 2011). Studies of these great earthquake events suggested that weak locking south of the Arauco peninsula was due to local enhanced water circulation associated with subduction of the Valdivia and Mocha fracture zones (Moreno et al., 2011). The small Mocha fracture zone impinges the trench at ~38° S, yet the Valdivia fracture zone is thought to be the northernmost major fracture zone intersecting the Andean trench at 40° S (Moreno et al., 2011). There is a high density of fracture zones intersecting the Andean trench south of 40° S, which are associated with the close proximity to the Chile Rise spreading ridge. Therefore, it is hard to distinguish between the weakening of the oceanic plate due to the presence of fracture zones from the plate being weak due to the young age. Both are likely to be complimentary though, as the number of fracture zones increases close to the spreading ridge and the age of the plate also decreases closer to the spreading ridge.

Sediment thickness in the Andean trench increases dramatically south of ~33° S (Table 1; Heuret et al., 2012). A lack of trench sediments in the Central Andes has previously been attributed to enhancement of plate coupling and upper plate strain (Lamb and Davis, 2003; Heuret et al., 2012; Armijo et al., 2015; Lee et al., 2015). However, there is a disparity between the location of the change in stress regime at the trench (at ~39° S; Figure 17a) and where the sediment thickness increases at the trench (at ~33° S), indicating that sediment lubrication is not the only cause of weakening at the subduction interface.

In this study, by looking at the seismicity distribution on a larger scale, we note the striking coincidence between slab age becoming less than 30 Myr and a lack of any seismicity in the slab. Weakening of the young slab would be further enhanced by water-carrying fracture zones and an increased sediment load.

The present day strong linear relationship between slab age at the trench and crustal thickness along the Andes observed in this study we suggest results from the amount of time each arc segment has been exposed to intermediate plate ages between (~40-80 Ma), combined with overriding plate motion towards the trench. Trench normal velocities of South America have remained in a trench-ward direction along the entire Andean margin (excluding Patagonia) over the last 100 Ma (Seton et al., 2012; Maloney et al., 2013). In the Southern Andes, between 33-42° S, ocean plate ages entering the trench have remained dominantly younger than 40 Myr for the last 170 Ma (Figure 19). In the Central Andes before 80 Ma (Jurassic-Cretateous), slab ages entering the trench have been younger than 40 Myr (Figure 19). Bordering the northern Altiplano, at ~12° S, the slab entering the trench became older than 40 Myr at ~90 Ma (Profile

19 on Figure 19); by the Arica Bend, ~20° S, slab age became older than 40 Myr at ~60 Ma (Profile 25 on Figure 19); and by the Puna, at ~27° S, the slab age became older than 40 Myr between 50-40 Ma (Profile 31 on Figure 19; Seton et al., 2012; Maloney et al., 2013). These dates correspond to the onset of compressional deformation in the Central Andes between 70-50 Ma (McQuarrie et al., 2005; Oncken et al., 2006; Barnes and Ehlers, 2009; Garzione et al., 2017). The southward younging of slab ages over time can provide a possible explanation for the degree of crustal shortening being greatest in the Altiplano region and decreasing systematically both to the north and south (McQuarrie, 2002a; Schepers et al., 2017). In the northern Andes (10° S to 10° N), oceanic plate ages have remained between 40-80 Myr, but have ages that gradually became younger throughout the Cenozoic (Figure 19; Sdrolias and Müller, 2006; Seton et al., 2012; Maloney et al., 2013). The northern Andes has very complex tectonics, including the accretion of an oceanic terrane along the Ecuadorian margin in the Late Cretaceous (Ramos, 2008; Chiaradia et al., 2009) and more recent collision of the Nazca and Caribbean plates at depth (Syracuse et al., 2016).

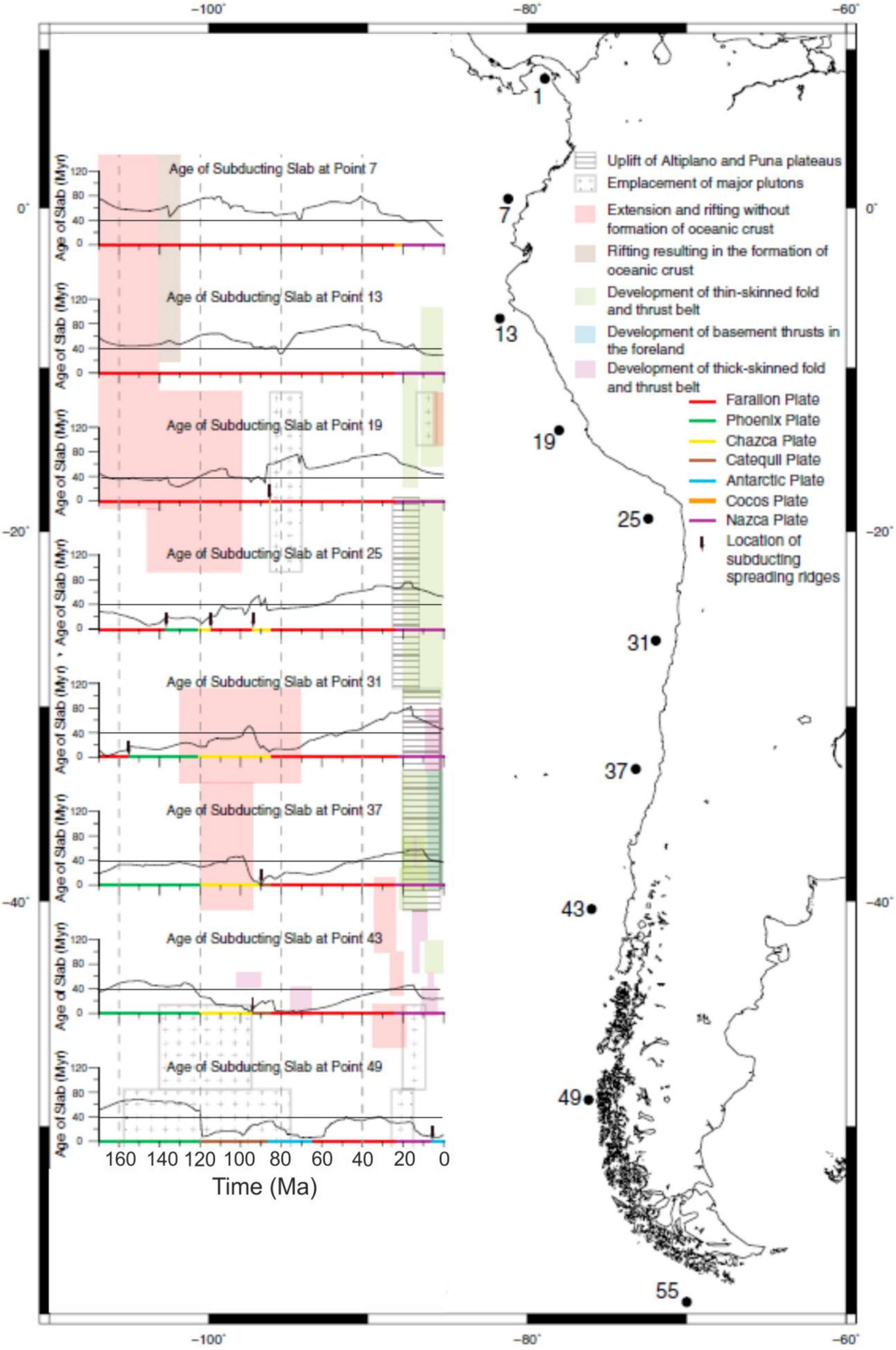

Figure 19: Graphical representations of the distribution of age of the oceanic lithosphere entering the South American trench over the last 190 Ma adapted from Maloney et al. (2013).

Analysis of global subduction zone systematics has attributed slab dip to be an important control on back-arc stress (Lallemand et al., 2005). Initially both slab dip and slab age are positively correlated with overriding plate crustal thickness (Figure 15 & Figure 16), supporting the hypothesis that initial dip angles better represent the age dependence of the slab, as at these depths the slab better retains its rigidity and shape (Sdrolias and Müller, 2006). In contrast, deep slab dips have a weak negative correlation with crustal thickness. Deep dips are consistently ~25° under both the Central Andes and the Southern Andes, despite large variations in both slab age and overriding plate crustal thickness. Slabs lose their rigidity as pressure and temperature increase with depth and the slab dip can be more easily influenced by upper mantle processes (e.g. Sdrolias and Müller, 2006). Slab dip is transient in nature over time and a result of numerous force balances related to properties of the slab, mantle and overriding plate (van Hunen et al., 2004; Lallemand et al., 2005; Faccenna et al., 2007; Manea et al., 2017). We suggest that slab dip alone is not a major driving force of long-term compression in the Andes.

Subduction of intermediate slab ages combined with high plate convergence rates alone cannot explain the expansion of deformation over 400 km into back arc regions, which occurred at ~50-40 Ma in the Central Andes and in the last 5 Ma above the region currently overlying the Chilean flat slab. Neither can slab age explain the switches in deformation style between thin-skinned and thick-skinned tectonics. In the correlation between slab age and overriding plate crustal thickness (Figure 16), there is a deviation from the relationship in the region above the Chilean flat slab segment. Above the flat slab, overriding plate crustal thicknesses are up to 15 km thicker than would be predicted by the incoming slab age, consistent with the hypothesis that plate coupling and overriding plate deformation are increased during periods of flat slab subduction (Gutscher et al., 2000; Gutscher, 2002). Results from numerical models also indicate that subduction of aseismic ridges can cause local increases in overriding plate elevation which can be greater than the original height of the ridge, and that such elevations can be sustained for several million years after the ridge has been subducted (Gerya et al., 2009).

The higher density of thrust focal mechanisms at the plate interface where oceanic plateaus and aseismic ridges collide with the trench have been previously observed (Gutscher et al., 1999a; Hampel, 2002; Rosenbaum et al., 2005). Previous observations have also noted increased intensity of thrust earthquakes in the overriding plate above the flat slab segments (Gutscher et al., 2000; Gutscher, 2002) and that earthquakes above the flat slab can occur in the usually aseismic lower crust (Devlin et al., 2012). Periods of flat slab subduction are linked to thick-skinned compressional deformation in the overriding plate over a broad region in the back arc, involving small degrees of shortening, deep crustal faulting and basement uplifts (Jordan et al., 1983a; Martinod et al., 2010; Marot et al., 2014). These deformation styles are observed above the modern Bucaramanga flat slab (Gutscher et al., 1999a), Peruvian flat slab (Hampel, 2002) and Chilean flat slab (Sierras Pampeanas and Santa Barbra systems; Jordan et al., 1983; Kley et al., 1999; Marot et al., 2014). Such thick-skinned deformation styles have been related to low heat flow anomalies and thick continental lithosphere imaged for overriding plates above flat slab segments (Marot et al., 2014; Manea et al., 2017).

Partial melting in the mantle wedge above subduction zones alters the thermal structure of the mantle by up to ~300 K, which thins the overriding plate lithosphere directly below the arc (Macpherson, 2008; Perrin et al., 2016; Rees Jones et al., 2018). Thermal erosion of the overriding plate lithosphere is also thought to occur by mantle wedge corner flow (Tao and O'Connell, 1992). Here, we propose that local increased rates of compression during oceanic plateau/aseismic ridge collision discussed above could allow the rate of lithospheric thickening in the overriding plate to overcome the rate of thermal erosion of continental lithosphere below the location of the arc. Results of 3D numerical models have indicated that thickened (relatively cold) overriding plate lithosphere is key to generating flat slab segments by generating hydrodynamic suction in the mantle wedge which causes slab shallowing (Rodríguez-González et al., 2012; Rodríguez-González et al., 2014; Hu et al., 2016; Manea et al., 2017). Over-thrusting or overriding plate advance are also considered crucial mechanisms for flat slab formation (van Hunen et al., 2002b, 2004; Schepers et al., 2017), which is consistent with the observation that the overriding plate velocity is larger than the sea-ward trench migration above both the Chilean flat slab and Central Andes (Figure 11b). The expansion of compressional deformation into back-arc regions above flat slab segments has been suggested to be a key mechanism related to the widening of the Andean Plateau (Jordan et al., 1983a; Gutscher et al., 2000).

Future work to test the hypotheses suggested here could explore simulation of the relationships identified between slab age and crustal thickening with numerical models, which is discussed in Chapter 6.

2.6 Conclusions

- Synthesis and analysis of multiple geological and geodynamical datasets allows us to relate incoming slab age to the initiation of crustal thickening in the Andes. Key observations outlined in this study are summarised in Figure 18.
- High degrees of plate coupling with a high density of mega-thrust events at the Nazca-South America plate interface occur only where the slab age at the trench is older than >30 Myr or where oceanic plateaux or aseismic ridges are being subducted.
- In Southern Chile, where the slab is younger than 30 Myr, we note there is a lack of seismicity at the plate interface or within the slab at depth. Young slabs are hot and weak and deform plastically or by stable sliding. Thick sediment accumulation at the

trench and the high number of fracture zones likely increase weakening of the young slab in the southern Andes.

- For intermediate slab ages (~30-80 Myr) the elastic thickness (T e-slab) of the oceanic plate is great enough that the slab increases in mechanical strength and becomes resistant to bending, but the young age means intermediate slabs are still relatively buoyant compared to older slabs. In slabs older than ~80 Myr, the greater negative buoyancy can overcome the resistance to bending, allowing the slab to descend into the mantle more steeply or to be more easily influenced by mantle flow.
- In the Southern Andes, between 33-42° S, ocean plate ages entering the trench have remained dominantly younger than 40 Myr for the last 170 Ma of subduction. In the Central Andes, from 170-80 Ma (Jurassic-Cretaceous), slab ages entering the trench were consistently younger than 40 Myr. Slab ages entering the trench along the entire Andean margin have been less than 80 Myr since the Jurassic.
- Bordering the northern Altiplano (at ~12° S) the slab entering the trench became older than 40 Myr at ~90 Ma; by the Arica Bend (~20° S) slab age became older than 40 Myr at ~60 Ma; and by the Puna (at ~27° S) the slab age became older than 40 Myr between 50-40 Ma (Seton et al., 2012; Maloney et al., 2013). These dates correspond to the onset of compressional deformation in the Central Andes between 70-50 Ma. We suggest the southward younging of slab ages over time can provide a possible explanation for the degree of crustal shortening being greatest in the Altiplano region and decreasing systematically both to the north and south.
- Strong positive correlations observed between overriding plate thickness and slab age ($r = 0.939$; $r^2 = 0.882$; p value < 0.01; Figure 16) can therefore be attributed to increased plate coupling and overriding plate compression caused by both seaward overriding plate motion and long-term subduction of intermediate aged slabs (~30-80 Myr).
- Where plate convergence rates are high and slab ages are betwee 30-80 Myr, ridge collision further enhances increased plate coupling and overriding plate thickening, and crucially, allows the overriding plate lithosphere to thicken faster than it can be thermally eroded. This generates a hydrodynamic suction force in the mantle wedge which shallows the slab and shuts off arc magmatism. The expansion of compressional deformation into back-arc regions above flat slab segments is key to the widening of the Andean Plateau.

Chapter 3: Crustal thickness controls on Quaternary Andean arc geochemistry

3.1 Chapter summary

For over three decades, the global geochemical systematics of arc volcanoes have been observed to correlate with crustal thickness in the overriding plate. Other physical properties of subduction zones also affect arc systematics, such as slab temperature and trench sediment thickness. Before we can attempt to use geochemical parameters as a proxy for crustal thickness (and thereby elevation; Chapters 4 and 5), we must first test if the relationships between geochemical parameters and crustal thickness are truly causal or not. Geochemical compilations of Quaternary SVZ and CVZ arc lavas are combined with compilations of published models of geophysical boundary depths and slab parameters (from Chapter 2). Major and trace element compositions are plotted against fractionation indices (SiO_2 wt. %) and colour coded by both slab thermal parameter (ϕ) and crustal thickness, respectively, to see if systematic changes in fractionation trends are defined by either parameter. A 'most-mafic' filtered dataset is used to quantitatively compare 21 geochemical parameters (major and trace element concentrations, trace element ratios and Sr- and Nd-isotope ratios) to 7 different physical parameters (elevation, crustal thickness, lithosphere-asthenosphere depth, depth to slab, slab age, trench sediment thickness, and $Log_{10}[\phi]$) which vary along strike in the study area (see Chapter 2).

The strongest correlations indicate that $^{143}Nd/^{144}Nd$, $^{87}Sr/^{86}Sr$, K_2O, La, La/Sm, and SiO_2 increase with crustal thickness, and by cross correlation elevation and slab age. These results emphasise the importance of increasing crustal thicknesses on increasing the residence times of arc magmas within the crust, which in turn increases the minimum degree of fractionation and crustal contamination seen at each volcano. 'Adakitic' trace element ratios (high Sr/Y and La/Yb in intermediate compositions) increase with increasing crustal thickness and, in contrast, not with increasing slab temperatures (decreasing slab age and slab thermal parameter). Our results support previous hypotheses that garnet becomes an increasingly important fractionating or residual phase with increasing overriding plate crustal thickness, and slab melting is not an important process within our study area (18-42° S).

3.2 Introduction

The geochemical systematics of arc front stratovolcanoes have been found to reflect variations in physical parameters related to both the thermal structure of the down-going slab and to heterogeneities within the overriding plate (Hildreth and Moorbath, 1988; Plank and Langmuir, 1988; Davidson et al., 1990, 2005; Defant and Drummond, 1990; Wörner et al., 2000; Mamani et al., 2008; Cooper et al., 2012; McLeod et al., 2013; Jones et al., 2014, 2015; Turner and Langmuir, 2015b). Continental crust is destroyed and recycled at subduction zones by processes of sediment subduction, delamination and forearc erosion (Stern, 1991; Kay and Kay, 1993; Rudnick, 1995; Plank and Langmuir, 1998; Plank, 2005; Kay and Coira, 2009; Currie et al., 2015). Distinguishing the relative contributions of mantle derived material and recycled crustal material at subduction zones is essential for understanding continental growth rates and the evolution of continents over Earth's history (e.g. Davidson et al., 2005; Dhuime et al., 2015), as subduction zones are thought to have a pivotal role in the generation of juvenile continental crust (Eichelberger, 1978; Rudnick, 1995; Gazel et al., 2015; Ducea et al., 2017).

Subduction zone magmas are the product of complex interactions between: (1) dehydration of the down-going slab and subducted sediments (± potential slab or sediment melting); (2) hydration and partial melting of the mantle wedge; and (3) differentiation of mantle melts within the overlying plate and assimilation of crustal material. In spite of these complex processes, geochemical parameters of arc magmas have long been observed to form strong correlations with overriding plate crustal thickness (Leeman, 1983; Hildreth and Moorbath, 1988; Plank and Langmuir, 1988). There are three main schools of thought as to why certain geochemical parameters form correlations with increasing crustal thickness. Increasing crustal thickness in the overriding plate: (1) provides a filter which increases magma storage time, and therefore the degree of fractionation and crustal assimilation (Hildreth and Moorbath, 1988; Davidson et al., 1990; Kent et al., 2010; Freymuth et al., 2015; Farner and Lee, 2017); (2) increases the pressure at the Moho and hence changes the stability of residual and crystallising mineral phases during magma differentiation (e.g. Garrison and Davidson, 2003; Macpherson et al., 2006; Alonso-Perez et al., 2008; Davidson et al., 2013; Chiaradia, 2015; Chapman et al., 2015; Profeta et al., 2015a); and (3) decreases the thickness of the mantle wedge, reducing corner flow and limits the extent of partial melting in the mantle (Plank and Langmuir, 1988; Turner and Langmuir, 2015b, 2015a; Turner et al., 2016). However, the extent of mantle wedge melting (controlled by the thermal structure and composition of the mantle wedge), is also strongly controlled by the slab temperature. A proxy for slab temperature, the 'slab thermal parameter', ϕ, is defined as the product of the age of the subducting oceanic lithosphere and the vertical descent rate of the slab (Kirby et al., 1996; van Keken et al., 2002; Magni et al., 2014).

Debate ensues over the relative importance of each of the above mechanisms, and especially on the relative importance of both mantle, slab and crustal processes. Filtering and normalising geochemical datasets to leave only primitive compositions are used to minimize the effects of crystal fractionation and crustal contamination, and are used to explore mantle melting, source contamination and mantle heterogeneity (Plank and Langmuir, 1988; Turner and Langmuir, 2015a; Turner et al., 2017).

Volcanic rocks produced at subduction zones are dominantly basaltic-andesite to andesite in composition (Kent et al., 2010; Adam et al., 2016), although, arc compositions can vary greatly both between individual arc segments and along a single arc (Hildreth and Moorbath, 1988; Plank and Langmuir, 1988; McCulloch and Gamble, 1991; Schmidt et al., 2008; Cooper et al., 2012; Turner and Langmuir, 2015b). Studies exploring the systematic geochemical variations within the Andean Southern Volcanic Zone (SVZ) in relation to changing crustal thickness are numerous (Hickey et al., 1986; Hildreth and Moorbath, 1988; Futa and Stern, 1988; Tormey et al., 1991; Holm et al., 2014; Hickey-Vargas et al., 2016; Turner et al., 2016) and geochemical variations within the SVZ have been shown to correspond well with global arc systematics (Turner et al., 2016). In contrast, Central Andean arc lavas, erupted through the Andean Plateau, are distinctly more evolved than global arc average compositions and recent mafic lavas (basalts and basaltic-andesites) are exceptionally rare (Davidson et al., 1990; Davidson and de Silva, 1995; Mamani et al., 2010). The Central Volcanic Zone (CVZ) of the Andes is often removed from compilations and statistical analyses of global subduction zones (e.g. Turner and Langmuir, 2015b, 2015a), with the justification that magmas are erupted through anomalously thick crust (>70 km; Figure 20).

In this Chapter, the aims are to explore the relative influence of several physical parameters of the Andean subduction zone (including both crustal thickness and slab thermal parameter) on the geochemical systematics of Andean arc lavas. Geochemical compilations of both the Quaternary SVZ and CVZ are combined with compilations of published models of geophysical boundary depths and slab parameters presented in Chapter 2 (Heuret and Lallemand, 2005; Tassara and Echaurren, 2012). The study area (Figure 20) has the same north-south extent as geophysical boundary data (18-42 °S; Chapter 2; Tassara and Echaurren, 2012), which encompasses the majority of both the Central Volcanic Zone (CVZ) and the Southern Volcanic Zone (SVZ), although both extend beyond the study area. As discussed in Chapter 2, the Andean subduction zone is characterised by a relatively young and hot slab compared to the global range of slab ages and thermal parameters (Turner et al., 2016). The slab age increases northwards across the study area and is the main reason why slab temperatures decrease northward (thermal parameters are higher; Figure 20). Crustal thickness and slab depth both increase systematically northwards through the SVZ. Slab depth increases northward through the CVZ, while crustal thickness remains constantly thick (60-65±5 km; Figure 20).

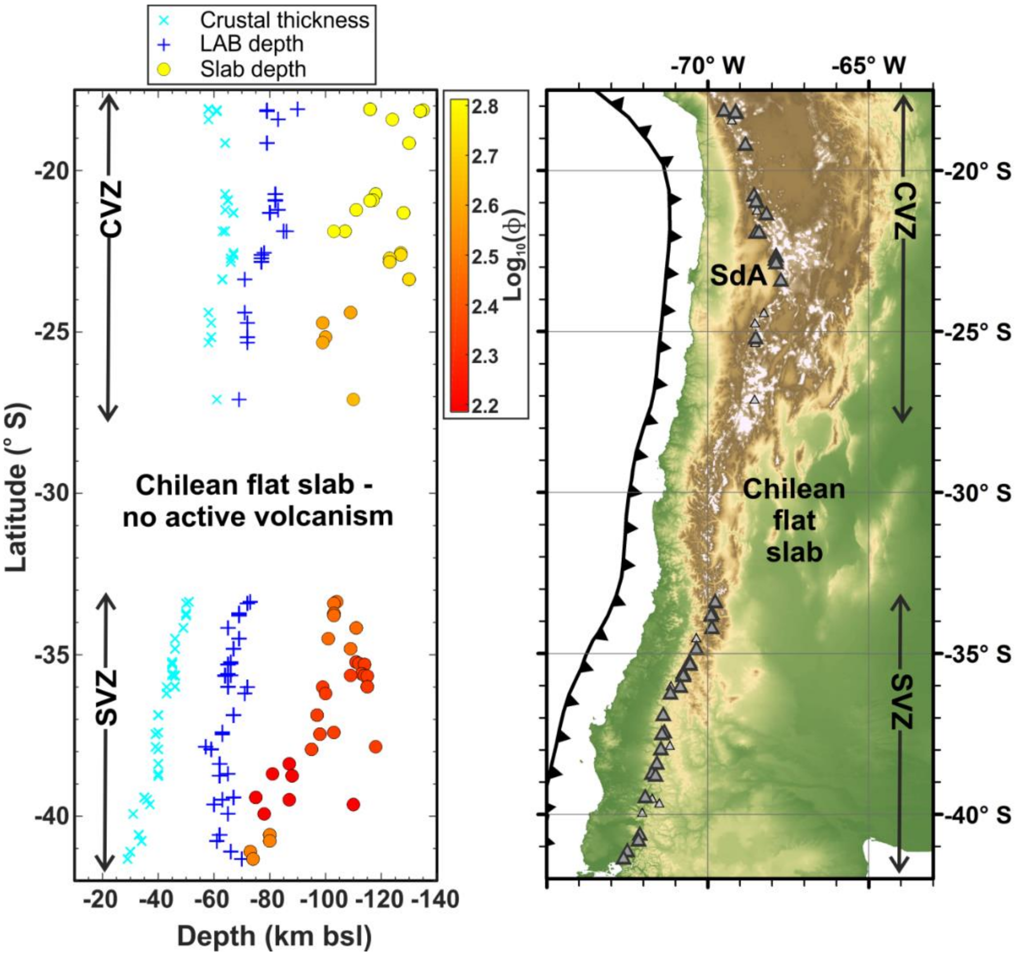

Figure 20: Right panel, a topographic map of the study area, including labels for the Central Volcanic Zone (CVZ), the Salar de Atacama basin (SdA), the Chilean flat slab segment and the Southern Volcanic Zone (SVZ). Grey triangles are volcanoes included in the geochemical compilations, larger triangles represent volcanoes included after the mafic filter is applied. The left panel shows the depth to the base of the crust (CT, light blue), lithosphere-asthenosphere boundary (LAB, mid-blue) and slab surface extracted for each volcanic centre. Geophysical boundary data are the same as Chapter 2, based on the models of Tassara and Echaurren (2012). Errors on depth estimates are ±5 km, ±10 km and ±10 km, respectively. Slab depth is coloured according to $\mathrm{Log}_{10}[\phi]$), to give an approximation of the thermal state of the slab (see main text and Kirby et al., 1996).

The Andes are central to the 'adakite' debate (Stern and Kilian, 1996; Kay and Kay, 2002; Garrison and Davidson, 2003). Adakites are high pressure diagnostic trace element signatures of intermediate (andesite to dacite) lavas (Kay and Kay, 2002). Adakitic signatures are characterised by high Sr/Y, Sm/Yb and La/Yb ratios are indicative of the presence of magmatic garnet (±amphibole or clinopyroxene) in either the residual source or fractionating assemblage (and with very little or no plagioclase or olivine), as heavy Rare Earth Elements (REEs) Y and Yb are preferentially incorporated into garnet over lighter REEs (Van Westrenen et al., 1999). Magmatic garnet is a high-pressure phase (~>45 km) and under hydrous conditions its stability field widens (>0.8-1.2 GPa, ~>35 km depth; Alonso-Perez et al., 2008).

Originally, adakites were proposed to result from partial melting of young (<30 Ma) and relatively hot subducting slabs which have undergone the gabbro-eclogite transition (Kay, 1978; Defant and Drummond, 1990; Stern and Kilian, 1996). The Andean Austral Volcanic Zone (49-54° S) is a classic case study for the slab melt model, as in this region the subduction rate is slow (~2 cm/year), the subducting slab is very young (<24 Ma, due to close proximity to the Chile Rise), and the overriding plate crust is thin (<35 km; plagioclase is dominantly stable rather than garnet or amphibole) (Stern and Kilian, 1996). The slab melt hypothesis has been suggested to be relevant to Archean subduction due to Archean continental crust having 'adakite-like' signatures, with associated implications for early continental crust formation (e.g. Drummond and Defant, 1990). Spatial associations between large copper ore formations and adakites led to the suggestion that slab melting is a mechanism to oxidise the mantle wedge, in turn increasing concentrations of chalcophile elements (e.g. Cu, Ag, Au) in subsequent melts (Mungall, 2002). Yet, replicating slab melting using numerical modelling techniques has proved difficult, even during subduction of young oceanic lithosphere (e.g. Bouilhol et al., 2015; Spinelli et al., 2016).

In contrast, it was noted that adakite lavas are also found at Tupungato volcano in the northern SVZ which has an older slab (~30 Myr) and thicker crust (~55 km) (Kay and Kay, 2002). Neogene adakites were also found above the Chilean flat slab (Kay et al., 1987; Kay and Mpodozis, 2002; Goss et al., 2013) and Neogene-Quaternary andesites from the CVZ reach very high Sr/Y and La/Yb ratios (e.g. Mamani et al., 2010). Integration of geochemical and geophysical data in the Northern Volcanic Zone of the Andes led to the conclusion that slab melting there was unlikely despite the presence of adakite lavas (Garrison and Davidson, 2003; Chiaradia, 2009). Such compositions have been suggested not to be related to slab melting, but instead have been attributed to: (1) high-pressure melting of the refractory lower crust (Kay and Kay, 2002); (2) melting of forearc eroded crust or trench sediments (Kay et al., 1987; Kay and Mpodozis, 2002; Goss et al., 2013); (3) high pressure differentiation or fractionation of magmatic garnet during magma storage either in the mantle wedge or lower crust (Garrison and Davidson, 2003; Macpherson et al., 2006; Alonso-Perez et al., 2008; Chiaradia, 2009). Regional and global compilations of averaged Sr/Y and La/Yb ratios from arcs and collision zones correlate strongly with crustal thickness, which supports the hypothesis of increasing importance of garnet as a fractionating or residual phase in the lower crust with increasing crustal thickness (Chiaradia, 2015; Turner and Langmuir, 2015b, 2015a; Chapman et al., 2015a; Profeta et al., 2015a; Farner and Lee, 2017; Hu et al., 2017). Statistical analysis of global arc compositions indicated calc-alkaline lavas are consistently erupted though thicker crust and are preferentially associated with thick-crusted arcs (Chiaradia, 2014), which has since been suggested to be due to crustal thickness modulating the onset and extent of oxide formation in lower crustal cumulates (Chin et al., 2018). It is important to attempt to separate slab and crustal processes, and as yet, direct statistical comparisons between the slab parameter and crustal thickness and geochemical systematics of both the Andean Southern and Central Volcanic Zones have not been done before.

3.3 Methods

3.3.1 Geochemical database

The GEOROC (Geochemistry of Rocks of the Oceans and Continents) database is an open-access, online dataset of published analyses of volcanic rocks and mantle xenoliths (Sarbas et al., 2018). This comprehensive global compilation is grouped by tectonic setting. To generate our dataset, the query criteria was set as follows:

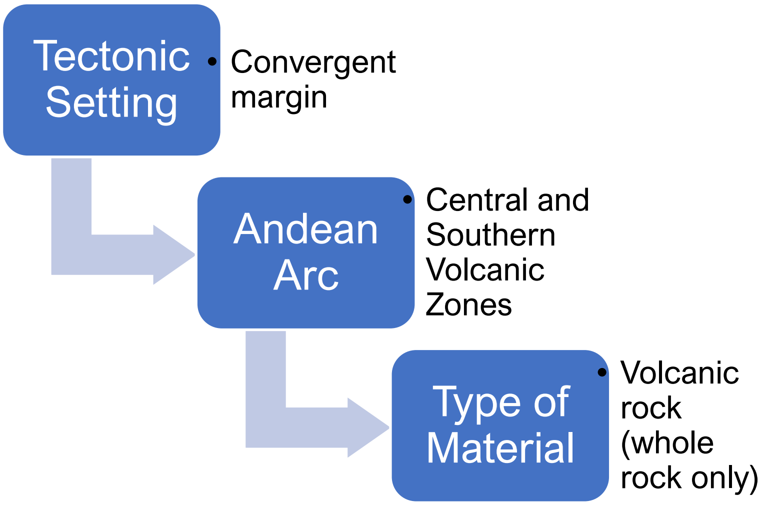

After download, the data were filtered to obtain only Quaternary frontal arc lavas (not including ignimbrites, tuffs, scoria or rocks from monogenetic cones or plutonic rocks). The data were sorted by volcano name, and volcanoes that are not included in either the Holocene or Pleistocene (<2.5 Ma) volcano lists of the Global Volcanism Program (Smithsonian Institution, 2013) were removed. This gave a more complete dataset than by filtering for age alone due to many analyses not containing age data. The cited literature for each volcanic centre were then checked to make sure there were no errors in the database. This process revealed that SVZ analyses were correct when compared to original sources but CVZ trace element compositions did not match with the original published analyses. CVZ trace element compositions were within a similar order of magnitude for each element but were consistently wrong. GEOROC data for the CVZ were discarded and not used in this study. Instead, CVZ data were taken from the Quaternary section of the Central Andean Database (Mamani et al., 2010). Spatial coverage of CVZ data are poorer than the compilation generated from GEOROC for the SVZ (Figure 20), especially in the Southern Puna, as the Central Andean Database lacks the last 8 years of published data. Future work could look into updating the Central Andean Database by mining the vast quantity of more recent analyses from the CVZ. The final number of samples in each of the unfiltered datasets are as follows: n=348 for the CVZ, and n=1048 for the SVZ.

3.3.2 Combination of geophysical and geochemical datasets

As the original sampling locations of lava flows can often be several 10s of kilometres away from the volcanic centre where the melts originated, individual samples are grouped by the parent stratovolcano and assigned a new location corresponding to the centre of the parent volcanic centre. Each stratovolcano is then assigned data for geophysical estimates of crustal thickness, lithosphere depth and slab depth (see Chapter 2, Methods; Tassara and Echaurren, 2012) and subduction parameters according to closest proximity to each profile listed in Table 1 (Chapter 2; Heuret and Lallemand, 2005).

3.3.3 Most mafic filter

There are many methods to filter geochemical datasets of arc volcanoes for quantitative analysis. One such is normalising to 6 wt. % MgO (adapted from methods of normalising to 8 wt. % MgO for mid-ocean ridges), which involves plotting elements and element ratios against wt. % MgO, extrapolating trend lines back to 6 wt. % and selecting the corresponding value of the element being tested (Plank and Langmuir, 1988). Andean lavas do not follow conventional trend lines and have a high degree of scatter due to high degrees of assimilation and fractional crystallisation processes. Therefore, extrapolating back to 6 wt. % MgO generates large errors in the resulting dataset. Another method is to filter datasets to a range of MgO or SiO_2 content. For example, taking only samples between $5.5<MgO<6.5$ wt. % (Turner and Langmuir, 2015b). However, these methods cannot be employed here as nearly all CVZ magmas are <4 wt. % MgO and primitive CVZ lavas are exceptionally rare (Davidson and de Silva, 1995; Blum-Oeste and Wörner, 2016). We devised a method to filter the dataset to the most mafic sample for each volcanic centre, so that the processes controlling the most mafic sample erupted at each volcano can be explored. Samples were grouped by the parent stratovolcano. Where data permit, composite stratovolcanoes (made up of two or more stratovolcanoes in one volcanic complex) were kept separate in the filtering process. For example, the Quizapu-Azul complex in the SVZ is kept in the database as two distinct centres. For each remaining stratovolcano, samples were sorted by increasing SiO_2 content and the four most mafic (lowest SiO_2) were selected. These four samples had to have SiO_2 contents which agree within 5 wt. %. Any volcanoes with <4 appropriate analyses within 5 wt. % were removed from the dataset. For repeat analyses of the same sample, the most recent analysis of the sample was selected, and the older analysis not counted in the selected sample number. This filtering method removes biases from over sampled volcanoes, such as Taapaca-Parinacota in the CVZ and San Pedro-Pellado and Quizapu in the SVZ, as the same number of samples are selected for each centre. The likelihood that a volcanic centre is not well represented at the mafic end is reduced by ensuring that samples selected for each volcanic centre agree within 5 wt. % SiO_2. The final number of samples in each of the filtered datasets are as follows: n=60 for the CVZ, and n=122 for the SVZ.

3.4 Results

3.4.1 Whole-rock geochemistry: Unfiltered dataset

Figure 21 shows major element variation diagrams for both CVZ and SVZ lavas plotted against SiO_2, so the degree of magmatic differentiation increases to the right. Colour scales are plotted according to both crustal thickness and slab thermal parameter for each volcanic centre to see if any compositional trends vary systematically with either parameter. Changing crustal thickness picks out systematic variations in differentiation trends in plots of Fe_2O_3, TiO_2, P_2O_5, K_2O and Total Alkalis (K_2O+Na_2O). Of these four major elements, K_2O shows the clearest trend. K_2O contents are higher in areas with greater crustal thicknesses over similar ranges in SiO_2 content.

The CVZ has the highest slab thermal parameters, which are taken to represent colder slabs as a given isotherm reaches a deeper depth (Kirby et al., 1996). The SVZ has lower slab thermal parameter values than the CVZ (warmer, younger slab). Both northern and southern SVZ volcanoes within the study area have slightly higher slab thermal parameters than the central SVZ. The plot of Na_2O against SiO_2 shows the differentiation trend varies systematically with slab thermal parameter. All major element variation diagrams, apart from Na_2O, show no systematic variation with increasing slab thermal parameter. The gradient of the trend between Na_2O and SiO_2 systematically decreases as slab thermal parameter values increase.

The distribution of SiO_2 contents varies as a function of crustal thickness, particularly between the SVZ and the CVZ (Figure 21). Figure 22 shows the frequency of samples for ranges in SiO_2 and MgO content. However, samples are not normalised to sampling number per volcano, so these distributions should be treated with some caution. Generally, the SVZ is dominated by samples ranging between 50-57 wt. % SiO_2 and >4 wt. % MgO contents, while the CVZ is characterised by samples between 58-65 wt. % SiO_2 and mostly <4 wt. % MgO.

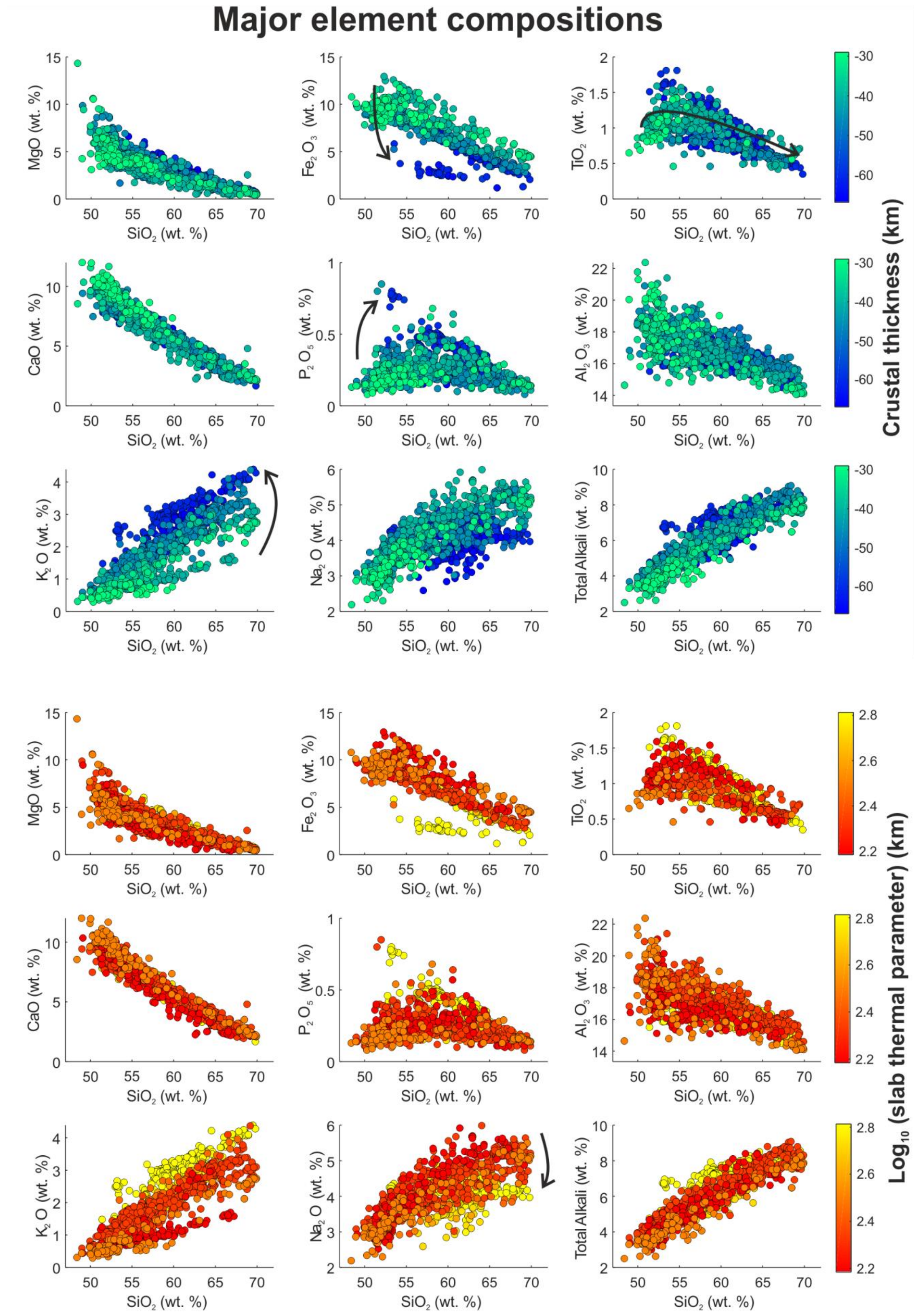

Figure 21: Major element compositions of CVZ and SVZ rocks in relation to crustal thickness (upper plots) and slab thermal parameter (lower plots). The lightest green colours in the upper plots represent the thin crust of the SVZ, crustal thickness increases northward through the SVZ and the CVZ has the thickest crust (dark blue). The curly arrows pick out where magmatic differentiation trends appear to vary systematically with either crustal thickness or slab thermal parameter. Note that there are more systematic variations in trends coloured by crustal thickness than by slab thermal parameter.

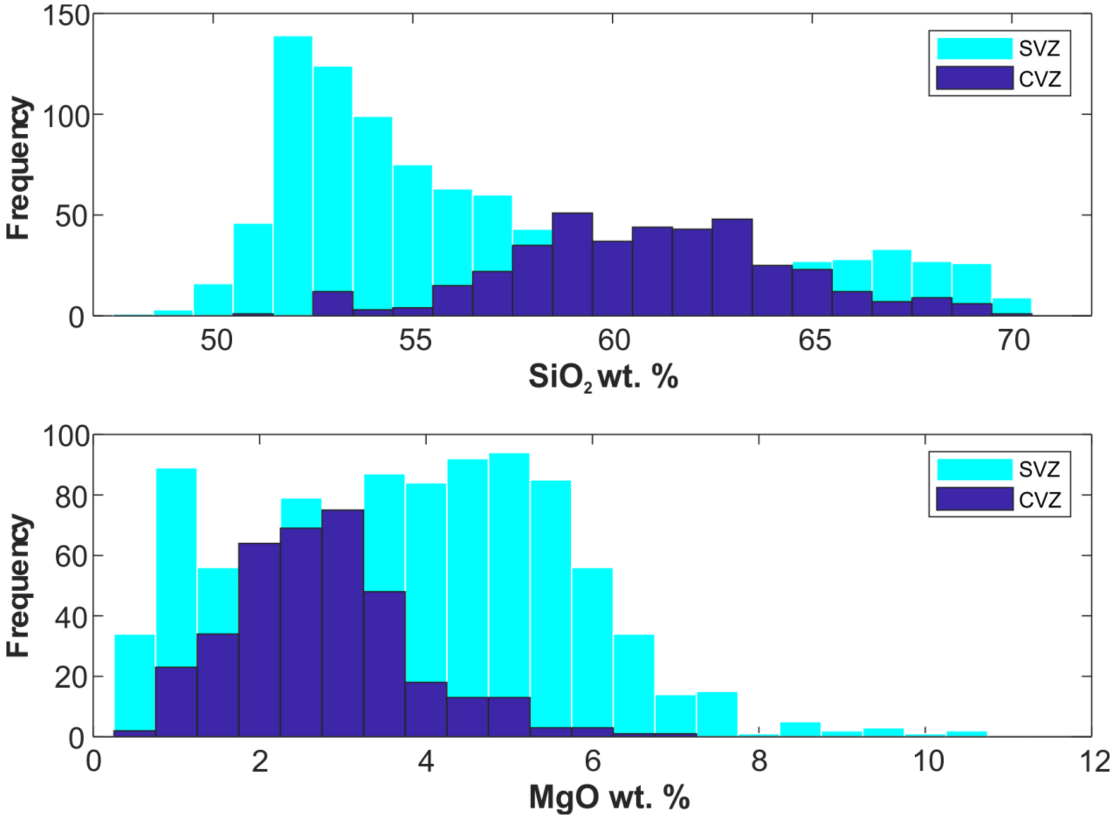

Figure 22: The distribution of SiO_2 and MgO contents in samples from both the SVZ and CVZ. n=348 for the CVZ, and n=1048 for the SVZ.

Figure 23 shows trace element compositions as a function of differentiation (SiO_2 content) and colour coded by both crustal thickness and slab thermal parameter. Again, like the major element compositions, systematic changes in differentiation trends occur with increasing crustal thickness and less so (or not at all) with the slab thermal parameter. The arrows show the general differentiation trends for both CVZ and SVZ lavas, in black and grey, respectively. CVZ lavas are enriched in Sr, Ba, La and, to a lesser extent, Sm (all highly incompatible elements) compared to SVZ lavas. CVZ and SVZ trends of Sr, Ba and La compositions converge with increasing SiO_2 content. CVZ and SVZ trends also converge for Nb (a High Field Strength Element, HFSE). In the CVZ, Sr, Ba, La and Nb are enriched in intermediate compositions and then decrease with increasing SiO_2 indicating general compatibility. In the south-central SVZ, all trace elements, apart from Sr, increase with increasing SiO_2 indicating incompatible behaviour.

For Zr, the slope of fractionation trends observed for any given crustal thickness becomes increasingly flatter as crustal thickness increases, indicating increasing Zr compatibility with increasing crustal thickness for intermediate to silicic magmas. Y and Yb both show diverging trends picked out by crustal thickness on Figure 23. Rare Earth Elements (REEs), La, Sm and Yb, are in order from light to heavy and show systematic variation in converging to diverging trends between SVZ and CVZ compositions and increasing crustal thickness.

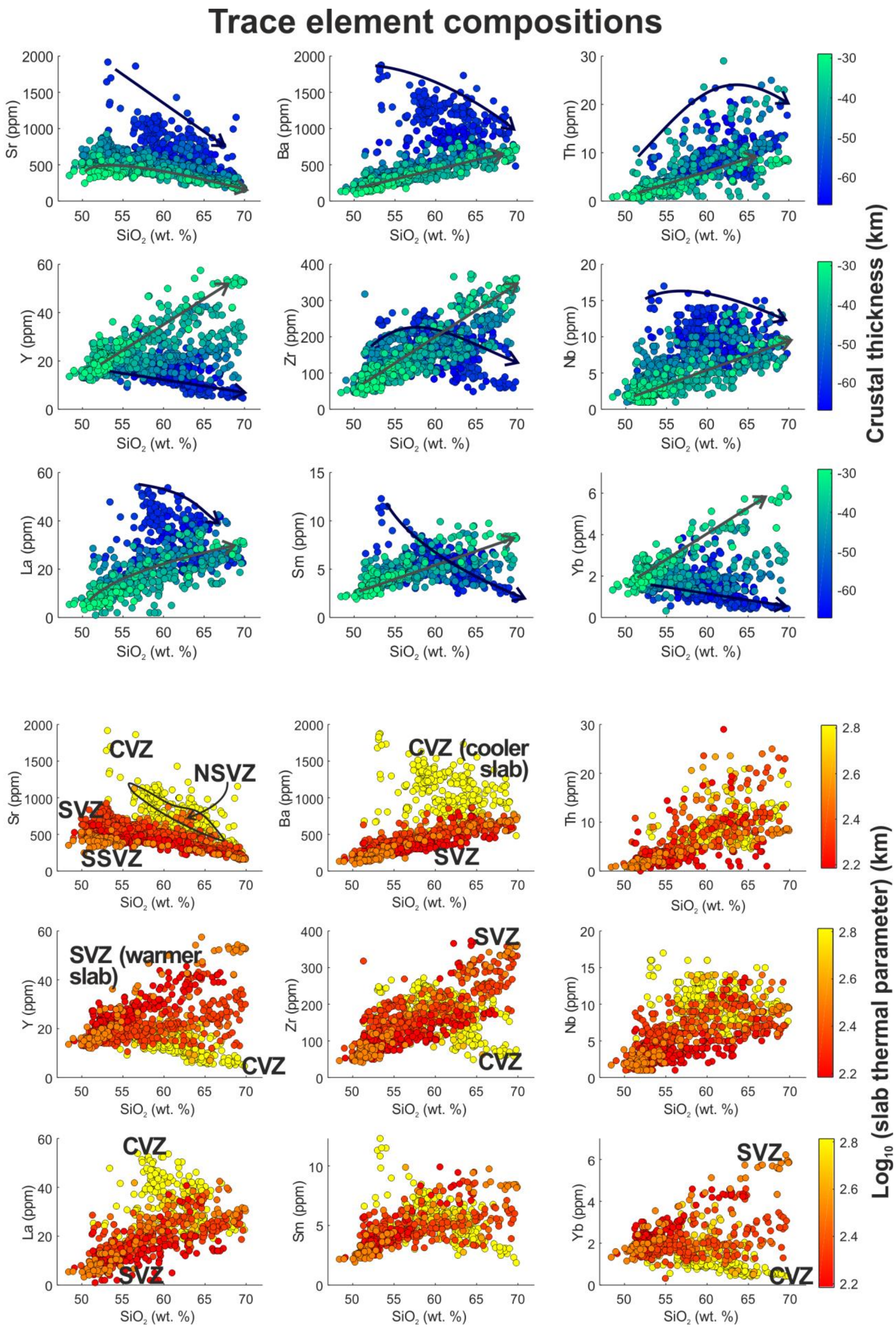

Figure 23: Trace element compositions of CVZ and SVZ rocks in relation to crustal thickness (upper plots) and slab thermal parameter (lower plots). Note that the CVZ has the highest slab thermal parameter (Log_{10} [ϕ] >2.6; representing the coolest slab), and SVZ has the lowest (Log_{10} [ϕ] <2.4; representing the warmest slab), while both the northern SVZ and the south-central SVZ have mid-range slab thermal parameters (Log_{10} [ϕ] ~2.5) for the Andes.

3.5 Discussion

3.5.1 The importance of fractionation in thick crusted arcs

Rare Earth Element (REE) concentrations of arc lavas can provide insights into pressure sensitive phases present in residual, source or fractionating assemblages of magmatic systems (Kay and Kay, 2002; Garrison and Davidson, 2003; Müntener and Ulmer, 2006; Davidson et al., 2007, 2013; Alonso-Perez et al., 2008; Chiaradia, 2009). The lower crust of volcanic arcs is thought to be plagioclase poor, for example, comparisons between seismic investigations of arcs to experimentally produced crustal lithologies and lower crustal xenoliths led to the conclusion that low seismic velocities (<7 km/s; 'upper crust-like') may reflect residual lithologies dominated by hornblende and plagioclase, while higher seismic velocities (>7.3 km/s; mid- to lower- crust transition) are likely the result of ultra-mafic plutonic rocks such as pyroxinites, garnet-hornblendites and garnet-gabbros (Müntener and Ulmer, 2006). The stability of pressure-sensitive mineral phases are affected by hydrous conditions (Sisson and Grove, 1993). For any given pressure in a water saturated magma, crystallisation of plagioclase is supressed (onset of plagioclase fractionation occurs at higher SiO_2, lower MgO) and the plagioclase produced tends to be more anorthite (Ca-)rich (Sisson and Grove, 1993). Magmatic garnet is generally stable at depths greater than ~40-45 km, but the stability field of garnet widens under hydrous (water saturated) conditions where the 'garnet-out' depth can be as shallow as ~30-35 km (Alonso-Perez et al., 2008). A magma which is sourced below or equilibrates within the garnet stability field may carry a 'garnet signature' in the trace element composition of the resultant volcanic products ($Sm/Yb > 5$, $La/Yb > 30$; e.g. Van Westrenen et al., 1999). Several tectonic processes have been used to interpret such elevated REE ratios, such as: slab melting (Kay, 1978; Defant and Drummond, 1990; Stern and Kilian, 1996; Mungall, 2002); fore-arc subduction erosion (Stern, 1991; Kay and Kay, 2002; Kay et al., 2014); high-pressure melting of the refractory lower crust in the overriding plate (Kay and Kay, 2002; Chiaradia, 2009); and magma differentiation within the garnet stability field (Garrison and Davidson, 2003; Macpherson et al., 2006; Alonso-Perez et al., 2008; Chiaradia, 2009). For the slab melt hypothesis, high La/Yb and Sr/Y ratios in high Mg lavas would be expected above young and hot subducting oceanic lithosphere (Kay, 1978; Defant and Drummond, 1990; Stern and Kilian, 1996; Mungall, 2002).

Variations in trace element ratios as a function of slab thermal parameter are shown in Figure 24. Figure 25 shows the variations in selected trace element ratios in comparison to both increasing fractionation (SiO_2 content) and crustal thickness. Clear diverging fractionation trends for trace element ratios Sr/Y, La/Yb and Sm/Yb can be distinguished between the CVZ (thick crust) and SVZ (thin crust). Divergent trends in Figure 25 show that large variations in La/Yb, Sr/Y and Sm/Yb occur in the thick-crusted CVZ and northern SVZ (NSVZ), but not in the southern SVZ which has younger slab ages and lower slab thermal parameters than the CVZ. These ratios only increase during differentiation at intermediate to silicic compositions (Figure 25). These plots emphasise the importance of magmatic garnet fractionation with increasing crustal thickness (Garrison and Davidson, 2003; Macpherson et al., 2006; Alonso-Perez et al., 2008; Chiaradia, 2015; Profeta et al., 2015b; Farner and Lee, 2017).

Opposing fractionation trends between SVZ and CVZ lavas occur in plots of the ratios Ba/Zr and La/Sm (Figure 25). In the CVZ, Zr becomes increasingly depleted in intermediate to felsic magmas (Figure 23), which may reflect the increasing importance of zircon crystallisation in silicic magmas from the CVZ. The thin crust region of the SVZ is characterised by low Nb contents and higher La/Nb ratios (Figure 25). Thicker-crust sections (NSVZ and CVZ) trend towards higher Nb contents and lower La/Nb ratios.

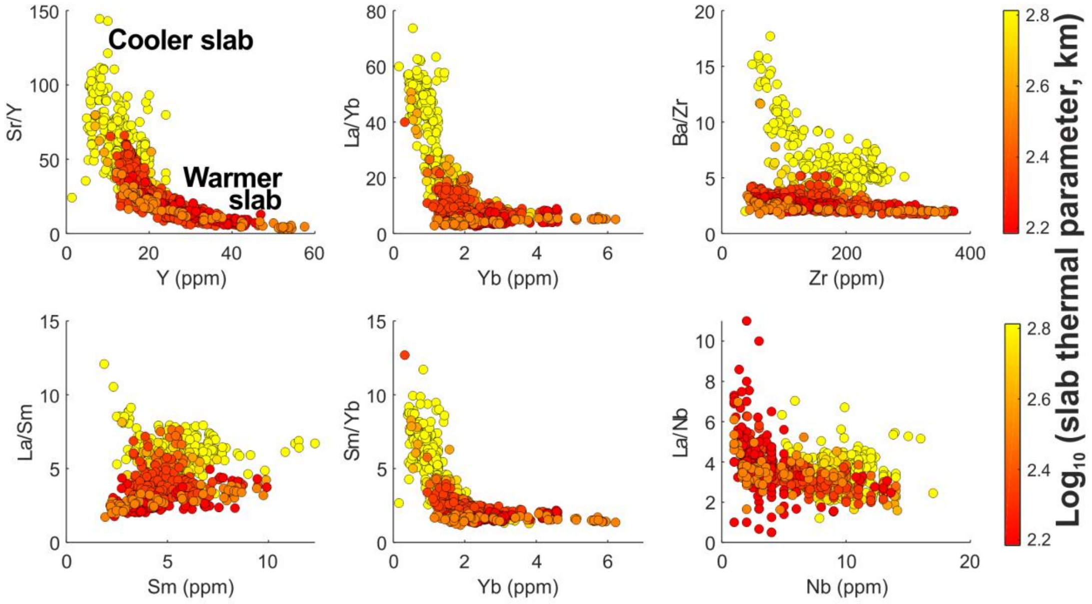

Figure 24: Trace element ratios vs the heavier denominator element, as a function of Log10 [ϕ]. Higher values of ϕ suggest cooler slab temperatures at a given depth, whereas lower values of ϕ indicate warmer slab temperatures. These plots show that higher Sr/Y and La/Yb ratios occur in the CVZ and NSVZ where slab temperatures are relatively cooler than the SVZ (due to the age of the slab increasing northwards).

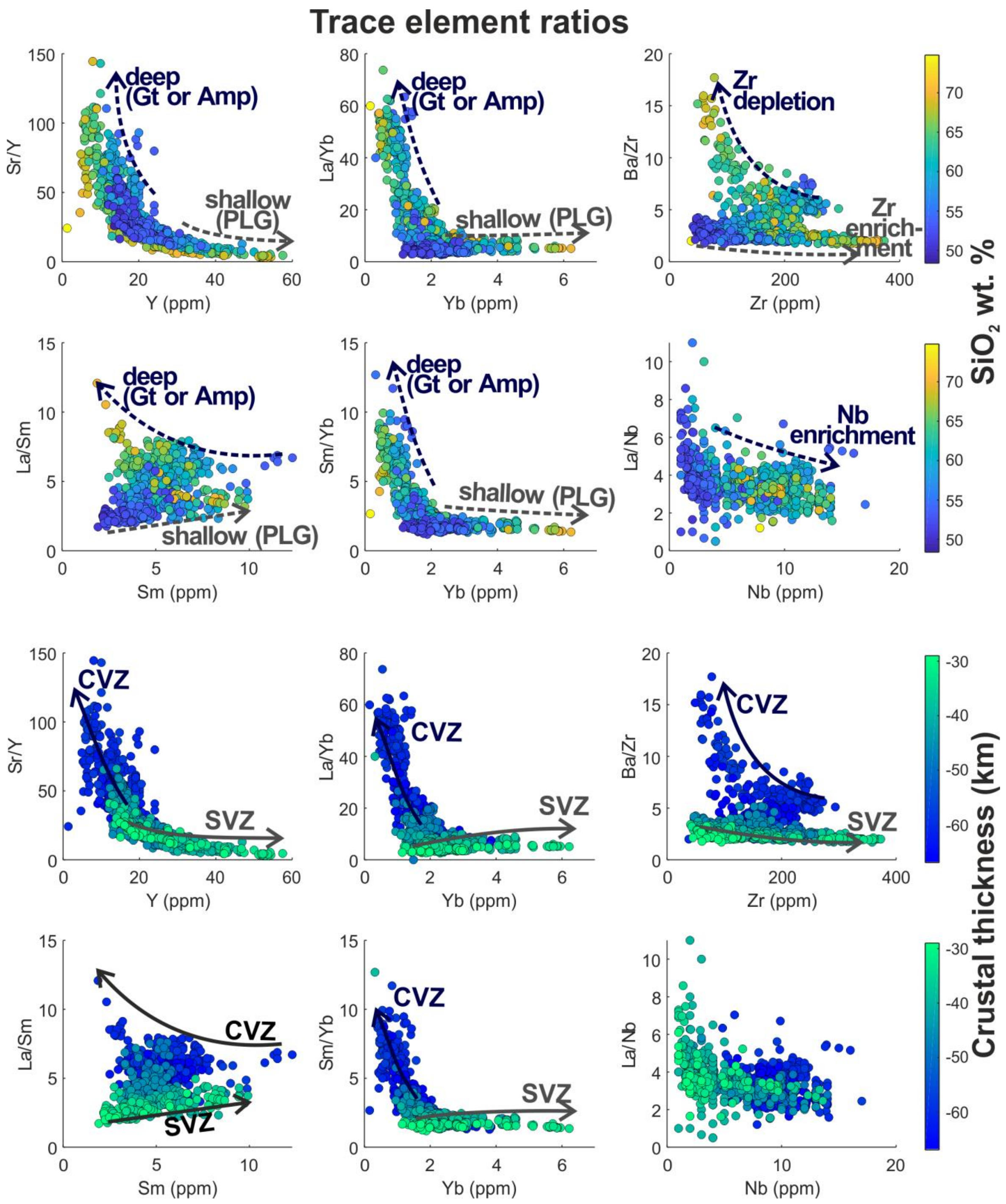

Figure 25: Trace element ratios vs the heavier denominator element, both as a function of fractionation (SiO$_2$ content, upper panels) and crustal thickness (lower panels). Curly arrows represent differentiation trends for both the CVZ and SVZ, identified by comparing both plots together. Potential mineral phases associated with such fractionation trends are labelled (Gt=garnet; Amp=amphibole; PLG=plagioclase; e.g. (Van Westrenen et al., 1999; Kay and Kay, 2002; Macpherson et al., 2006; Davidson et al., 2007; Alonso-Perez et al., 2008). The arrow labelled 'Nb enrichment' is not a differentiation trend but shows that Nb is relatively enriched in the CVZ compared to SVZ.

3.5.2 Quantified correlations

Figure 26 shows examples of linear regression analysis for 'most-mafic' filtered major element compositions against crustal thickness. K_2O, CaO and total alkalis (K_2O+Na_2O) have the strongest correlations with crustal thickness. The correlation between crustal thickness and K_2O presented here is especially strong compared to analyses of global arc systematics which show no strong correlation between K_2O and crustal thickness. For example, Turner and Langmuir (2015b) found r^2=0.51 between crustal thickness and global arc-averaged $K_{6.0}$ values. Hildreth and Moorbath (1988) pointed out that K_2O varies systematically with increasing elevation and crustal thickness within the SVZ. Increasing K_2O, alongside increasing variability in Rb and Cs concentrations and increasing enrichment of radiogenic isotope compositions, with increasing crustal thickness is attributed to increasing degrees of deep-crustal contamination and selective contamination of mafic magmas percolating through silicic-alkaline crustal rocks (Hildreth and Moorbath, 1988).

Both MgO and Na_2O have weak correlations with crustal thickness in the Andes and there is no correlation between TiO_2 and crustal thickness (Figure 26). There is a wide spread of compositions for many of the elements shown in Figure 26 at crustal thicknesses of ~40 km.

Na contents within the CVZ do not follow the positive trend between Na_2O and crustal thickness in the SVZ. In the more silicic compositions from the CVZ, Na might be more compatible due to fractionation of albitic plagioclase. The lack of correlation between crustal thickness and Na_2O wt. % is in contrast to the results of Plank and Langmuir (1988), who found the strongest correlations between subduction parameters and major element compositions (normalised to 6 wt.% MgO) globally were between crustal thickness and both $Na_{6.0}$ (R=0.83) and $Ca_{6.0}$ (R=-0.89), respectively. Turner and Langmuir (2015b) also found strong correlations between crustal thickness and global arc-average $Na_{6.0}$ (R^2=0.74) and $Ca_{6.0}$ (R^2=0.66) compositions.

Figure 27 displays histograms of the results from linear regression analysis between the same nine major element compositions now compared to 6 other different physical parameters. The strongest correlations are between compositions of SiO_2, CaO, Fe_2O_3, Al_2O_3, K_2O, and total alkalis, with elevation, crustal thickness, and slab age, respectively. As shown in Chapter 2, slab age and crustal thickness are strongly correlated in the Andes, and crustal thickness and elevation are strongly correlated along the arc due to isostasy (Appendix 8.2), so cross correlations are to be expected between these three parameters.

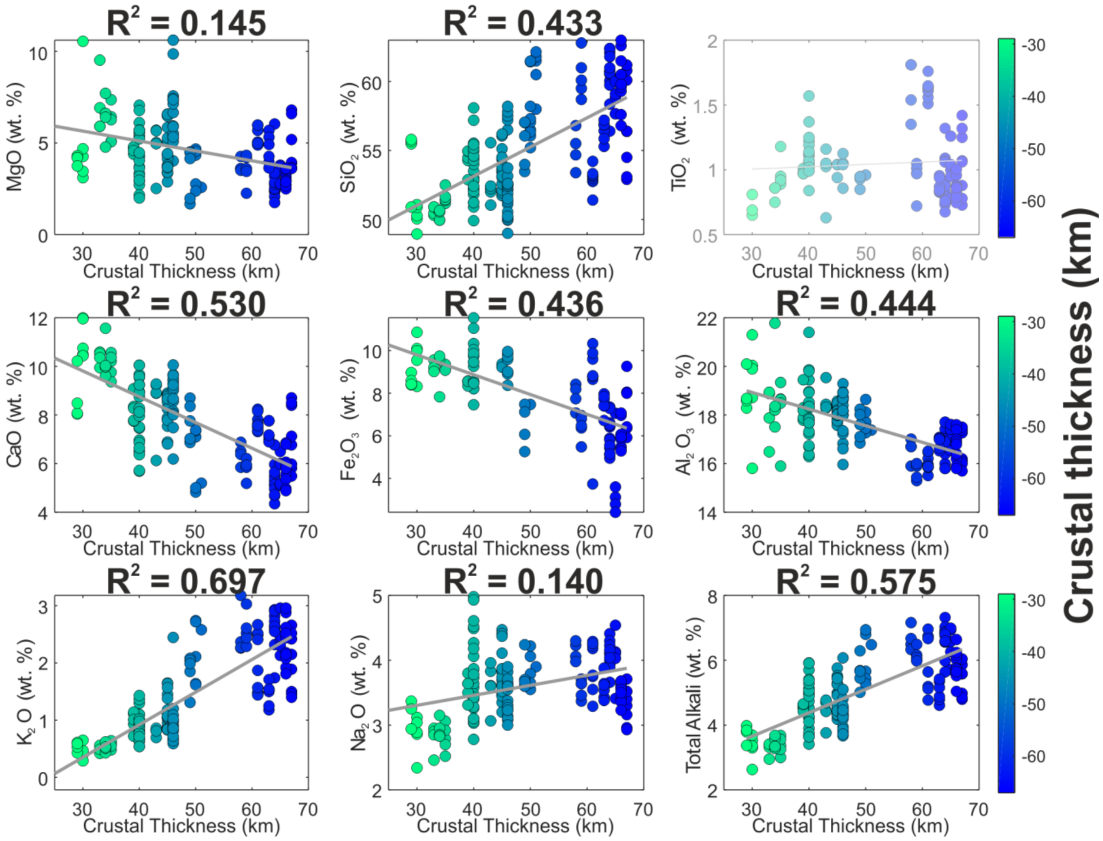

Figure 26: Linear regression analyses for 'most-mafic' filtered major element compositions of CVZ and SVZ lavas against overriding plate crustal thickness. All correlations are weak, except for K_2O which shows a good correlation, and TiO_2 which is greyed out as the correlation was found to be statistically insignificant (p-value>0.01). For the CVZ n=60, and for SVZ n= 122.

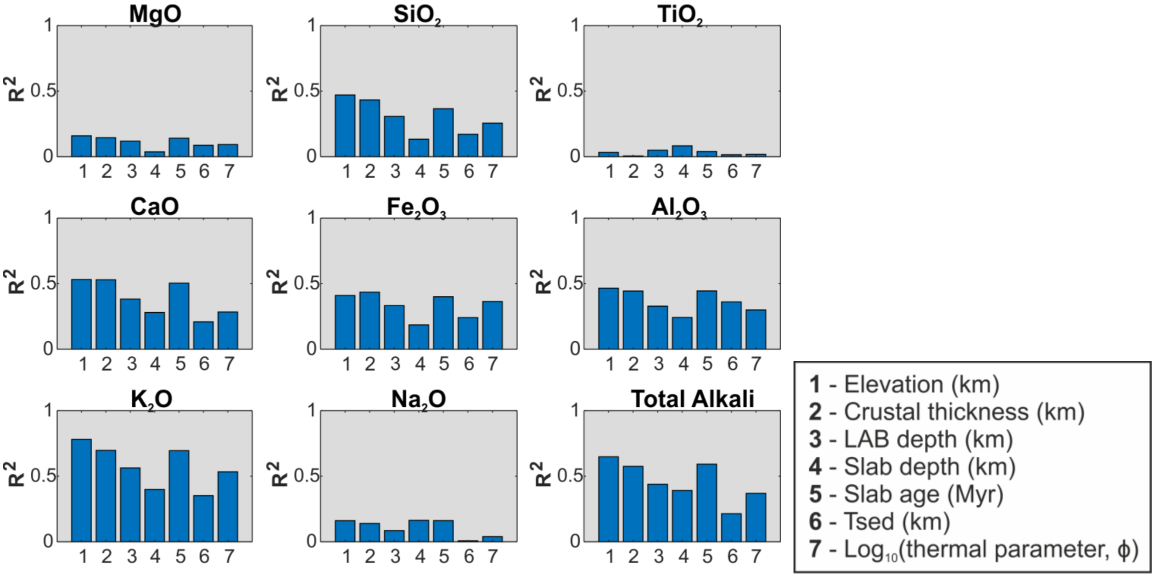

Figure 27: Results of R^2-tests for correlations between 'most-mafic' filtered major element compositions and seven different physical parameters (elevation, crustal thickness, lithosphere-asthenosphere depth, depth to slab, slab age, trench sediment thickness, and Log_{10}[ϕ]).

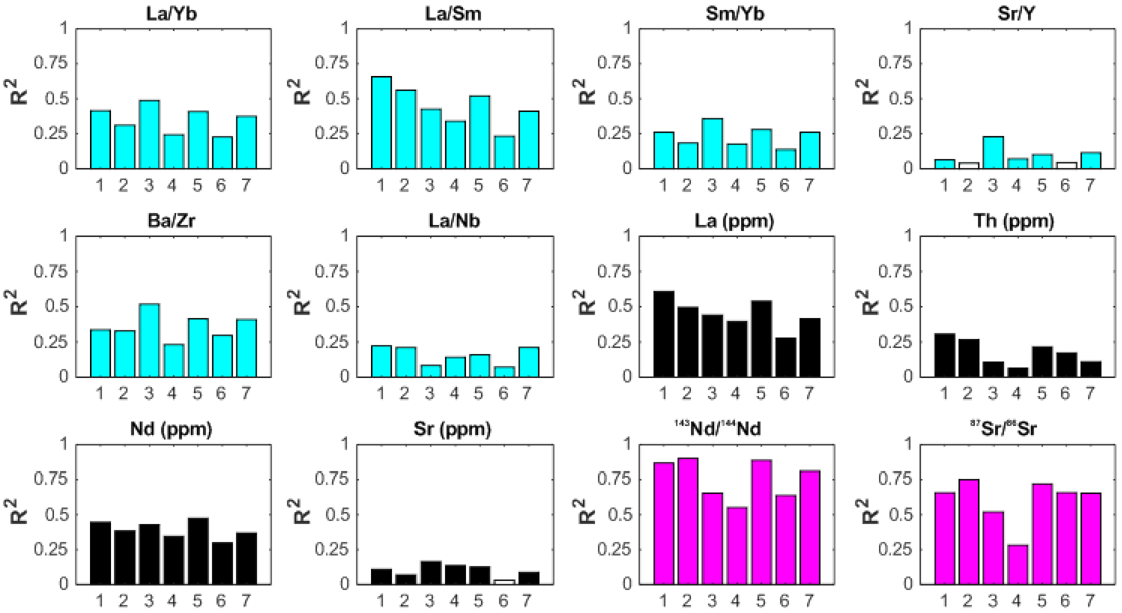

Figure 28: Results of R^2-tests for correlations between 'most-mafic' filtered trace element, trace element ratio and radiogenic isotope compositions against seven different physical parameters (elevation, crustal thickness, lithosphere-asthenosphere depth, depth to slab, slab age, trench sediment thickness, and $\mathrm{Log}_{10}[\phi]$). The numbering system for physical parameters is the same as Figure 27. White coloured bars represent insignificant correlations (p-value>0.01).

Results for linear regression analysis for trace element and isotope compositions are shown in Figure 28. Results for La/Sm and La have a very similar distribution of R^2 values as results for K_2O (and total alkalis). Incompatible elements are progressively enriched with increasing crustal thickness and SiO_2 content. Such results are unsurprising and similar results have been observed in global arc geochemical systematics by Farner and Lee (2017), who use smoothed elevation as a proxy for crustal thickness. Our results show that K_2O, SiO_2, La/Sm and La all have slightly stronger correlations with smoothed elevation than with crustal thickness, but this could be due to less uncertainty in smoothed elevation values compared to crustal thickness estimates. Increasing enrichment of incompatible elements and SiO_2 northward through the SVZ and into the CVZ fits with previous hypotheses of crustal thickness increasing the minimum degree of fractionation due to longer transit and cooling times in thick crust settings (Farner and Lee, 2017). Results do not preclude suggestions for source contamination such as forearc subduction erosion, delamination or continental lithosphere erosion (Kay and Kay, 1993; Ducea et al., 2013; Kaislaniemi et al., 2014; Currie et al., 2015; Turner et al., 2017), which are likely to become increasingly important processes in thickened orogens (Currie et al., 2015).

$^{143}Nd/^{144}Nd$ and $^{87}Sr/^{86}Sr$ have the strongest correlations with crustal thickness (and by cross correlation, elevation and slab age), and these relationships are explored further in the next two chapters. In Chapter 4, we suggest that $^{143}Nd/^{144}Nd$ and $^{87}Sr/^{86}Sr$ isotopes can be used as paleo-elevation proxies for the Andes due to the strong influence of crustal thickness on these isotope compositions. In Chapter 5, pre-Quaternary isotope compositions are analysed and related to the crustal thickening and uplift history of the Andes.

Geochemical systematics correlate strongly with crustal thickness and less so with the slab thermal parameter, which is consistent with results from studies of global arc systematics (Turner and Langmuir, 2015b, 2015a). It is possible that weak correlations between geochemical parameters and the slab thermal parameter are a product of stronger correlations with slab age (as slab age is the main variant controlling slab thermal parameters at the Andean margin). The slab age increases northward through the study area and in turn, the slab thermal parameter increases indicating cooler slabs in the north (Figure 20). Incompatible element and isotope enrichment, increasing SiO_2 contents and high La/Yb, Sr/Y and Sm/Yb occur with increasing crustal thickness and not with increasing slab thermal parameter (the Nazca slab becomes warmer southwards due to the decreasing slab age). These results therefore do not agree with previous hypotheses of slab melting during subduction of hot, young slabs, causing 'adakitic' signatures (Kay, 1978; Defant and Drummond, 1990; Stern and Kilian, 1996), but instead supports the hypothesis that the presence of magmatic garnet and/or amphibole in the lower crust of thickened arcs is more important at generating these geochemical signatures (Garrison and Davidson, 2003; Macpherson et al., 2006; Alonso-Perez et al., 2008; Chiaradia, 2015; Profeta et al., 2015b).

3.6 Conclusions

- We quantify variations in several geochemical parameters of both CVZ and SVZ lavas (18-42° S) in relation to different physical parameters which vary along-strike in the Andean subduction zone.
- 'Adakitic' trace element ratios (high Sr/Y and La/Yb) in intermediate lavas increase with increasing crustal thickness and not with increasing slab temperatures (decreasing slab age). This result supports the hypothesis that 'adakitic' signatures are the result of the increasing importance of garnet and/or amphibole fractionation with increasing crustal thickness, and do not need to be explained by slab melting.
- The strongest correlations found in this study are between increasing elevation, crustal thickness and slab age with increasing enrichment of $^{143}Nd/^{144}Nd$, $^{87}Sr/^{86}Sr$, K_2O, La, and La/Sm and increasing SiO_2 contents.
- These results emphasise the importance of increasing crustal thicknesses on arc magma compositions. Crustal thickness can affect arc magma compositions by increasing the minimum degree of fractionation and crustal contamination seen at each volcano. Results do not preclude source contamination such as forearc subduction erosion, delamination or continental lithosphere erosion by mantle corner flow, which are likely to become increasingly important processes in thickened Cordilleran arcs.
- Na_2O (filtered to the most-mafic compositions for each volcanic centre) has a very weak correlation with crustal thickness along the Andes, which may be related to more significant fractionation of albite in the more silicic rocks within the CVZ.
- Therefore, there is a strong case for the effect of crustal thickness on arc front compositions in the Central and Southern Andes. In the next two Chapters, we explore further the applications of arc geochemistry as a crustal thickness and (indirect) paleo-elevation proxy.

Chapter 4: Andean surface uplift constrained by radiogenic isotopes of arc lavas

This chapter is based on published work in Nature Communications:

Scott, E.M., Allen, M.B., Macpherson, C.G., McCaffrey, K.J.W., Davidson, J.P., Saville, C., and Ducea, M.N., 2018, Andean surface uplift constrained by radiogenic isotopes of arc lavas: Nature Communications, v. 9, no. 969, doi:10.1038/s41467-018-03173-4.

Author Contributions: The work for this chapter and manuscript are my own, and were conducted with the help, guidance and expertise of my co-authors that would be usual of a supervisory team.

4.1 Chapter summary

Climate and tectonics have complex feedback systems which are difficult to resolve and remain controversial. Here we propose a new climate-independent approach to constrain regional Andean surface uplift. $^{87}Sr/^{86}Sr$ and $^{143}Nd/^{144}Nd$ ratios of Quaternary frontal arc lavas from the Andean Plateau are distinctly crustal (>0.705 and <0.5125, respectively) compared to non-plateau arc lavas, which we identify as a plateau discriminant. Strong linear correlations exist between smoothed elevation and $^{87}Sr/^{86}Sr$ (R^2=0.858, n=17) and $^{143}Nd/^{144}Nd$ (R^2=0.919, n=16) ratios of non-plateau arc lavas. These relationships are used to constrain 200 Myr of surface uplift history for the Western Cordillera (present elevation 4200±516 m). Between 16-26°S, Miocene to recent arc lavas have comparable isotopic signatures which we infer indicates that current elevations were attained in the Western Cordillera from 23 Ma. From 23-10 Ma, surface uplift gradually propagated southwards by ~400 km.

4.2 Introduction

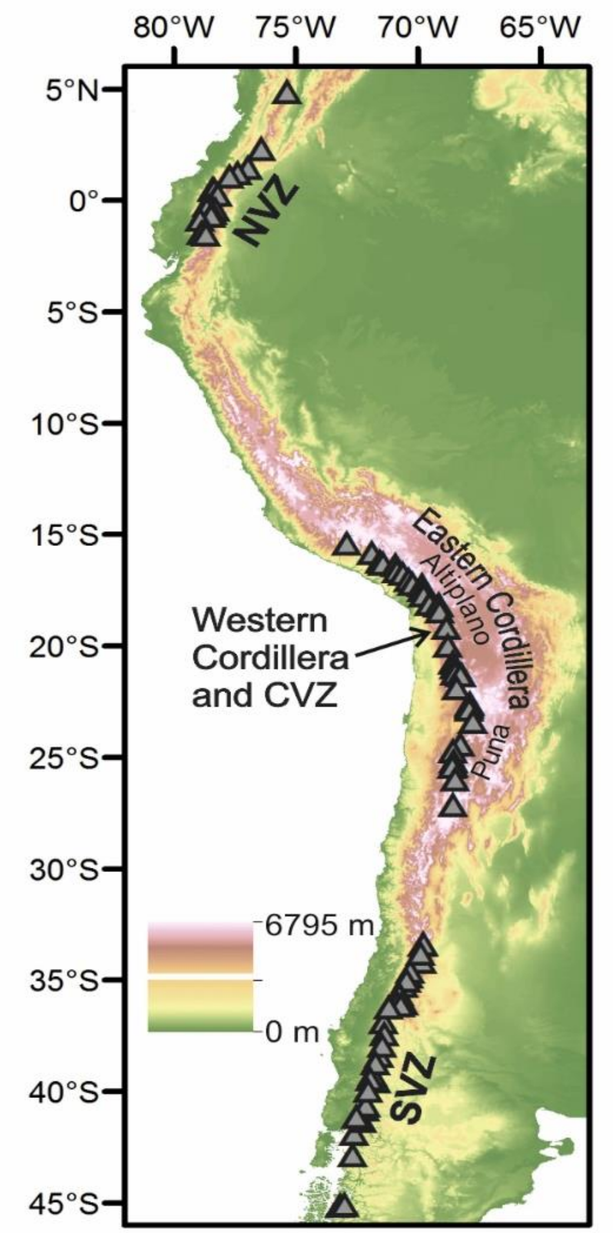

Figure 29: Topographic map of western South America. Grey triangles are locations of Quaternary arc front volcanoes from the N, C & SVZ (North, Central and Southern Volcanic Zones) included in our geochemical compilation (Methods). CVZ centres are located within the Western Cordillera of the Andean Plateau

Orogenic plateaux have complex tectonics and variable climates which provide a unique ecological niche. Knowledge of the tectonic evolution and surface uplift of such high, wide regions is fundamental to understanding feedbacks between climate change and tectonics (Lamb and Davis, 2003; Lee et al., 2015). Orogenic plateaux affect atmospheric circulation and precipitation patterns (Armijo et al., 2015). Uplift of high plateaux changes the efficiency of erosion and sediment flux into internal and oceanic basins, leading to atmospheric CO_2 drawdown via silicate weathering and hence long-term global climate cooling (Armijo et al., 2015; Lee et al., 2015). Conversely, arcs erupted through high plateaux emit large quantities of CO_2 during magmatic flare-ups which have been linked to global greenhouse events (McKenzie et al., 2014). Climate-driven aridification and subsequent trench sediment starvation can also focus plate boundary stresses at subduction zones and enhance compressional deformation (Lamb and Davis, 2003). Despite numerous multidisciplinary studies the topographic, tectonic and geodynamic evolution of orogenic plateaux remains ambiguous (Lamb and Davis, 2003; Barnes and Ehlers, 2009; Jamieson and Beaumont, 2013; Garzione et al., 2017).

The Andean Plateau is the second largest tectonically active plateau in the world. From west to east the Andean Plateau spans over 400 km and is divided into three tectonically distinct zones: the Western Cordillera (including the active Central Volcanic Zone, CVZ, of the Andean arc), the internally drained Altiplano and Puna plateaux, and the Eastern Cordillera fold-and-thrust belt (Figure 29). North and south of the plateau Andean arc magmatism continues in the Northern and Southern Volcanic Zones (NVZ and SVZ, respectively) which are separated from the CVZ by two volcanic gaps. Large volumes of Andean arc magmatism have been emplaced along the South American margin since >200 Ma as result of oceanic subduction under the South American continent (Coira et al., 1982). During this time the locus of Central Andean arc magmatism has progressively shifted eastward from the modern coastline to its present location (Coira et al., 1982; Kay et al., 2006).

Many studies have attempted to quantify Andean Plateau surface uplift but most of these works concentrate on regions east of the active arc in the Altiplano, Puna and Eastern Cordillera (Garzione et al., 2017). Two end-member models of Andean Plateau uplift remain prevalent (Barnes and Ehlers, 2009; Garzione et al., 2017): slow, steady uplift from at least 40 Ma primarily due to crustal thickening (Mamani et al., 2010; McQuarrie et al., 2005; Carrapa et al., 2006; Carlotto, 2013; Canavan et al., 2014; Chapman et al., 2015b; Zhou et al., 2017); and rapid, recent surface uplift post 16 Ma as a result of lower lithosphere removal, magmatic thickening or lower crustal flow (Garzione et al., 2006, 2008; Leier et al., 2013; Kar et al., 2016; Garzione et al., 2014; Schildgen et al., 2009; Lamb, 2011, 2016; Perkins et al., 2016). Currently-used paleoelevation proxies, such as paleobotany (e.g. (Gregory-Wodzicki et al., 1998; Kar et al., 2016); and references therein) and stable isotope techniques (Garzione et al., 2006, 2008; Leier et al., 2013; Canavan et al., 2014; Kar et al., 2016), rely on the assumption that the dependence of parameters such as air temperature and humidity upon elevation in the past were the same as the present (Garzione et al., 2017). However, regional climate change related to surface uplift may account for some signals used to interpret elevation gain (Barnes and Ehlers, 2009; Insel et al., 2012; Fiorella et al., 2015). Paleoclimate conditions are often not corrected for, resulting in large errors on paleoelevation estimates of up to a few kilometres (Insel et al., 2012; Fiorella et al., 2015).

Very few studies have constrained paleoelevation estimates for the Western Cordillera (Garzione et al., 2017). However, geological evidence shows that the Jurassic to Early Cretaceous Andean arc initially developed in an extensional tectonic setting which gradually changed from marine to continental conditions (Mamani et al., 2010; Rossel et al., 2015). The onset of compressional deformation in the Western Cordillera between 90-70 Ma is evident from angular unconformities, intrusive relationships and extensive conglomerate deposition in back-arc regions (Haschke et al., 2002b; Carlotto, 2013). Deformation and crustal shortening then became diachronous in both the Western and Eastern cordilleras from c. 50-40 Ma (McQuarrie et al., 2005; Oncken et al., 2006). At this time the present high Altiplano-Puna was a ~300 km wide basin close to sea level which separated the two deformation belts (Lamb et al., 1997; Lamb and Hoke, 1997). Marked differences in provenance of Late Eocene-Oligocene sediments between basins east and west of the 'Proto'-Western Cordillera provide evidence of relief formation at this time (Wotzlaw et al., 2011); with further confirmation from facies changes related to uplift dated around ~35 Ma in forearc basins (Decou et al., 2013).

Here we utilize published geochemical and isotopic data for Andean arc lavas to constrain a regional surface uplift history for the Western Cordillera. Arc magma compositions are related to the processes of mantle melting, intra-crustal differentiation and crustal assimilation (Hildreth and Moorbath, 1988; Turner and Langmuir, 2015b). It has long been observed that there are links between crustal thickness and certain geochemical parameters of arc lavas (Leeman, 1983; Feigenson and Carr, 1986; Hildreth and Moorbath, 1988; Plank and Langmuir, 1988). Increasing crustal thickness of the overriding plate can affect arc systematics by: (1) reducing the thickness of the mantle wedge, decreasing wedge corner flow and thus limiting the extent of mantle melting (Plank and Langmuir, 1988; Turner and Langmuir, 2015b, 2015a; Turner et al., 2016); (2) raising the pressure of magma fractionation at the Moho and hence changing the stability of certain mineral phases (Chiaradia, 2015; Chapman et al., 2015a; Profeta et al., 2015a); and (3) increasing the degree of intra-crustal differentiation and crustal assimilation (Hildreth and Moorbath, 1988; Davidson et al., 1990; Farner and Lee, 2017). Such links have been previously used to infer crustal thickening in the Central Andes from 40-30 Ma (Haschke et al., 2002b; Mamani et al., 2010; Profeta et al., 2015a).

Similarities between chemical and isotopic signatures of Central Andean lavas and middle Cenozoic lavas from the Great Basin in western Utah and Nevada have led to the interpretation that an orogenic plateau was present at this time (Best et al., 2009), commonly termed the 'Nevadaplano'. Recently, regional and global compilations of geochemical parameters (such as Sr/Y and La/Yb) of both arc and continental collision zone magmatism have been calibrated to modern crustal thickness (Chiaradia, 2015; Turner and Langmuir, 2015b, 2015a; Chapman et al., 2015a; Profeta et al., 2015a; Hu et al., 2017). Global arc systematics have also been found to correlate with elevation and, assuming isostatic equilibrium (Lee et al., 2015), crustal thickness (Farner and Lee, 2017). Despite these numerous findings, arc geochemistry has not previously been directly calibrated to elevation and used to infer a regional surface uplift history. Using age corrected Sr- and Nd- isotope ratios we infer that the Western Cordillera was close to current elevations (4200±516 m) by the Early Miocene. From 23-10 Ma, surface uplift propagated southwards through the region of the current volcanic gap and northern SVZ, c. 26-35°S.

4.3 Methods

4.3.1 Geochemical compilation

We have compiled a geochemical database for Andean arc lavas, dated from Jurassic to present day, from 41 previously published studies (Electronic Appendix 4.1-4.3). We have not included ignimbrites, plutonic rocks or back-arc lavas in this database. Jurassic centres that are known to have been erupted underwater and hence have isotope signatures which are affected by seawater contamination (Rossel et al., 2015) are not included. The maximum analytical error reported in our compilation is $<\pm0.00007$ 2σ for Sr isotope ratios and ±0.00003 2σ for Nd isotope ratios.

$^{87}Sr/^{86}Sr$ ratios of each of the two standards (Eimer and Amend and NBS 987) reported by different laboratories in our compilation are within analytical error so data can be directly compared, except for data published by Francis et al. (1977) and Rogers and Hawkesworth (1989), which we normalised to 0.70800 (Eimer and Amend) and 0.71025 (NBS 987), respectively, so that they can also be directly compared. Quaternary $^{143}Nd/^{144}Nd$ ratios of reported standards are also within error, except data from Marín-Cerón et al. (2010) and Nyström et al. (2003), which we normalised to 0.511840 (La Jolla). No other isotope ratios have been normalised.

4.3.2 Defining baseline isotopic signatures

A 'most-mafic' filter is used to leave only the isotope ratios of the least silicic sample from each volcanic centre in our compilation, in a similar way to filtering methods used in Chapter 3. Where major element compositions are not published, we choose the least radiogenic sample for that volcanic centre. We do not include centres with only one sample.

4.4 Results

4.4.1 $^{87}Sr/^{86}Sr$ and $^{143}Nd/^{144}Nd$ ratios as plateau discriminants

$^{87}Sr/^{86}Sr$ and $^{143}Nd/^{144}Nd$ ratios are particularly useful in studying interactions between continental crust and depleted mantle, as these reservoirs have a large isotopic contrast (e.g. Hildreth and Moorbath, 1988; Figure 30). Qualitative comparisons between $^{87}Sr/^{86}Sr$ and $^{143}Nd/^{144}Nd$ ratios of Quaternary Andean arc lavas, crustal thickness and present-day topography (Figure 31) confirm previous findings that radiogenic isotopes can be linked to elevation and crustal thickness. Good correlations between present-day surface elevation and crustal thickness along the Andean arc (Appendix 8.2) support the hypothesis of a dominant isostatic control on regional elevation at the arc (e.g. Lee et al., 2015).

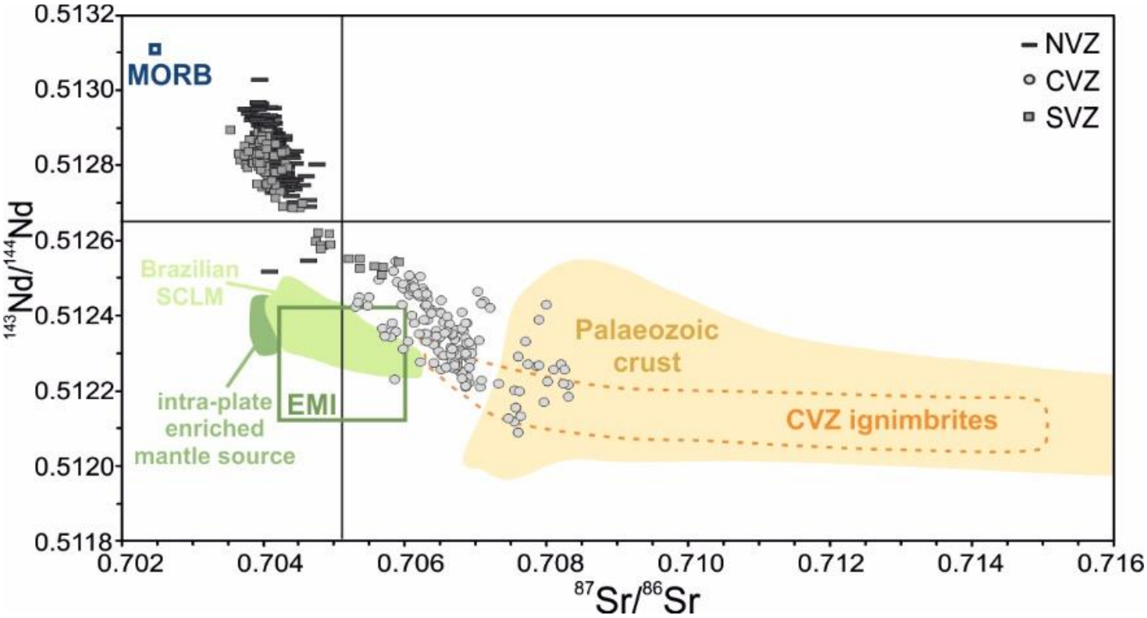

Figure 30: Andean lavas are produced by mixing of depleted mantle melts with radiogenic crust. Sr-Nd radiogenic isotope plot of Quaternary lavas from the N, C & SVZ (compilation from this study, Methods and Electronic Appendix 4.1) and CVZ ignimbrites (Franz et al., 2006) in comparison to Paleozoic continental crust and mantle end members including Depleted Mantle (Pacific MORB), enriched sub-continental lithospheric mantle (SCLM) and Enriched Mantle I (EMI); from ref. (Lucassen et al., 2006) and references therein. Andean frontal arc lavas follow a trend from a depleted mantle source to Palaeozoic crust and are not thought to be influenced by enriched mantle sources (Lucassen et al., 2006).

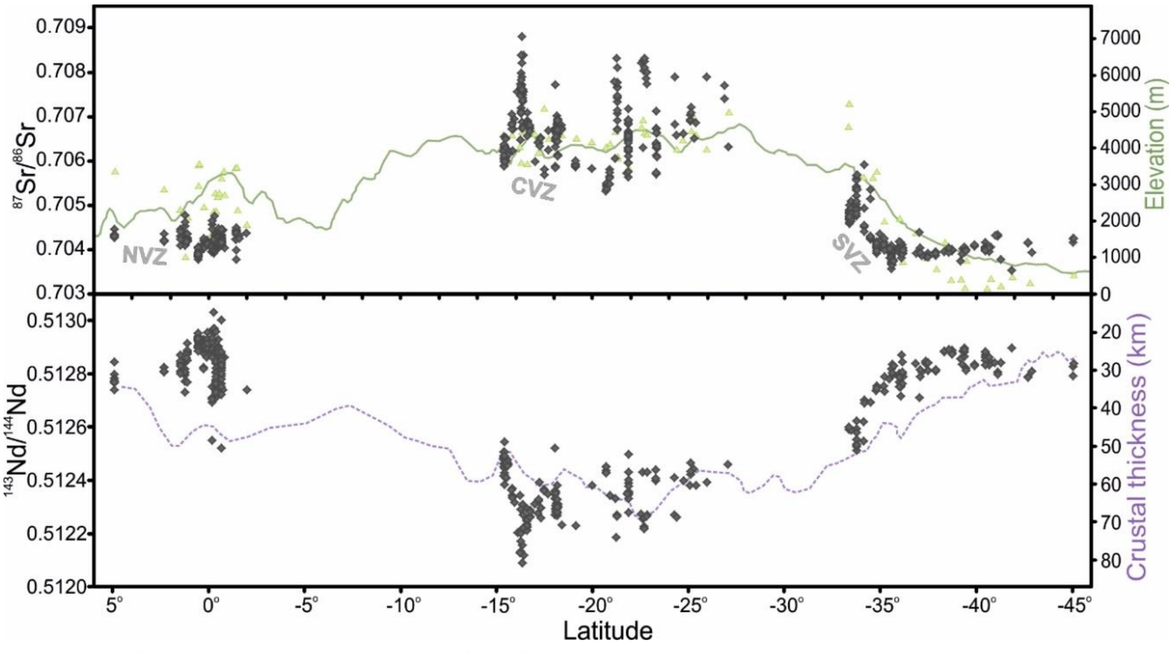

Figure 31: Comparison of whole rock ^{87}Sr/^{86}Sr and ^{143}Nd/^{144}Nd ratios of arc lavas with crustal thickness and elevation. Quaternary whole-rock Sr- and Nd- isotope ratios of frontal arc lavas (diamonds, compilation from this study; see Methods and Electronic Appendix 4.1) compared to volcano base elevation (triangles; this study, see Methods; de Silva and Francis, 1991; Völker et al., 2011), arc front mean elevation (100 km wide swath, GTOPO30 digital elevation model (DEM); US Geological Survey, 1996) and crustal thickness profiles (5 period moving average; Assumpção et al., 2013; RMS <3.5 km).

Isotope ratios from CVZ (plateau) arc lavas are clearly distinct from either NVZ or SVZ (non-plateau) arc lavas. For example NVZ and SVZ lavas have an arithmetic mean (±2 SD) $^{87}Sr/^{86}Sr$ ratio of 0.70418 (±0.00036, n=210) and 0.70426 (±0.00098, n=189), respectively, while CVZ lavas have a mean of 0.70671 (±0.00138, n=297). Northern SVZ volcanoes have base elevations over 4000 m (Appendix 8.6) and are erupted through crust approximately 55 km thick (Assumpção et al., 2013; Figure 31 & Figure 32). Such base elevation and crustal thickness values are similar to CVZ volcanoes from the Andean Plateau, yet baseline isotope ratios from SVZ centres do not overlap with those from the CVZ (Figure 32).

The baseline isotopic signature at each volcanic centre is achieved in zones of melting, assimilation, storage and homogenization (MASH) at the base of the crust (Hildreth and Moorbath, 1988; Davidson et al., 1990; Freymuth et al., 2015; Walker et al., 2015). Rising mantle melts experience assimilation of variable amounts of arc crust (Hildreth and Moorbath, 1988; Davidson et al., 1990). CVZ frontal arc lavas are produced by mixing of mantle melts with 7-37% continental crust (Davidson et al., 1990; Mamani et al., 2010). To minimize the effect of variable mid- to upper-crustal assimilation and allow direct comparison between different volcanic centres, we define the 'baseline' isotope composition at each volcanic centre as the least silicic sample (Figure 32; Methods). CVZ (plateau) lavas have baseline isotopic signatures ($^{87}Sr/^{86}Sr > 0.7050$ and $^{143}Nd/^{144}Nd < 0.5125$) which are clearly distinct from NVZ and SVZ (non-plateau) lavas over a similar range in SiO_2 content (Davidson et al., 1990; Figure 32a,b). Decoupling between isotopic enrichment and major element composition is inferred to reflect prolonged MASH processes in the lower crust (Walker et al., 2015). We suggest that this isotopic step change is a result of the tectonic setting varying from a high but narrow arc (northern SVZ and NVZ) to an orogenic plateau (CVZ), as discussed below. Baseline isotope ratios of $^{87}Sr/^{86}Sr > 0.7050$ and $^{143}Nd/^{144}Nd < 0.5125$ discriminate between plateau and non-plateau settings for Andean arc volcanism.

4.4.2 Correlations between elevation and baseline isotope ratios

Baseline Sr and Nd isotopes of SVZ centres follow strong linear relationships when plotted against both smoothed volcano elevation (Figure 32c, d) and un-smoothed volcano base elevation (Appendix 8.6). Isotope ratios in the SVZ approach CVZ values from south to north. Sr isotope ratios of southern SVZ (SSVZ; south of 38.5°S) lavas are offset to higher values (Figure 32d) which can be attributed to numerous large fracture zones on the incoming Nazca plate which project below the SSVZ (Jacques et al., 2014). Hydrothermal alteration and serpentinization along these fracture zones increases fluid flux to the mantle wedge, causing a shift to higher $^{87}Sr/^{86}Sr$ compositions in the mantle source and in the resultant arc lavas (Jacques et al., 2014; Figure 32c). Therefore, we do not include SSVZ volcanoes in our linear regression analysis.

The Central and Southern Andes have pre-Andean basements mostly comprised of Paleozoic accreted terranes intruded by Mesozoic arc plutons (Hildreth and Moorbath, 1988; Mamani et al., 2008). NVZ arc lavas are erupted through a young, accreted oceanic plateau basement of Mesozoic age (Chiaradia, 2009). NVZ lavas have more mantle-like isotopic ratios than SVZ lavas regardless of regional elevation or crustal thickness. For this reason, the NVZ is not included in the same linear regression analysis as SVZ lavas (Figure 32) and we do not attempt a paleoelevation reconstruction for the NVZ. Basements within the CVZ and SVZ produce comparable Sr- and Nd-isotopic shifts for the same degree of crustal contamination if other factors such as the slab parameter and mantle source are equivalent (Hildreth and Moorbath, 1988; Mamani et al., 2008). Geochemical studies indicate the Andean arc front (18-40°S) has tapped a relatively homogenous depleted mantle source since the Jurassic (Lucassen et al., 2006). Back-arc lavas have chemical signatures which indicate a range of mantle sources (Rossel et al., 2015), for this reason we do not include them in our compilation. Therefore, our regional paleoelevation estimates only apply to the arc front and present Western Cordillera, not to the back arc regions in the Altiplano-Puna.

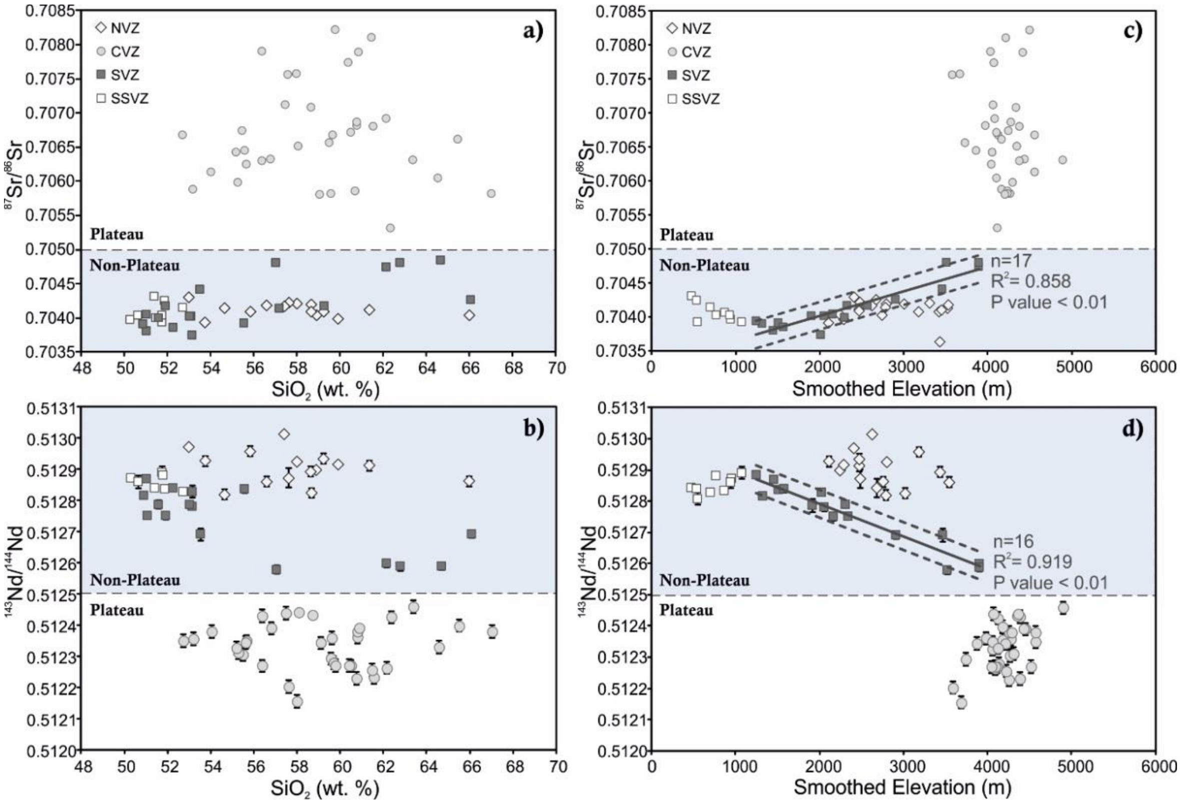

Figure 32: Baseline Sr- and Nd- isotopes as a plateau discriminant and paleoelevation proxy. (a) and (b) Baseline isotopic compositions within each volcanic zone vary little with differentiation from basaltic andesite to rhyolite (Davidson et al., 1990); even the least silicic CVZ rocks are enriched in ^{87}Sr/^{86}Sr (>0.7050) and depleted in ^{143}Nd/^{144}Nd (<0.5125). (c) and (d) Baseline isotope compositions compared to smoothed elevation. Elevation smoothed to a radius of 37.5 km was calculated from the Shuttle Radar Topography Mission DEM (SRTM1, pixel resolution 90 m; Farr et al., 2007). A radius of 37.5 km is selected as this is half of the maximum crustal thickness in the Andes. Smoothing to this degree filters out non-isostatic, short wave-length topography. 95% confidence intervals are represented as dashed lines (excluding samples south of 38.5° S, see text). Volcano locations are shown in Figure 29. Symbols are bigger than the maximum analytical error on isotope data, except where shown. Typical quoted analytical precision on SiO$_2$ compositions are ~3% RSD. All data shown here are listed in Electronic Appendix 4.2.

4.4.3 Regional surface uplift history for the Western Cordillera

We apply both our plateau discriminant and Sr-isotope paleoelevation proxy to age-corrected pre-Quaternary isotope data (^{87}Sr/^{86}Sr$_{(i)}$ and ^{143}Nd/^{144}Nd$_{(i)}$; Appendix 8.7) for the CVZ and SVZ to estimate paleoelevations of the Jurassic-Pliocene Andean arc (~200-2 Ma). We interpret a baseline ^{87}Sr/^{86}Sr$_{(i)}$ ratio of >0.7050 and ^{143}Nd/^{144}Nd$_{(i)}$ ratio of <0.5125 as a 'plateau signature'. We suggest that the isotopic 'plateau signature' corresponds to arc elevations similar to the modern Western Cordillera and CVZ (4200±516 m, mean smoothed elevation of the Western Cordillera along the arc ±2 SD), but does not correspond to the current width of the entire Andean Plateau. Less radiogenic isotope ratios (^{87}Sr/^{86}Sr$_{(i)}$<0.7050, ^{143}Nd/^{144}Nd$_{(i)}$>0.5125) are interpreted to correspond to regional elevations according to the linear relationships we have identified for the SVZ (Figure 32c and d). Due to better data coverage of ^{87}Sr/^{86}Sr$_{(i)}$ ratios for pre-Quaternary samples we show only our paleoelevation estimates based on Sr isotope compositions. We divide pre-Quaternary radiogenic isotope data into age intervals selected according to the data density (Figure 33), which permits two broad groups for the Miocene-Pliocene (23-10 Ma and 10-2 Ma), but only one each for the Paleogene, Cretaceous and Jurassic periods. Jurassic Central Andean lavas have $^{87}Sr/^{86}Sr_{(i)}$ ratios analogous to the modern southern SVZ, with baseline initial Sr-isotope ratios gradually increasing through the Cretaceous and Paleogene (Figure 33; Appendix 8.7). The largest increase in $^{87}Sr/^{86}Sr_{(i)}$ occurs by ~23 Ma (Early Miocene) between 16-26°S where baseline initial isotope ratios reach values $^{87}Sr/^{86}Sr_{(i)}>0.7050$. From 23 to 10 Ma, in the region between 26-33°S there is a gradual increase in $^{87}Sr/^{86}Sr_{(i)}$ from ~0.7035 to ~0.7050.

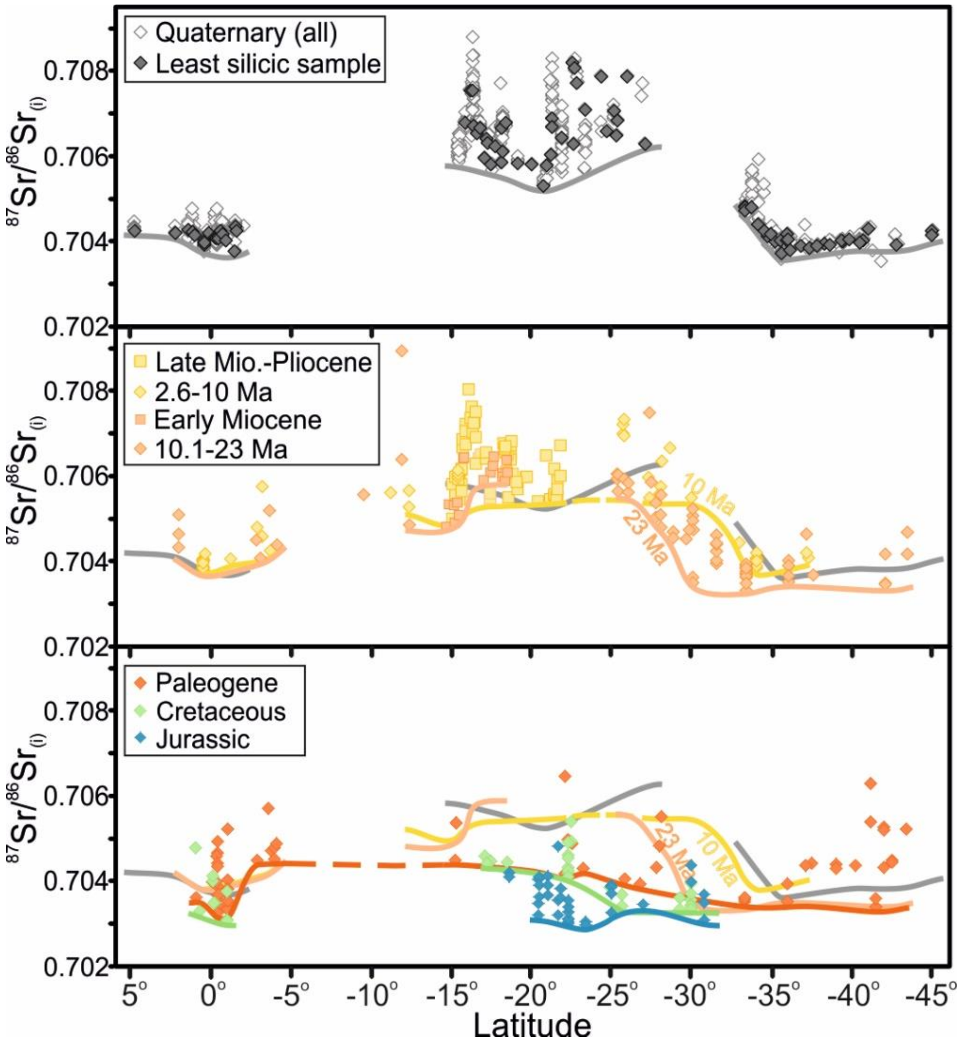

Figure 33: Evolution of Andean arc initial Sr-isotope compositions from the Jurassic to present. Age corrected Sr-isotope ratios of arc lavas (compilation of this study; Scott et al., 2018) grouped by age show the gradual increase in $^{87}Sr/^{86}Sr_{(i)}$ with time. Baselines are drawn joining minimum values for each age group. Symbols are bigger than the maximum analytical error. Plots of CVZ isotope compositions versus age are shown in Appendix 8.7. All data shown here are listed in Electronic Appendix 4.3.

4.5 Discussion

Figure 34 shows our regional paleoelevation estimates for the Andean arc and Western Cordillera compared to previous paleoelevation estimates for the Western Cordillera, Altiplano-Puna and Eastern Cordillera (boxes). A limitation of our method is it will produce over-estimates on paleoelevation where volcanic suites are not analysed or preserved at the least radiogenic end of the range of compositions. We anticipate this issue may only apply to the Jurassic to Paleogene periods for which data are sparse. Jurassic arc baseline compositions and consequent paleoelevation estimates are consistent with geological observations of marine sedimentary rocks intercalated with lavas of that age (Mamani et al., 2010; and references therein). However, geological evidence suggests that Central Andean basins remained dominantly marine up until the mid-Cretaceous (91 Ma) (Mamani et al., 2010), indicating lack of Sr-isotope data for this period are causing overestimates in our elevation model (Figure 34). A marked shift in Central Andean baseline compositions between the Paleogene and Early Miocene indicates an increase in arc elevation of ~2 km. Our results suggest that by 23 Ma, between at least 16 and 26°S, the Andean arc was part of a tectonic plateau, which we suggest attained elevations comparable to that of the modern Western Cordillera (4200±516 m; Figure 34). Our results do not preclude minor uplift or tilting of the Western Cordillera in the Miocene (Jordan et al., 2010), as the Western Cordillera could have been at the lower limit of our estimated range at 23 Ma and risen to its current elevations since. The width of elevated areas at this time may have been similar to the modern Western Cordillera (~50-100 km). Such widths are much narrower than the modern Andean Plateau (~400 km, which encompasses the Western Cordillera, Altiplano-Puna and Eastern Cordillera), but are wider than either the NVZ or SVZ (mostly <50km). This conclusion is consistent with sediment providence data and facies changes indicating the presence of a 'Proto'-Western Cordillera by the Late Eocene-Oligocene (Wotzlaw et al., 2011; Decou et al., 2013), and also with evidence of eastward propagation of a narrow, early fold-thrust belt into the Eastern Cordillera at ~40 Ma (McQuarrie et al., 2005; Oncken et al., 2006).

We propose the Western Cordillera was ~2 km higher at 23 Ma than a study from ~15° S (Saylor and Horton, 2014) which suggests paleoelevations of ~2 km by 19 Ma (Figure 34). Our result predates rapid Late Miocene (10-6 Ma) surface uplift interpreted for the Altiplano to the east (Garzione et al., 2008; Kar et al., 2016), but is consistent with sediment provenance data which indicates that the Western Cordillera rose earlier than the Altiplano (Horton et al., 2001; Wotzlaw et al., 2011). Our results agree with stable isotope evidence suggesting the south-eastern Puna plateau was at similar to modern elevations by ~36 Ma (Canavan et al., 2014). Between 23 and 10 Ma we interpret surface uplift of the Western Cordillera to have propagated further south by ~400 km.

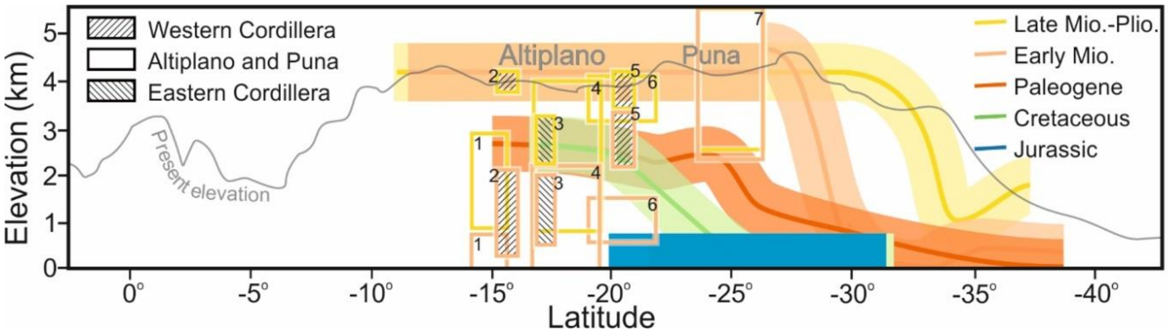

Figure 34: Surface uplift of the Central and Southern Andes from Jurassic-present. Coloured lines are our inferred regional paleoelevation estimates for the Western Cordillera using our Sr-isotope plateau discriminant and SVZ calibration. Past plateau elevation is inferred to be similar to present day Western Cordillera elevations (4200±516 m, mean CVZ volcano elevation ±2 SD, using 37.5 km smoothing). Non-plateau paleoelevation estimates have lines set to a thickness representing 95% confidence (±564 m). For general comparison, previously published paleoelevation estimates are shown in boxes, simplified to fit the same time intervals used in this study (1 = Kar et al., 2016; 2 = Saylor and Horton, 2014; 3 = Leier et al., 2013; 4 = Garzione et al., 2006, 2008; 5 = Cooper et al., 2016; 6 = Garzione et al., 2014; 7 = Canavan et al., 2014).

Studies on Altiplano paleoelevation have emphasized largescale loss of lower lithosphere as a mechanism for generating rapid surface uplift in this region between 10-6 Ma (Garzione et al., 2006, 2008). Delamination of the lower lithosphere and asthenospheric upwelling results in preferential melting of the most fertile, decompressed or heated mantle (Ducea et al., 2013). Pliocene-Quaternary back-arc lavas within the Altiplano and Puna have geochemical signatures suggested to be consistent with small scale delamination or dripping (Kay et al., 1994; Davidson and de Silva, 1995; Ducea et al., 2013; Kaislaniemi et al., 2014), which are not present in the frontal arc to the west (Mamani et al., 2010). Hence, we only calibrate isotope signatures of frontal arc lavas to elevation and our regional paleo-elevation estimates apply only to the (proto-) Western Cordillera.

We have identified strong linear correlations between baseline Sr- and Nd-radiogenic isotope compositions of SVZ arc lavas and elevation, and by implication, crustal thickness. Our findings using radiogenic isotope chemistry are complementary to previous studies on relationships between trace element chemistry of arc lavas and crustal thickness (Chiaradia, 2015; Turner and Langmuir, 2015b, 2015a; Profeta et al., 2015a). Crustal thickness of the overriding plate in a subduction zone controls arc lava chemistry by some of, or a combination of all, the following processes: (1) mantle wedge thermal structure and melting regime (Plank and Langmuir, 1988; Turner and Langmuir, 2015b, 2015a; Turner et al., 2016); (2) pressure of magma fractionation at the base of the crust (Chiaradia, 2015; Chapman et al., 2015a; Profeta et al., 2015a); and (3) the degree of crustal assimilation (Hildreth and Moorbath, 1988; Davidson et al., 1990; Farner and Lee, 2017). Correlations between $^{87}Sr/^{86}Sr$ and $^{143}Nd/^{144}Nd$ isotopes and SVZ elevation (and crustal thickness) does not preclude either of the first two processes but indicates that there is a relationship between crustal thickness and the degree of crustal assimilation. Therefore, we can indirectly gain an insight on the paleoelevation and tectonic history of the Central Andes using age corrected radiogenic isotope data, which is consistent with the geological record for this region.

The slopes of the correlations we have identified here (Figure 32c,d) cannot be directly applied to other arcs. If correlations between Sr- and Nd- isotopes and elevation can be found elsewhere, the slope will depend principally upon the isotopic difference between the mantle source and overriding crust. Our method in determining regional elevation may be applied to other arcs as long as all the steps we have laid out here are followed. There must be an active segment of the arc where Quaternary isotope compositions can be directly correlated to present day elevation. Careful work needs to go into checking arc segments in question to determine if there is reasonable justification to study the elevation (and crustal thickness) control on isotope compositions in isolation. Furthermore, there must be sufficient isotope data available to reliably find the baseline isotope ratio for each volcanic centre. The Central American arc has potential for quantitative relationships between radiogenic isotopes and elevation to be explored further, as qualitative correlations between isotope ratios and crustal thickness have already been found (Feigenson and Carr, 1986).

The isotopic step change we utilize as a plateau discriminant indicates the relationship between elevation, crustal thickness and isotope composition is not a simple linear trend like that observed for the SVZ (Figure 32c,d; Turner et al., 2016). The isotopic shift between lavas that are and that are not emplaced on the plateau implies more crustal contamination in CVZ lavas than would be expected from linear extrapolation of the SVZ trend. However, the mechanism for this isotopic enrichment within plateau is relatively unknown and is a topic we highlight as an area of further research. It is possible that the great width (>400 km) of thick (>60 km) crust across the Andean Plateau raises the geothermal gradient across this broad region rather than along a narrow arc leading to a hot, weak lower crust (Jamieson and Beaumont, 2013). Lower crustal heating due to potential asthenosphere upwelling must also be taken into account (Ducea et al., 2013; Kay et al., 2014).

4.6 Conclusions

Our approach utilizes abundant radiogenic isotope data from previous studies of Andean arc geochemistry to provide a regional perspective on the surface uplift and tectonic history of the Andes through time. Calibrating radiogenic isotope compositions of arc lavas to smoothed elevation provides a new indirect paleoelevation proxy and plateau discriminant that does not rely on paleoclimate. Miocene (from 23 Ma) to recent Central Andean arc lavas all have a 'plateau' isotope signature ($^{87}Sr/^{86}Sr>0.705$ and $^{143}Nd/^{144}Nd<0.5125$). We suggest that between 16-26°S the Western Cordillera attained current elevations (4200 ± 516 m) by 23 Ma. Our results do not preclude minor tilting or uplift of the Western Cordillera during the Early Miocene. We suggest Western Cordillera elevations were reached ~15 Myr before significant surface uplift previously determined for the adjacent Altiplano to the east. During the Early-Mid Miocene, surface uplift propagated southward between ~26-35°S.

Chapter 5: A geochemical investigation of the Paleogene Central Andean arc and its tectonic setting

5.1 Chapter summary

Building on the results of Chapters 3 and 4, here a detailed geochemical investigation of the Central Andean Paleogene arc is conducted to better constrain the crucial early Cenozoic stages of Andean crustal thickening and uplift, including new data for the Paleogene period (66-23 Ma). A 'petrological switch' is identified at the Late Cretaceous-Paleogene boundary. Assimilation and fractional crystallisation (AFC) models using the Sr isotope system, as well as low Sr/Y and La/Yb ratios and negative Eu anomalies suggest that plagioclase was the dominant early fractionating phase in Central Andean lavas older than 66 Ma. Indicating that, at this time, magmas were initially stored within the plagioclase stability field (~<30-35 km depth). Paleogene Central Andean lavas younger than ~60 Ma have higher Sr/Y and La/Yb ratios and fit AFC models of amphibole-pyroxene dominant fractionation, indicating equilibration below the plagioclase stability field. The petrological switch corresponds to a tectonic regime change in the Central Andes from the Salta Rift phase in the Late Jurassic-Early Cretaceous to retroarc shortening from the Late Cretaceous-Paleogene. The thin crust in the Central Andes after the Salta Rift phase explains the predominant evidence of shallow fractionation of plagioclase in lavas older than 66 Ma. Further evidence of crustal thickening comes from Sr and Nd isotope systems, which become increasingly radiogenic both northward and with decreasing age consistent with previous models of southward propagation of crustal thickening over time. Such changes in petrology and geochemistry at the Late Cretaceous-Paleogene boundary support geological evidence indicating the onset of crustal thickening and uplift in the Western Cordillera by the early Paleogene (~66-60 Ma).

5.2 Introduction

The Andean Plateau is currently the only tectonic plateau formed by oceanic subduction under a continental plate and is commonly referred to as an end-member subduction system. Yet, key initiating mechanisms and timings of Central Andean compressional deformation are still debated (Garzione et al., 2017; Horton, 2018b). Understanding the uplift of the Andean Plateau is critical to understanding feedbacks between mountain building and climate (Lamb and Davis, 2003; Armijo et al., 2015; Lee et al., 2015) and to unlocking more elusive subduction and mantle geodynamics (Gephart, 1994; Crameri et al., 2017).

As discussed in Chapters 3 and 4, the geochemical record of over 200 Ma of Andean arc magmatism provides insights into the changing tectonic setting of the Andean subduction zone (Kay et al., 1991, 2014; Trumbull et al., 1999; Haschke et al., 2002b, 2002a; Mamani et al., 2010). Certain geochemical signatures of arc volcanic products are especially sensitive to changes in crustal thickness due to: (1) increasing degrees of crustal contamination with increasing crustal thickness (Hildreth and Moorbath, 1988; Davidson et al., 1990; Freymuth et al., 2015; Farner and Lee, 2017); (2) raising the pressure and degree of magma fractionation at the Moho and hence changing the stability of certain mineral phases (Chiaradia, 2015; Chapman et al., 2015a; Profeta et al., 2015b); and (3) overriding plate thickness controlling mantle wedge thermal structure and degree of mantle melting (Plank and Langmuir, 1988; Turner and Langmuir, 2015b, 2015a; Turner et al., 2016). Quaternary Andean volcanism is divided into four volcanic zones, the Northern Volcanic Zone (NVZ; of Ecuador and Columbia), Central Volcanic Zone (CVZ; Peru, Bolivia and Northern Chile and Argentina), the Southern Volcanic Zone (SVZ; on the border between Chile and Argentina), and the Austral Volcanic Zone (in Patagonia). Quaternary CVZ arc lavas are located within the Western Cordillera of the Andean Plateau (Figure 35).

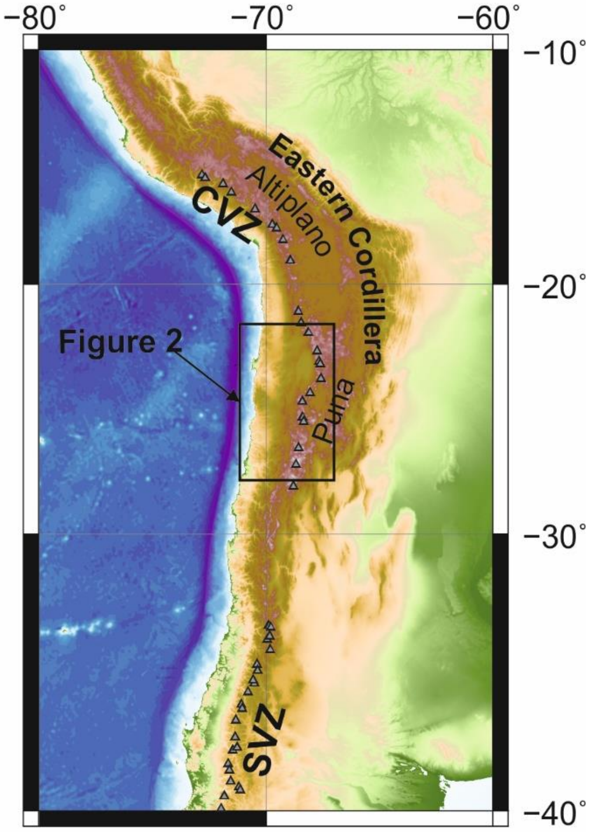

Figure 35: Overview map of the Andean Plateau. The active Central Volcanic Zone defines the Western Cordillera of the Andean Plateau. The Altiplano and Puna basins from the core of the Andean Plateau. The Eastern Cordillera fold and thrust belt make up the eastern boundary. The box shows the location of the study area for this Chapter, shown in further detail in Figure 2.

Arc geochemistry can be used as a discriminant for the tectonic setting of the Andean Plateau (Chapters 3 & 4; Scott et al., 2018). For example, CVZ arc lavas have radiogenic baseline isotopic signatures ($^{87}Sr/^{86}Sr > 0.7050$ and $^{143}Nd/^{144}Nd < 0.5125$) which are clearly distinct from NVZ and SVZ (non-plateau) arc lavas over a similar range in SiO_2 content (Davidson et al., 1990). Although this is an observation made almost three decades ago (Davidson et al., 1990), the mechanisms of Sr- and Nd-radiogenic isotope enrichment within the Andean Plateau remain disputed (e.g. Stern, 1991; Kay et al., 2014; Wörner et al., 2018). Mixing, fractional crystallization and crustal assimilation processes are all recognized as fundamental processes in producing the enriched signatures of CVZ magmas (Blum-Oeste and Wörner, 2016). Enriched mantle sources (Wieser et al., in review; Kay et al., 2010; Turner et al., 2017) and source contamination by subduction erosion (Stern, 1991; Kay et al., 2014) could also explain a proportion of enriched signatures. A combination of these mechanisms of enrichment can explain the distinctly enriched isotope signals of CVZ lavas and can be used as a discriminant for the tectonic setting of the Andean Plateau back through time as discussed in Chapter 4 and in Scott et al. (2018).

New geochemical data from Paleogene Central Andean arc products are combined with compilations of Jurassic-Recent Andean arcs to explore: (1) if similarities between Central Andean Paleogene lavas and modern Andean lavas from either the CVZ or SVZ are discernible; (2) if age progressions in geochemical characteristics from the Jurassic to Paleogene can be linked to the changing tectonic environment or changing mantle source; and (3) what conclusions can be drawn from the Andean geochemical record on the crustal thickening and surface uplift history of the Andean Plateau. Results from petrological and geochemical analysis indicate crustal thickening from <30 km in the Jurassic-Cretaceous to ~35-45 km from the Late Cretaceous and Early Paleogene. Such results correspond to geological evidence indicating the onset of crustal thickening in the Western Cordillera in the Late Cretaceous. Central Andean arc compositions do not reach the distinct 'plateau' signatures of Quaternary CVZ lavas until the Neogene (<23 Ma), after an eastward migration of the arc and a period of increased compressional deformation in the Western and Eastern Cordilleras.

5.3 Geological and Tectonic Setting

The present Andean Plateau is the second largest tectonically active plateau in the world. From west to east the Andean Plateau spans over 400 km and is divided into three tectonically distinct zones: the Western Cordillera (including the active CVZ of the Andean arc), the internally drained Altiplano and Puna plateaux, and the Eastern Cordillera fold-and-thrust belt (Figure 35). Between the western coastline and the Andean Plateau are: the Coastal Cordillera comprised of uplifted Jurassic-Cretaceous batholiths and lavas; the Central Depression containing uplifted Jurassic marine sediments and Miocene-recent sedimentary basin infills; and the Pre-Cordillera which leads up to the Western Cordillera of the Andean Plateau. The Paleogene arc is dominantly located in the Central Depression and Precordillera, with some 'proximal back-arc' centres (Kay et al., 2014) located in the Western Cordillera (Figure 36). There has been a gradual eastward migration of the arc front from the Jurassic to present day, which has been attributed to both subduction erosion (Stern, 1991; Kay et al., 2014) and slab shallowing processes (Kay and Mpodozis, 2002).

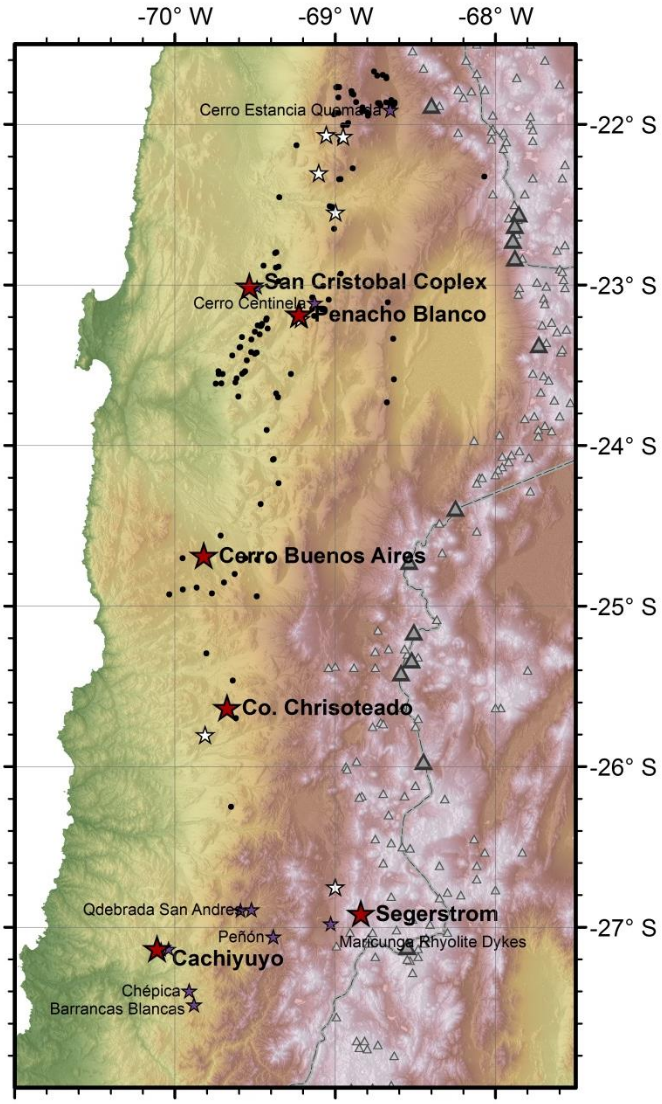

Figure 36: Topographic map of the study area. Recent volcanic edifices from the CVZ are shown in grey triangles (large triangles are Holocene centres and small triangles are from the database of de Silva and Francis, 1991). Paleogene lavas which have previously been dated but do not have radiogenic isotope data are shown as black dots (compilations of Haschke et al, 2002; Trumbull et al. 2006; and Mamani et al. 2010). White stars are samples previously analysed for radiogenic isotopes (compilation of Scott et al., 2018). Large red stars are the six main dated suites selected for geochemical and isotopic analysis in this study. Smaller, purple stars are other localities sampled during fieldwork in 2017 and described in the Appendix.

Foreland basin deposits and sediment provenance data indicate the initiation of mountain building in the present location of the Western Cordillera in the Late Cretaceous-Paleocene (Horton et al., 2001; McQuarrie et al., 2005; Wotzlaw et al., 2011; Decou et al., 2013). This early fold-and-thrust belt then became bivergent, with a second belt of deformation initiating in the present location of the Eastern Cordillera by 40 Ma (McQuarrie et al., 2005; Oncken et al., 2006). The eastward jump of the compressional deformation front occurred at the same time as the eastward expansion of the arc (Trumbull et al., 2006; Mamani et al., 2010), which has in turn been related to slab shallowing (Jordan et al., 1983b; Haschke et al., 2002b; Kay and Mpodozis, 2002; Ramos and Folguera, 2009).

Two major compressional tectonic events are recorded in the morpho-structural units of the Central Andes: one in the Upper Eocene-Lower Oligocene between 42-34 Ma and the second in the Upper Oligocene, prior to 23-17 Ma (Lahsen, 1982). The majority of Central Andean compressional deformation and surface uplift is inferred to have occurred in the earlier Eocene-Oligocene compressional event (Haschke et al., 2002b; McQuarrie et al., 2005; Oncken et al., 2006; Mamani et al., 2010; Reiners et al., 2015). Interpretations of early Andean uplift remain contentious as stable isotope data and paleobotany studies indicate 1-2 km of Andean Plateau uplift after 16-10 Ma (Graham et al., 2001; Garzione et al., 2008, 2017; Leier et al., 2013), as discussed in Chapter 4.

5.4 Samples & field location descriptions

Paleogene arc lavas from Chile (22-27° S) were identified which have K-Ar dates, but which had not yet been sampled for isotope analysis (Figure 36) by comparing compilations of Andean geochemistry (Haschke et al., 2002b; Mamani et al., 2010; Scott et al., 2018) to published geological maps and a database of age and locations of Cenozoic volcanoes (Trumbull et al., 2006). Due to the large field area, and limited outcrop exposure at each locality, detailed field studies of each centre were not conducted. However great care was taken to sample the main units least affected by secondary alteration processes and, where possible, to sample a representative suite from each centre.

70 basalt-rhyolite lava samples were collected which have been previously mapped or dated between 66 and 23 Ma but which do not have radiogenic isotope data. The youngest suite analysed here, the Segerstrom suite, is included in a detailed geochemical analysis of the Neogene (<25 Ma) Central Andean arc (Kay et al., 2014) and studied here so that the two paleo-arcs can be directly compared. Sample sites, dating methods and references are shown in Figure 36 and listed in Table 2 & Table 3. Samples listed in Table 3 do not have well constrained ages and therefore were not used in the geochemical analysis. Many of the sample sites showed signs of compressional deformation such as folding, faulting and fracturing. Deformation was particularly evident at sample sites in the Pre-cordillera fold-and-thrust belt.

Table 2: Previously dated samples selected for geochemical analysis. Note that all rocks were dated by the K-Ar method, which can be imprecise (Funkhouser et al., 1966).

Sample	**Name**	**Composition**	**Rock type**	**Latitude**	**Longitude**	**Age (Ma)**	**Age error**	**Age source**
AT11.2	Segerstrom	Basaltic Andesite	Lava	-26.920	-68.833	25	0.9	K-Ar, Mpodozis et al. (1996)
AT12.1	Segerstrom	Basaltic Andesite	Lava	-26.915	-68.840	25	0.9	K-Ar, Mpodozis et al. (1996)
AT12.2	Segerstrom	Basalt	Lava	-26.915	-68.840	25	0.9	K-Ar, Mpodozis et al. (1996)
AT12.3	Segerstrom	Basaltic Andesite	Lava	-26.915	-68.840	25	0.9	K-Ar, Mpodozis et al. (1996)
AT12.4	Segerstrom	Basalt	Lava	-26.915	-68.840	25	0.9	K-Ar, Mpodozis et al. (1996)
AT12.6	Segerstrom	Basaltic Andesite	Lava	-26.915	-68.840	25	0.9	K-Ar, Mpodozis et al. (1996)
AT39.1	Penacho Blanco	Basaltic Andesite	Lava	-23.181	-69.225	45	1.5	K-Ar (WR), Cornejo and Mpodozis (1997)
AT39.2	Penacho Blanco	Trachy-andesite	Lava	-23.181	-69.225	45	1.5	K-Ar (WR), Cornejo and Mpodozis (1997)
AT39.3	Penacho Blanco	Trachy-andesite	Lava	-23.181	-69.225	45	1.5	K-Ar (WR), Cornejo and Mpodozis (1997)
AT20.1	Co. Chrisoteado	Andesite	Lava	-25.632	-69.674	54	2	K-Ar (WR), SFB-267 internal report, projects C2, D1b
AT20.3	Co. Chrisoteado	Dacite	Lava	-25.632	-69.674	54	2	K-Ar (WR), SFB-267 internal report, projects C2, D1b
AT16.1	Cachiyuyo	Basalt	Lava	-27.134	-70.115	59.6	2.8	K-Ar (WR), Zentilli (1991)
AT16.2	Cachiyuyo	Dacite	Lava	-27.134	-70.115	59.6	2.8	K-Ar (WR), Zentilli (1991)
AT16.3	Cachiyuyo	Dacite	Lava	-27.134	-70.115	59.6	2.8	K-Ar (WR), Zentilli (1991)
AT16.4	Cachiyuyo	Andesite	Lava	-27.134	-70.115	59.6	2.8	K-Ar (WR), Zentilli (1991)
AT16.5	Cachiyuyo	Andesite	Lava	-27.134	-70.115	59.6	2.8	K-Ar (WR), Zentilli (1991)
AT16.6	Cachiyuyo	Andesite	Lava	-27.135	-70.040	59.6	2.8	K-Ar (WR), Zentilli (1991)
AT17.1	Cachiyuyo	Basalt	Lava	-27.134	-70.111	59.6	2.8	K-Ar (WR), Zentilli (1991)
AT17.2	Cachiyuyo	Basalt	Lava	-27.134	-70.111	59.6	2.8	K-Ar (WR), Zentilli (1991)
AT18.1	Cachiyuyo	Basaltic Andesite	Lava	-27.137	-70.087	59.6	2.8	K-Ar (WR), Zentilli (1991)
AT41.1	Cerro Buenos Aires	Andesite	Lava	-24.685	-69.820	60	2.2	K-Ar (WR), Naranjo and Puig (1984)
AT41.2	Cerro Buenos Aires	Andesite	Lava	-24.685	-69.820	60	2.2	K-Ar (WR), Naranjo and Puig (1984)
AT41.3	Cerro Buenos Aires	Andesite	Lava	-24.685	-69.820	60	2.2	K-Ar (WR), Naranjo and Puig (1984)
AT25.1	San Cristobal Coplex	Dacite	Lava	-23.026	-69.530	66	2	K-Ar (WR), Naranjo and Puig (1984)
AT26.1	San Cristobal Coplex	Andesite	Lava	-23.008	-69.534	66	2	K-Ar (WR), Naranjo and Puig (1984)
AT26.2	San Cristobal Coplex	Basaltic Andesite	Lava	-23.008	-69.534	66	2	K-Ar (WR), Naranjo and Puig (1984)
AT27.1	San Cristobal Coplex	Basaltic Andesite	Lava	-23.014	-69.489	66	2	K-Ar (WR), Naranjo and Puig (1984)

Table 3: Other samples collected during the field campaign but not used in the geochemical analysis, due to the less well constrained ages. Field locations are described in the Appendices.

Sample	Name	Composition	Rock type	Latitude	Longitude	Age (Ma)	Age error	Age source
AT37.1	Cerro Centinela	Dacite	Lava	-23.112	-69.128	48	Estimated	Boric et al. (1987)
AT6.1	Chépica	Basaltic Andesite	Dyke (in intrusion)	-27.396	-69.911	63	Estimated	Arevalo (1995)
AT32.1	Cerro Estancia Quemada	Dacite	Lava	-21.910	-68.656	66.6	1.8	K-Ar (Bt); Maksaev (1990)
AT3.1	Barrancas Blancas	Basaltic Andesite	Dyke	-27.483	-69.882	Paleocene	Mapped	Sernageomin (2003)
AT3.2	Barrancas Blancas	Basalt	Dyke	-27.483	-69.882	Paleocene	Mapped	Sernageomin (2003)
AT7.1	Peñón	Basaltic Andesite	Lava	-27.059	-69.387	L. Cretaceous-Paleocene	Mapped	Sernageomin (2003)
AT13.1	Maricunga Rhyolite Dykes	Rhyolite	Dyke	-26.979	-69.029	Paleocene	Mapped	Sernageomin (2003)
AT13.2	Maricunga Rhyolite Dykes	Rhyolite	Dyke	-26.979	-69.029	Paleocene	Mapped	Sernageomin (2003)
AT1.1	Qdebrada San Andres	Andesite	Lava	-26.894	-69.591	Paleocene-Eocene	Mapped	Sernageomin (2003)
AT1.2	Qdebrada San Andres	Andesite	Lava	-26.894	-69.591	Paleocene-Eocene	Mapped	Sernageomin (2003)
AT1.3a	Qdebrada San Andres	Basaltic Andesite	Lava	-26.891	-69.524	Paleocene-Eocene	Mapped	Sernageomin (2003)
AT1.3b	Qdebrada San Andres	Dacite	Lava	-26.891	-69.524	Paleocene-Eocene	Mapped	Sernageomin (2003)
AT1.4	Qdebrada San Andres	Andesite	Lava	-26.891	-69.524	Paleocene-Eocene	Mapped	Sernageomin (2003)

5.4.1 Sample locations

5.1.1.1 Segerstrom Lavas (AT11-12)

Segerstrom lavas from the Maricunga belt in the Western Cordillera are the youngest, most easterly and at the highest elevation (up to 4654 m) of the rocks sampled during this study (Figure 36). K/Ar ages range from 25.0 ±0.9 Ma to 23.4 ±1.5 Ma (Mpodozis et al., 1995, 1996). Segerstrom lavas belong to the Claudio Gay Sequence and are described by Kay et al. (2014) as tholeiitic mafic lavas from a proximal backarc setting. Kay et al. (2014) analysed two samples from the Segerstrom suite for Sr and Nd radiogenic isotopes in their study of the Central Andean Neogene arc. The aim is to increase the data for these rare basalts and to allow comparisons between the Neogene and Paleogene Central Andean arcs. Sampling sites in this study are from the east facing flank of a long N-S trending ridge where the Segerstrom lavas crop out, ~5-6 km north of highway R-31. Outcrops showed no evidence of tectonic deformation. The lavas contain <10 % vesicles and have remnant pahoehoe ropes with glassy surfaces.

5.1.1.2 Penacho Blanco (AT39)

Penacho Blanco (Figure 36) is named after a triangulation station close to our sample site, which we infer to be correlated with a lava sample dated at 45 ±1.5 Ma (Mpodozis et al., 1995; Cornejo and Mpodozis, 1997), included in the compilation of Trumbull et al. (2006). The exact locality of the dated sampling site (Mpodozis et al., 1995; Cornejo and Mpodozis, 1997) could not be reached due to washed-out roads. Tectonic deformation across the area means it is not certain the samples in this study are co-genetic with the dated sample. However, the 2017 sampling site is part of a belt of Paleogene lavas and volcanic rocks mapped by Boric et al. (1987) which is the same as the dated 45 Ma sample. Presence of a fault zone is evident from increasing degrees of fracturing and alteration towards a dry river gully trending ~NE-SW, ~30-40 m from the sampling sites.

5.1.1.3 Co. Chrisoteado (AT20)

Co. Chrisoteado is located in the Central Depression, almost 90 km directly ESE of Taltal (Figure 36). Co. Chrisoteado is bounded to the north and south by two river valleys: Quebrada Encrucijaga and Quebrada de la Cachina. The centre has two whole rock K-Ar dates. Approximately 3 km to the west of the main heavily incised centre has been dated at 78 ±5 Ma, while the south-east flank of the main centre has been dated at 54 ±2 Ma (Naranjo and Puig, 1984; Trumbull et al., 2006). The southeast flank was sampled in this study. Lavas are andesite-dacite in composition with plagioclase and amphibole phenocrysts. Abundant scoria clasts and ash surround the main centre, most likely derived from more recent eruptions related to the Altiplano-Puna Volcanic Complex (APVC).

5.1.1.4 Cachiyuyo Lavas (AT16-18)

Plutòn Cachiyuyo and associated lava deposits are part of the abandoned Distrito Cachiyuyo de Oro mining district in the Central Depression (Figure 36) and have been mapped by Arévalo (1995). The granodiorite pluton is host to Cu, Au and Ag mineralisation and hence many of the rocks are heavily affected by hydrothermal alteration. Cachiyuyo is still morphologically recognisable as a deeply incised polygenetic volcanic centre on satellite imagery which has been excavated by mining activity. The main granodiorite pluton is at the centre, with finer basalt-dacite lavas and variable volcaniclastic rocks surrounding the pluton. Large gouge-filled faults and fracture networks are common across the centre. Plutòn Cachiyuyo has been dated at 62±2 Ma (K/Ar, biotite) and 59±3 Ma (K/Ar, whole rock; Zentilli et al., 1991; Arévalo, 1995). Samples range in composition from basalt to dacite. Amphibole phenocrysts are present in the more evolved samples (see Petrographic overview).

5.1.1.5 Cerro Buenos Aires (AT41)

Cerro Buenos Aires is located east of highway R-5 between Taltal and Antofagasta (Figure 36). It is a complex of faulted andesites, volcaniclastic rocks and ignimbrites, overlain in places by loose scoria. The complex has been dated at 60±2.2 Ma (K-Ar, whole rock; Naranjo and Puig, 1984). Three andesite samples were collected here. Due to the high degree of deformation at the centre it cannot be certain lavas sampled here are cogenetic. Feldspar phenocrysts ranged from 0.1-6 mm in length and constituted 30-40% of the rocks.

5.1.1.6 San Cristobal Complex (AT25-27)

The San Cristobal Complex is located just south of the small mining town of Seirra Gorda (Figure 36), between 2-5.5 km NW from highway R-25 near the abandoned nitrate mine of Oficina Maria. These rocks are correlated with samples from the suite dated at 66 ±2 Ma from the San Cristobal Complex (Williams, 1992) and published in the compilation of (Haschke et al., 2002b). Outcrop density and quality at this location are particularly poor. Most outcrops are heavily altered and contain large hydrothermal veins.

5.6 Petrographic overview

Basaltic andesites and andesites are the most common rock type represented in this study, with only a few basalts collected from both Segerstrom and Cachiyuyo centres. Nearly all rocks have a porphyritic texture (Figure 37, Figure 38 & Figure 39). Plagioclase (lamellar twinning and often zoned; Figure 37, Figure 38 b and Figure 39b) is the most common phenocryst phase followed by clinopyroxene. Amphibole phenocrysts are present in more evolved Cachiyuyo and Co. Chrisoteado lavas but rare in other suites (Figure 39). Olivine phenocrysts are only found in one sample from the Segerstrom suite (Figure 38c). Most rocks have a glassly matrix with plagioclase microlites, and some samples show a seriate texture. Glomerocrysts of plagioclase and clinopyroxene are common in rocks from the Segerstrom suite (Figure 38). In some samples magma mingling textures can be seen, for example a change in the average matrix microlite size across a discrete boundary and the presence of partially resorbed phenocrysts (Figure 37). Resorption of plagioclase is indicative of crystal-melt disequilibrium (Davidson and de Silva, 1995).

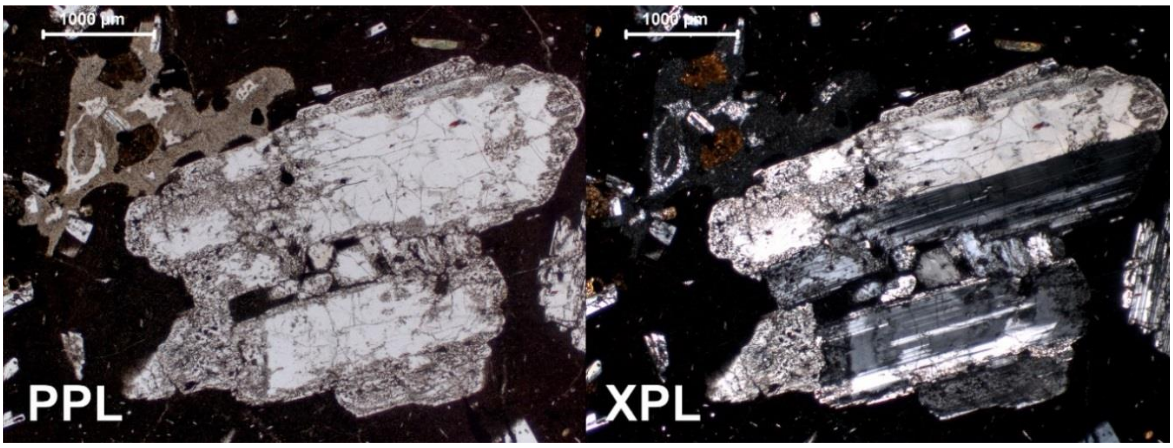

Figure 37: Partially resorbed plagioclase phenocryst in sample AT25.1 from the San Cristobal Complex.

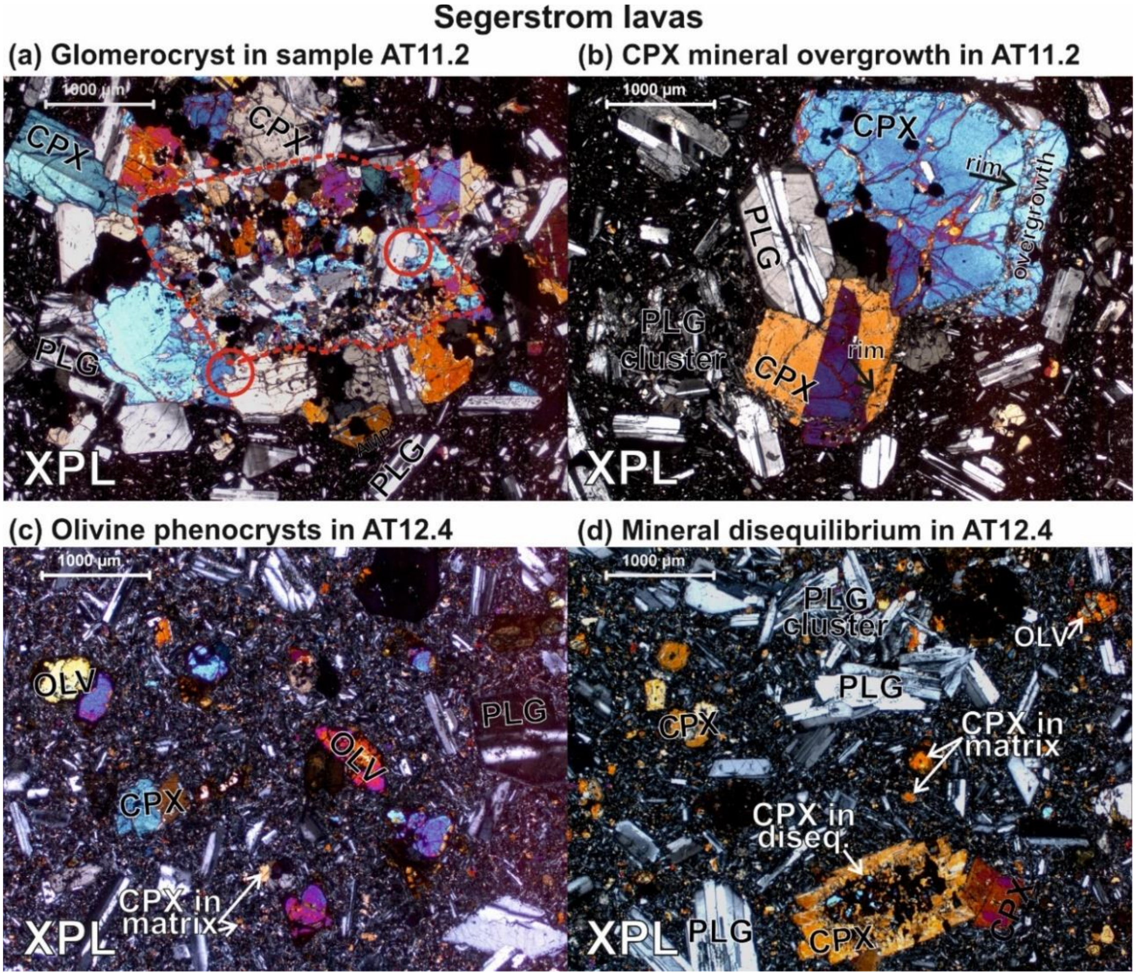

Figure 38: Photomicrographs of two samples from the Segerstrom suite. (a) and (b) show clinopyroxene-plagioclase glomerocrysts from sample AT11.2. (a) has a bi-modal crystal size population. Crystals in the centre (within the dashed line) are ~200 µm and there is ~30 % oxides and accessory phases. Outside the dashed line crystals are over 1000 µm, there is a smaller proportion of oxides and evidence of crystal intergrowth (red circles). (b) clinopyroxene phenocrysts have a 200 µm mineral overgrowth which has incorporated matrix microliths. (c) and (d) are micrographs from the most mafic sample analysed in this study, AT12.4, which is the only sample where olivine phenocrysts are observed. The core of the CPX phenocryst at the bottom centre of view has numerous mineral & melt inclusions. Plagioclase phenocrysts are subhedral to euhedral and do not show resorbtion textures like those seen in Figure 5.

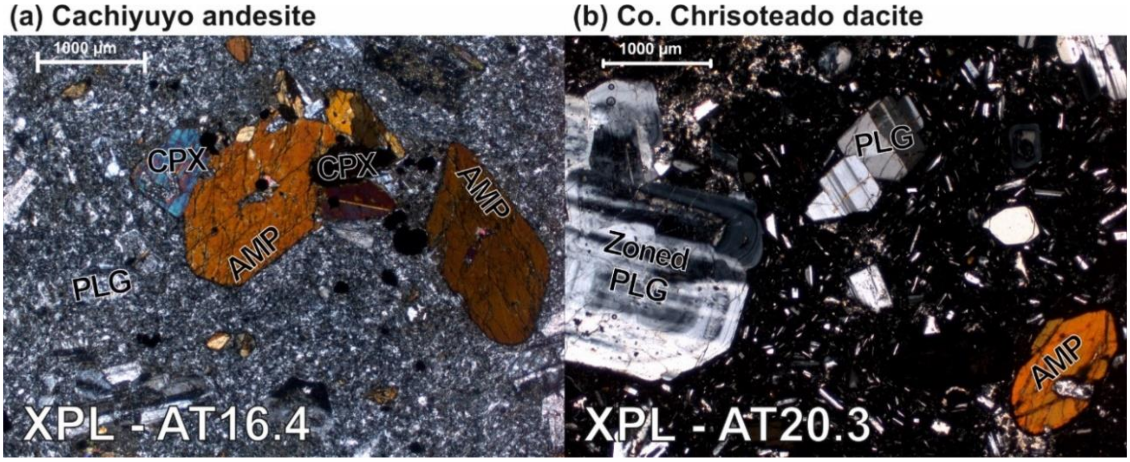

Figure 39: Two examples of samples containing amphibole phenocrysts, which are rare in most suites but common in both Cachiyuyo and Co. Chrisoteado suites. Both samples have strongly zoned plagioclase phenocrysts and euhedral to subhedral amphibole and plagioclase phenocryst phases.

5.7 Analytical Techniques

Rock samples were prepared by removing all veins and weathered material and crushing on a fly press to chip size. Rock chips were then powdered in an agate ball mill (~60-80 g of powder produced per sample). Major element abundances were determined by X-ray Fluorescence (XRF) at the University of Leicester using the PANalytical Axios Advanced PW4400 X-ray spectrometer. To determine the loss on ignition (LOI), sample powders were weighed before and after igniting at 950°C for approximately two hours. Ignited samples were then individually mixed with a lithium metaborate flux, precisely weighed at a ratio of 3 g flux (with LOI of flux taken into account) to 0.6 g of sample, each measurement being within ± 0.0002 g. Flux-sample mixtures were heated in platinum crucibles for approximately 5 minutes and shaken so they were thoroughly mixed. Melts produced were set in platinum casting plates and cooled to form fusion beads ready for analysis. Major elements are reported in Table 4.

Trace element analyses were performed by inductively coupled plasma mass spectroscopy (ICP-MS) on a Perkin Elmer-Sciex Elan 6000 at Durham University. 100±5 mg of each sample powder was digested in a 3:1 HF-HNO_3 mixture in a sealed Teflon beaker for ~24 hours on a hot plate (Ottley et al., 2003). Silicon was removed as SiF_4 during two dry down stages with further additions of HNO_3 in between. Prior to analysis, samples were diluted to 3.5% HNO_3 and spiked with internal standards Re and Rh at 50 ppb used to correct for instrument drift and matrix-related signal suppression. Results for duplicate analyses and six international standards were in good agreement. Precision is <5% RSD for all elements. Trace elements are reported in Table 5.

For Sr and Nd isotope analysis, 100-130 mg of sample powder were dissolved 3:1 HF-HNO_3 mixture in a sealed Teflon beaker for ~48 hrs. Following dry down the remaining residue was taken up in 1ml concentrated HNO_3 and dried down twice to drive off any remaining HF and to remove fluorides. The sample was then taken up in 1 ml of 3 M HNO_3 and passed through a column containing Eichrom Sr resin. Details of the column procedure for Sr are described by Font et al. (2008). Nd was collected in the initial eluent from the Sr column and put through a cation column (Dowall et al., 2003) to separate the Rare Earth Elements (REEs) from the remaining sample matrix. Purified Sr and Nd separates were taken up in 3% HNO_3 for analysis. Sr and Nd isotope ratios were measured on a Thermo Scientific Neptune Multi-Collector ICP Mass Spectrometer (MC-ICP-MS) at Durham University. The basic analytical method used for each element on the Neptune comprises a static multi-collection routine of 1 block of 50 cycles with an integration time of 4 seconds per cycle; total analysis time 3.5 minutes. Prior to analysis of Sr a small aliquot was first tested to establish the Sr concentration of each sample by monitoring the size of the ^{84}Sr beam (^{88}Sr is too high in non-diluted aliquot to measure directly) from which a dilution factor was calculated to yield a beam of approximately 20V ^{88}Sr.

Instrumental mass bias was corrected for using an ^{88}Sr/^{86}Sr ratio of 8.375209 (the reciprocal of the ^{86}Sr/^{88}Sr ratio of 0.1194 and an exponential law). Corrections were applied for Kr interferences on ^{84}Sr and ^{86}Sr, derived from Ar gas supply, and the Rb interference on ^{87}Sr, derived from the sample, by monitoring masses ^{82}Kr, ^{83}Kr and ^{85}Rb respectively. The average ^{83}Kr intensity throughout the analytical session was ~0.3mV, which is insignificant considering the average Sr beam size (^{88}Sr= 22±2V). The average ^{85}Rb intensity was slightly greater at ~5.7±19mV (2 samples at 27 and 88mV) but again, given the range in Sr beam size, the Rb correction on the ^{87}Sr/^{86}Sr was very small for most samples and is accurate even for the two samples with 27 and 88mV of ^{85}Rb. Samples were analysed in a single session during which the average ^{87}Sr/^{86}Sr value for NBS987 was 0.710262±0.000016 (23ppm 2SD; n=10). Total procedural blanks for Sr were less than 20 pg.

For Nd analysis beam sizes never exceeded the maximum 50V so no additional dilution was required. Instrumental mass bias was corrected for using a ^{146}Nd/^{145}Nd ratio of 2.079143 (equivalent to the more commonly used ^{146}Nd/^{144}Nd ratio of 0.7219) and an exponential law. The ^{146}Nd/^{145}Nd ratio was used for correcting mass bias since Nd isotopes were measured on a total REE-cut from the cation columns and this is the only Ce and Sm-free stable Nd isotope ratio. This approach requires a correction for isobaric interferences from Sm on ^{144}Nd, ^{148}Nd and ^{150}Nd (Nowell and Parrish, 2001). The average ^{147}Sm/^{146}Nd ratios measured on the samples during the Nd isotope analytical session was 0.191±0.03, which was just below the level at which the JNdi standard was doped with Sm (^{147}Sm/^{146}Nd 0.201). The accuracy of the Sm correction method during analysis of a total REE fraction was demonstrated by repeat analyses of BHVO-1, which gave an average ^{143}Nd/^{144}Nd ratio of 0.512982±0.000007 (13.5ppm 2SD; n=13) after Sm correction, which is the same within error to the TIMS ratio of 0.512986±0.000009 (17.5ppm 2SD; n=19; Weis et al., 2005). Samples were analysed in a single session during which the average ^{143}Nd/^{144}Nd value for pure and Sm-doped JNd$_i$ standard was 0.512119±0.000006 (12ppm 2SD; n=15). Total procedural blanks for Nd were less than 10 pg.

Results of isotope analyses are reported in Table 6. For isotope age correction calculations, please see Electronic Appendix 5.1.

Table 4: Major element compositions in (wt. %).

Name	**Segerstrom**						**Penacho Blanco**			**Co. Chrisoteado**		**Cachiyuyo**		
Sample	**AT11.2**	**AT12.1**	**AT12.2**	**AT12.3**	**AT12.4**	**AT12.6**	**AT39.1**	**AT39.2**	**AT39.3**	**AT20.1**	**AT20.3**	**AT16.1**	**AT16.2**	**AT16.3**
SiO_2	55.33	52.12	51.60	55.65	49.73	53.21	56.73	57.15	57.40	61.25	63.86	51.96	65.05	64.91
TiO_2	0.86	1.19	1.25	0.99	1.20	1.13	1.03	0.99	0.99	0.72	0.67	0.92	0.57	0.57
Al_2O_3	17.98	18.97	19.63	17.68	16.93	18.32	17.04	16.50	16.56	16.58	16.08	19.75	17.09	16.71
Fe_2O_3	7.71	9.07	9.04	8.07	10.19	9.21	8.21	5.71	5.59	5.62	5.15	9.66	4.44	5.30
MnO	0.15	0.16	0.13	0.12	0.13	0.16	0.13	0.09	0.09	0.10	0.10	0.15	0.08	0.09
MgO	3.01	3.61	3.37	3.72	7.23	4.00	2.83	3.02	2.87	1.80	1.73	4.35	1.36	1.73
CaO	7.00	8.42	7.73	7.30	9.41	8.19	6.15	5.69	5.81	5.54	4.54	7.67	4.08	4.56
Na_2O	3.43	3.47	3.58	3.42	2.85	3.55	3.21	3.71	3.85	4.14	4.12	3.82	4.30	4.21
K_2O	2.00	1.85	1.97	2.21	1.33	1.82	2.74	4.48	4.34	2.29	2.64	0.98	2.67	1.06
P_2O_5	0.34	0.30	0.34	0.25	0.22	0.35	0.27	0.62	0.62	0.22	0.24	0.15	0.17	0.17
SO_3	0.03	0.01	0.05	0.02	0.00	0.01	0.03	0.07	0.02	0.73	0.24	0.01	0.01	0.00
LOI	0.66	0.90	1.58	0.82	1.16	0.68	1.76	1.45	1.35	1.42	0.96	1.48	0.65	1.18
Total	98.50	100.07	100.27	100.26	100.38	100.62	100.14	99.48	99.49	100.42	100.31	100.90	100.45	100.51
$Na_2O + K_2O$	5.44	5.32	5.55	5.63	4.18	5.37	5.95	8.19	8.19	6.43	6.75	4.80	6.97	5.28

Table 4 (continued): Major element compositions in (wt. %).

Name	**Cachiyuyo**						**Cerro Buenos Aires**			**San Cristobal Coplex**			
Sample	**AT16.4**	**AT16.5**	**AT16.6**	**AT17.1**	**AT17.2**	**AT18.1**	**AT41.1**	**AT41.2**	**AT41.3**	**AT25.1**	**AT26.1**	**AT26.2**	**AT27.1**
SiO_2	60.70	62.66	60.65	51.82	51.86	56.75	60.28	60.68	59.80	65.49	62.49	52.01	53.89
TiO_2	0.61	0.57	0.61	0.90	0.95	0.95	0.72	0.69	0.72	0.94	0.88	1.18	1.20
Al_2O_3	18.60	17.42	18.46	19.10	19.16	17.93	16.50	16.30	16.12	15.05	15.21	19.56	17.03
Fe_2O_3	5.25	4.96	4.93	9.52	9.09	7.14	6.10	5.53	5.76	5.35	6.38	9.50	9.40
MnO	0.08	0.11	0.10	0.17	0.22	0.12	0.10	0.09	0.10	0.04	0.13	0.06	0.15
MgO	2.33	2.44	2.42	4.29	4.93	3.89	2.95	2.75	2.79	0.37	2.04	3.31	4.40
CaO	5.58	4.77	5.68	8.37	8.54	6.80	4.69	4.39	4.02	3.63	4.57	8.66	8.23
Na_2O	4.81	3.53	4.54	3.35	3.18	4.26	3.27	3.25	3.32	3.19	4.44	3.68	3.38
K_2O	1.35	1.48	1.34	1.00	0.86	1.93	2.97	3.25	3.75	4.34	2.25	0.96	1.34
P_2O_5	0.14	0.17	0.14	0.14	0.14	0.25	0.26	0.24	0.27	0.21	0.19	0.17	0.18
SO_3	0.00	0.01	0.01	0.01	0.00	0.01	0.05	0.04	0.38	0.02	0.02	0.01	0.00
LOI	0.73	2.08	1.25	1.43	1.25	0.40	2.29	2.66	3.12	1.81	1.77	1.27	1.05
Total	100.17	100.20	100.13	100.09	100.18	100.42	100.19	99.86	100.13	100.46	100.35	100.35	100.24
$Na_2O + K_2O$	6.15	5.01	5.87	4.35	4.04	6.19	6.24	6.49	7.07	7.53	6.68	4.63	4.72

Table 5: Trace element compositions (ppm).

Name	**Segerstrom**						**Penacho Blanco**		
Sample	**AT11.2**	**AT12.1**	**AT12.2**	**AT12.3**	**AT12.4**	**AT12.6**	**AT39.1**	**AT39.2**	**AT39.3**
Sc	11.5	18.3	16.0	16.3	28.3	17.1	21.4	13.3	13.2
V	119.4	264.2	240.7	193.1	299.0	208.5	220.3	147.4	154.6
Cr	9.7	30.8	10.0	43.0	160.4	20.6	26.4	21.7	20.1
Mn	0.15	0.17	0.13	0.13	0.15	0.17	0.14	0.09	0.09
Co	16.2	24.0	23.4	21.8	36.3	23.7	23.3	17.2	16.8
Ni	7.4	23.2	15.5	26.3	70.6	18.5	17.4	18.7	17.9
Cu	13.3	70.5	59.8	37.8	52.5	53.4	56.1	56.7	94.6
Zn	88.3	83.6	85.9	79.7	79.2	88.4	97.8	74.2	73.2
Ga	20.9	21.1	21.9	20.5	18.7	21.3	19.4	21.5	21.4
Rb	63.6	50.0	51.4	81.1	34.5	54.7	94.6	104.6	105.1
Sr	584	556	608	503	492	578	578	1676	1969
Y	20.9	22.0	22.4	22.1	19.3	24.1	28.6	22.5	22.6
Zr	192	128	131	144	95	163	196	311	285
Nb	14.5	12.8	13.8	13.3	8.9	14.6	10.4	11.5	11.5
Rh	0.92	0.92	0.93	0.91	0.91	0.93	0.86	0.88	0.88
Cs	1.73	4.66	1.73	3.60	7.03	2.16	4.38	2.55	2.94
Ba	589	410	557	471	275	406	587	1455	1368
La	26.56	18.94	19.83	21.75	13.20	21.14	23.77	80.17	79.38
Ce	55.59	40.26	42.19	46.19	28.80	45.03	49.23	166.80	173.70
Pr	7.32	5.39	5.70	6.05	4.05	6.07	6.66	22.34	21.91
Nd	28.51	21.74	23.03	23.59	17.12	24.50	26.71	86.23	84.70
Sm	5.45	4.62	4.93	4.76	3.89	5.14	5.71	13.92	13.68
Eu	1.58	1.37	1.45	1.31	1.20	1.49	1.39	3.76	3.72
Gd	4.81	4.53	4.66	4.48	3.96	4.94	5.41	9.32	9.19
Tb	0.70	0.69	0.71	0.68	0.61	0.75	0.83	1.06	1.04
Dy	3.79	3.89	4.00	3.79	3.47	4.21	4.75	4.60	4.54
Ho	0.73	0.78	0.79	0.76	0.68	0.83	0.98	0.77	0.76
Er	1.92	2.03	2.06	2.00	1.78	2.19	2.67	1.83	1.80
Tm	0.30	0.31	0.32	0.31	0.27	0.34	0.42	0.25	0.25
Yb	1.88	1.97	2.02	1.99	1.71	2.13	2.71	1.54	1.51
Lu	0.31	0.32	0.33	0.32	0.28	0.35	0.43	0.24	0.24
Hf	4.73	3.36	3.48	3.76	2.60	4.10	4.94	7.74	7.59
Ta	0.87	0.86	0.89	0.96	0.57	0.93	0.76	0.77	0.78
Re	0.98	0.99	1.00	0.99	0.98	1.01	0.87	0.88	0.88
Pb	9.04	7.10	6.66	7.76	4.91	7.81	10.85	16.15	15.63
Th	5.96	5.55	5.34	7.43	3.36	5.16	8.44	18.91	18.66
U	1.18	1.29	1.45	1.81	0.78	1.30	2.51	4.22	4.33

Table 5 continued: Trace element compositions (ppm)

Name	**Cachiyuyo**								
Sample	**AT16.1**	**AT16.2**	**AT16.3**	**AT16.4**	**AT16.5**	**AT16.6**	**AT17.1**	**AT17.2**	**AT18.1**
Sc	24.7	9.3	9.2	9.8	9.7	10.0	24.0	26.6	16.1
V	271.9	70.9	87.0	134.4	70.1	132.3	243.2	233.6	205.6
Cr	17.1	8.4	4.2	13.6	5.3	17.4	17.2	25.1	18.1
Mn	0.17	0.08	0.10	0.08	0.11	0.10	0.17	0.23	0.12
Co	27.4	9.6	9.3	13.7	12.9	14.0	25.7	27.1	23.0
Ni	11.7	7.2	4.5	14.5	6.4	17.0	11.2	14.8	24.4
Cu	9.5	22.9	41.9	67.0	8.1	31.2	74.0	225.6	61.7
Zn	81.1	56.6	86.1	62.1	88.2	149.6	71.5	102.6	102.9
Ga	21.3	19.1	17.9	19.8	20.2	20.0	20.9	20.5	21.1
Rb	20.0	60.3	23.9	26.3	36.4	24.5	18.5	16.9	41.9
Sr	664	465	531	588	485	598	603	585	900
Y	16.0	18.3	16.3	9.1	17.8	9.2	15.9	15.8	12.9
Zr	37	135	132	68	141	74	35	44	25
Nb	2.3	4.1	3.6	2.3	3.9	2.3	2.3	2.2	4.6
Rh	0.89	0.87	0.89	0.96	0.95	0.96	0.91	0.93	0.91
Cs	1.74	1.15	0.77	1.27	0.78	1.64	1.54	2.42	1.47
Ba	272	784	382	459	459	499	413	342	635
La	7.46	13.58	10.95	8.77	11.76	9.00	7.99	7.71	15.36
Ce	17.47	31.60	25.53	18.63	26.30	19.08	17.85	17.44	33.51
Pr	2.71	4.58	3.73	2.68	3.71	2.70	2.72	2.70	4.75
Nd	12.36	18.73	15.47	11.10	15.52	11.19	12.21	12.07	19.42
Sm	2.99	3.95	3.27	2.27	3.28	2.32	2.94	2.95	3.73
Eu	1.09	0.98	0.98	0.77	0.84	0.82	1.09	1.05	1.08
Gd	3.05	3.56	3.08	2.03	2.98	2.06	3.00	3.03	3.12
Tb	0.48	0.54	0.47	0.29	0.46	0.29	0.46	0.47	0.43
Dy	2.78	3.07	2.74	1.56	2.72	1.59	2.67	2.71	2.25
Ho	0.57	0.62	0.56	0.31	0.59	0.32	0.57	0.58	0.45
Er	1.49	1.66	1.51	0.79	1.64	0.82	1.46	1.48	1.13
Tm	0.23	0.26	0.24	0.12	0.26	0.13	0.22	0.22	0.17
Yb	1.40	1.70	1.56	0.76	1.69	0.79	1.32	1.36	1.01
Lu	0.21	0.28	0.26	0.13	0.27	0.13	0.20	0.21	0.16
Hf	1.30	4.05	3.81	1.97	4.15	2.05	1.21	1.42	0.97
Ta	0.17	0.33	0.29	0.17	0.31	0.16	0.15	0.15	0.28
Re	0.96	0.94	0.95	0.96	0.96	0.96	0.92	0.94	0.94
Pb	7.57	9.09	9.94	4.30	5.28	12.95	3.98	5.72	11.69
Th	1.18	4.86	4.15	1.74	4.54	1.83	1.11	1.11	3.24
U	0.30	1.29	1.07	0.48	1.08	0.50	0.30	0.27	0.88

Table 5 continued: Trace element compositions (ppm)

Name	**Co. Chrisoteado**		**Cerro Buenos Aires**			**San Cristobal Coplex**			
Sample	**AT20.1**	**AT20.3**	**AT41.1**	**AT41.2**	**AT41.3**	**AT25.1**	**AT26.1**	**AT26.2**	**AT27.1**
Sc	9.0	8.1	16.3	14.6	15.8	15.4	19.1	32.2	33.1
V	107.5	77.2	147.2	128.9	122.8	98.7	92.1	255.0	268.2
Cr	9.8	7.1	11.4	11.8	9.3	22.1	36.5	34.2	60.8
Mn	0.10	0.10	0.09	0.09	0.10	0.04	0.12	0.06	0.15
Co	14.5	13.5	17.3	16.1	16.7	11.8	13.0	30.6	28.6
Ni	8.6	7.8	11.7	11.4	10.1	12.8	16.6	33.8	15.1
Cu	27.3	26.4	25.1	102.3	19.8	28.1	48.0	99.7	46.1
Zn	64.9	61.4	69.3	65.3	65.4	104.6	75.5	91.7	89.8
Ga	18.4	17.7	19.1	19.0	18.0	16.9	17.6	20.6	19.1
Rb	75.4	91.6	111.7	124.4	132.4	249.3	267.4	34.4	51.6
Sr	509	459	571	563	570	201	191	361	299
Y	18.5	19.5	20.0	19.9	18.9	38.4	49.0	22.0	29.7
Zr	94	85	112	108	108	269	432	77	157
Nb	9.3	9.7	8.3	8.7	8.4	10.4	17.6	4.9	7.0
Rh	0.87	0.90	0.87	0.84	0.80	0.83	0.92	0.89	0.91
Cs	4.46	4.13	7.63	8.99	6.28	23.53	18.71	10.63	3.22
Ba	590	1091	687	714	766	404	637	234	228
La	22.83	25.23	22.18	23.25	20.51	23.56	36.08	13.16	13.22
Ce	44.71	49.22	46.03	48.10	42.60	52.89	79.16	27.94	30.29
Pr	5.77	6.36	6.01	6.22	5.57	7.39	10.41	3.75	4.36
Nd	22.14	24.00	22.97	23.65	21.44	29.40	40.44	15.86	18.76
Sm	4.29	4.59	4.51	4.56	4.17	6.49	8.44	3.74	4.57
Eu	1.18	1.17	1.09	1.06	1.00	1.20	1.27	1.23	1.28
Gd	3.83	4.13	3.96	3.93	3.71	6.36	8.22	4.04	4.94
Tb	0.56	0.60	0.60	0.58	0.54	1.03	1.32	0.65	0.80
Dy	3.09	3.31	3.30	3.23	3.00	6.04	7.71	3.85	4.89
Ho	0.63	0.68	0.66	0.65	0.60	1.25	1.62	0.80	1.03
Er	1.64	1.77	1.77	1.76	1.62	3.37	4.46	2.12	2.80
Tm	0.26	0.27	0.28	0.28	0.26	0.55	0.71	0.33	0.44
Yb	1.63	1.79	1.81	1.83	1.67	3.38	4.54	2.14	2.84
Lu	0.26	0.29	0.29	0.30	0.27	0.53	0.72	0.34	0.46
Hf	2.66	2.56	3.25	3.17	3.06	6.92	11.81	2.22	3.98
Ta	0.75	0.82	0.70	0.73	0.66	0.81	1.26	0.35	0.48
Re	0.88	0.89	0.88	0.85	0.83	0.87	0.92	0.89	0.91
Pb	10.58	10.29	12.05	11.51	10.87	13.30	16.92	4.06	6.09
Th	10.69	13.02	13.90	15.14	13.01	23.92	28.33	1.94	4.77
U	2.86	3.38	3.90	4.23	3.47	6.17	7.31	0.54	1.17

5.8 Results

5.8.1 Whole-rock geochemistry

The measured samples are from a wide spatial and temporal range. Therefore, it is not possible to present and interpret them collectively as a coeval suite, unlike studies which compare samples from one individual stratovolcano (for example, Davidson et al., 1988, 1990; Dungan et al., 2001). Coeval suites were collected wherever exposure permitted (Segerstrom, Cachiyuyo, San Cristobal, Co. Christoeado, Panacho Blanco and Cerro Buenos Aires) and this study focusses on analysis of these suites. Although all suites were dated by the K-Ar method, which can be in imprecise due to release of radiogenic argon during rock crushing (Funkhouser et al., 1966), their more general ages can be assured due to their locations along mapped Paleogene volcanic belts (Naranjo and Puig, 1984; Boric et al., 1987a, 1987b; Arévalo, 1995; Servicio Nacional de Geología y Minería, 2003). The collective geochemistry of Paleogene lavas are compared to previously published Central Andean data from Jurassic-Present (Haschke et al., 2002b; Kay et al., 2006, 2014; Mamani et al., 2010) to help determine changing petrogenic and tectonic processes through time.

5.1.1.7 Major element compositions

All the Paleogene dated samples analysed in this study are calc-alkaline and mainly lie on the boundary between the basaltic series and the more alkaline trachybasalt series (Figure 40a). Basaltic andesite to andesite compositions dominate all the studied suites. Only mafic endmembers from the Segerstrom, Cachiyuyo and San Cristobal Complexes are basaltic. AT12.4 (Segerstrom) is the most mafic rock in this study at 49.7% wt. SiO_2 and 7.2% wt. MgO and contains olivine phenocrysts (~<500 µm) with oxidised rims (Figure 38c). Olivine phenocrysts are either very rare or not present in all other samples. All other samples also have MgO contents too low to be considered truly primary magmas (<5 wt.%). The two youngest suites of rocks analysed here, Segerstrom (25 Ma) and Penacho Blanco (45 Ma), have high-K contents (Figure 40b). Cerro Buenos Aires (60 Ma) lavas are also high-K. Two samples from the Penacho Blanco suite are very highly alkaline and have high-K contents (Figure 40a, b). Like most arc lavas, major element compositions form a continuum when plotted against fractionation indices such as SiO_2 or MgO. Fractionation processes are the dominant control on major element trends observed in Harker variation plots shown in Figure 41, involving phases observed in the rocks, namely plagioclase, pyroxenes, amphibole and minor olivine. MgO, Al_2O_3, Fe_2O_3, TiO_2 and CaO contents all generally decrease with increasing SiO_2 (Figure 40) as they are all compatible in fractionating phases. For example, decreasing Al_2O_3, CaO and Na_2O with increasing SiO_2 is indicative of plagioclase as a fractionating phase and is consistent with the presence of plagioclase as both phenocryst and matrix phases in the samples. AT12.4 (~49 wt. % SiO_2) has relatively low Al_2O_3 and Na_2O contents and has proportionally less plagioclase (and more clinopyroxene) in thin section (Figure 38c,d). Na_2O contents in the Cachiyuyo and San Cristobal suites increase up to ~60 wt. % SiO_2 and then decrease at $SiO_2 > 60$ wt. % (Figure 40), which could potentially indicate the involvement of Na rich plagioclase at higher silica contents in these suites. Cachiyuyo, San Cristobal and Co. Chrisoteado lavas have relatively high Al_2O_3 and Na_2O contents at >60 wt. % SiO_2 compared to other suites (Figure 40).

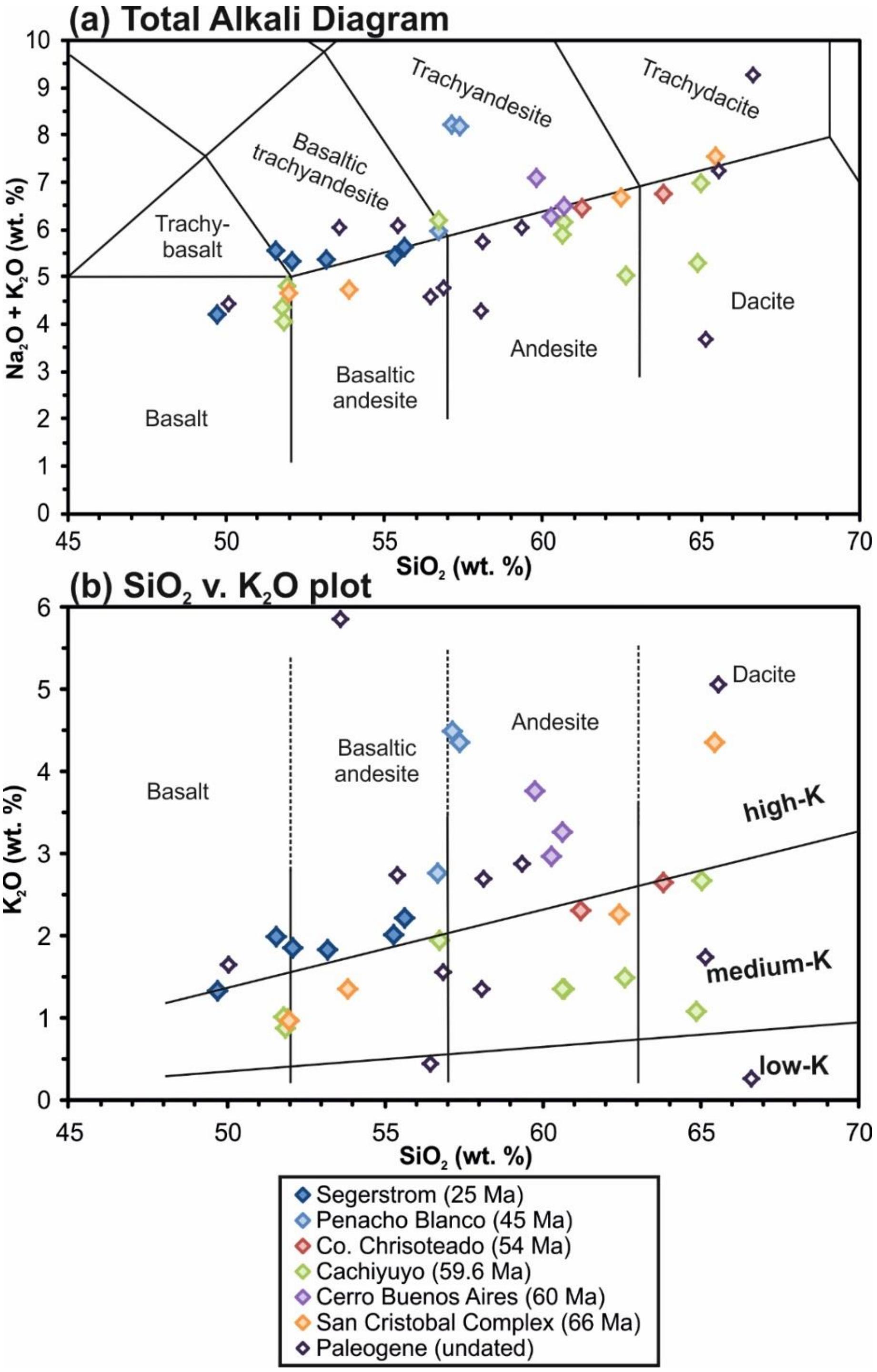

Figure 40: (a) Total alkali vs. SiO_2 classification diagram for the main dated suites collected in this study. (b) K_2O vs SiO_2 variation plot. The Sergerstrom, Penacho Blanco and Cerro Buenos Aires suites are in the high-K field. Cachiyuyo, San Cristobal and Co. Chrisoteado lavas are in the medium-K field. Both plots after (Maitre et al., 2002).

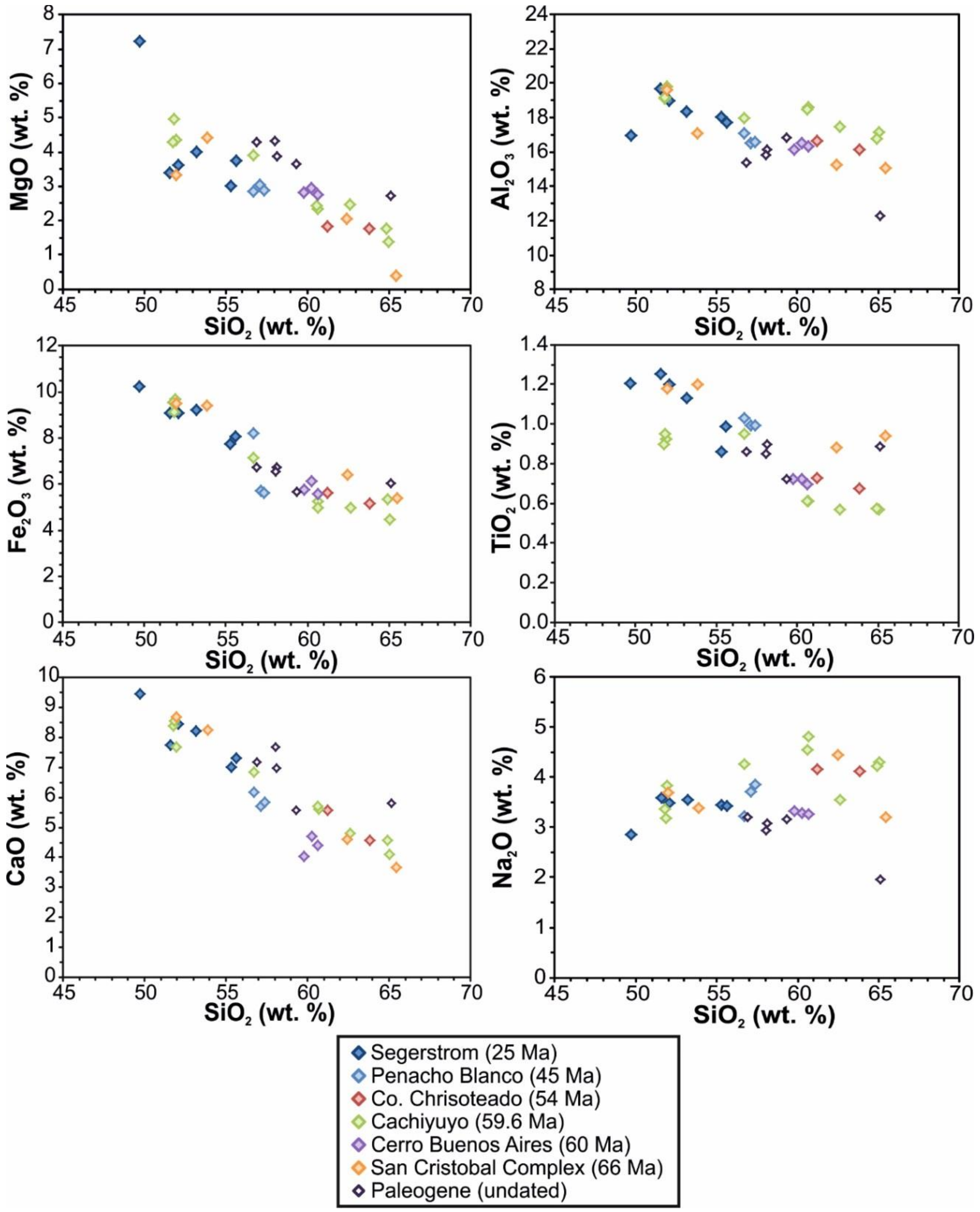

Figure 41: Harker variation diagrams. The general negative trends in plots of compatible elements MgO, Al_2O_3, Fe_2O_3, TiO_2 and CaO with increasing SiO_2 are the result of increasing degrees of fractional crystallisation. Cachiyuyo and San Cristobal lavas have relatively high Al_2O_3 and Na_2O contents at >60 wt. % SiO_2 compared to other suites.

5.1.1.8 Trace element compositions

Trace element compositions of all samples show a typical ‘subduction signature’ on Depleted Mantle (DM; Salters and Stracke, 2004) normalised spiderdiagrams, with low Nb and Ta concentrations relative to neighbouring elements U and K (Figure 42). Figure 42a shows trace element concentrations for all samples. Figure 42b shows the most mafic sample from each of the cogenetic and dated suites of this study. All samples have positive spikes at elements K and Pb. The basaltic endmembers of the Segerstrom, Cachiyuyo and San Cristobal are relatively depleted in incompatible elements (e.g. Rb, Ba, Th, U) compared to other suites analysed. Yet, San Cristobal and Cachiyuyo lavas have lower K_2O (also generally incompatible) than Segerstrom lavas at similar SiO_2 contents (Figure 40).

High Field Strength Elements (HFSE) Nb and Ta are relatively depleted in Paleogene lavas both from this study and from the data compilation (Figure 43a; Haschke et al., 2002; Mamani et al., 2010). Cachiyuyo lavas have the lowest Nb and Ta concentrations for any given degree of fractionation (Figure 42a), and are potentially slightly anomalous compared to other Paleogene lavas (Figure 43a).

Average concentrations of ‘most mafic’ Quaternary CVZ lavas and Quaternary SVZ lavas (see Chapter 3) are shown in Figure 43b. Quaternary CVZ lavas are relatively enriched in incompatible elements (Rb, Ba, Th, and U) and more depleted in Heavy Rare Earth Elements (HREEs) compared to Quaternary SVZ lavas. Central Andean Paleogene lavas, both from this study and from the Paleogene compilation (Haschke et al., 2002b; Mamani et al., 2010), have average compositions which lie midway between Quaternary CVZ and SVZ lavas for the incompatible elements from Rb to Ce on trace element spiderdiagrams (Figure 43b).

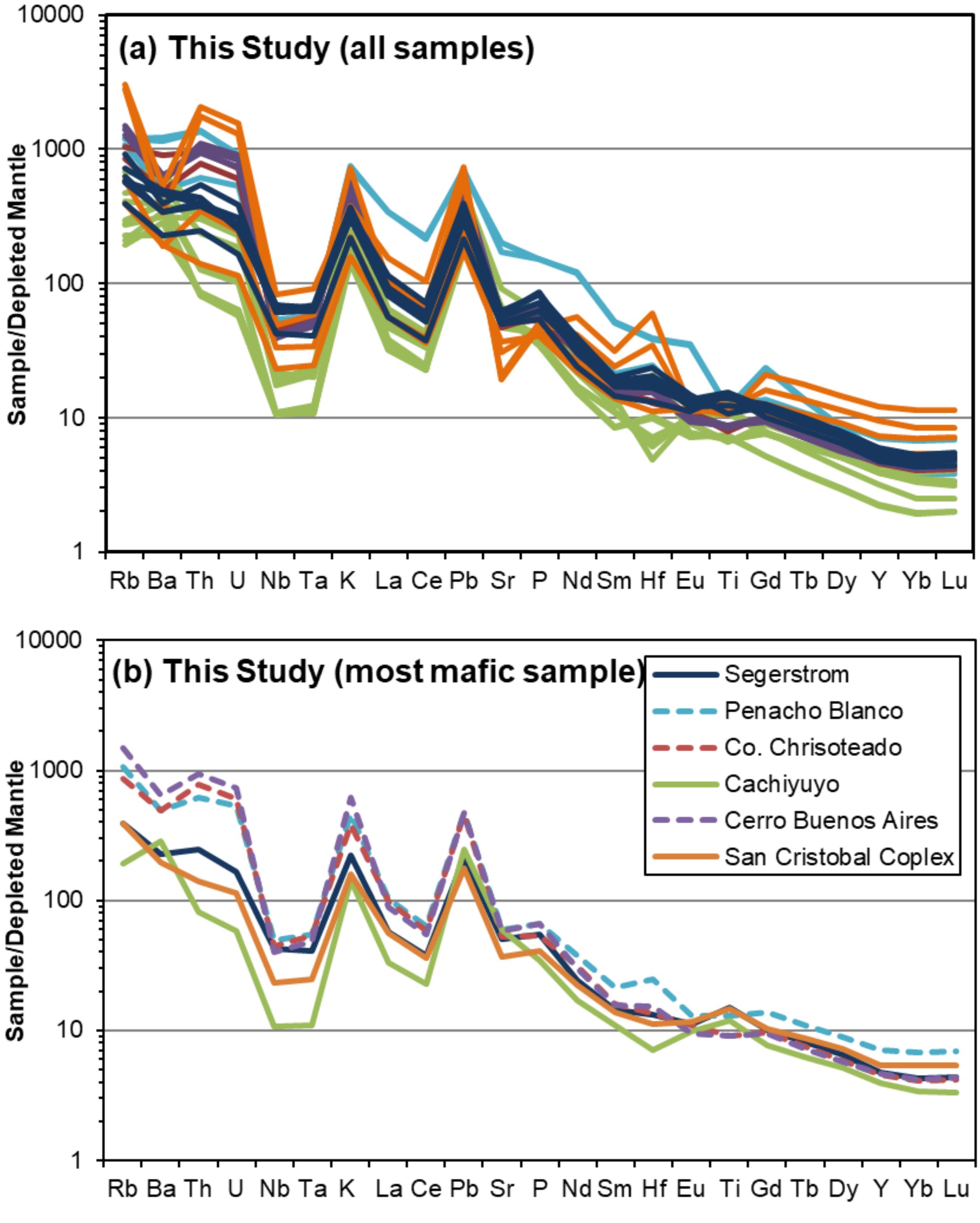

Figure 42: Depleted Mantle-normalised (Salters and Stracke, 2004) trace element spiderdiagrams showing variations in all samples from each of the six suites (top) and the most mafic sample from each suite analysed in this study (bottom panel). For Segerstrom, Cachiyuyo and San Cristobal the most mafic samples are basaltic (solid lines). Penacho Blanco, Co. Chrisoteado and Cerro Buenos Aires the most mafic samples are andesites (dashed lines). Line colours given in the key of panel (b) are the are the same for both plots.

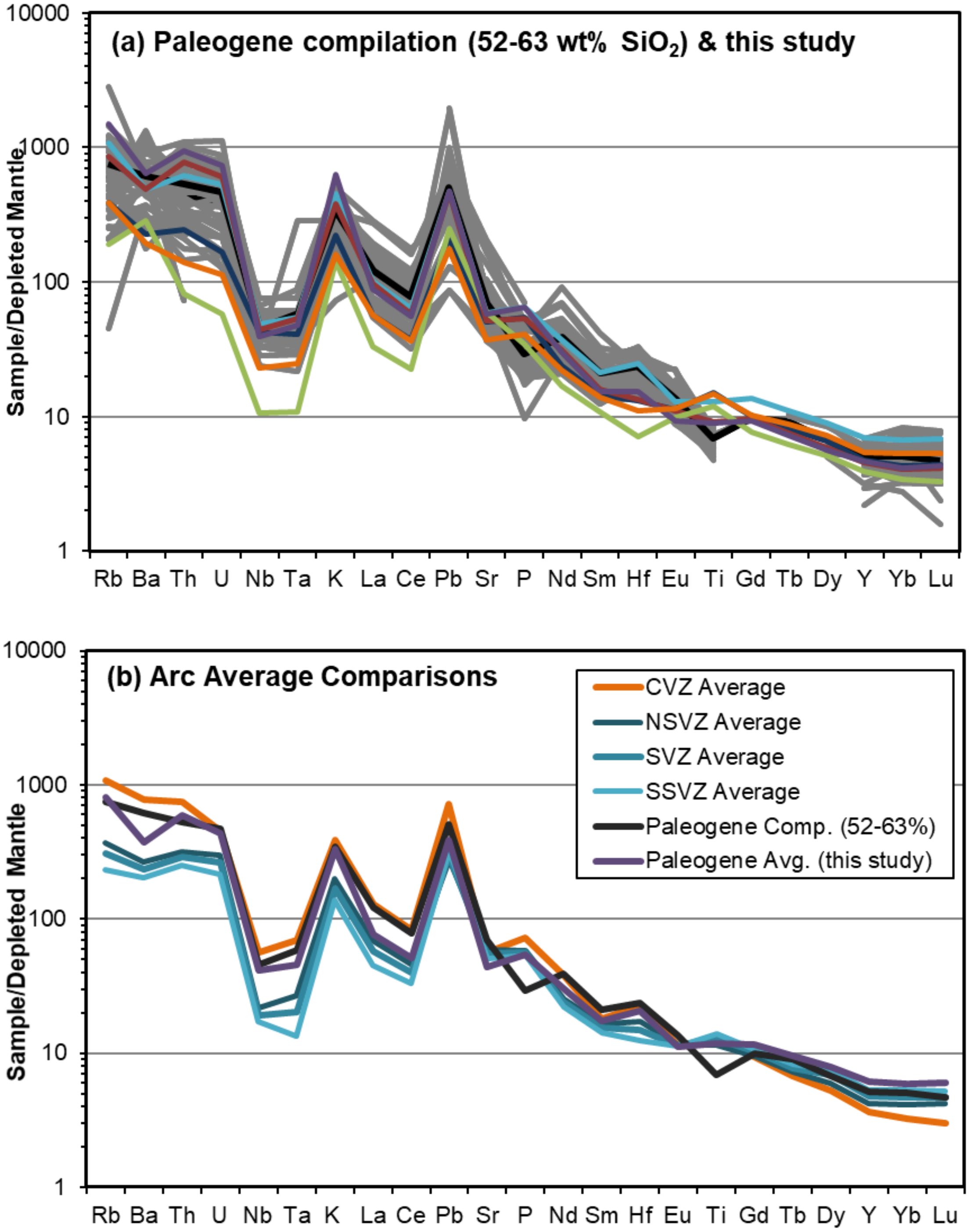

Figure 43: Depleted Mantle-normalised trace element spiderdiagrams showing variations in Quaternary and Paleogene Andean arc lavas. The average composition of each filtered dataset is shown in bold. The most mafic samples from compilations of Quaternary CVZ and SVZ samples described in Chapter 4 are shown in the left panels. The compilation of (Haschke et al., 2002b) is filtered to 52-63 wt. % SiO_2 (basaltic andesite-andesite) as there are not enough data to find the most mafic sample for each centre. Data from this study (coloured lines are the same as Figure 42b) fit within the range of data from Haschke et al. (2002), except for the Cachiyuyo most mafic sample (in green). The bottom right panel is a plot of the averages shown on the other 3 panels for comparison.

Large Ion Lithophile elements (LILEs), Rb, Sr, Cs and Ba are highly fluid mobile and incompatible in most crystal phases. Sr^{2+} can substitute for Ca^{2+} in plagioclase making it a useful element for petrology and geochemical barometry. Sr^{2+} is compatible at low pressures where plagioclase is generally stable in the crust and incompatible at higher pressures where plagioclase becomes unstable (as discussed in Chapter 3 and later in this Chapter). The San Cristobal lavas are all relatively depleted in Sr compared to other samples, and Sr content decreases with increasing SiO_2 across the whole suite (from 52 wt. % SiO_2; Figure 44). Both Th and Rb are relatively depleted in Cachiyuyo lavas compared to our other samples, with the degree of relative depletion increasing with increasing fractionation (Figure 44). The fact that the Ba contents of Cachiyuyo lavas are similar to other Paleogene lavas and not coupled with Rb depletion suggests this is not the product of post-emplacement fluid alteration, which would strip the rock of both fluid mobile elements. Two samples from Penacho Blanco are very enriched in Ba, Sr and Th but not in Rb (Figure 44). These two samples are high-K trachyandesites and have extremely steep patterns on the DM-normalised spiderdiagram (Figure 42), and are anomalous compared to other Paleogene compositions (Figure 43a).

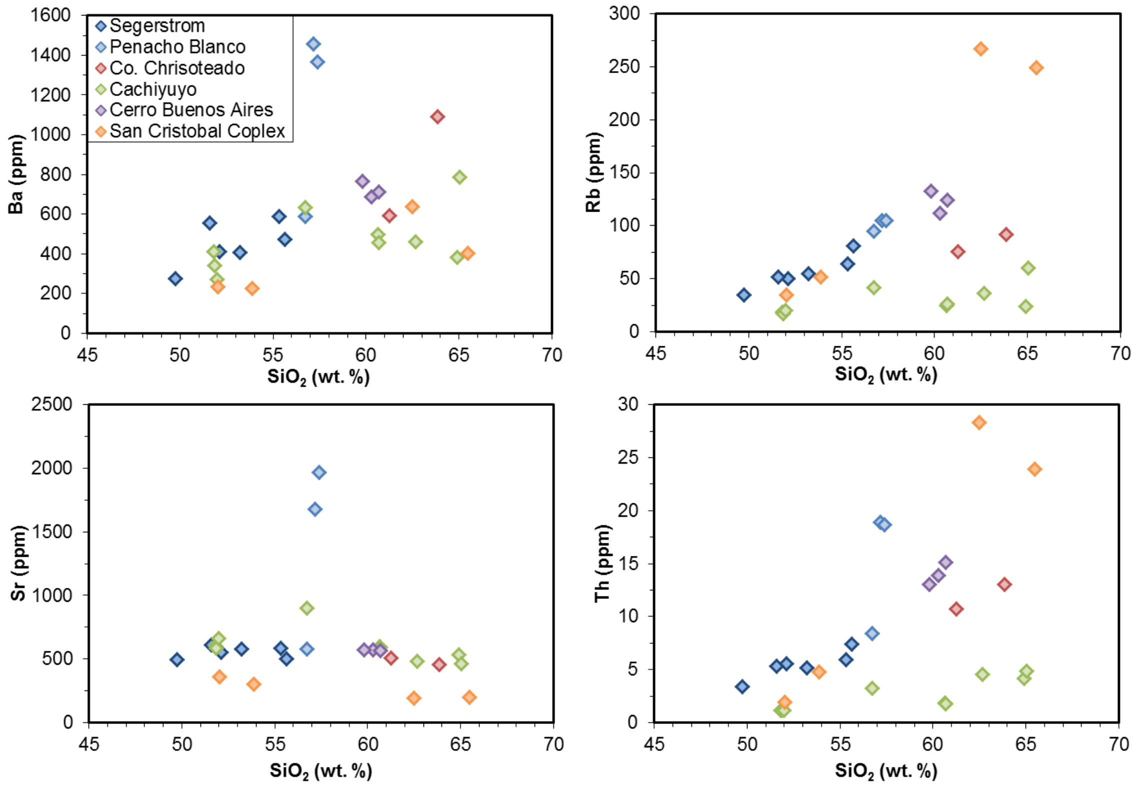

Figure 44: Ba, Rb, Sr and Th concentrations in relation to SiO_2 content of dated Paleogene suites from this study.

5.1.1.9 Radiogenic isotope compositions

Paleogene Central Andean lavas analysed here have $^{87}Sr/^{86}Sr_{(i)}$ ratios between 0.7037 and 0.7052 and $^{143}Nd/^{144}Nd_{(i)}$ ratios from 0.51262 to 0.51295 (Table 6), which overlap with previous analyses of the Paleogene Central Andean arc (Figure 45; Haschke et al., 2002). The Cachiyuyo suite (c. 59 Ma), has the lowest $^{87}Sr/^{86}Sr_{(i)}$ (0.70370) and highest $^{143}Nd/^{144}Nd_{(i)}$ (0.512940) ratios and are therefore the most similar to DM compositions compared to any of the other suites analysed in this study or to the Paleogene compilation. The Cachiyuyo lavas have therefore seen the least contribution from the more radiogenic mid- to upper-continental crust, which we explore and quantify in the Discussion section.

In Chapter 4, we observed that Central Andean Sr and Nd isotope compositions became increasingly radiogenic (more 'continental crust-like') from the Jurassic to Neogene (Scott et al., 2018; see also Rogers and Hawkesworth, 1989; Haschke et al., 2002b; Mamani et al., 2010). Central Andean Paleogene lavas share the same Sr-Nd isotope space as both Central Andean Cretaceous arc lavas and Quaternary SVZ lavas (Figure 45). Central Andean Jurassic lavas have a similar range of Nd isotope ratios but have less radiogenic $^{87}Sr/^{86}Sr_{(i)}$ compositions (Rossel et al., 2013), and follow a variation line between Depleted Mantle and Enriched Mantle 1.

One of the most radiogenic samples analysed in this study is from the youngest suite (Segerstrom, 25 Ma; from the Paleogene-Neogene boundary; Figure 45). Segerstrom is one of the oldest centres sampled in a study of the Neogene-present arc by Kay et al. (2014). The Segerstrom and Máquinas (c. 22-25 Ma) lavas have the lowest $^{87}Sr/^{86}Sr_{(i)}$ and highest $^{143}Nd/^{144}Nd_{(i)}$ of the Neogene lavas analysed by Kay et al. (2014). For the Segerstrom suite, Kay et al. (2014) obtained results for two samples with $^{87}Sr/^{86}Sr_{(i)}$ ratios ranging between 0.7039-0.7043 and $^{143}Nd/^{144}Nd_{(i)}$ ratios of 0.51270-0.51284. Our results for the same suite overlap with the more evolved end of Kay et al. (2014)'s results (range $^{87}Sr/^{86}Sr_{(i)}$: 0.70427-0.70522 and $^{143}Nd/^{144}Nd_{(i)}$: 0.51262-0.51279). Quaternary CVZ lavas are much more radiogenic than any of the Central Andean Jurassic-Paleogene compositions or Quaternary SVZ compositions (Figure 45), as discussed in Chapter 4.

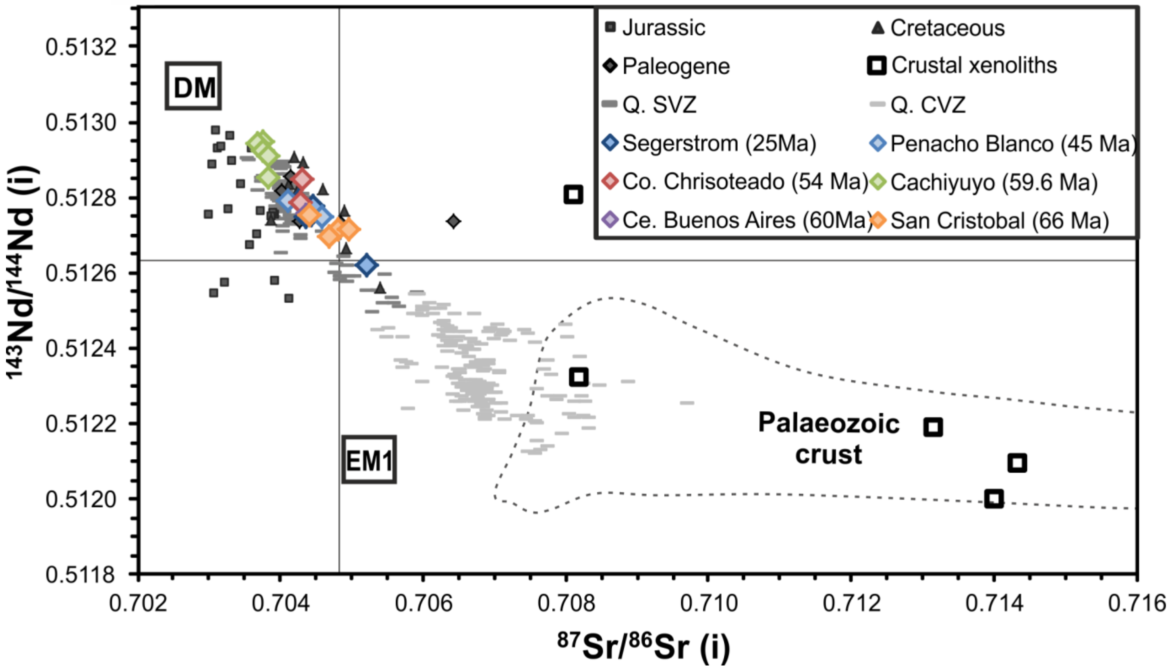

Figure 45: Sr and Nd radiogenic isotope compositions of Paleogene samples analysed in this study compared to Central Andean Jurassic-Paleogene arc lavas and Quaternary SVZ and CVZ lavas. Errors for samples analysed in this study are smaller than the symbols used, except for two of the San Cristobal samples which have higher $^{87}Sr/^{86}Sr$(i) errors (2σ ±0.0004, see Table 6) due to high Rb contents (see Electronic Appendix 5.1 for error propagation calculations). Mantle end-members DM (Depleted Mantle; Salters and Stracke, 2004) and EM1 (Enriched Mantle 1; Zindler and Hart, 1986). Lower crustal xenoliths from Late Cretaceous rift related magmatism represent Andean basement compositions (Lucassen et al., 1999), and are used as end-member compositions later in assimilation and fractional crystallisation modelling (Figure 50 & Figure 51).

Table 6: Sr and Nd radiogenic isotope ratios. Subscript (i) refers to age corrected isotope compositions in each case. The error on the uncorrected isotope ratios is the analytical error. Errors for the age corrected ratios are calculated from propagation of errors on the Rb/Sr and Sm/Nd ratios. Spreadsheets containing the age correction and error propagation calculations can be found in Electronic Appendix 5.1.

Name	Sample	Age (Ma)	SiO$_2$ (wt. %)	^{87}Sr/^{86}Sr	±2σ	^{87}Rb/^{86}Sr	^{87}Sr/^{86}Sr(i)	±2σ	^{143}Nd/^{144}Nd	±2σ	^{147}Sm/^{144}Nd	^{143}Nd/^{144}Nd(i)	±2σ	εNd (i)
Segerstrom	AT11.2	25±0.9	55.33	0.705327	0.000008	0.314847	0.705215	0.000012	0.512639	0.000004	0.115465	0.512620	0.000002	0.279
	AT12.1	25±0.9	52.12	0.704533	0.000010	0.260095	0.704441	0.000010	0.512771	0.000006	0.128325	0.512750	0.000002	2.813
	AT12.2	25±0.9	51.60	0.704561	0.000008	0.244517	0.704474	0.000009	0.512797	0.000006	0.129325	0.512776	0.000002	3.317
	AT12.4	25±0.9	49.73	0.704447	0.000009	0.202640	0.704375	0.000008	0.512770	0.000004	0.137254	0.512748	0.000002	2.765
	AT12.6	25±0.9	53.21	0.704371	0.000008	0.273468	0.704274	0.000010	0.512811	0.000004	0.126697	0.512790	0.000002	3.598
Cachiyuyo	AT16.2	59.6±2.8	65.05	0.704088	0.000006	0.375010	0.703770	0.000033	0.512995	0.000008	0.127593	0.512945	0.000005	7.491
	AT16.4	59.6±2.8	60.70	0.703805	0.000010	0.129436	0.703695	0.000012	0.512988	0.000008	0.123603	0.512940	0.000005	7.384
	AT16.5	59.6±2.8	62.66	0.703949	0.000011	0.216906	0.703765	0.000019	0.512970	0.000006	0.127578	0.512920	0.000005	7.003
	AT17.2	59.6±2.8	51.86	0.703906	0.000010	0.083615	0.703835	0.000007	0.512967	0.000008	0.147520	0.512909	0.000006	6.793
	AT18.1	59.6±2.8	56.75	0.703966	0.000009	0.134751	0.703852	0.000012	0.512897	0.000006	0.116085	0.512852	0.000005	5.666
Co. Chrisoteado	AT20.1	54±2	61.25	0.704639	0.000008	0.428693	0.704310	0.000035	0.512886	0.000006	0.117029	0.512845	0.000004	5.387
	AT20.3	54±2	63.86	0.704735	0.000008	0.577185	0.704292	0.000047	0.512824	0.000004	0.115562	0.512783	0.000004	4.188
San Cristobal Complex	AT25.1	66±2	65.49	0.708185	0.000009	3.596992	0.704812	0.000355	0.512770	0.000004	0.133393	0.512712	0.000006	3.109
	AT26.1	66±2	62.49	0.708773	0.000011	4.056647	0.704969	0.000400	0.512765	0.000004	0.126090	0.512711	0.000006	3.073
	AT26.2	66±2	52.01	0.704670	0.000011	0.275415	0.704412	0.000027	0.512814	0.000004	0.142558	0.512752	0.000006	3.890
	AT27.1	66±2	53.89	0.705158	0.000009	0.497943	0.704691	0.000049	0.512759	0.000006	0.147323	0.512695	0.000007	2.777
Penacho Blanco	AT39.1	45±1.5	56.73	0.704889	0.000008	0.472843	0.704587	0.000032	0.512783	0.000006	0.129111	0.512745	0.000004	3.217
	AT39.3	45±1.5	57.40	0.704228	0.000009	0.154355	0.704129	0.000010	0.512816	0.000004	0.097614	0.512787	0.000003	4.042
Cerro Buenos Aires	AT41.1	60±2.2	60.28	0.704855	0.000009	0.566124	0.704372	0.000051	0.512802	0.000004	0.118744	0.512755	0.000005	3.797

5.9 Discussion

Neogene-Quaternary Central Volcanic Zone (CVZ) lavas have a distinctively 'crustal' geochemical signature (Davidson et al., 1988; Haschke et al., 2002b; Mamani et al., 2010; Wörner et al., 2018) related to the >60 km thick crust (Tassara and Echaurren, 2012; Assumpção et al., 2013) of the Andean Plateau. Enriched 'crust-like' isotope signatures are related to assimilation of continental basement (Hildreth and Moorbath, 1988; Davidson et al., 1990; Feeley and Sharp, 1995; Annen et al., 2006; Solano et al., 2012; Freymuth et al., 2015) and/or an enriched mantle source, possibly due to contamination by fore-arc erosion (Kay et al., 1991; Stern, 1991; Kay and Kay, 2002; Goss et al., 2013). As well as distinct radiogenic isotopic signatures, Quaternary CVZ lavas have trace element compositions relating to petrological processes indicating both deep magma equilibration (where plagioclase is not stable), sometimes overprinted by extensive shallow crustal fractionation (within the plagioclase stability field), as discussed in Chapter 3. These distinct Central Andean geochemical signatures developed during the Paleogene period, a critical time of Andean deformation (66-23 Ma; Haschke et al., 2002; Mamani et al., 2010; Scott et al., 2018). A previous lack of data for the Paleogene period, especially for whole rock Sr- and Nd-radiogenic isotopes, has led to lack of constraint on a more precise timing of Central Andean geochemical evolution, and thereby inferences on the timing of crustal thickening and uplift in the Western Cordillera. Conclusions from Chapters 3 and Chapter 4 are applied in this Chapter to new data for the Central Andean Paleogene period and to compilations of Central Andean lavas from the Jurassic-Present in order to gain insight into the changing tectonic environment.

5.9.1 Fractionation processes

Averaged Sr/Y, La/Yb, and Sm/Yb ratios have been calibrated with crustal thickness and utilised as first-order crustal thickness proxies in magmatic arcs, both globally and within individual arc segments (Haschke et al., 2002b; Kay et al., 2006; Mamani et al., 2010; Chiaradia, 2015; Chapman et al., 2015a; Profeta et al., 2015b; Farner and Lee, 2017). Other processes have also been used to interpret elevated REE ratios, such as fore-arc subduction erosion (Kay et al., 1991, 2014; Stern, 1991) or a slab melt component (Kay, 1978; Defant and Drummond, 1990; Stern and Kilian, 1996; Mungall, 2002). As discussed in Chapter 3, modern Andean lavas within the CVZ and SVZ have trace element ratios which are strongly influenced by increasing crustal thickness, and not by increasing slab temperature which would be expected by the slab melt hypothesis. Subduction erosion is a process which is thought to occur during increased plate compression during tectonic thickening of the overriding plate (e.g. Kay et al., 1991), so this mechanism would be synchronous with crustal thickening at the arc. The following interpretations are therefore based on crustal thickening and subduction erosion processes being the main driver for increasing Sr/Y and La/Yb ratios.

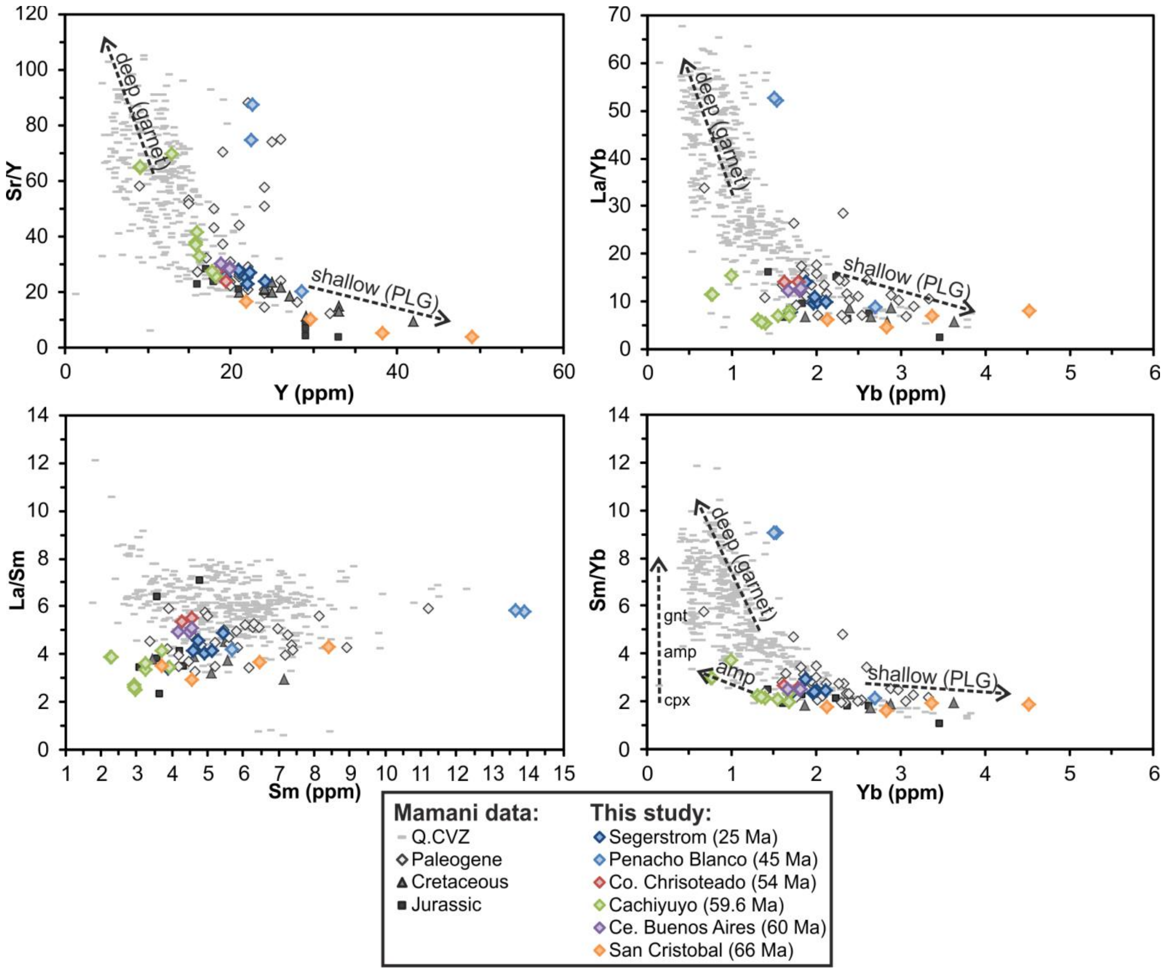

Figure 46: Sr/Y, La/Yb, La/Sm and Sm/Yb plotted against the heavier denominator element. Paleogene Central Andean lavas from this study are compared to Jurassic-Paleogene Central Andean lavas (Haschke et al., 2002b; Mamani et al., 2010), and Quaternary frontal arc lavas from the CVZ (see Chapter 3). Interpretations of fractionating phases (Gt=garnet; Amp=amphibole; PLG=plagioclase) responsible for trends observed are based on conclusions from Chapter 3 and (Van Westrenen et al., 1999; Kay and Kay, 2002; Garrison and Davidson, 2003; Macpherson et al., 2006; Davidson et al., 2007; Alonso-Perez et al., 2008).

San Cristobal lavas (66 Ma) have low Sr/Y, Sm/Yb and La/Yb ratios and high Y and Yb concentrations (Figure 46). San Cristobal lavas have increasing Y and Yb concentrations with increasing SiO_2 content, showing fractionation occurred in the shallow crust where HREEs are not compatible in the fractionating phases and thus become more enriched in the residual melt. Jurassic and Cretaceous Central Andean lavas occupy a similar field in Sr/Y and Sm/Yb plots as the San Cristobal lavas (Figure 46), and Quaternary SVZ lavas erupted through crust ~30 km thick (Chapter 3; Figure 25). Indicating that all these magmas underwent dominantly shallow crustal fractionation (<30 km depth). Segerstrom, Co. Chrisoteado and Cerro Buenos Aires form a data cluster at Y = ~20 ppm, Sr/Y = 20-25, and Yb = ~2, Sm/Yb = 2.5-3 (Figure 46). Samples from Cachiyuyo contain large hornblende phenocrysts (Figure 39), which corresponds to their higher Sr/Y, Sm/Yb and La/Yb ratios compared to other lavas sampled in this study (Figure 46). Cachiyuyo lavas may have undergone deeper initial fractionation and must have contained higher water contents than other samples. No interpretations are made for the two samples from Penacho Blanco, as we previously showed they have anomalous trace element compositions (Figure 42 & Figure 43).

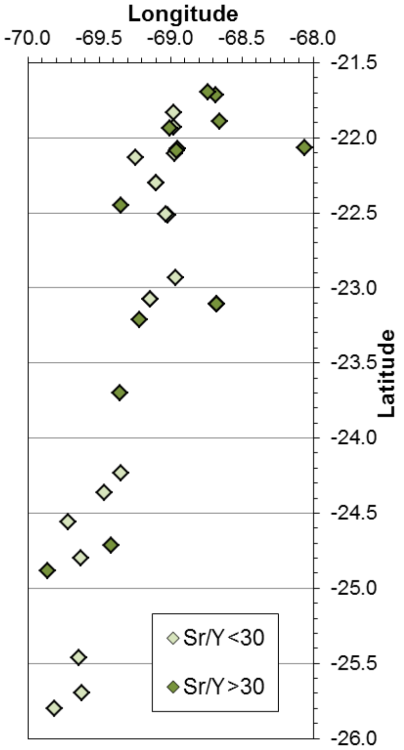

Figure 47: Plot showing no spatial trend between high and low Sr/Y ratios of Paleogene lavas (Haschke et al. 2002).

Central Andean Paleogene arc lavas from the data compilation have Sr/Y>30 and Sm/Yb>3 (Figure 46). Yet, elevated trace element ratio signatures in the Paleogene arc do not appear to define any spatial (Figure 47) or temporal trend, as might be expected if they resulted solely from crustal thickening processes. For example, Cachiyuyo lavas are dated as Early Paleogene 59 Ma (Zentilli et al., 1991; Arévalo, 1995), and younger samples such as Segerstrom (25 Ma; Mpodozis et al., 1996, 1995) have lower Sr/Y ratios. Only magmas which do not re-equilibrate at shallower depths in the crust will show a trace element signal of high pressure phases such amphibole or garnet in the resultant erupted lavas. The degree of melting will also affect trace element systematics, as smaller degree melts have steeper REE patterns than higher degree melts, and it is difficult to differentiate between such processes looking at trace element ratios alone.

5.1.1.10 *Europium anomalies and plagioclase fractionation*

Plagioclase is a dominant fractionating phase in intermediate magmas in the shallow crust (~<30 km), but is thought to be absent/unstable at higher pressures (e.g. Müntener and Ulmer, 2006 and references within, as discussed in Chapter 3). Like strontium, europium can take the form Eu^{2+} in reducing magmas and can substitute for Ca^{2+} in plagioclase. Plagioclase is the only major fractionating phase in andesitic-rhyolitic magmas that can incorporate significant amounts of Sr and Eu (e.g. Weill and Drake, 1973). Both elements are incompatible in the absence of plagioclase (e.g. >>30 km) and behave compatibly when plagioclase is the dominant fractionating phase (e.g. <<30 km). However, in oxidising magmas Eu takes the Eu^{3+} form and is not compatible. The Eu anomaly is an expression of the degree to which Eu is either enriched (Eu/Eu*>1, a 'positive' anomaly) or depleted (Eu/Eu*<1, a 'negative' anomaly) relative to Eu's neighbouring Rare Earth Elements (Sm and Gd) on a trace element spiderdiagram (e.g. Weill and Drake, 1973). Eu/Eu* value is calculated:

$$Eu/Eu^* = Eu_N \,/\, \sqrt{(Sm_N) \times (Gd_N)} \quad (1)$$

If a hypothetical magma crystallises plagioclase, most of the Eu will be incorporated into the plagioclase leading to a relative enrichment of Eu within the crystals and depletion in the residual magma. If the residual magma is separated from the plagioclase crystals and erupted, the resultant lava will display a negative Eu anomaly (e.g. Weill and Drake, 1973). A magma which has assimilated plagioclase or contains abundant plagioclase phenocrysts might have positive Eu/Eu* values.

Low Sr contents combined with very negative Eu anomalies in the San Cristobal lavas (Figure 48) could indicate shallow magma storage where plagioclase was crystallising. The hypothesis of shallow magma equilibration and plagioclase dominant fractionation also fits with a lack of HREE depletion in San Cristobal lavas (low Sr/Y, La/Yb and Sm/Yb ratios; Figure 46). Most other samples also have negative Eu anomalies although not to the same extent as San Cristobal lavas (Figure 48). Caution must be taken when interpreting Eu anomalies to plagioclase fractionation as it has been noted that Quaternary CVZ arc lavas commonly have very limited or no Eu anomalies, despite obvious evidence of significant plagioclase fractionation. Conditions under the current CVZ arc are thought to be too oxidising for Eu^{2+} to be stable, meaning Eu remains incompatible (Davidson and de Silva, 1995).

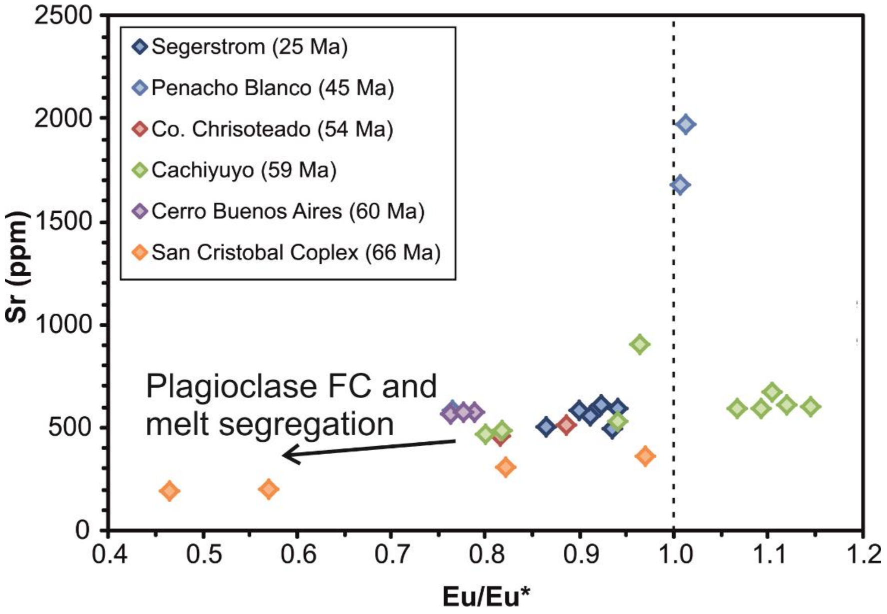

Figure 48: Europium Anomaly (Eu/Eu*) against Sr (ppm). San Cristobal lavas have very low Eu/Eu* anomalies, potentially indicating melt segregation after extensive plagioclase fractional crystallisation (FC). Five samples from the Cachiyuyo suite have positive Eu anomalies.

Five samples from the Cachiyuyo suite (AT17.1, AT17.2, AT16.1, AT16.4, AT16.6) have positive Eu anomalies (Figure 48). These are the five most mafic samples from the Cachiyuyo centre (51.8-60.7 wt. % SiO_2), excluding AT18.1 (56.75 wt. % SiO_2) which is the sample at ~0.96 Eu/Eu*. The five positive Eu/Eu* samples contain amphibole and clinopyroxene phenocrysts in thin section (Figure 39) and have elevated La/Yb, Sm/Yb and Sr/Y ratios and low Y and Yb concentrations. The more evolved Cachiyuyo lavas (with negative Eu/Eu*) also have high Al_2O_3 and Na_2O compared to other suites at similar SiO_2 contents (Figure 41), which could also be explained by plagioclase accumulation.

5.9.2 Andean end-member compositions

Blum-Oeste and Wörner (2016) identified three end-member compositions using polytopic vector analysis which they suggested explains the entire compositional range of Quaternary Central Andean magmatism. Their three endmembers are called: (1) a calc-alkaline basaltic andesite (BA); (2) an enriched basalt (EB); and (3) a high-K rhyodacite (RD). The two more mafic end-members (BA and EB) represent the variable compositions that recharge and/or mix with a rhyodacite magma (RD) suggested to be resident in the shallow portions of the thickened crust of the Andean Plateau (Blum-Oeste and Wörner, 2016). Quaternary CVZ lavas have a high degree of involvement with the enriched basalt end-member (Blum-Oeste and Wörner, 2016), which may originate from an enriched mantle source (Rogers and Hawkesworth, 1989; Kay et al., 2010; Turner et al., 2017), or source contamination by subduction erosion or subducted sediments (Stern, 1991; Plank and Langmuir, 1998; Kay et al., 2014), or melting of refractory cumulates in the thickened lower crust, potentially by foundering into the mantle wedge (>45 km; Ducea et al., 2013; Blum-Oeste and Wörner, 2016). The basaltic andesite (BA) end-member is suggested to originate from the mantle wedge due to its calc-alkaline character and was observed by Blum-Oeste and Wörner (2016) to be almost identical to high-Al basalts from Volcan San Pedro in the SVZ. They suggest the BA end-member is an evolved product typical of the sub-Andean mantle wedge (Blum-Oeste and Wörner, 2016). The end-members identified by Blum-Oeste and Wörner (2016) are thought to be ubiquitous of thick-crust settings, where mid-crustal melt ponding is common (such as the Altiplano-Puna Magma Body; Ward et al., 2014; Delph et al., 2017).

In this study, the CVZ endmembers identified by Blum-Oeste and Wörner (2016) are compared to the compilations created in Chapters 3 and 4 (Figure 49a). Quaternary CVZ lavas have much higher Sr contents for a given degree of fractionation than Quaternary SVZ lavas or Pre-Neogene Central Andean lavas (Figure 49a and Chapter 3). On both plots in Figure 49, two new endmembers are defined (red circles) which are tentatively suggested to encompass Quaternary SVZ and pre-Quaternary Andean compositions (although these should be constrained further by polytopic vector analysis in future work). These are a parent Basalt (Ba) and an Evolved Rhyolite (ER). The new Ba end-member is consistent with Blum-Oeste and Wörner's hypothesis that the Central Andean Basaltic Andesite (BA) end-member is derived from a typical sub-Andean mantle wedge parent but has undergone fractionation and contamination (Blum-Oeste and Wörner, 2016). Paleogene Central Andean arc lavas >55 wt. % SiO_2 generally follow a more Sr-enriched trend than Quaternary southern SVZ lavas or Jurassic-Cretaceous Central Andean lavas, but are still less enriched than most Quaternary CVZ lavas (Figure 49). As previously mentioned, San Cristobal lavas (~66 Ma) are more depleted in Sr compared to other Paleogene samples, and are more similar to older Cretaceous and Jurassic Central Andean lavas. Penacho Blanco and a scatter of other Paleogene samples from the Central Andean compilation (Haschke et al., 2002b) have very high Sr contents that seem to follow no particular overall trends. It is possible that the source of Central Andean lavas may be becoming more enriched (toward an EM1 end-member) over time (Kay et al., 2010). It has been suggested that the modern northern SVZ may have significant contributions from an enriched mantle source (Wieser et al., in review; Turner et al., 2017). Erosion of more enriched sub-continental lithosphere and incorporation into depleted mantle wedge melts would be enhanced during periods of crustal & lithospheric thickening. Such a mechanism could explain the progression toward the EB endmember over time in the Central Andes see in Figure 49.

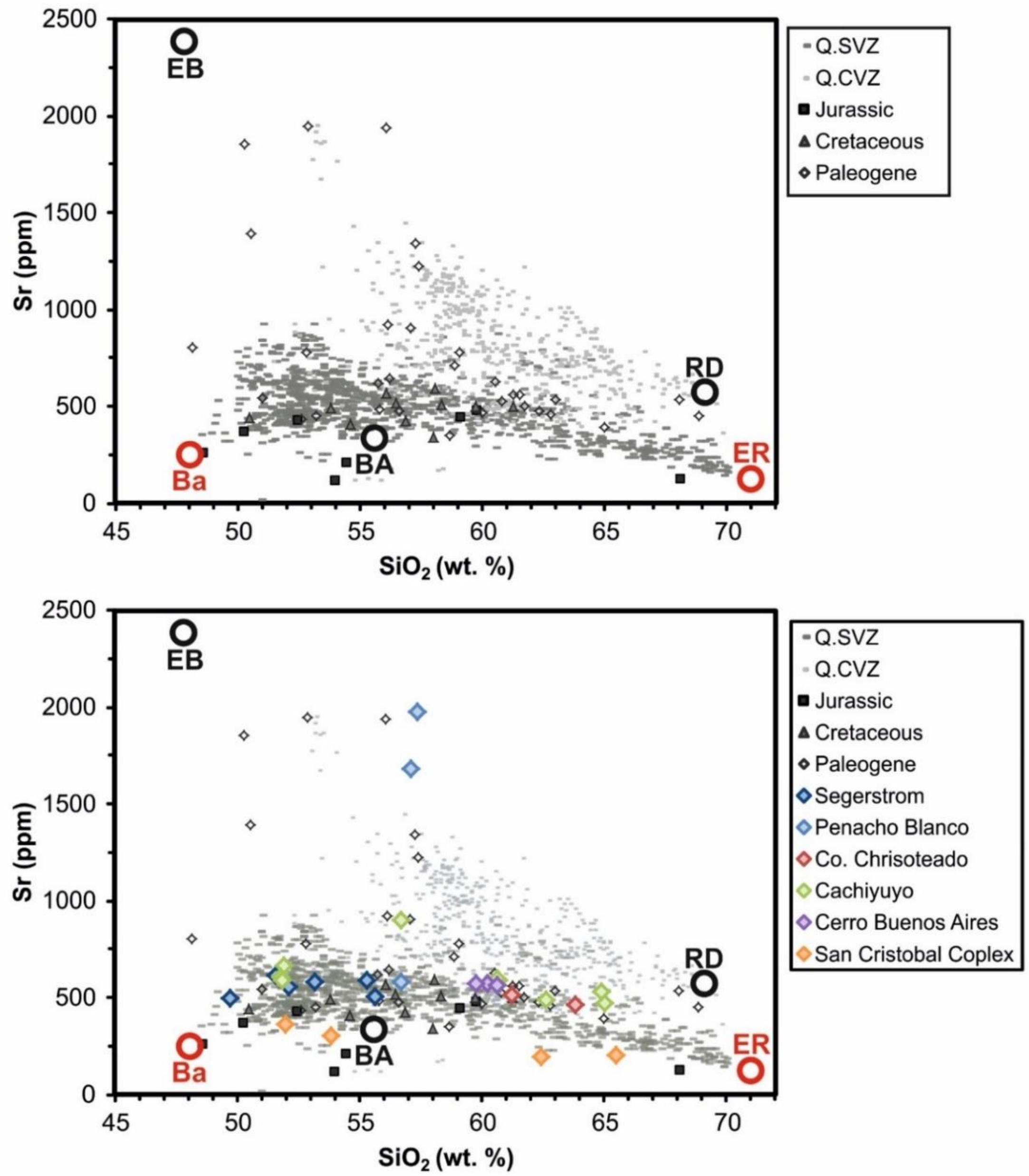

Figure 49: Sr vs. SiO_2 diagrams. Upper panel shows Quaternary SVZ (Q.SVZ) and Quaternary CVZ (Q.CVZ) Andean lavas (compilations of Chapter 3) alongside Central Andean Jurassic-Paleogene lavas (Mamani et al., 2010). Blum-Oeste & Worner's three end-member compositions for the Q.CVZ are: Enriched Basalt (EB), Basaltic Andesite (BA) and Rhyodacite (RD). The BA endmember is likely a fractionated derivative of the newly defined Basaltic parent (Ba), which encompasses more depleted Quaternary SVZ and Central Andean pre-Quaternary compositions. The new Evolved Rhyolite (ER) endmember represents the most evolved Q.SVZ compositions. Lower panel is the same as the upper panel with the addition of dated suites from this study.

5.9.3 Mixing, assimilation and fractional crystallisation

Crustal contamination is the process by which magma from the mantle wedge assimilates continental crust or mixes with *in situ* partially molten crust. The density and/or temperature contrast between the mantle and lower continental crust is thought to provide a stalling point which mantle melts cannot cross until they have undergone some degree of fractionation and/or crustal contamination. Zones of melt-crust interaction have been described in the literature as melting, assimilation, storage and homogenisation zones (MASH; Hildreth and Moorbath, 1988; Davidson et al., 1990; Delph et al., 2017) and lower crustal hot zones (Annen et al., 2006; Solano et al., 2012). Defining the mantle source in the Central Andes has remained contentious due to the lack of primitive magmas erupted (e.g. Wieser et al., in review; Davidson et al., 1990; Kay et al., 2010; Blum-Oeste and Wörner, 2016; Turner et al., 2017). Sr- and Nd-isotope compositions of both Enriched Mantle I (EMI) and Depleted Mantle (DM) endmembers were shown previously in Figure 45. Andean arc lavas have been suggested to have tapped a depleted mantle source since the Jurassic (since 200 Ma; Lucassen et al., 2005, 2006). However, Jurassic arc lavas have very unradiogenic $^{87}Sr/^{86}Sr_{(i)}$ ratios for a wider range of more radiogenic Nd isotope ratios, potentially indicating some degree of mantle source heterogeneity (Rossel et al., 2013; Figure 45).

The degree of crustal contamination can be estimated using assimilation and fractional crystallisation models (e.g. DePaolo, 1981), although such modelling requires constraints on the composition of both the melt source and contaminant. Results from such models are simplistic estimates as Sr concentrations and isotope compositions of initial parent magmas probably vary both spatially and temporally (as Discussed in the previous section). AFC models are used in this study to provide insight into the evolution of changing source and fractionation processes through time in the Central Andes. Two models were run with different starting compositions (Figure 50 & Figure 51). For each case, the sample with the least radiogenic $^{87}Sr/^{86}Sr(i)$ ratio was used as the starting isotope composition. This means that resultant contamination estimates represent the minimum degree of crustal contamination. Starting Sr compositions could be vary variable, as discussed in the previous section. Primitive and Depleted Mantle estimates of Sr concentrations range from ~10-90 ppm (Sun and McDonough, 1989; Salters and Stracke, 2004) and enriched mantle estimates are ~150 ppm (Sun and McDonough, 1989). Sr contents of slab fluids are extremely high due to the fluid mobile nature of Sr (>2000 ppm; Kogiso et al., 1997; Salters and Stracke, 2004). Sr concentrations for mantle-derived basaltic melts generally range from 200-550 ppm (e.g. DePaolo, 1981). We selected Sr=400-420 ppm as starting compositions as these are consistent with AFC models for Quaternary CVZ volcanics (Freymuth et al., 2015).

Late Cretaceous lower crustal xenoliths represent the composition of the basement for the Paleogene period, and are therefore appropriate to use as contaminants in AFC models for Paleogene Andean lavas. Lower crustal xenoliths found in Late Cretaceous rift magmatism of NW Argentina have been described by Lucassen et al. (1999, 2005). The Sr-Nd isotope compositions of these Late Cretaceous xenoliths are shown in Figure 45. Most xenoliths have been described to be granitoid in composition with quartz-plagioclase-garnet-rutile (±K feldspar) as the major mineral phases (Lucassen et al., 1999, 2005). Rare (<5 % of xenolith population) mafic xenoliths have plagioclase-clinopyroxene-garnet (±horneblende). Isotopic compositions of the xenoliths are indistinguishable from the Early Paleozoic metamorphic basement exposed in NW Argentina and Northern Chile (same as this study area), except for $^{208}Pb/^{204}Pb$ isotope compositions which are lower in the exposed basement (Lucassen et al., 1999). Sample A-112b (Lucassen et al., 1999) was chosen for lower crustal AFC models as it is the least radiogenic ($^{87}Sr/^{86}Sr_{(i)} = 0.708113$) and has the lowest Sr concentration (307 ppm) of the analysed xenoliths. It is therefore the best estimate of the more refractory lower crust. Note that the following models represent higher degrees of contamination than if more enriched contaminants (e.g. upper crustal xenoliths) were used, as more radiogenic contaminants would produce the same degree of isotopic enrichment in the melt with a lower degree of assimilation. Figure 50 shows the results for an AFC model representing potential sources and contaminants (as discussed) compared to the six main suites analysed in this study. A starting composition of Sr ~400 ppm fits with the Paleogene data, as San Cristobal lavas have decreasing Sr concentrations with increasing degrees of fractionation, while Segerstrom and Cachiyuyo lavas have increasing Sr concentrations with increasing degrees of fractionation (below 55 wt. % SiO_2; Figure 49). The Cachiyuyo lavas, which are the most isotopically depleted suite studied here, fit well with a model of fractional crystallisation in the lower crust where plagioclase fractionation is minimal and pyroxene and amphibole are the dominant fractionating phases (therefore $D_{Sr} < 1$). The relatively low $^{87}Sr/^{86}Sr(i)$ ratios of the Cachiyuyo suite indicate these lavas have undergone very limited to no mid- to upper-crustal contamination. Segerstrom, Co. Chrisoteado and Cerro Buenos Aires suites also fit with models of lower crustal fractional crystallisation, but unlike the Cachiyuyo lavas they include a higher component of lower crustal assimilation of 4-16%. All samples show signs of fractionation to some extent and no suite shows signs of pure mixing between our starting composition and the lower crustal xenolith end-member (Figure 50), which would be geologically unrealistic. San Cristobal lavas are the oldest suite studied here dated at 66 Ma. They have very negative Eu/Eu* anomalies (Figure 48) and become increasing depleted in Sr concentration with increasing SiO_2 (Figure 41 & Figure 49). The results of AFC models support the interpretation that San Cristobal lavas underwent plagioclase dominant fractional crystallisation (therefore $D_{Sr} > 1$) in the shallow crust (Figure 50).

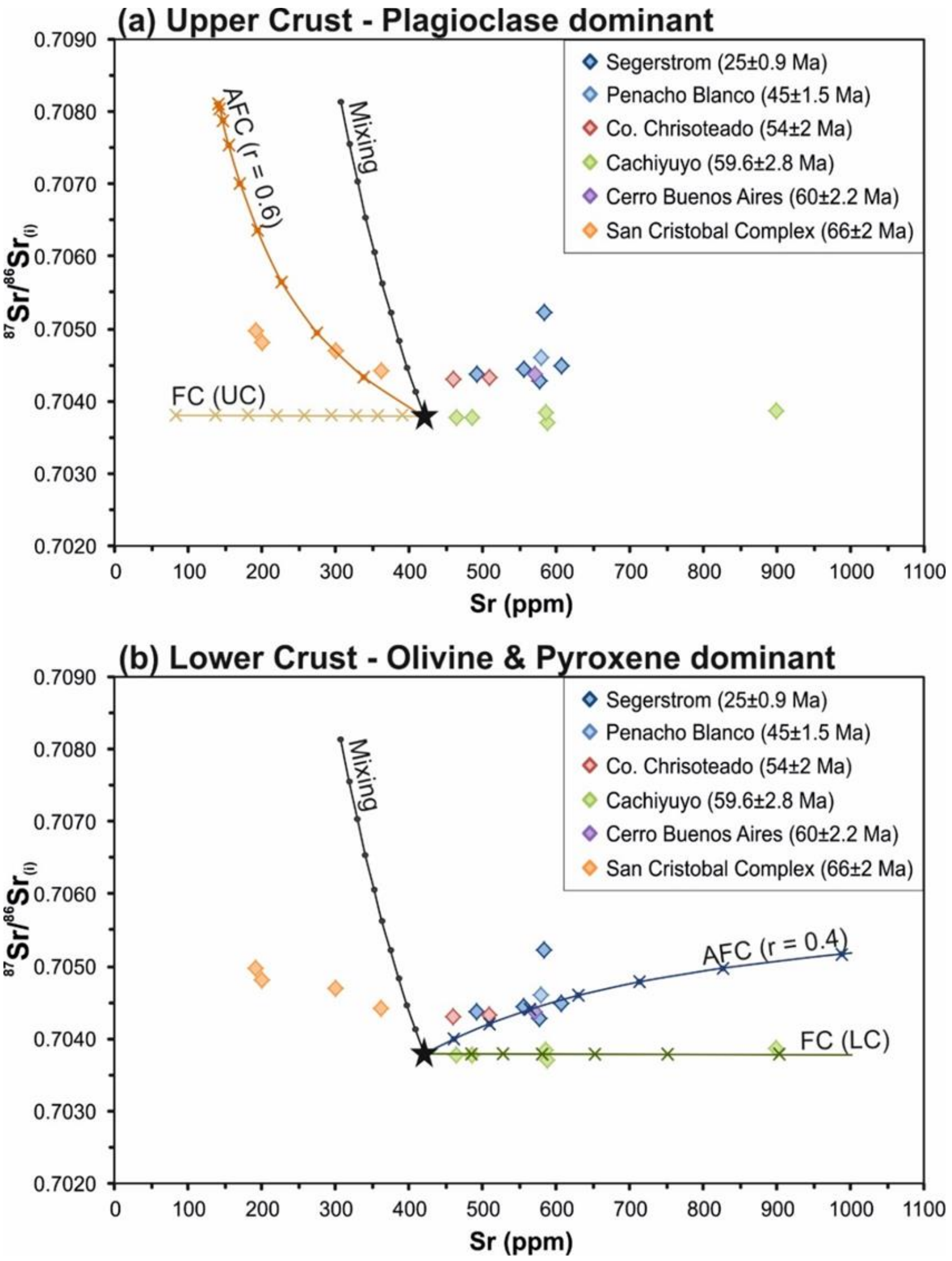

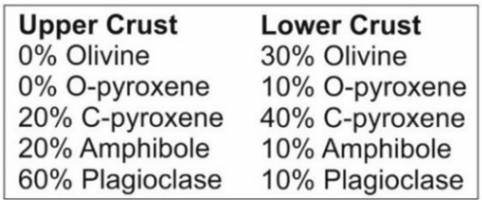

Upper Crust	Lower Crust
0% Olivine	30% Olivine
0% O-pyroxene	10% O-pyroxene
20% C-pyroxene	40% C-pyroxene
20% Amphibole	10% Amphibole
60% Plagioclase	10% Plagioclase

Figure 50: Fractional crystallisation (FC, crosses), assimilation and fractional crystallisation (AFC, crosses with dot) and mixing (dots) models of intermediate melts using the method and calculations of (DePaolo, 1981) and the computer programme of (Ersoy and Helvacı, 2010). A starting composition of $^{87}Sr/^{86}Sr=0.7038$ and Sr=420 ppm is used in consistency with AFC models of Quaternary CVZ lavas (Freymuth et al., 2015). Contaminant composition is set as lower crustal xenolith A-112b from Late Cretaceous rift related magmatism (Lucassen et al., 1999), as discussed in the main text. In all cases, markers on model lines indicate 10% intervals. For FC and AFC models, crystallisation ends at 90%. For AFC models, the r value sets the ratio of assimilation to FC. For example, r=0.4 means there is 4 parts assimilation to every 6 parts of fractional crystallisation. (a) shows models for shallow crustal, plagioclase dominant fractionation (therefore $D_{Sr} > 1$). (b) shows model results for lower crustal FC, where plagioclase is generally unstable and a minor fractionating phase (therefore $D_{Sr} < 1$).

The less radiogenic Jurassic-Cretaceous lavas cannot be explained by a starting composition of ^{87}Sr/^{86}Sr=0.7038 (Figure 51). Therefore a starting composition representing the least radiogenic Jurassic samples (^{87}Sr/^{86}Sr=0.7030) was used, which is similar to Depleted Mantle estimated compositions (^{87}Sr/^{86}Sr=0.7028; Salters and Stracke, 2004). Most Jurassic-Cretaceous lavas extend to lower Sr concentrations similar to the San Cristobal Complex (Sr <400 ppm; Figure 51). Jurassic Central Andean lavas are the least radiogenic, indicating a depleted source, while the Sr concentrations indicate plagioclase dominant fractionation less than <30 km depth. Such evidence is supported by pressure-temperature estimates from geochemical barometry of Late Cretaceous lower crustal xenoliths, which indicate relatively thin crustal thicknesses of ~36 km, assuming a 24° C/km geotherm (Lucassen et al., 2005). All Neogene (and Quaternary) Central Andean lavas plot in the top right hand of the Sr v ^{87}Sr/^{86}Sr(i) plot (Figure 51). Quaternary CVZ lavas and ignimbrites all have ^{87}Sr/^{86}Sr > 0.7055 and variable enriched Sr contents (Chapter 3). Variable Sr contents in CVZ volcanics reflect variable degrees of both plagioclase dominant fractionation in shallow magma bodies, such as the Altiplano-Puna Magma Body, and deeper fractionation where plagioclase is unstable (Godoy et al., 2014, 2017; Freymuth et al., 2015). It is therefore suggested that there is a switch in the dominant fractionating phase from the Late Cretaceous-Paleogene boundary. Jurassic-Cretaceous lavas have compositions indicative of plagioclase dominant fractionation (~<30 km), whereas Paleogene lavas younger than 66 Ma show evidence of deeper initial magma equilibration below the plagioclase stability field (~>30 km; Figure 51). Shallow storage and plagioclase fractionation may still overprint signals of deeper AFC in Paleogene-recent volcanic rocks.

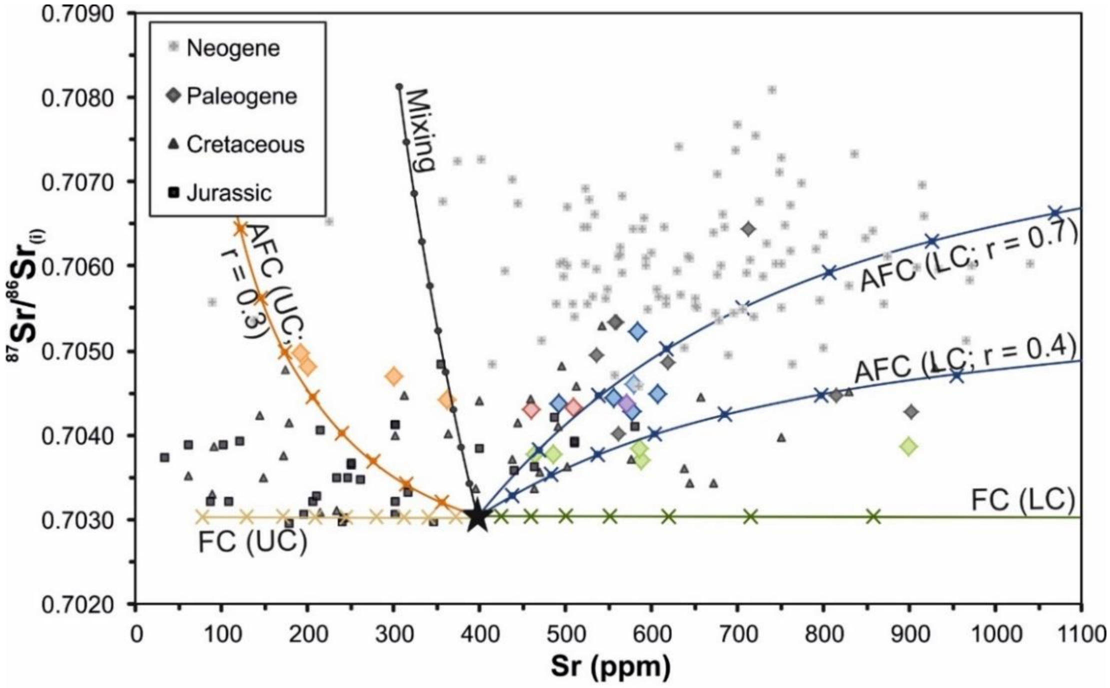

Figure 51: AFC model set up is the same as Figure 50, with a more depleted starting composition of ^{87}Sr/^{86}Sr=0.7030 and Sr=400 ppm to account for Jurassic compositions. Compilations of Jurassic, Cretaceous and Neogene Central Andean lavas (Mamani et al., 2010) are added for comparison.

5.9.4 Fluid interaction and subduction components

Nb and Ta depletion seen on multi-element spiderdiagrams (Figure 42 & Figure 43) is typical in arc magmas as both fluid immobile elements are retained in accessory phases (such as oxides) in the down-going slab. Nb and Ta depletion relative to light REE concentrations are often termed subduction signatures. Cachiyuyo lavas show strong signs of containing a high proportion of slab fluid component or subduction component, as they have low Nb contents and high La/Nb ratios (Figure 52). Cachiyuyo lavas also have high Ba/Zr ratios and low Th/Zr ratios, which supports the hypothesis that these lavas had a high slab fluid component and relatively minimal crustal interaction (e.g. low Rb and Th concentrations and depleted isotope ratios; Figure 44 & Figure 45). In contrast, Segerstrom lavas have lower La/Nb ratios indicating a smaller slab fluid component. This is consistent with the hypothesis of Kay et al. (2014), that Segerstrom lavas were generated from smaller degrees of slab-derived fluids fluxing into the mantle wedge in a 'proximal back-arc' setting.

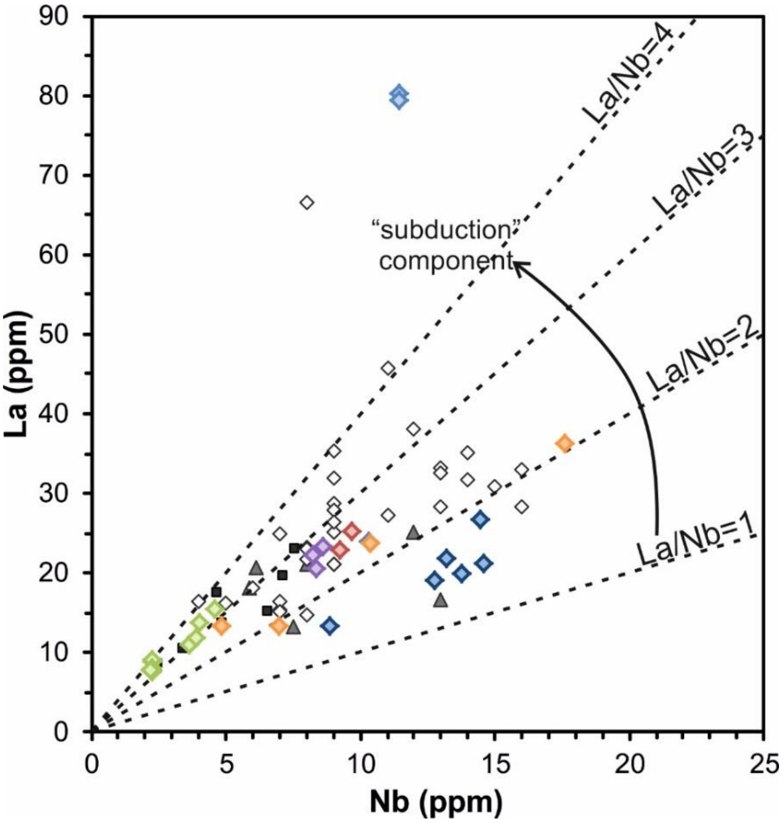

Figure 52: Nb vs La plot with lines representing set La/Nb ratios. Symbols are the same as previous plots.

5.10 Paleogene Central Andean tectonic setting

Sr and Nd radiogenic isotope compositions of Central Andean lavas have become gradually more radiogenic over time (Figure 45, Figure 53; Chapter 4). Many studies have shown that the changing geochemistry of Andean arc lavas over time correlates well with Andean crustal thickening history (e.g. Coira et al., 1982; Rogers and Hawkesworth, 1989; Kay et al., 1991, 2014; Haschke et al., 2002b; Mamani et al., 2010; Garzione et al., 2017). In Chapter 4 it is discussed how the relationships between Sr- and Nd-radiogenic isotope compositions and crustal thickness can be linked to elevation through the principal of isostasy (Scott et al., 2018). However, a previous lack of data for the Paleogene arc meant inferences on crustal thickening and surface uplift from the Late Cretaceous-Paleogene were based mainly on extrapolation. Figure 53 shows new data for the Paleogene arc from this study combined with the compilation of Scott et al. (2018) presented in Chapter 4. Paleogene arc rocks have $^{87}Sr/^{86}Sr_{(i)}$ ratios between 0.704-0.705 and $^{143}Nd/^{144}Nd_{(i)}$ ratios from 0.5129-7. In comparison, Quaternary central Andean lavas have isotope ratios of >0.705 and <0.5125, respectively (see Chapters 3 & 4). Current NSVZ arc lavas have isotope ratios ranging between 0.7038-0.706 for Sr and 0.5129-0.5125 for Nd. These isotope ratios are more radiogenic (crustal) than the Jurassic-Cretaceous periods, but less radiogenic (mantle like) than the more recent Neogene period. Sr- and Nd-isotope ratios of Paleogene arc lavas indicate paleo-elevations between 1400-2600 ± 570 m based on the calibrations presented in Chapter 4 (Figure 53; Scott et al., 2018).

As discussed in Chapters 2 & 4, the Central Andes is known to have been below sea level for extensive periods in the Jurassic-Cretaceous (Coira et al., 1982; Buchelt and Cancino, 1988; Lamb et al., 1997; Wotzlaw et al., 2011; Horton, 2018a). Intercalations of shallow marine fossil-containing sediments separate Jurassic to Early Cretaceous arc lavas (Buchelt and Cancino, 1988). Thick packages of both shallow marine and continental sediments were deposited in Early Cretaceous back-arc basins (Coira et al., 1982). In the Early- to Mid-Cretaceous, there was a period of localised extension and crustal thinning as the Salta rift developed at the current location of the Eastern Cordillera-Santa Barbara system, coincident with opening of the South Atlantic (130-120 Ma; Horton, 2018). A switch from post-rift subsidence to retro-arc shortening in the Late Cretaceous is evident from the development of fold and thrust systems observed in the Coastal Cordillera and Chilean Precordillera and deposition of conglomerates and non-marine sediments in the associated developing foreland basin (Arriagada et al., 2006b; Horton, 2018b). A period of southward migrating magmatic quiescence and eastward expansion of arc magmatism from ~50-40 Ma (Southern Altiplano-Northern Puna area) and 45-25 Ma (Puna-Southern Puna) has been used to infer periods of flat slab subduction, as discussed in Chapter 2 (Jordan et al., 1983b; Kley et al., 1999; Haschke et al., 2002b; Kay and Mpodozis, 2002; Ramos and Folguera, 2009; Goss et al., 2013; Kay et al., 2014). Southward migration of deformation and the flat slab are associated with the southward passage of the

Juan-Fernandez ridge (Jordan et al., 1983b; Kay et al., 1991; Ramos and Folguera, 2009; Freymuth et al., 2015; de Silva and Kay, 2018). Over the same time periods, increased rates of crustal shortening led to the formation of a bivergent thrust system, with deformation expanding into the Eastern Cordillera (McQuarrie et al., 2005; Elger et al., 2005; Oncken et al., 2006; Barnes and Ehlers, 2009; Garzione et al., 2017).

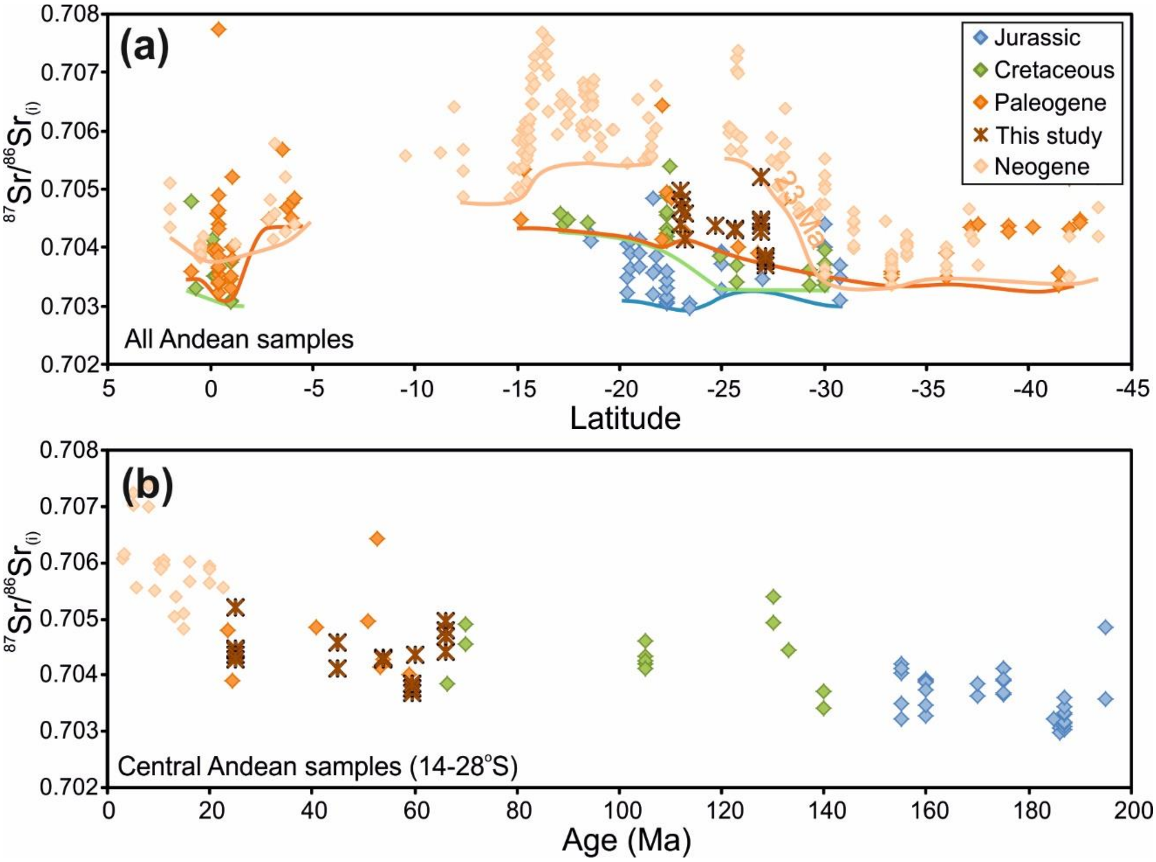

Figure 53: New isotope data for the Paleogene arc combined with Central Andean data from the isotope compilation of Scott et al. (2018), presented in Chapter 4.

Results from trace element systematics, petrological modelling and radiogenic isotope compositions of the Central Andean arc are therefore consistent with geological evidence and sediment providence data of initiation of crustal thickening and uplift in the Western Cordillera from the Late Cretaceous-Paleogene (Horton et al., 2001; McQuarrie et al., 2005; Carrapa et al., 2006; Barnes and Ehlers, 2009; Wotzlaw et al., 2011; Decou et al., 2013; Garzione et al., 2017; Horton, 2018b). Paleogene lavas also do not reach the distinct, ‘crust-like’ compositions of Neogene-recent Central Andean lavas, which are inferred to be related to the >60 km thick crust of the Andean Plateau.

5.11 Summary and conclusions

- A detailed petrological and geochemical study of the previously under-analysed Central Andean Paleogene arc provides new insights into the tectonic setting and timing of crustal thickening and uplift in the Western Cordillera.
- A switch from plagioclase dominant fractionation in the shallow crust (<~30 km) before ~66 Ma, to deeper crustal amphibole and pyroxene dominant fractionation (>~30 km) after ~60 Ma is identified from assimilation and fractional crystallisation models and increasing Sr/Y, La/Sm and Sm/Yb ratios.
- The petrological switch corresponds to a tectonic regime change in the Central Andes, from the Salta Rift phase in the Late Jurassic-Early Cretaceous to retroarc shortening from the Late Cretaceous-Paleogene. The thin crust in the Central Andes immediately after the Salta Rift phase explains the predominant evidence of shallow (<30 km depth) plagioclase fractionation in lavas >66 Ma.
- Further evidence of crustal thickening comes from Sr and Nd isotope systems, which become increasingly radiogenic both northward and with decreasing age consistent with previous models of southward propagation of crustal thickening over time. Sr- and Nd-isotope compositions of the Paleogene arc could indicate Western Cordillera paleo-elevations ranging between 1400-2600 ± 570 m based on the model of Scott et al. (2018), shown in Chapter 4.
- Paleogene lavas do not reach the enriched, 'crust-like' compositions of Neogene-recent Central Andean lavas, which are related to the >70 km thick crust of the Andean Plateau. Trace element signatures of Paleogene lavas do not show evidence of magma equilibration in the garnet stability field (>35-45 km), unlike Neogene-recent volcanics.
- Central Andean Paleogene arc petrology and geochemistry are consistent with geological evidence of the onset of crustal thickening in the Western Cordillera during the early Paleogene (66-60 Ma). Crustal thicknesses are suggested to increase from <30 km thick in the Jurassic-Cretaceous to ~35-45 km through the Early Paleogene.

Chapter 6: Synthesis, conclusions and future work

6.1 Synthesis and conclusions

6.1.1 A new causative mechanism related to the onset of Andean shortening and thickening

Present day observations: Oceanic plate age along the Andean margin currently ranges between 0-60 Myr. High degrees of plate coupling with a high density of mega-thrust events at the Nazca-South America plate interface occur only where the slab age at the trench is older than >30 Myr or where oceanic plateaux or aseismic ridges are being subducted. In Southern Chile, where the slab is younger than 30 Myr, we note there is a lack of seismicity at the plate interface or within the slab at depth. These results are summarised in Figure 54. A very strong positive correlation exists between overriding plate thickness (along a trench-parallel profile distanced 300 km from the trench) and slab age ($r = 0.939$; $r^2 = 0.882$; p value < 0.01).

Importance of intermediate aged slabs: Young slabs have a consistently thin elastic thickness (Zhang et al., 2018), and are relatively hot and weak. The lack of seismicity in slabs <30 Myr could be explained by the plate deforming plastically or by stable sliding. The high number of fracture zones and thick sediment accumulation at the trench in the southern Andes increase weakening of the young slab in the southern Andes. For intermediate slab ages (~30-80 Myr) the elastic thickness (T e-slab) of the oceanic plate is great enough that the slab increases in mechanical strength and becomes resistant to bending (Hu et al., 2016), but the still relatively young age means intermediate slabs are still buoyant compared to older slabs. In slabs older than ~80 Myr, the greater negative buoyancy can overcome the resistance to bending, allowing the slab to descend into the mantle more steeply or to be more easily influenced by mantle flow.

Distribution of oceanic plate age entering the trench through time: Slab ages entering the trench along the entire Andean margin have been younger than 80 Myr since the Jurassic. In the Southern Andes, between 33-42° S, ocean plate ages entering the trench have remained dominantly younger than 40 Myr for the last 170 Ma of subduction. In the Central Andes, from 170-80 Ma (Jurassic-Cretaceous), slab ages entering the trench were consistently younger than 40 Myr in age. Bordering the northern Altiplano (at ~12° S) the slab entering the trench became older than 40 Myr at ~90 Ma; by the Arica Bend (~20° S) slab age became older than 40 Myr at ~60 Ma; and by the Puna (at ~27° S) the slab age became older than 40 Myr between 50-40 Ma (Seton et al., 2012; Maloney et al., 2013).

Correspondence of subduction of intermediate age slabs with Andean deformation history: The dates corresponding to onset of subduction of intermediate aged slabs match with timings related to the onset of compressional deformation in the Central Andes between 70-50 Ma (McQuarrie et al., 2005; Oncken et al., 2006; Barnes and Ehlers, 2009; Garzione et al., 2017). The Altiplano segment has been exposed to subduction of intermediate aged slabs for the greatest length of time and we suggest that this could explain why the degree of crustal shortening is greatest in the Altiplano region, inboard of the Arica bend (~420 km; McQuarrie, 2002; Schepers et al., 2017). Land-ward trench migration due to subduction of a stronger and more resistive slab could explain paleo-magnetic rotation data from the Andean fore-arc which indicates that the concave margin developed from ~70 Ma, synchronous with and accommodated by shortening in the Eastern Cordillera and Sub-Andean belt (Arriagada et al., 2006b, 2008; Schepers et al., 2017). The strong positive correlation between slab age and crustal thickness can therefore be attributed to increased plate coupling and overriding plate compression associated with long term subduction of intermediate aged slabs (~30-80 Myr) combined with seaward overriding plate motion.

6.1.2 Crustal thickness controls on Quaternary Andean arc compositions

Andean lavas within the CVZ and SVZ have trace element ratios (e.g. Sr/Y and La/Yb) which are strongly influenced by increasing crustal thickness, and not by increasing slab temperature which would be expected by the slab melt hypothesis. Changing the crustal thickness affects the depth magmas at which magmas are initially stored (e.g. Hildreth and Moorbath, 1988), and the pressure they are stored at influences the phases present in the fractionating assemblages (Kay et al., 1991; Garrison and Davidson, 2003; Macpherson et al., 2006; Alonso-Perez et al., 2008; Chiaradia, 2009, 2015; Davidson et al., 2013; Chapman et al., 2015a; Profeta et al., 2015b). These relationships are shown schematically in Figure 54 and the top panel of Figure 55. Strong correlations are found between increasing crustal thickness (and by cross correlation slab age and elevation) and increasing enrichment of $^{143}Nd/^{144}Nd$, $^{87}Sr/^{86}Sr$, K_2O, La, and increasing SiO_2 contents, which emphasise the importance of increasing crustal thickness on increasing residence times of arc magmas within the crust, which in turn increase the minimum degree of fractionation and crustal contamination seen at each volcano (Hildreth and Moorbath, 1988; Davidson et al., 1990; Kent et al., 2010; Freymuth et al., 2015; Farner and Lee, 2017). Results do not preclude suggestions for source contamination such as forearc subduction erosion, delamination or continental lithosphere erosion by mantle corner flow, which probably become increasingly important processes in thickened Cordilleran orogens (Kay et al., 1991; Stern, 1991; Tao and O'Connell, 1992; Kay and Kay, 1993; Rudnick, 1995; Currie et al., 2015; Turner et al., 2017).

Central Andes (23° S)

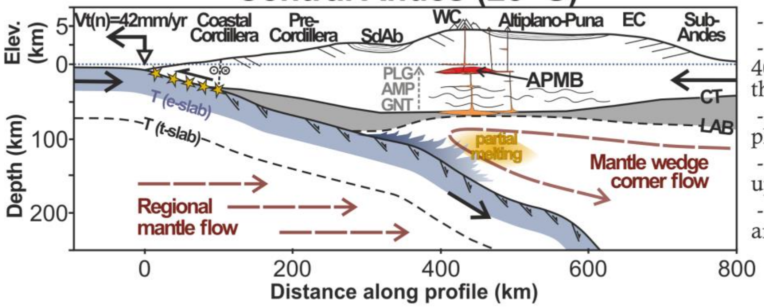

- Current slab age: **51 Myr**
- Slab age entering the trench was between 40-80 Myr from 60-50 Ma, and younger than 40 Myr from 200-60 Ma
- Current high density of thrusts at the plate interface and slab extension at depth
- Crustal thickness in the overriding plate up to 65 km and relatively thin lithosphere
- Arc geochemistry is 'distinctly-crustal' and trace elements evidence garnet FC.

Chilean flat slab (29° S)

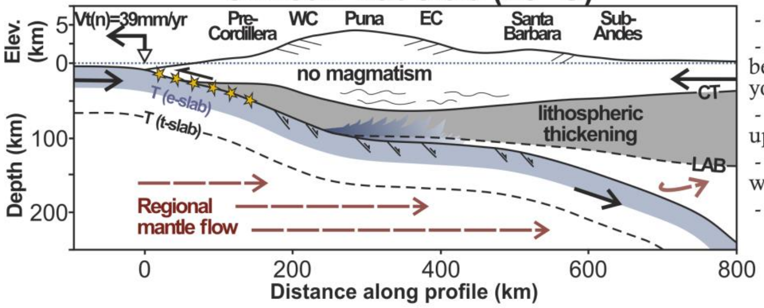

- Current slab age: **45 Myr**
- Slab age entering the trench was between 40-80 Myr from 50-40 Ma, and younger than 40 Myr from 200-50 Ma
- Crustal thickness in the overriding plate up to ~55 km and a thickened lithosphere
- Thickened lithosphere generates mantle wedge suction and slab shallowing
- No active volcanism

Northern SVZ (35° S)

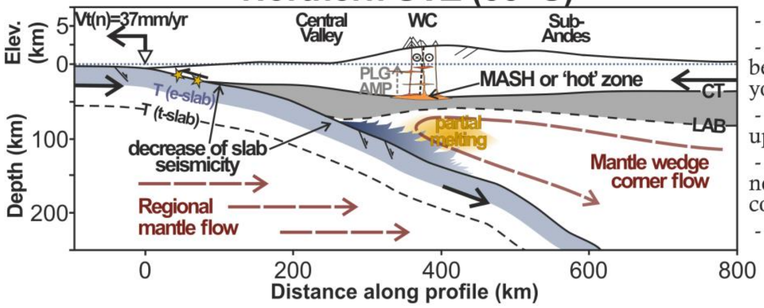

- Current slab age: **34 Myr**
- Slab age entering the trench was between 40-60 Myr from 30-10 Ma, and younger than 40 Myr from 200-30 Ma
- Crustal thickness in the overriding plate up to ~50-55 km
- NSVZ compositions approach (but do not reach) evolved and enriched CVZ compositions
- Evidence of garnet &/or amphibole FC

South-Central SVZ (39° S)

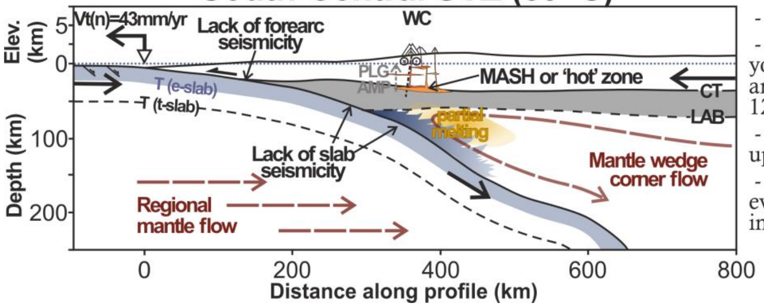

- Current slab age: **29 Myr**
- Slab age entering the trench has been younger than 40 Myr for the last 120 Ma, and was between 40-50 Myr old before 120 Ma.
- Crustal thickness in the overriding plate up to ~25-30 km. Lack of slab seismicity.
- NSVZ compositions are the least evolved or enriched in the study area and indicate shallow, plagioclase dominant FC

Figure 54: Summary of the modern Andean subduction zone, drawing on conclusions from Chapters 2 and 3. Schematic cross sections (to scale), with a vertical exaggeration on elevation profiles of x10. Overriding plate smoothed elevation, crustal thickness (CT), lithosphere-asthenosphere boundary (LAB) and slab surface data are from the models of Tassara and Echaurren (2012). Oceanic lithosphere thickness (T, t-slab) and elastic thickness (T, e-slab) are from the SubMap database (Heuret and Lallemand, 2005a; see also McKenzie et al., 2005), both thicknesses are a function of the slab age, which decreases from north to south. The normal components of trench velocity (Vt(n)) are in the HS3 reference frame; Gripp and Gordon, 2002). Yellow stars represent the shallow thrust seismicity and normal faults in the lower portion of the slab north of 38° S represent the extensional seismicity within the slab. Estimates of the stability fields of plagioclase, amphibole and garnet with the overriding crust are labelled.

6.1.3 Radiogenic isotopes, crustal thickening and uplift

A new method is proposed to constrain regional Andean surface uplift in the Western Cordillera (Scott et al., 2018), based on the findings that $^{87}Sr/^{86}Sr$ and $^{143}Nd/^{144}Nd$ ratios of Andean arc lavas are strongly influenced by crustal thickness, and that crustal thickness and elevation are strongly correlated along the active volcanic arc due to isostacy (Appendix 8.2). The resultant regional paleo-elevation model and crustal thickening history correspond with independent geological evidence, and both are summarised in Figure 55.

Furthermore, a detailed geochemical investigation of the Central Andean Paleogene arc (66-23 Ma) reveals a 'petrological switch' at the Late Cretaceous-Paleogene boundary. Incompatible behaviour of Sr, low Sr/Y ratios and very negative Eu anomalies indicate that plagioclase was dominant in the early fractionating phase of Central Andean lavas older than 66 Ma. Paleogene Central Andean lavas younger than ~60 Ma have higher Sr/Y and La/Yb ratios and fit AFC models of amphibole-pyroxene dominant fractionation, which indicate magma equilibration occurred below the plagioclase stability field. The petrological switch corresponds to a tectonic regime change in the Central Andes, from the Salta Rift phase in the Late Jurassic-Early Cretaceous to retroarc shortening from the Late Cretaceous to Paleogene (shown in Figure 55). The thin crust in the Central Andes immediately after the Salta Rift phase explains the predominant evidence of shallow fractionation of plagioclase (~<30 km depth) in lavas older than 66 Ma. Further evidence of crustal thickening comes from Sr and Nd isotope systems, which become increasingly radiogenic both northward and with decreasing age consistent with previous models of southward propagation of crustal thickening over time. Such changes in petrology and geochemistry at the Late Cretaceous-Paleogene boundary support geological evidence indicating the onset of crustal thickening and uplift in the Western Cordillera by the early Paleogene (~66-60 Ma).

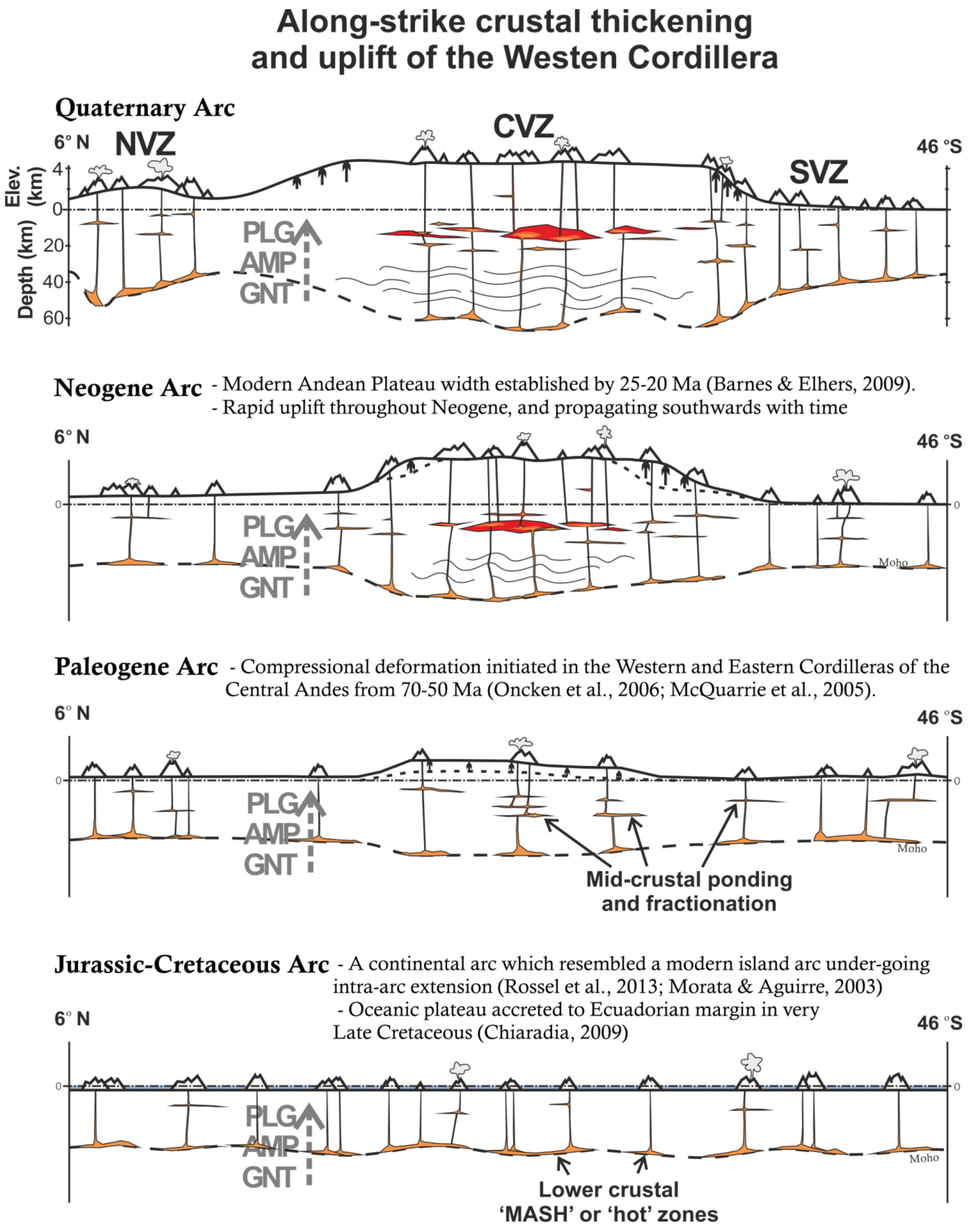

Figure 55: A schematic diagram which synthesises results of interpretations of along-strike variability in crustal thickening and uplift over time presented in Chapters 4 and 5.

6.2 Future work

6.2.1 Numerical modelling of relationships between slab age and overriding plate crustal thickening

Thermomechanical numerical models of subduction using the ASPECT (Advanced Solver for Problems in Earth's ConvecTion; https://aspect.geodynamics.org/) code could be used to test the hypotheses presented in Chapter 2. The use of ASPECT for modelling subduction has been described and benchmarked by Glerum et al. (2018), for example Figure 56.

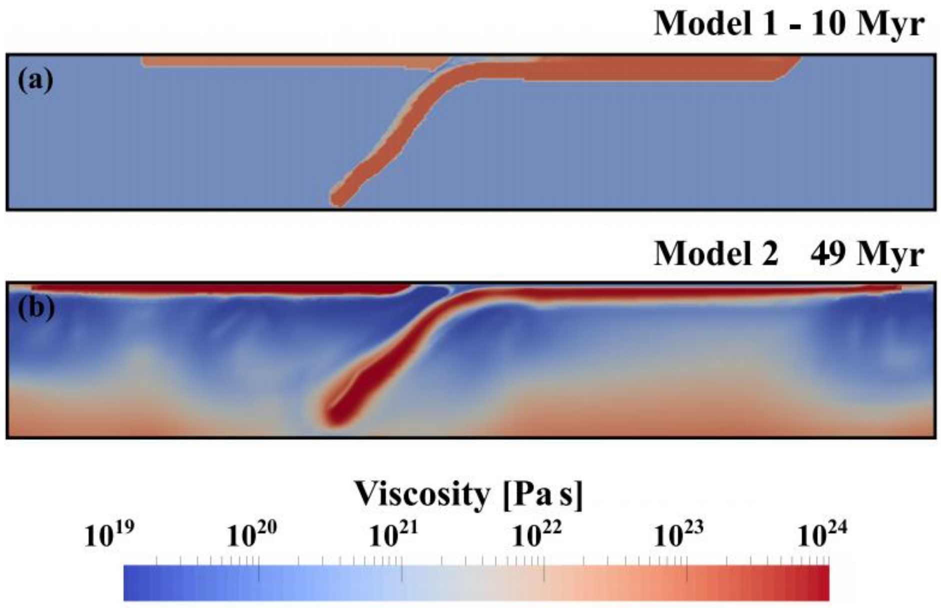

Figure 56: An example of a 2-D numerical model of subduction using the ASPECT code, taken from Glerum et al. (2018).

A 2-D or 3-D model could be set up which initially replicates the early Andean subduction system (e.g. in the Jurassic to Cretaceous). The overriding plate would represent a thin continental plate with a potential area of strain weakening in the back arc representing lithospheric weaknesses related to the Salta Rift phase in the Late Cretaceous. A westward imposed motion of the overriding plate could be set up in the code to replicate observed trench-ward motion of the South American plate over the last 100 Ma. This could be done by generating a super-plume in the lower mantle to the east of the plate (simulating the mid-Atlantic ridge). The key component of the model would be to set the slab age to change over time in accordance with the distribution of slab ages which entered the Andean trench identified from plate reconstructions (Seton et al., 2012). The result of the model could identify if long term subduction of intermediate aged slabs (between ~40-80 Myr) does in fact induce thickening in the overriding plate as we have proposed. It would also be interesting to see if changing the age of the slab entering the trench affects subduction dynamics at depth. For example, if slab dynamics are different when the oceanic lithosphere gradually increases or decreases during the course of subduction.

6.2.2 In depth statistical analysis of recent Central Andean magmatism: Rates, volumes, locations and compositions

Volcanic arcs can display significant heterogeneities in eruption timescales, volumes and compositions both along-strike and through time (Kirsch et al., 2016; Brandmeier and Wörner, 2016). The causes for such volcanic diversity, especially in segments where crustal thickness and slab parameters are similar (such as within the Central Volcanic Zone), are relatively unknown. Integration of geophysical and geochemical datasets is key to further understandings of arc processes, and the use of rigorous statistics to synthesise such 'big data' compilations can be used as a tool to identify statistically significant variations (Pitcher and Kent, in review). Results presented in Chapter 3 could be vastly improved with more rigorous statistical methods and a new, updated geochemical compilation for the Central Volcanic Zone. For example:

Andesite filter: An andesite range filter (filtering arc front volcanoes to only 57-63 wt. % SiO_2) could be developed which could be used to better constrain the variability in seen in Sr/Y and La/Yb ratios. This filtering method would have to include a method to reduce sampling bias, such as:

Weight bootstrap Monte-Carlo approach: Statistical techniques can be devised to minimise inherent sampling biases in geochemical datasets. A combination of bootstrap resampling (iterative random sampling of a population) with Monte-Carlo repetition ($n>10\,000$) can be used to increase the likelihood that the mean and standard deviation of the sample set accurately represent that of the entire population (Pitcher and Kent, in review). For example, under-sampled volcanoes or regions can be given a higher probability of being selected and inverse for over-sampled regions. Pitcher and Kent (in review), developed this technique to track compositional variability along the Cascades subduction system. A similar approach could be employed using the datasets generated for the Andes in this study.

Digital mapping techniques: Statistically robust geochemical datasets for volcanic centres could then be combined with digital mapping techniques to track compositional variations over space and time. Such techniques have been developed to map ignimbrite compositions and volumes in the Central Andes (Brandmeier and Wörner, 2016), but have not yet been used to track compositional variability and migration of frontal arc stratovolcanoes. The Andes are particularly well suited for digital mapping and a spatio-temporal study of recent arc products due to their high level of preservation in an arid climate.

7 References

Adam, J., Turner, S., and Rushmer, T., 2016, The genesis of silicic arc magmas in shallow crustal cold zones: Lithos, v. 264, p. 472–494, doi:10.1016/j.lithos.2016.07.036.

Aitcheson, S.J., Harmon, R.S., Moorbath, S., Schneider, A., Soler, P., Soria-Escalante, E., Steele, G., Swainbank, I., and Wörner, G., 1995, Pb isotopes define basement domains of the Altiplano, central Andes: Geology, v. 23, p. 555–558, doi:10.1130/0091-7613(1995)023<0555:PIDBDO>2.3.CO;2.

Allen, M.B., Walters, R.J., Song, S., Saville, C., De Paola, N., Ford, J., Hu, Z., and Sun, W., 2017, Partitioning of oblique convergence coupled to the fault locking behavior of fold-and-thrust belts: Evidence from the Qilian Shan, northeastern Tibetan Plateau: Tectonics, v. 36, p. 1679–1698, doi:10.1002/2017TC004476.

Allibon, J., Monjoie, P., Lapierre, H., Jaillard, E., Bussy, F., Bosch, D., and Senebier, F., 2008, The contribution of the young Cretaceous Caribbean Oceanic Plateau to the genesis of late Cretaceous arc magmatism in the Cordillera Occidental of Ecuador: Journal of South American Earth Sciences, v. 26, p. 355–368, doi:10.1016/j.jsames.2008.06.003.

Allmendinger, R.W., Jordan, T.E., Kay, S.M., and Isacks, B.L., 1997, The Evolution of the Altiplano-Puna Plateau of the Central Andes: Annual Review of Earth and Planetary Sciences, v. 25, p. 139–174, doi:10.1146/annurev.earth.25.1.139.

Alonso-Perez, R., Müntener, O., and Ulmer, P., 2008, Igneous garnet and amphibole fractionation in the roots of island arcs: experimental constraints on andesitic liquids: Contributions to Mineralogy and Petrology, v. 157, p. 541, doi:10.1007/s00410-008-0351-8.

Annen, C., Blundy, J.D., and Sparks, R.S.J., 2006, The Genesis of Intermediate and Silicic Magmas in Deep Crustal Hot Zones: Journal of Petrology, v. 47, p. 505–539, doi:10.1093/petrology/egi084.

Annen, C., and Sparks, R.S.J., 2002, Effects of repetitive emplacement of basaltic intrusions on thermal evolution and melt generation in the crust: Earth and Planetary Science Letters, v. 203, p. 937–955, doi:10.1016/S0012-821X(02)00929-9.

Arévalo, C.V., 1995, Mapa Geologico de la Hoja Copiapo, Region de Atacama: Servicio Nacional de Geologia y Mineria Carta Geologica de Chile.

Armijo, R., Lacassin, R., Coudurier-Curveur, A., and Carrizo, D., 2015, Coupled tectonic evolution of Andean orogeny and global climate: Earth-Science Reviews, v. 143, p. 1–35, doi:10.1016/j.earscirev.2015.01.005.

Arriagada, C., Cobbold, P.R., and Roperch, P., 2006a, Salar de Atacama basin: A record of compressional tectonics in the central Andes since the mid-Cretaceous: Tectonics, v. 25, doi:10.1029/2004TC001770.

Arriagada, C., Roperch, P., Mpodozis, C., and Cobbold, P.R., 2008, Paleogene building of the Bolivian Orocline: Tectonic restoration of the central Andes in 2-D map view: Tectonics, v. 27, doi:10.1029/2008TC002269.

Arriagada, C., Roperch, P., Mpodozis, C., and Fernandez, R., 2006b, Paleomagnetism and tectonics of the southern Atacama Desert (25–28°S), northern Chile: Tectonics, v. 25, p. TC4001, doi:10.1029/2005TC001923.

Assumpção, M., Feng, M., Tassara, A., and Julià, J., 2013, Models of crustal thickness for South America from seismic refraction, receiver functions and surface wave tomography: Tectonophysics, v. 609, p. 82–96, doi:10.1016/j.tecto.2012.11.014.

Barnes, J.B., and Ehlers, T.A., 2009, End member models for Andean Plateau uplift: Earth-Science Reviews, v. 97, p. 105–132, doi:10.1016/j.earscirev.2009.08.003.

Barth, M.G., Foley, S.F., and Horn, I., 2002, Partial melting in Archean subduction zones: constraints from experimentally determined trace element partition coefficients between eclogitic minerals and tonalitic melts under upper mantle conditions: Precambrian Research, v. 113, p. 323–340, doi:10.1016/S0301-9268(01)00216-9.

Bercovici, D., 2003, The generation of plate tectonics from mantle convection: Earth and Planetary Science Letters, v. 205, p. 107–121, doi:10.1016/S0012-821X(02)01009-9.

Best, M.G., Barr, D.L., Christiansen, E.H., Gromme, S., Deino, A.L., and Tingey, D.G., 2009, The Great Basin Altiplano during the middle Cenozoic ignimbrite flareup: insights from volcanic rocks: International Geology Review, v. 51, p. 589–633, doi:10.1080/00206810902867690.

Bloch, W., Schurr, B., Kummerow, J., Salazar, P., and Shapiro, S.A., 2018, From Slab Coupling to Slab Pull: Stress Segmentation in the Subducting Nazca Plate: Geophysical Research Letters, v. 45, p. 5407–5416, doi:10.1029/2018GL078793.

Blum-Oeste, M., and Wörner, G., 2016, Central Andean magmatism can be constrained by three ubiquitous end-members: Terra Nova, v. 28, p. 434–440, doi:10.1111/ter.12237.

Boric, R.P., Diaz, F.F., and Maksaev, V., 1987a, Geologia y Yacimientos Metaliferos de la Region de Antofagasta (Sector Norte): Servicio Nacional de Geologia y Mineria Carta Geologica de Chile.

Boric, R.P., Diaz, F.F., and Maksaev, V., 1987b, Geologia y Yacimientos Metaliferos de la Region de Antofagasta (Sector Sur): Servicio Nacional de Geologia y Mineria Carta Geologica de Chile.

Bouilhol, P., Magni, V., van Hunen, J., and Kaislaniemi, L., 2015, A numerical approach to melting in warm subduction zones: Earth and Planetary Science Letters, v. 411, p. 37–44, doi:10.1016/j.epsl.2014.11.043.

Brandmeier, M., and Wörner, G., 2016, Compositional variations of ignimbrite magmas in the Central Andes over the past 26Ma — A multivariate statistical perspective: Lithos, v. 262, p. 713–728, doi:10.1016/j.lithos.2016.07.011.

Buchelt, M., and Cancino, C.T., 1988, The Jurassic La Negra formation in the area of Antofagasta, Northern Chile (lithology, petrography, geochemistry), *in* Bahlburg, H., Breitkreuz, P.D.D.C., and Giese, P.D.P. eds., The Southern Central Andes, Springer Berlin Heidelberg, Lecture Notes in Earth Sciences, v. 17, p. 169–182, doi:10.1007/BFb0045181.

Burns, D.H., de Silva, S.L., Tepley III, F., Schmitt, A.K., and Loewen, M.W., 2015, Recording the transition from flare-up to steady-state arc magmatism at the Purico–Chascon volcanic complex, northern Chile: Earth and Planetary Science Letters, v. 422, p. 75–86, doi:10.1016/j.epsl.2015.04.002.

Byerlee, J., 1978, Friction of Rocks, *in* Byerlee, J.D. and Wyss, M. eds., Rock Friction and Earthquake Prediction, Basel, Birkhäuser Basel, Contributions to Current Research in Geophysics (CCRG), p. 615–626, doi:10.1007/978-3-0348-7182-2_4.

Caldwell, J.G., and Turcotte, D.L., 1979, Dependence of the thickness of the elastic oceanic lithosphere on age: Journal of Geophysical Research: Solid Earth, v. 84, p. 7572–7576, doi:10.1029/JB084iB13p07572.

Canavan, R.R., Carrapa, B., Clementz, M.T., Quade, J., DeCelles, P.G., and Schoenbohm, L.M., 2014, Early Cenozoic uplift of the Puna Plateau, Central Andes, based on stable isotope paleoaltimetry of hydrated volcanic glass: Geology, v. 42, p. 447–450, doi:10.1130/G35239.1.

Capitanio, F.A., Faccenna, C., Zlotnik, S., and Stegman, D.R., 2011, Subduction dynamics and the origin of Andean orogeny and the Bolivian orocline: Nature, v. 480, p. 83–86, doi:10.1038/nature10596.

Carlotto, V., 2013, Paleogeographic and tectonic controls on the evolution of Cenozoic basins in the Altiplano and Western Cordillera of southern Peru: Tectonophysics, v. 589, p. 195–219, doi:10.1016/j.tecto.2013.01.002.

Carlson, R.L., Hilde, T.W.C., and Uyeda, S., 1983, The driving mechanism of plate tectonics: Relation to age of the lithosphere at trenches: Geophysical Research Letters, v. 10, p. 297–300, doi:10.1029/GL010i004p00297.

Carrapa, B., Strecker, M.R., and Sobel, E.R., 2006, Cenozoic orogenic growth in the Central Andes: Evidence from sedimentary rock provenance and apatite fission track thermochronology in the Fiambalá Basin, southernmost Puna Plateau margin (NW Argentina): Earth and Planetary Science Letters, v. 247, p. 82–100, doi:10.1016/j.epsl.2006.04.010.

Cerpa, N.G., Guillaume, B., and Martinod, J., 2018, The interplay between overriding plate kinematics, slab dip and tectonics: Geophysical Journal International, v. 215, p. 1789–1802, doi:10.1093/gji/ggy365.

Chapman, J.B., Ducea, M.N., DeCelles, P.G., and Profeta, L., 2015a, Tracking changes in crustal thickness during orogenic evolution with Sr/Y: An example from the North American Cordillera: Geology, v. 43, p. 919–922, doi:10.1130/G36996.1.

Chapman, A.D., Ducea, M.N., McQuarrie, N., Coble, M., Petrescu, L., and Hoffman, D., 2015b, Constraints on plateau architecture and assembly from deep crustal xenoliths, northern Altiplano (SE Peru): Geological Society of America Bulletin, v. 127, p. 1777–1797, doi:10.1130/B31206.1.

Chiaradia, M., 2009, Adakite-like magmas from fractional crystallization and melting-assimilation of mafic lower crust (Eocene Macuchi arc, Western Cordillera, Ecuador): Chemical Geology, v. 265, p. 468–487, doi:10.1016/j.chemgeo.2009.05.014.

Chiaradia, M., 2014, Copper enrichment in arc magmas controlled by overriding plate thickness: Nature Geoscience, v. 7, p. 43–46, doi:10.1038/ngeo2028.

Chiaradia, M., 2015, Crustal thickness control on Sr/Y signatures of recent arc magmas: an Earth scale perspective: Scientific Reports, v. 5, p. 8115, doi:10.1038/srep08115.

Chiaradia, M., Müntener, O., Beate, B., and Fontignie, D., 2009, Adakite-like volcanism of Ecuador: lower crust magmatic evolution and recycling: Contributions to Mineralogy and Petrology, v. 158, p. 563–588, doi:10.1007/s00410-009-0397-2.

Chin, E.J., Shimizu, K., Bybee, G.M., and Erdman, M.E., 2018, On the development of the calc-alkaline and tholeiitic magma series: A deep crustal cumulate perspective: Earth and Planetary Science Letters, v. 482, p. 277–287, doi:10.1016/j.epsl.2017.11.016.

Christensen, N.I., 2015, The Abundance of Serpentinites in the Oceanic Crust: The Journal of Geology, doi:10.1086/627796.

Clark, S.P., Burchfiel, B.C., and Suppe, J., 1988, Processes in Continental Lithospheric Deformation: Geological Society of America, 222 p.

Coira, B., Davidson, J., Mpodozis, C., and Ramos, V., 1982, Tectonic and magmatic evolution of the Andes of northern Argentina and Chile: Earth-Science Reviews, v. 18, p. 303–332, doi:10.1016/0012-8252(82)90042-3.

Conrad, C.P., Bilek, S., and Lithgow-Bertelloni, C., 2004, Great earthquakes and slab pull: interaction between seismic coupling and plate–slab coupling: Earth and Planetary Science Letters, v. 218, p. 109–122, doi:10.1016/S0012-821X(03)00643-5.

Conrad, C.P., and Lithgow-Bertelloni, C., 2002, How Mantle Slabs Drive Plate Tectonics: Science, v. 298, p. 207–209, doi:10.1126/science.1074161.

Cooper, F.J., Adams, B.A., Blundy, J.D., Farley, K.A., McKeon, R.E., and Ruggiero, A., 2016, Aridity-induced Miocene canyon incision in the Central Andes: Geology, v. 44, p. 675–678, doi:10.1130/G38254.1.

Cooper, L.B., Ruscitto, D.M., Plank, T., Wallace, P.J., Syracuse, E.M., and Manning, C.E., 2012, Global variations in H2O/Ce: 1. Slab surface temperatures beneath volcanic arcs: Geochemistry, Geophysics, Geosystems, v. 13, doi:10.1029/2011GC003902.

Cordani, U.G., Cardona, A., Jimenez, D.M., Liu, D., and Nutman, A.P., 2005, Geochronology of Proterozoic basement inliers in the Colombian Andes: tectonic history of remnants of a fragmented Grenville belt: Geological Society, London, Special Publications, v. 246, p. 329–346, doi:10.1144/GSL.SP.2005.246.01.13.

Cornejo, P., and Mpodozis, C., 1997, Eventos volcánicos discretos en el Paleógeno del norte de Chile: el caso de la Formación Chile Alemania en la región de Sierra Exploradora (25^{o}-26^{o} S): VIII Congreso Geológico Chileno,Antofagasta, v. Actas I, p. 31–35.

Crameri, F., Lithgow-Bertelloni, C.R., and Tackley, P.J., 2017, The dynamical control of subduction parameters on surface topography: Geochemistry, Geophysics, Geosystems, v. 18, p. 1661–1687, doi:10.1002/2017GC006821.

Cruciani, C., Carminati, E., and Doglioni, C., 2005, Slab dip vs. lithosphere age: No direct function: Earth and Planetary Science Letters, v. 238, p. 298–310, doi:10.1016/j.epsl.2005.07.025.

Currie, C.A., Ducea, M.N., DeCelles, P.G., and Beaumont, C., 2015, Geodynamic models of Cordilleran orogens: Gravitational instability of magmatic arc roots: Geological Society of America Memoirs, v. 212, p. 1–22, doi:10.1130/2015.1212(01).

Damm, K.-W., Harmon, R.S., and Kelley, S., 1994, Some Isotopic and Geochemical Constraints on the Origin and Evolution of the Central Andean Basement (19°–24°S), *in* Reutter, K.-J., Scheuber, E., and Wigger, P.J. eds., Tectonics of the Southern Central Andes, Berlin Heidelberg, Springer, p. 263–276, doi:10.1007/978-3-642-77353-2_19.

Davidson, J.P., Ferguson, K.M., Colucci, M.T., and Dungan, M.A., 1988, The origin and evolution of magmas from the San Pedro-Pellado volcanic complex, S. Chile: multicomponent sources and open system evolution: Contributions to Mineralogy and Petrology, v. 100, p. 429–445, doi:10.1007/BF00371373.

Davidson, J.P., Hora, J.M., Garrison, J.M., and Dungan, M.A., 2005, Crustal forensics in arc magmas: Journal of Volcanology and Geothermal Research, v. 140, p. 157–170, doi:10.1016/j.jvolgeores.2004.07.019.

Davidson, J.P., McMillan, N.J., Moorbath, S., Wörner, G., Harmon, R.S., and Lopez-Escobar, L., 1990, The Nevados de Payachata volcanic region (18°S/69°W, N. Chile) II. Evidence for widespread crustal involvement in Andean magmatism: Contributions to Mineralogy and Petrology, v. 105, p. 412–432, doi:10.1007/BF00286829.

Davidson, J.P., and de Silva, S., 1995, Late Cenozoic magmatism of the Bolivian Altiplano: Contributions to Mineralogy and Petrology, v. 119, p. 387–408, doi:10.1007/BF00286937.

Davidson, J., Turner, S., Handley, H., Macpherson, C., and Dosseto, A., 2007, Amphibole “sponge” in arc crust? Geology, v. 35, p. 787–790, doi:10.1130/G23637A.1.

Davidson, J., Turner, S., and Plank, T., 2013, Dy/Dy*: Variations Arising from Mantle Sources and Petrogenetic Processes: Journal of Petrology, v. 54, p. 525–537, doi:10.1093/petrology/egs076.

DeCelles, P.G., Ducea, M.N., Kapp, P., and Zandt, G., 2009, Cyclicity in Cordilleran orogenic systems: Nature Geoscience, v. 2, p. 251–257, doi:10.1038/NGEO469.

DeCelles, P.G., and Horton, B.K., 2003, Early to middle Tertiary foreland basin development and the history of Andean crustal shortening in Bolivia: Geological Society of America Bulletin, v. 115, p. 58–77, doi:10.1130/0016-7606(2003)115<0058:ETMTFB>2.0.CO;2.

Decou, A., von Eynatten, H., Dunkl, I., Frei, D., and Wörner, G., 2013, Late Eocene to Early Miocene Andean uplift inferred from detrital zircon fission track and U–Pb dating of Cenozoic forearc sediments (15–18°S): Journal of South American Earth Sciences, v. 45, p. 6–23, doi:10.1016/j.jsames.2013.02.003.

Deeken, A., Sobel, E.R., Coutand, I., Haschke, M., Riller, U., and Strecker, M.R., 2006, Development of the southern Eastern Cordillera, NW Argentina, constrained by apatite fission track thermochronology: From early Cretaceous extension to middle Miocene shortening: Tectonics, v. 25, p. TC6003, doi:10.1029/2005TC001894.

Defant, M.J., and Drummond, M.S., 1990, Derivation of some modern arc magmas by melting of young subducted lithosphere: Nature, v. 347, p. 662–665, doi:10.1038/347662a0.

Delph, J.R., Ward, K.M., Zandt, G., Ducea, M.N., and Beck, S.L., 2017, Imaging a magma plumbing system from MASH zone to magma reservoir: Earth and Planetary Science Letters, v. 457, p. 313–324, doi:10.1016/j.epsl.2016.10.008.

DePaolo, D.J., 1981, Trace element and isotopic effects of combined wallrock assimilation and fractional crystallization: Earth and Planetary Science Letters, v. 53, p. 189–202, doi:10.1016/0012-821X(81)90153-9.

Devlin, S., Isacks, B.L., Pritchard, M.E., Barnhart, W.D., and Lohman, R.B., 2012, Depths and focal mechanisms of crustal earthquakes in the central Andes determined from teleseismic waveform analysis and InSAR: Tectonics, v. 31, doi:10.1029/2011TC002914.

Dhuime, B., Wuestefeld, A., and Hawkesworth, C.J., 2015, Emergence of modern continental crust about 3 billion years ago: Nature Geoscience, v. 8, p. 552–555, doi:10.1038/ngeo2466.

Dobson, D.P., Meredith, P.G., and Boon, S.A., 2002, Simulation of Subduction Zone Seismicity by Dehydration of Serpentine: Science, v. 298, p. 1407–1410, doi:10.1126/science.1075390.

Dowall, D.P., Nowell, G.M., and Pearson, D.G., 2003, Chemical Pre-Concentration procedures for high-precision analysis of HF-Nd-Sr isotopes in geological materials by plasma techniques ionisation multi-collector mass spectrometry (PIMMS), *in* Plasma Source Mass Spectrometry: Applications and Emerging Technologies, Cambridge, The Royal Society of Chemistry, v. Eds.: Holland, J. G. and Tanner, S. D., doi:10.1039/9781847551689-00321.

Drummond, M.S., and Defant, M.J., 1990, A model for Trondhjemite-Tonalite-Dacite Genesis and crustal growth via slab melting: Archean to modern comparisons: Journal of Geophysical Research: Solid Earth, v. 95, p. 21503–21521, doi:10.1029/JB095iB13p21503.

Ducea, M.N., Bergantz, G.W., Crowley, J.L., and Otamendi, J., 2017, Ultrafast magmatic buildup and diversification to produce continental crust during subduction: Geology, p. G38726.1, doi:10.1130/G38726.1.

Ducea, M.N., Seclaman, A.C., Murray, K.E., Jianu, D., and Schoenbohm, L.M., 2013, Mantle-drip magmatism beneath the Altiplano-Puna plateau, central Andes: Geology, v. 41, p. 915–918, doi:10.1130/G34509.1.

Dunai, T.J., López, G.A.G., and Juez-Larré, J., 2005, Oligocene–Miocene age of aridity in the Atacama Desert revealed by exposure dating of erosion-sensitive landforms: Geology, v. 33, p. 321–324, doi:10.1130/G21184.1.

Dungan, M.A., Wulff, A., and Thompson, R., 2001, Eruptive Stratigraphy of the Tatara–San Pedro Complex, 36°S, Southern Volcanic Zone, Chilean Andes: Reconstruction Method and Implications for Magma Evolution at Long-lived Arc Volcanic Centers: Journal of Petrology, v. 42, p. 555–626, doi:10.1093/petrology/42.3.555.

Dzierma, Y., Rabbel, W., Thorwart, M., Koulakov, I., Wehrmann, H., Hoernle, K., and Comte, D., 2012, Seismic velocity structure of the slab and continental plate in the region of the 1960 Valdivia (Chile) slip maximum — Insights into fluid release and plate coupling: Earth and Planetary Science Letters, v. 331–332, p. 164–176, doi:10.1016/j.epsl.2012.02.006.

Eichelberger, J.C., 1978, Andesitic volcanism and crustal evolution: Nature, v. 275, p. 21–27, doi:10.1038/275021a0.

Ekström, G., Nettles, M., and Dziewoński, A.M., 2012, The global CMT project 2004–2010: Centroid-moment tensors for 13,017 earthquakes: Physics of the Earth and Planetary Interiors, v. 200, p. 1–9, doi:10.1016/j.pepi.2012.04.002.

Elger, K., Oncken, O., and Glodny, J., 2005, Plateau-style accumulation of deformation: Southern Altiplano: Tectonics, v. 24, p. TC4020, doi:10.1029/2004TC001675.

England, P., Engdahl, R., and Thatcher, W., 2004, Systematic variation in the depths of slabs beneath arc volcanoes: Geophysical Journal International, v. 156, p. 377–408, doi:10.1111/j.1365-246X.2003.02132.x.

England, P.C., and Katz, R.F., 2010, Melting above the anhydrous solidus controls the location of volcanic arcs: Nature, v. 467, p. 700–703, doi:10.1038/nature09417.

Ersoy, Y., and Helvacı, C., 2010, FC–AFC–FCA and mixing modeler: A Microsoft® Excel© spreadsheet program for modeling geochemical differentiation of magma by crystal fractionation, crustal assimilation and mixing: Computers & Geosciences, v. 36, p. 383–390, doi:10.1016/j.cageo.2009.06.007.

Espurt, N., Funiciello, F., Martinod, J., Guillaume, B., Regard, V., Faccenna, C., and Brusset, S., 2008, Flat subduction dynamics and deformation of the South American plate: Insights from analog modeling: Tectonics, v. 27, doi:10.1029/2007TC002175.

Faccenna, C., Heuret, A., Funiciello, F., Lallemand, S., and Becker, T.W., 2007, Predicting trench and plate motion from the dynamics of a strong slab: Earth and Planetary Science Letters, v. 257, p. 29–36, doi:10.1016/j.epsl.2007.02.016.

Faccenna, C., Oncken, O., Holt, A.F., and Becker, T.W., 2017, Initiation of the Andean orogeny by lower mantle subduction: Earth and Planetary Science Letters, v. 463, p. 189–201, doi:10.1016/j.epsl.2017.01.041.

Farner, M.J., and Lee, C.-T.A., 2017, Effects of crustal thickness on magmatic differentiation in subduction zone volcanism: A global study: Earth and Planetary Science Letters, v. 470, p. 96–107, doi:10.1016/j.epsl.2017.04.025.

Farr, T.G. et al., 2007, The Shuttle Radar Topography Mission: Reviews of Geophysics, v. 45, p. RG2004, doi:10.1029/2005RG000183.

Feeley, T.C., and Sharp, Z.D., 1995, 18O16O isotope geochemistry of silicic lava flows erupted from Volcán Ollagüe, Andean Central Volcanic Zone: Earth and Planetary Science Letters, v. 133, p. 239–254, doi:10.1016/0012-821X(95)00094-S.

Feigenson, M.D., and Carr, M.J., 1986, Positively correlated Nd and Sr isotope ratios of lavas from the Central American volcanic front: Geology, v. 14, p. 79–82, doi:10.1130/0091-7613(1986)14<79:PCNASI>2.0.CO;2.

Fiorella, R.P., Poulsen, C.J., Pillco Zolá, R.S., Barnes, J.B., Tabor, C.R., and Ehlers, T.A., 2015, Spatiotemporal variability of modern precipitation δ18O in the central Andes and implications for paleoclimate and paleoaltimetry estimates: Journal of Geophysical Research: Atmospheres, v. 120, p. 4630–4656, doi:10.1002/2014JD022893.

Font, L., Davidson, J.P., Pearson, D.G., Nowell, G.M., Jerram, D.A., and Ottley, C.J., 2008, Sr and Pb Isotope Micro-analysis of Plagioclase Crystals from Skye Lavas: an Insight into Open-system Processes in a Flood Basalt Province: Journal of Petrology, v. 49, p. 1449–1471, doi:10.1093/petrology/egn032.

Francis, P.W., Moorbath, S., and Thorpe, R.S., 1977, Strontium isotope data for Recent andesites in Ecuador and North Chile: Earth and Planetary Science Letters, v. 37, p. 197–202, doi:10.1016/0012-821X(77)90164-9.

Franz, G., Lucassen, F., Kramer, W., Trumbull, R.B., Romer, R.L., Wilke, H.-G., Viramonte, J.G., Becchio, R., and Siebel, W., 2006, Crustal Evolution at the Central Andean Continental Margin: a Geochemical Record of Crustal Growth, Recycling and Destruction, *in* Oncken, O., Chong, G., Franz, G., Giese, P., Götze, H.-J., Ramos, V.A., Strecker, M.R., and Wigger, P. eds., The Andes: Active Subduction Orogeny, Springer Berlin Heidelberg, Frontiers in Earth Sciences, p. 45–64, doi:10.1007/978-3-540-48684-8_3.

Freymuth, H., Brandmeier, M., and Wörner, G., 2015, The origin and crust/mantle mass balance of Central Andean ignimbrite magmatism constrained by oxygen and strontium isotopes and erupted volumes: Contributions to Mineralogy and Petrology, v. 169, p. 58, doi:10.1007/s00410-015-1152-5.

Funkhouser, J.G., Barnes, I.L., and Naughton, J.J., 1966, Problems in the dating of volcanic rocks by the potassium-argon method: Bulletin Volcanologique, v. 29, p. 709–717, doi:10.1007/BF02597188.

Futa, K., and Stern, C.R., 1988, Sr and Nd isotopic and trace element compositions of Quaternary volcanic centers of the Southern Andes: Earth and Planetary Science Letters, v. 88, p. 253–262, doi:10.1016/0012-821X(88)90082-9.

Gaetani, G.A., and Grove, T.L., 1998, The influence of water on melting of mantle peridotite: Contributions to Mineralogy and Petrology, v. 131, p. 323–346, doi:10.1007/s004100050396.

Garrison, J.M., and Davidson, J.P., 2003, Dubious case for slab melting in the Northern volcanic zone of the Andes: Geology, v. 31, p. 565–568, doi:10.1130/0091-7613(2003)031<0565:DCFSMI>2.0.CO;2.

Garzione, C.N. et al., 2017, The Tectonic Evolution of the Central Andean Plateau and Geodynamic Implications for the Growth of Plateaus: Annual Review of Earth and Planetary Sciences, v. 45, doi:DOI: 10.1146/annurev-earth-063016-020612.

Garzione, C.N., Auerbach, D.J., Jin-Sook Smith, J., Rosario, J.J., Passey, B.H., Jordan, T.E., and Eiler, J.M., 2014, Clumped isotope evidence for diachronous surface cooling of the Altiplano and pulsed surface uplift of the Central Andes: Earth and Planetary Science Letters, v. 393, p. 173–181, doi:10.1016/j.epsl.2014.02.029.

Garzione, C.N., Hoke, G.D., Libarkin, J.C., Withers, S., MacFadden, B., Eiler, J., Ghosh, P., and Mulch, A., 2008, Rise of the Andes: Science, v. 320, p. 1304–1307, doi:10.1126/science.1148615.

Garzione, C.N., Molnar, P., Libarkin, J.C., and MacFadden, B.J., 2006, Rapid late Miocene rise of the Bolivian Altiplano: Evidence for removal of mantle lithosphere: Earth and Planetary Science Letters, v. 241, p. 543–556, doi:10.1016/j.epsl.2005.11.026.

Gazel, E. et al., 2015, Continental crust generated in oceanic arcs: Nature Geoscience, v. 8, p. 321–327, doi:10.1038/ngeo2392.

Gephart, J.W., 1994, Topography and subduction geometry in the central Andes: Clues to the mechanics of a noncollisional orogen: Journal of Geophysical Research: Solid Earth, v. 99, p. 12279–12288, doi:10.1029/94JB00129.

Gerbault, M., Martinod, J., and Hérail, G., 2005, Possible orogeny-parallel lower crustal flow and thickening in the Central Andes: Tectonophysics, v. 399, p. 59–72, doi:10.1016/j.tecto.2004.12.015.

Gerya, T.V., Fossati, D., Cantieni, C., and Seward, D., 2009, Dynamic effects of aseismic ridge subduction: numerical modelling: European Journal of Mineralogy, v. 21, p. 649–661, doi:10.1127/0935-1221/2009/0021-1931.

Gill, J.B., 1981, Orogenic Andesites and Plate Tectonics: Berlin, Heidelberg, New York, Springer, 403 p.

Glerum, A., Thieulot, C., Fraters, M., Blom, C., and Spakman, W., 2018, Nonlinear viscoplasticity in ASPECT: benchmarking and applications to subduction: Solid Earth, v. 9, p. 267–294, doi:https://doi.org/10.5194/se-9-267-2018.

Godoy, B., Wörner, G., Kojima, S., Aguilera, F., Simon, K., and Hartmann, G., 2014, Low-pressure evolution of arc magmas in thickened crust: The San Pedro–Linzor volcanic chain, Central Andes, Northern Chile: Journal of South American Earth Sciences, v. 52, p. 24–42, doi:10.1016/j.jsames.2014.02.004.

Godoy, B., Wörner, G., Le Roux, P., de Silva, S., Parada, M.Á., Kojima, S., González-Maurel, O., Morata, D., Polanco, E., and Martínez, P., 2017, Sr- and Nd- isotope variations along the Pleistocene San Pedro – Linzor volcanic chain, N. Chile: Tracking the influence of the upper crustal Altiplano-Puna Magma Body: Journal of Volcanology and Geothermal Research, v. 341, p. 172–186, doi:10.1016/j.jvolgeores.2017.05.030.

Goss, A.R., Kay, S.M., and Mpodozis, C., 2013, Andean Adakite-like high-Mg Andesites on the Northern Margin of the Chilean–Pampean Flat-slab (27–28·5°S) Associated with Frontal Arc Migration and Fore-arc Subduction Erosion: Journal of Petrology, v. 54, p. 2193–2234, doi:10.1093/petrology/egt044.

Graham, A., Gregory-Wodzicki, K.M., and Wright, K.L., 2001, Studies in Neotropical Paleobotany. XV. A Mio-Pliocene palynoflora from the Eastern Cordillera, Bolivia: implications for the uplift history of the Central Andes: American Journal of Botany, v. 88, p. 1545–1557.

Gregory-Wodzicki, K.M., 2000, Uplift history of the Central and Northern Andes: A review: Geological Society of America Bulletin, v. 112, p. 1091–1105, doi:10.1130/0016-7606(2000)112<1091:UHOTCA>2.0.CO;2.

Gregory-Wodzicki, K.M., McIntosh, W.C., and Velasquez, K., 1998, Climatic and tectonic implications of the late Miocene Jakokkota flora, Bolivian Altiplano: Journal of South American Earth Sciences, v. 11, p. 533–560, doi:10.1016/S0895-9811(98)00031-5.

Gripp, A.E., and Gordon, R.G., 2002, Young tracks of hotspots and current plate velocities: Geophysical Journal International, v. 150, p. 321–361, doi:10.1046/j.1365-246X.2002.01627.x.

Guillaume, B., Hertgen, S., Martinod, J., and Cerpa, N.G., 2018, Slab dip, surface tectonics: How and when do they change following an acceleration/slow down of the overriding plate? Tectonophysics, v. 726, p. 110–120, doi:10.1016/j.tecto.2018.01.030.

Gutscher, M.-A., 2001, An Andean model of interplate coupling and strain partitioning applied to the flat subduction zone of SW Japan (Nankai Trough): Tectonophysics, v. 333, p. 95–109, doi:10.1016/S0040-1951(00)00269-9.

Gutscher, M.-A., 2002, Andean subduction styles and their effect on thermal structure and interplate coupling: Journal of South American Earth Sciences, v. 15, p. 3–10, doi:10.1016/S0895-9811(02)00002-0.

Gutscher, M.-A., Malavieille, J., Lallemand, S., and Collot, J.-Y., 1999a, Tectonic segmentation of the North Andean margin: impact of the Carnegie Ridge collision: Earth and Planetary Science Letters, v. 168, p. 255–270, doi:10.1016/S0012-821X(99)00060-6.

Gutscher, M.-A., Olivet, J.L., Aslanian, D., Eissen, J.P., and Maury, R., 1999b, The "lost inca plateau": cause of flat subduction beneath peru? Earth and Planetary Science Letters, v. 171, p. 335–341, doi:10.1016/S0012-821X(99)00153-3.

Gutscher, M.-A., Spakman, W., Bijwaard, H., and Engdahl, E.R., 2000, Geodynamics of flat subduction: Seismicity and tomographic constraints from the Andean margin: Tectonics, v. 19, p. 814–833, doi:10.1029/1999TC001152.

Hampel, A., 2002, The migration history of the Nazca Ridge along the Peruvian active margin: a re-evaluation: Earth and Planetary Science Letters, v. 203, p. 665–679, doi:10.1016/S0012-821X(02)00859-2.

Hartley, A., 2003, Andean uplift and climate change: Journal of the Geological Society, v. 160, p. 7–10, doi:10.1144/0016-764902-083.

Haschke, M.R., Scheuber, E., Günther, A., and Reutter, K.-J., 2002a, Evolutionary cycles during the Andean orogeny: repeated slab breakoff and flat subduction? Terra Nova, v. 14, p. 49–55, doi:10.1046/j.1365-3121.2002.00387.x.

Haschke, M., Siebel, W., Günther, A., and Scheuber, E., 2002b, Repeated crustal thickening and recycling during the Andean orogeny in north Chile (21°–26°S): Journal of Geophysical Research: Solid Earth, v. 107, p. ECV 1-18, doi:10.1029/2001JB000328.

Hawkesworth, C.J., and Kemp, A.I.S., 2006, Evolution of the continental crust: Nature, v. 443, p. 811–817, doi:10.1038/nature05191.

Hayes, G.P., Wald, D.J., and Johnson, R.L., 2012, Slab1.0: A three-dimensional model of global subduction zone geometries: Journal of Geophysical Research: Solid Earth, v. 117, p. B01302, doi:10.1029/2011JB008524.

Heuret, A., Conrad, C.P., Funiciello, F., Lallemand, S., and Sandri, L., 2012, Relation between subduction megathrust earthquakes, trench sediment thickness and upper plate strain: Geophysical Research Letters, v. 39, doi:10.1029/2011GL050712.

Heuret, A., and Lallemand, S., 2005a, Plate motions, slab dynamics and back-arc deformation: Physics of the Earth and Planetary Interiors, v. 149, p. 31–51, doi:10.1016/j.pepi.2004.08.022.

Heuret, A., and Lallemand, S., 2005b, Submap 4.2:, http://submap.gm.univ-montp2.fr/index.php (accessed August 2018).

Hickey, R.L., Frey, F.A., Gerlach, D.C., and Lopez-Escobar, L., 1986, Multiple sources for basaltic arc rocks from the southern volcanic zone of the Andes (34°–41°S): Trace element and isotopic evidence for contributions from subducted oceanic crust, mantle, and continental crust: Journal of Geophysical Research: Solid Earth, v. 91, p. 5963–5983, doi:10.1029/JB091iB06p05963.

Hickey-Vargas, R., Holbik, S., Tormey, D., Frey, F.A., and Moreno Roa, H., 2016, Basaltic rocks from the Andean Southern Volcanic Zone: Insights from the comparison of along-strike and small-scale geochemical variations and their sources: Lithos, v. 258–259, p. 115–132, doi:10.1016/j.lithos.2016.04.014.

Hildreth, W., and Moorbath, S., 1988, Crustal contributions to arc magmatism in the Andes of Central Chile: Contributions to Mineralogy and Petrology, v. 98, p. 455–489, doi:10.1007/BF00372365.

Holm, P.M., Søager, N., Dyhr, C.T., and Nielsen, M.R., 2014, Enrichments of the mantle sources beneath the Southern Volcanic Zone (Andes) by fluids and melts derived from abraded upper continental crust: Contributions to Mineralogy and Petrology, v. 167, p. 1004, doi:10.1007/s00410-014-1004-8.

Horodyskyj, U.N., Lee, C.-T.A., and Ducea, M.N., 2007, Similarities between Archean high MgO eclogites and Phanerozoic arc-eclogite cumulates and the role of arcs in Archean continent formation: Earth and Planetary Science Letters, v. 256, p. 510–520, doi:10.1016/j.epsl.2007.02.006.

Horton, B.K., 2018a, Sedimentary record of Andean mountain building: Earth-Science Reviews, v. 178, p. 279–309, doi:10.1016/j.earscirev.2017.11.025.

Horton, 2018b, Tectonic Regimes of the Central and Southern Andes: Responses to Variations in Plate Coupling During Subduction: Tectonics, v. 37, p. 402–429, doi:10.1002/2017TC004624.

Horton, B.K., Hampton, B.A., and Waanders, G.L., 2001, Paleogene synorogenic sedimentation in the Altiplano plateau and implications for initial mountain building in the central Andes: Geological Society of America Bulletin, v. 113, p. 1387–1400, doi:10.1130/0016-7606(2001)113<1387:PSSITA>2.0.CO;2.

Houseman, G.A., McKenzie, D.P., and Molnar, P., 1981, Convective instability of a thickened boundary layer and its relevance for the thermal evolution of continental convergent belts: Journal of Geophysical Research: Solid Earth, v. 86, p. 6115–6132, doi:10.1029/JB086iB07p06115.

Hu, F., Ducea, M.N., Liu, S., and Chapman, J.B., 2017, Quantifying Crustal Thickness in Continental Collisional Belts: Global Perspective and a Geologic Application: Scientific Reports, v. 7, doi:10.1038/s41598-017-07849-7.

Hu, J., Liu, L., Hermosillo, A., and Zhou, Q., 2016, Simulation of late Cenozoic South American flat-slab subduction using geodynamic models with data assimilation: Earth and Planetary Science Letters, v. 438, p. 1–13, doi:10.1016/j.epsl.2016.01.011.

van Hunen, J., van den Berg, A.P., and Vlaar, N.J., 2000, A thermo-mechanical model of horizontal subduction below an overriding plate: Earth and Planetary Science Letters, v. 182, p. 157–169, doi:10.1016/S0012-821X(00)00240-5.

van Hunen, J., van den Berg, A.P., and Vlaar, N.J., 2002a, On the role of subducting oceanic plateaus in the development of shallow flat subduction: Tectonophysics, v. 352, p. 317–333, doi:10.1016/S0040-1951(02)00263-9.

van Hunen, J., van den Berg, A.P., and Vlaar, N.J., 2002b, The impact of the South-American plate motion and the Nazca Ridge subduction on the flat subduction below South Peru: Geophysical Research Letters, v. 29, p. 35-1-35–4, doi:10.1029/2001GL014004.

van Hunen, J., van den Berg, A.P., and Vlaar, N.J., 2004, Various mechanisms to induce present-day shallow flat subduction and implications for the younger Earth: a numerical parameter study: Physics of the Earth and Planetary Interiors, v. 146, p. 179–194, doi:10.1016/j.pepi.2003.07.027.

Insel, N., Poulsen, C.J., Ehlers, T.A., and Sturm, C., 2012, Response of meteoric δ18O to surface uplift — Implications for Cenozoic Andean Plateau growth: Earth and Planetary Science Letters, v. 317–318, p. 262–272, doi:10.1016/j.epsl.2011.11.039.

Isacks, B.L., 1988, Uplift of the Central Andean Plateau and bending of the Bolivian Orocline: Journal of Geophysical Research: Solid Earth, v. 93, p. 3211–3231, doi:10.1029/JB093iB04p03211.

Jacques, G., Hoernle, K., Gill, J., Wehrmann, H., Bindeman, I., and Lara, L.E., 2014, Geochemical variations in the Central Southern Volcanic Zone, Chile (38–43°S): The role of fluids in generating arc magmas: Chemical Geology, v. 371, p. 27–45, doi:10.1016/j.chemgeo.2014.01.015.

Jagoutz, O., 2014, Arc crustal differentiation mechanisms: Earth and Planetary Science Letters, v. 396, p. 267–277, doi:10.1016/j.epsl.2014.03.060.

Jamieson, R.A., and Beaumont, C., 2013, On the origin of orogens: Geological Society of America Bulletin, v. 125, p. 1671–1702, doi:10.1130/B30855.1.

Jarrard, R.D., 1986, Relations among subduction parameters: Reviews of Geophysics, v. 24, p. 217–284, doi:10.1029/RG024i002p00217.

Jenner, F.E., 2017, Cumulate causes for the low contents of sulfide-loving elements in the continental crust: Nature Geoscience, v. 10, p. 524–529, doi:10.1038/ngeo2965.

Jones, R.E., De Hoog, J.C.M., Kirstein, L.A., Kasemann, S.A., Hinton, R., Elliott, T., and Litvak, V.D., 2014, Temporal variations in the influence of the subducting slab on Central Andean arc magmas: Evidence from boron isotope systematics: Earth and Planetary Science Letters, v. 408, p. 390–401, doi:10.1016/j.epsl.2014.10.004.

Jones, R.E., Kirstein, L.A., Kasemann, S.A., Dhuime, B., Elliott, T., Litvak, V.D., Alonso, R., and Hinton, R., 2015, Geodynamic controls on the contamination of Cenozoic arc magmas in the southern Central Andes: Insights from the O and Hf isotopic composition of zircon: Geochimica et Cosmochimica Acta, v. 164, p. 386–402, doi:10.1016/j.gca.2015.05.007.

Jordan, T.H., 1978, Composition and development of the continental tectosphere: Nature, v. 274, p. 544–548, doi:10.1038/274544a0.

Jordan, T.E., Isacks, B.L., Allmendinger, R.W., Brewer, J.A., Ramos, V.A., and Ando, C.J., 1983a, Andean tectonics related to geometry of subducted Nazca plate: Geological Society of America Bulletin, v. 94, p. 341–361, doi:10.1130/0016-7606(1983)94<341:ATRTGO>2.0.CO;2.

Jordan, T.E., Isacks, B.L., Allmendinger, R.W., Brewer, J.A., Ramos, V.A., and Ando, C.J., 1983b, Andean tectonics related to geometry of subducted Nazca plate: GSA Bulletin, v. 94, p. 341–361, doi:10.1130/0016-7606(1983)94<341:ATRTGO>2.0.CO;2.

Jordan, T.E., Nester, P.L., Blanco, N., Hoke, G.D., Dávila, F., and Tomlinson, A.J., 2010, Uplift of the Altiplano-Puna plateau: A view from the west: Tectonics, v. 29, p. TC5007, doi:10.1029/2010TC002661.

Kaislaniemi, L., Hunen, J. van, Allen, M.B., and Neill, I., 2014, Sublithospheric small-scale convection—A mechanism for collision zone magmatism: Geology, v. 42, p. 291–294, doi:10.1130/G35193.1.

Kar, N., Garzione, C.N., Jaramillo, C., Shanahan, T., Carlotto, V., Pullen, A., Moreno, F., Anderson, V., Moreno, E., and Eiler, J., 2016, Rapid regional surface uplift of the northern Altiplano plateau revealed by multiproxy paleoclimate reconstruction: Earth and Planetary Science Letters, v. 447, p. 33–47, doi:10.1016/j.epsl.2016.04.025.

Kay, R.W., 1978, Aleutian magnesian andesites: Melts from subducted Pacific ocean crust: Journal of Volcanology and Geothermal Research, v. 4, p. 117–132, doi:10.1016/0377-0273(78)90032-X.

Kay, S.M., Burns, W.M., Copeland, P., and Mancilla, O., 2006, Upper Cretaceous to Holocene magmatism and evidence for transient Miocene shallowing of the Andean subduction zone under the northern Neuquén Basin: Geological Society of America Special Papers, v. 407, p. 19–60, doi:10.1130/2006.2407(02).

Kay, S.M., and Coira, B.L., 2009, Shallowing and steepening subduction zones, continental lithospheric loss, magmatism, and crustal flow under the Central Andean Altiplano-Puna Plateau: Geological Society of America Memoirs, v. 204, p. 229–259, doi:10.1130/2009.1204(11).

Kay, S.M., Coira, B.L., Caffe, P.J., and Chen, C.-H., 2010, Regional chemical diversity, crustal and mantle sources and evolution of central Andean Puna plateau ignimbrites: Journal of Volcanology and Geothermal Research, v. 198, p. 81–111, doi:10.1016/j.jvolgeores.2010.08.013.

Kay, S.M., Coira, B., and Viramonte, J., 1994, Young mafic back arc volcanic rocks as indicators of continental lithospheric delamination beneath the Argentine Puna Plateau, central Andes: Journal of Geophysical Research: Solid Earth, v. 99, p. 24323–24339, doi:10.1029/94JB00896.

Kay, R., Hubbard, N.J., and Gast, P.W., 1970, Chemical characteristics and origin of oceanic ridge volcanic rocks: Journal of Geophysical Research, v. 75, p. 1585–1613, doi:10.1029/JB075i008p01585.

Kay, S.M., and Kay, R.W., 2002, Andean Adakites: Three Ways to Make Them: Acta Petrologica Sinica, v. 18, p. 303–311.

Kay, R.W., and Kay, S.M., 1993, Delamination and delamination magmatism: Tectonophysics, v. 219, p. 177–189, doi:10.1016/0040-1951(93)90295-U.

Kay, S.M., Maksaev, V., Moscoso, R., Mpodozis, C., and Nasi, C., 1987, Probing the evolving Andean Lithosphere: Mid-Late Tertiary magmatism in Chile (29°–30°30′S) over the modern zone of subhorizontal subduction: Journal of Geophysical Research: Solid Earth, v. 92, p. 6173–6189, doi:10.1029/JB092iB07p06173.

Kay, S.M., and Mpodozis, C., 2002, Magmatism as a probe to the Neogene shallowing of the Nazca plate beneath the modern Chilean flat-slab: Journal of South American Earth Sciences, v. 15, p. 39–57, doi:10.1016/S0895-9811(02)00005-6.

Kay, S.M., Mpodozis, C., and Gardeweg, M., 2014, Magma sources and tectonic setting of Central Andean andesites (25.5–28°S) related to crustal thickening, forearc subduction erosion and delamination: Geological Society, London, Special Publications, v. 385, p. 303–334, doi:10.1144/SP385.11.

Kay, S.M., Mpodozis, C., Ramos, V.A., and Munizaga, F., 1991, Magma source variations for mid–late Tertiary magmatic rocks associated with a shallowing subduction zone and a thickening crust in the central Andes (28 to 33°S): Geological Society of America Special Papers, v. 265, p. 113–138, doi:10.1130/SPE265-p113.

van Keken, P.E., Hacker, B.R., Syracuse, E.M., and Abers, G.A., 2011, Subduction factory: 4. Depth-dependent flux of H2O from subducting slabs worldwide: Journal of Geophysical Research: Solid Earth, v. 116, doi:10.1029/2010JB007922.

van Keken, P.E., Kiefer, B., and Peacock, S.M., 2002, High-resolution models of subduction zones: Implications for mineral dehydration reactions and the transport of water into the deep mantle: Geochemistry, Geophysics, Geosystems, v. 3, p. 1 of 20–20 20, doi:10.1029/2001GC000256.

Kent, A.J.R., Darr, C., Koleszar, A.M., Salisbury, M.J., and Cooper, K.M., 2010, Preferential eruption of andesitic magmas through recharge filtering: Nature Geoscience, v. 3, p. 631–636, doi:10.1038/ngeo924.

Kirby, S.H., Stein, S., Okal, E.A., and Rubie, D.C., 1996, Metastable mantle phase transformations and deep earthquakes in subducting oceanic lithosphere: Reviews of Geophysics, v. 34, p. 261–306, doi:10.1029/96RG01050.

Kirsch, M., Paterson, S.R., Wobbe, F., Ardila, A.M.M., Clausen, B.L., and Alasino, P.H., 2016, Temporal histories of Cordilleran continental arcs: testing models for magmatic episodicity: American Mineralogist, v. 101, p. 2133–2154, doi:10.2138/am-2016-5718.

Kley, J., and Monaldi, C.R., 1998, Tectonic shortening and crustal thickness in the Central Andes: How good is the correlation? Geology, v. 26, p. 723–726, doi:10.1130/0091-7613(1998)026<0723:TSACTI>2.3.CO;2.

Kley, J., Monaldi, C.R., and Salfity, J.A., 1999, Along-strike segmentation of the Andean foreland: causes and consequences: Tectonophysics, v. 301, p. 75–94, doi:10.1016/S0040-1951(98)90223-2.

Kogiso, T., Tatsumi, Y., and Nakano, S., 1997, Trace element transport during dehydration processes in the subducted oceanic crust: 1. Experiments and implications for the origin of ocean island basalts: Earth and Planetary Science Letters, v. 148, p. 193–205, doi:10.1016/S0012-821X(97)00018-6.

Lahsen, A., 1982, Upper Cenozoic volcanism and tectonism in the Andes of northern Chile: Earth-Science Reviews, v. 18, p. 285–302, doi:10.1016/0012-8252(82)90041-1.

Lallemand, S., Heuret, A., and Boutelier, D., 2005, On the relationships between slab dip, back-arc stress, upper plate absolute motion, and crustal nature in subduction zones: Geochemistry, Geophysics, Geosystems, v. 6, doi:10.1029/2005GC000917.

Lamb, S., 2016, Cenozoic uplift of the Central Andes in northern Chile and Bolivia—reconciling paleoaltimetry with the geological evolution: Canadian Journal of Earth Sciences, v. 53, p. 1227–1245, doi:10.1139/cjes-2015-0071.

Lamb, S., 2011, Did shortening in thick crust cause rapid Late Cenozoic uplift in the northern Bolivian Andes? Journal of the Geological Society, v. 168, p. 1079–1092, doi:10.1144/0016-76492011-008.

Lamb, S., and Davis, P., 2003, Cenozoic climate change as a possible cause for the rise of the Andes: Nature, v. 425, p. 792–797, doi:10.1038/nature02049.

Lamb, S., and Hoke, L., 1997, Origin of the high plateau in the central Andes, Bolivia, South America: Tectonics, v. 16, p. 623–649, doi:10.1029/97TC00495.

Lamb, S., Hoke, L., Kennan, L., and Dewey, J., 1997, Cenozoic evolution of the Central Andes in Bolivia and northern Chile: Geological Society, London, Special Publications, v. 121, p. 237–264, doi:10.1144/GSL.SP.1997.121.01.10.

Lee, C.-T.A., 2003, Compositional variation of density and seismic velocities in natural peridotites at STP conditions: Implications for seismic imaging of compositional heterogeneities in the upper mantle: Journal of Geophysical Research: Solid Earth, v. 108, doi:10.1029/2003JB002413.

Lee, C.-T.A., Thurner, S., Paterson, S., and Cao, W., 2015, The rise and fall of continental arcs: Interplays between magmatism, uplift, weathering, and climate: Earth and Planetary Science Letters, v. 425, p. 105–119, doi:10.1016/j.epsl.2015.05.045.

Leeman, W.P., 1983, The influence of crustal structure on compositions of subduction-related magmas: Journal of Volcanology and Geothermal Research, v. 18, p. 561–588, doi:10.1016/0377-0273(83)90026-4.

Leier, A., McQuarrie, N., Garzione, C., and Eiler, J., 2013, Stable isotope evidence for multiple pulses of rapid surface uplift in the Central Andes, Bolivia: Earth and Planetary Science Letters, v. 371–372, p. 49–58, doi:10.1016/j.epsl.2013.04.025.

Loewy, S.L., Connelly, J.N., and Dalziel, I.W.D., 2004, An orphaned basement block: The Arequipa-Antofalla Basement of the central Andean margin of South America: GSA Bulletin, v. 116, p. 171–187, doi:10.1130/B25226.1.

Lucassen, F., Becchio, R., Wilke, H.G., Franz, G., Thirlwall, M.F., Viramonte, J., and Wemmer, K., 2000, Proterozoic–Paleozoic development of the basement of the Central Andes (18–26°S) — a mobile belt of the South American craton: Journal of South American Earth Sciences, v. 13, p. 697–715, doi:10.1016/S0895-9811(00)00057-2.

Lucassen, F., Franz, G., Viramonte, J., Romer, R.L., Dulski, P., and Lang, A., 2005, The late Cretaceous lithospheric mantle beneath the Central Andes: Evidence from phase equilibria and composition of mantle xenoliths: Lithos, v. 82, p. 379–406, doi:10.1016/j.lithos.2004.08.002.

Lucassen, F., Kramer, W., Bartsch, V., Wilke, H.-G., Franz, G., Romer, R.L., and Dulski, P., 2006, Nd, Pb, and Sr isotope composition of juvenile magmatism in the Mesozoic large magmatic province of northern Chile (18–27°S): indications for a uniform subarc mantle: Contributions to Mineralogy and Petrology, v. 152, p. 571–589, doi:10.1007/s00410-006-0119-y.

Lucassen, F., Lewerenz, S., Franz, G., Viramonte, J., and Mezger, K., 1999, Metamorphism, isotopic ages and composition of lower crustal granulite xenoliths from the Cretaceous Salta Rift, Argentina: Contributions to Mineralogy and Petrology, v. 134, p. 325–341, doi:10.1007/s004100050488.

Macpherson, C.G., 2008, Lithosphere erosion and crustal growth in subduction zones: Insights from initiation of the nascent East Philippine Arc: Geology, v. 36, p. 311–314, doi:10.1130/G24412A.1.

Macpherson, C.G., Dreher, S.T., and Thirlwall, M.F., 2006, Adakites without slab melting: High pressure differentiation of island arc magma, Mindanao, the Philippines: Earth and Planetary Science Letters, v. 243, p. 581–593, doi:10.1016/j.epsl.2005.12.034.

Magni, V., 2017, Plate tectonics: Crustal recycling evolution: Nature Geoscience, v. 10, p. 623–624, doi:10.1038/ngeo3015.

Magni, V., Bouilhol, P., and Hunen, J. van, 2014, Deep water recycling through time: Geochemistry, Geophysics, Geosystems, v. 15, p. 4203–4216, doi:10.1002/2014GC005525.

Maitre, R.W.L., Streckeisen, A., Zanettin, B., Bas, M.J.L., Bonin, B., and Bateman, P., 2002, Igneous Rocks: A Classification and Glossary of Terms: Cambridge University Press, 252 p.

Maloney, K.T., Clarke, G.L., Klepeis, K.A., and Quevedo, L., 2013, The Late Jurassic to present evolution of the Andean margin: Drivers and the geological record: Tectonics, v. 32, p. 1049–1065, doi:10.1002/tect.20067.

Mamani, M., Tassara, A., and Wörner, G., 2008, Composition and structural control of crustal domains in the central Andes: Geochemistry, Geophysics, Geosystems, v. 9, p. Q03006, doi:10.1029/2007GC001925.

Mamani, M., Wörner, G., and Sempere, T., 2010, Geochemical variations in igneous rocks of the Central Andean orocline (13°S to 18°S): Tracing crustal thickening and magma generation through time and space: Geological Society of America Bulletin, v. 122, p. 162–182, doi:10.1130/B26538.1.

Manea, V.C., Manea, M., Ferrari, L., Orozco-Esquivel, T., Valenzuela, R.W., Husker, A., and Kostoglodov, V., 2017, A review of the geodynamic evolution of flat slab subduction in Mexico, Peru, and Chile: Tectonophysics, v. 695, p. 27–52, doi:10.1016/j.tecto.2016.11.037.

Manea, V.C., Pérez-Gussinyé, M., and Manea, M., 2012, Chilean flat slab subduction controlled by overriding plate thickness and trench rollback: Geology, v. 40, p. 35–38, doi:10.1130/G32543.1.

Marín-Cerón, M.I., Moriguti, T., Makishima, A., and Nakamura, E., 2010, Slab decarbonation and CO2 recycling in the Southwestern Colombian volcanic arc: Geochimica et Cosmochimica Acta, v. 74, p. 1104–1121, doi:10.1016/j.gca.2009.10.031.

Marot, M., Monfret, T., Gerbault, M., Nolet, G., Ranalli, G., and Pardo, M., 2014, Flat versus normal subduction zones: a comparison based on 3-D regional traveltime tomography and petrological modelling of central Chile and western Argentina (29°–35°S): Geophysical Journal International, v. 199, p. 1633–1654, doi:10.1093/gji/ggu355.

Martinod, J., Husson, L., Roperch, P., Guillaume, B., and Espurt, N., 2010, Horizontal subduction zones, convergence velocity and the building of the Andes: Earth and Planetary Science Letters, v. 299, p. 299–309, doi:10.1016/j.epsl.2010.09.010.

McCulloch, M.T., and Gamble, J.A., 1991, Geochemical and geodynamical constraints on subduction zone magmatism: Earth and Planetary Science Letters, v. 102, p. 358–374, doi:10.1016/0012-821X(91)90029-H.

McKenzie, N.R., Hughes, N.C., Gill, B.C., and Myrow, P.M., 2014, Plate tectonic influences on Neoproterozoic–early Paleozoic climate and animal evolution: Geology, v. 42, p. 127–130, doi:10.1130/G34962.1.

McKenzie, D., Jackson, J., and Priestley, K., 2005, Thermal structure of oceanic and continental lithosphere: Earth and Planetary Science Letters, v. 233, p. 337–349, doi:10.1016/j.epsl.2005.02.005.

McLeod, C.L., Davidson, J.P., Nowell, G.M., Silva, S.L. de, and Schmitt, A.K., 2013, Characterizing the continental basement of the Central Andes: Constraints from Bolivian crustal xenoliths: GSA Bulletin, v. 125, p. 985–997, doi:10.1130/B30721.1.

McQuarrie, N., 2002a, Initial plate geometry, shortening variations, and evolution of the Bolivian orocline: Geology, v. 30, p. 867–870, doi:10.1130/0091-7613(2002)030<0867:IPGSVA>2.0.CO;2.

McQuarrie, N., 2002b, The kinematic history of the central Andean fold-thrust belt, Bolivia: Implications for building a high plateau: Geological Society of America Bulletin, v. 114, p. 950–963, doi:10.1130/0016-7606(2002)114<0950:TKHOTC>2.0.CO;2.

McQuarrie, N., Horton, B.K., Zandt, G., Beck, S., and DeCelles, P.G., 2005, Lithospheric evolution of the Andean fold–thrust belt, Bolivia, and the origin of the central Andean plateau: Tectonophysics, v. 399, p. 15–37, doi:10.1016/j.tecto.2004.12.013.

Molnar, P., and Atwater, T., 1978, Interarc spreading and Cordilleran tectonics as alternates related to the age of subducted oceanic lithosphere: Earth and Planetary Science Letters, v. 41, p. 330–340, doi:10.1016/0012-821X(78)90187-5.

Molnar, P., and England, P., 1990, Late Cenozoic uplift of mountain ranges and global climate change: chicken or egg? Nature, v. 346, p. 29–34, doi:10.1038/346029a0.

Molnar, P., England, P., and Martinod, J., 1993, Mantle dynamics, uplift of the Tibetan Plateau, and the Indian Monsoon: Reviews of Geophysics, v. 31, p. 357–396, doi:10.1029/93RG02030.

Molnar, P., and Tapponnier, P., 1977, Relation of the tectonics of eastern China to the India-Eurasia collision: Application of slip-line field theory to large-scale continental tectonics: Geology, v. 5, p. 212–216, doi:10.1130/0091-7613(1977)5<212:ROTTOE>2.0.CO;2.

Moreno, M. et al., 2011, Heterogeneous plate locking in the South–Central Chile subduction zone: Building up the next great earthquake: Earth and Planetary Science Letters, v. 305, p. 413–424, doi:10.1016/j.epsl.2011.03.025.

Moreno, M.S., Bolte, J., Klotz, J., and Melnick, D., 2009, Impact of megathrust geometry on inversion of coseismic slip from geodetic data: Application to the 1960 Chile earthquake: Geophysical Research Letters, v. 36, doi:10.1029/2009GL039276.

Mpodozis, C., Arriagada, C., Basso, M., Roperch, P., Cobbold, P., and Reich, M., 2005, Late Mesozoic to Paleogene stratigraphy of the Salar de Atacama Basin, Antofagasta, Northern Chile: Implications for the tectonic evolution of the Central Andes: Tectonophysics, v. 399, p. 125–154, doi:10.1016/j.tecto.2004.12.019.

Mpodozis, C., Cornejo, P., Kay, S.M., and Tittler, A., 1995, La Franja de Maricunga: Síntesis de la evolución del frente volcánico oligoceno-mioceno de la zona sur sur de los Andes Centrales: Revista Geológica de Chile, v. 22, p. 273–314.

Mpodozis, C., Kay, S.M., Gardeweg, M., and Coira, B.L., 1996, Geología de la región Ojos del Salado (Andes Centrales, 27ºS): implicancias de la migración hacia el este del frente volcánico Cenozoico Superior: XIII Congreso Geológico Argentino, v. Actas III, p. 539–548.

Mulcahy, P., Chen, C., Kay, S.M., Brown, L.D., Isacks, B.L., Sandvol, E., Heit, B., Yuan, X., and Coira, B.L., 2014, Central Andean mantle and crustal seismicity beneath the Southern Puna plateau and the northern margin of the Chilean-Pampean flat slab: Tectonics, v. 33, p. 2013TC003393, doi:10.1002/2013TC003393.

Müller, R.D., Sdrolias, M., Gaina, C., and Roest, W.R., 2008, Age, spreading rates, and spreading asymmetry of the world's ocean crust: Geochemistry, Geophysics, Geosystems, v. 9, doi:10.1029/2007GC001743.

Mungall, J.E., 2002, Roasting the mantle: Slab melting and the genesis of major Au and Au-rich Cu deposits: Geology, v. 30, p. 915–918, doi:10.1130/0091-7613(2002)030<0915:RTMSMA>2.0.CO;2.

Müntener, O., and Ulmer, P., 2006, Experimentally derived high-pressure cumulates from hydrous arc magmas and consequences for the seismic velocity structure of lower arc crust: Geophysical Research Letters, v. 33, doi:10.1029/2006GL027629.

Naranjo, J.A., and Puig, A., 1984, Hojas Taltal y Chañaral: Servicio Nacional de Geologia y Mineria Carta Geologica de Chile.

Nowell, G.M., and Parrish, R.R., 2001, Simultaneous acquisition of isotope compositions and parent/daughter ratios by non-isotope dilution-mode Plasma Ionisation Multi-collector Mass Spectrometry (PIMMS): Special Publication-Royal Society Of Chemistry, v. 267, p. 298–310.

Nyström, J.O., Vergara, M., Morata, D., and Levi, B., 2003, Tertiary volcanism during extension in the Andean foothills of central Chile (33°15′–33°45′S): Geological Society of America Bulletin, v. 115, p. 1523–1537, doi:10.1130/B25099.1.

O'Driscoll, L.J., Richards, M.A., and Humphreys, E.D., 2012, Nazca–South America interactions and the late Eocene–late Oligocene flat-slab episode in the central Andes: Tectonics, v. 31, doi:10.1029/2011TC003036.

Oleskevich, D.A., Hyndman, R.D., and Wang, K., 1999, The updip and downdip limits to great subduction earthquakes: Thermal and structural models of Cascadia, south Alaska, SW Japan, and Chile: Journal of Geophysical Research: Solid Earth, v. 104, p. 14965–14991, doi:10.1029/1999JB900060.

Oncken, O., Boutelier, D., Dresen, G., and Schemmann, K., 2012, Strain accumulation controls failure of a plate boundary zone: Linking deformation of the Central Andes and lithosphere mechanics: Geochemistry, Geophysics, Geosystems, v. 13, doi:10.1029/2012GC004280.

Oncken, O., Hindle, D., Kley, J., Elger, K., Victor, P., and Schemmann, K., 2006, Deformation of the Central Andean Upper Plate System — Facts, Fiction, and Constraints for Plateau Models, *in* Oncken, O., Chong, G., Franz, G., Giese, P., Götze, H.-J., Ramos, V.A., Strecker, M.R., and Wigger, P. eds., The Andes: Active Subduction Orogeny, Springer Berlin Heidelberg, Frontiers in Earth Sciences, p. 3–27, doi:10.1007/978-3-540-48684-8_1.

Ottley, C.J., Pearson, D.G., and Irvine, G.J., 2003, A routine method for the dissolution of geological samples for the analysis of REE and trace elements via ICP-MS, *in* Plasma Source Mass Spectrometry: Applications and Emerging Technologies, Cambridge, Royal Society of Chemistry, v. Eds.: Holland, G. and Tanner, S. D., p. 221–230.

Ouimet, W.B., and Cook, K.L., 2010, Building the central Andes through axial lower crustal flow: Tectonics, v. 29, doi:10.1029/2009TC002460.

Pacey, A., Macpherson, C.G., and McCaffrey, K.J.W., 2013, Linear volcanic segments in the central Sunda Arc, Indonesia, identified using Hough Transform analysis: Implications for arc lithosphere control upon volcano distribution: Earth and Planetary Science Letters, v. 369–370, p. 24–33, doi:10.1016/j.epsl.2013.02.040.

Pearce, J.A., 1983, Role of the sub-continental lithosphere in magma genesis at active continental margins, *in* Hawkesworth, C.J. and Norry, M.J. eds., Continental basalts and mantle xenoliths, Nantwich, Cheshire, Shiva Publications, p. 230–249, http://orca.cf.ac.uk/8626/ (accessed October 2018).

Pearce, J.A., and Peate, D.W., 1995, Tectonic Implications of the Composition of Volcanic ARC Magmas: Annual Review of Earth and Planetary Sciences, v. 23, p. 251–285, doi:10.1146/annurev.ea.23.050195.001343.

Perkins, J.P., Ward, K.M., Silva, S.L. de, Zandt, G., Beck, S.L., and Finnegan, N.J., 2016, Surface uplift in the Central Andes driven by growth of the Altiplano Puna Magma Body: Nature Communications, v. 7, p. 13185, doi:10.1038/ncomms13185.

Perrin, A., Goes, S., Prytulak, J., Davies, D.R., Wilson, C., and Kramer, S., 2016, Reconciling mantle wedge thermal structure with arc lava thermobarometric determinations in oceanic subduction zones: Geochemistry, Geophysics, Geosystems, v. 17, p. 4105–4127, doi:10.1002/2016GC006527.

Perrin, A., Goes, S., Prytulak, J., Rondenay, S., and Davies, D.R., 2018, Mantle wedge temperatures and their potential relation to volcanic arc location: Earth and Planetary Science Letters, v. 501, p. 67–77, doi:10.1016/j.epsl.2018.08.011.

Pitcher, B.W., and Kent, A.J.R., in review, Statistics and segmentation: Using big data to assess Cascades arc compositional variability: Geochimica et Cosmochimica Acta,.

Plank, T., 2005, Constraints from Thorium/Lanthanum on Sediment Recycling at Subduction Zones and the Evolution of the Continents: Journal of Petrology, v. 46, p. 921–944, doi:10.1093/petrology/egi005.

Plank, T., and Langmuir, C.H., 1988, An evaluation of the global variations in the major element chemistry of arc basalts: Earth and Planetary Science Letters, v. 90, p. 349–370, doi:10.1016/0012-821X(88)90135-5.

Plank, T., and Langmuir, C.H., 1998, The chemical composition of subducting sediment and its consequences for the crust and mantle: Chemical Geology, v. 145, p. 325–394, doi:10.1016/S0009-2541(97)00150-2.

Profeta, L., Ducea, M.N., Chapman, J.B., Paterson, S.R., Gonzales, S.M.H., Kirsch, M., Petrescu, L., and DeCelles, P.G., 2015a, Quantifying crustal thickness over time in magmatic arcs: Scientific Reports, v. 5, p. 17786, doi:10.1038/srep17786.

Profeta, L., Ducea, M.N., Chapman, J.B., Paterson, S.R., Gonzales, S.M.H., Kirsch, M., Petrescu, L., and DeCelles, P.G., 2015b, Quantifying crustal thickness over time in magmatic arcs: Scientific Reports, v. 5, doi:10.1038/srep17786.

Ramos, V.A., 2008, The Basement of the Central Andes: The Arequipa and Related Terranes: Annual Review of Earth and Planetary Sciences, v. 36, p. 289–324, doi:10.1146/annurev.earth.36.031207.124304.

Ramos, V.A., and Folguera, A., 2009, Andean flat-slab subduction through time: Geological Society, London, Special Publications, v. 327, p. 31–54, doi:10.1144/SP327.3.

Rapp, R.P., and Watson, E.B., 1995, Dehydration Melting of Metabasalt at 8–32 kbar: Implications for Continental Growth and Crust-Mantle Recycling: Journal of Petrology, v. 36, p. 891–931, doi:10.1093/petrology/36.4.891.

Rees Jones, D.W., Katz, R.F., Tian, M., and Rudge, J.F., 2018, Thermal impact of magmatism in subduction zones: Earth and Planetary Science Letters, v. 481, p. 73–79, doi:10.1016/j.epsl.2017.10.015.

Reiners, P.W. et al., 2015, Low-temperature thermochronologic trends across the central Andes, 21°S–28°S: Geological Society of America Memoirs, v. 212, p. 215–249, doi:10.1130/2015.1212(12).

Reutter, K.-J. et al., 2006, The Salar de Atacama Basin: a Subsiding Block within the Western Edge of the Altiplano-Puna Plateau, *in* Oncken, O., Chong, G., Franz, G., Giese, P., Götze, H.-J., Ramos, V.A., Strecker, M.R., and Wigger, P. eds., The Andes: Active Subduction Orogeny, Berlin, Heidelberg, Springer Berlin Heidelberg, Frontiers in Earth Sciences, p. 303–325, doi:10.1007/978-3-540-48684-8_14.

Richards, J.P., 2003, Tectono-Magmatic Precursors for Porphyry Cu-(Mo-Au) Deposit Formation: Economic Geology, v. 98, p. 1515–1533, doi:10.2113/gsecongeo.98.8.1515.

Rodríguez-González, J., Billen, M.I., and Negredo, A.M., 2014, Non-steady-state subduction and trench-parallel flow induced by overriding plate structure: Earth and Planetary Science Letters, v. 401, p. 227–235, doi:10.1016/j.epsl.2014.06.013.

Rodríguez-González, J., Negredo, A.M., and Billen, M.I., 2012, The role of the overriding plate thermal state on slab dip variability and on the occurrence of flat subduction: Geochemistry, Geophysics, Geosystems, v. 13, doi:10.1029/2011GC003859.

Rogers, G., and Hawkesworth, C.J., 1989, A geochemical traverse across the North Chilean Andes: evidence for crust generation from the mantle wedge: Earth and Planetary Science Letters, v. 91, p. 271–285, doi:10.1016/0012-821X(89)90003-4.

Rosenbaum, G., Giles, D., Saxon, M., Betts, P.G., Weinberg, R.F., and Duboz, C., 2005, Subduction of the Nazca Ridge and the Inca Plateau: Insights into the formation of ore deposits in Peru: Earth and Planetary Science Letters, v. 239, p. 18–32, doi:10.1016/j.epsl.2005.08.003.

Rosenbaum, G., and Mo, W., 2011, Tectonic and magmatic responses to the subduction of high bathymetric relief: Gondwana Research, v. 19, p. 571–582, doi:10.1016/j.gr.2010.10.007.

Rossel, P., Oliveros, V., Ducea, M.N., Charrier, R., Scaillet, S., Retamal, L., and Figueroa, O., 2013, The Early Andean subduction system as an analog to island arcs: Evidence from across-arc geochemical variations in northern Chile: Lithos, v. 179, p. 211–230, doi:10.1016/j.lithos.2013.08.014.

Rossel, P., Oliveros, V., Ducea, M.N., and Hernandez, L., 2015, Across and along arc geochemical variations in altered volcanic rocks: Evidence from mineral chemistry of Jurassic lavas in northern Chile, and tectonic implications: Lithos, v. 239, p. 97–113, doi:10.1016/j.lithos.2015.10.002.

Rudnick, R.L., 1995, Making continental crust: Nature, v. 378, p. 571–578, doi:10.1038/378571a0.

Rudnick, R.L., and Fountain, D.M., 1995, Nature and composition of the continental crust: A lower crustal perspective: Reviews of Geophysics, v. 33, p. 267–309, doi:10.1029/95RG01302.

Salters, V.J.M., and Stracke, A., 2004, Composition of the depleted mantle: Geochemistry, Geophysics, Geosystems, v. 5, doi:10.1029/2003GC000597.

Sarbas, B., Nohl, U., Busch, U., and Kalbskopf, B., 2018, GEOROC:, http://georoc.mpch-mainz.gwdg.de/georoc/ (accessed August 2018).

Saylor, J.E., and Horton, B.K., 2014, Nonuniform surface uplift of the Andean plateau revealed by deuterium isotopes in Miocene volcanic glass from southern Peru: Earth and Planetary Science Letters, v. 387, p. 120–131, doi:10.1016/j.epsl.2013.11.015.

Schellart, W.P., 2004, Quantifying the net slab pull force as a driving mechanism for plate tectonics: Geophysical Research Letters, v. 31, doi:10.1029/2004GL019528.

Schellart, W.P., and Rawlinson, N., 2010, Convergent plate margin dynamics: New perspectives from structural geology, geophysics and geodynamic modelling: Tectonophysics, v. 483, p. 4–19, doi:10.1016/j.tecto.2009.08.030.

Schepers, G., van Hinsbergen, D.J.J., Spakman, W., Kosters, M.E., Boschman, L.M., and McQuarrie, N., 2017, South-American plate advance and forced Andean trench retreat as drivers for transient flat subduction episodes: Nature Communications, v. 8, doi:10.1038/ncomms15249.

Schildgen, T.F., Ehlers, T.A., Whipp, D.M., van Soest, M.C., Whipple, K.X., and Hodges, K.V., 2009, Quantifying canyon incision and Andean Plateau surface uplift, southwest Peru: A thermochronometer and numerical modeling approach: Journal of Geophysical Research: Earth Surface, v. 114, p. F04014, doi:10.1029/2009JF001305.

Schildgen, T.F., and Hoke, G.D., 2018, The Topographic Evolution of the Central Andes: Elements, v. 14, p. 231–236, doi:10.2138/gselements.14.4.231.

Schmidt, M.E., Grunder, A.L., and Rowe, M.C., 2008, Segmentation of the Cascade Arc as indicated by Sr and Nd isotopic variation among diverse primitive basalts: Earth and Planetary Science Letters, v. 266, p. 166–181, doi:10.1016/j.epsl.2007.11.013.

Scire, A., Zandt, G., Beck, S., Long, M., Wagner, L., Minaya, E., and Tavera, H., 2016, Imaging the transition from flat to normal subduction: variations in the structure of the Nazca slab and upper mantle under southern Peru and northwestern Bolivia: Geophysical Journal International, v. 204, p. 457–479, doi:10.1093/gji/ggv452.

Scott, E.M., Allen, M.B., Macpherson, C.G., McCaffrey, K.J.W., Davidson, J.P., Saville, C., and Ducea, M.N., 2018, Andean surface uplift constrained by radiogenic isotopes of arc lavas: Nature Communications, v. 9, no. 969, doi:10.1038/s41467-018-03173-4.

Sdrolias, M., and Müller, R.D., 2006, Controls on back-arc basin formation: Geochemistry, Geophysics, Geosystems, v. 7, doi:10.1029/2005GC001090.

Servicio Nacional de Geología y Minería, 2003, Mapa Geológico de Chile: Sernageomin.

Seton, M. et al., 2012, Global continental and ocean basin reconstructions since 200Ma: Earth-Science Reviews, v. 113, p. 212–270, doi:10.1016/j.earscirev.2012.03.002.

de Silva, S.L., and Francis, P.W., 1991, Volcanoes of the central Andes: Berlin Heidelberg, Springer-Verlag.

de Silva, S.L., and Kay, S.M., 2018, Turning up the Heat: High-Flux Magmatism in the Central Andes: Elements, v. 14, p. 245–250, doi:10.2138/gselements.14.4.245.

Sisson, T.W., and Grove, T.L., 1993, Experimental investigations of the role of H2O in calc-alkaline differentiation and subduction zone magmatism: Contributions to Mineralogy and Petrology, v. 113, p. 143–166, doi:10.1007/BF00283225.

Smithsonian Institution, 2013, Global Volcanism Program: Volcanoes of the World, v. 4.7.1, https://volcano.si.edu/ (accessed August 2018).

Sobolev, S.V., and Babeyko, A.Y., 2005, What drives orogeny in the Andes? Geology, v. 33, p. 617–620, doi:10.1130/G21557AR.1.

Solano, J.M.S., Jackson, M.D., Sparks, R.S.J., Blundy, J.D., and Annen, C., 2012, Melt Segregation in Deep Crustal Hot Zones: a Mechanism for Chemical Differentiation, Crustal Assimilation and the

Formation of Evolved Magmas: Journal of Petrology, v. 53, p. 1999–2026, doi:10.1093/petrology/egs041.

Spinelli, G.A., Wada, I., He, J., and Perry, M., 2016, The thermal effect of fluid circulation in the subducting crust on slab melting in the Chile subduction zone: Earth and Planetary Science Letters, v. 434, p. 101–111, doi:10.1016/j.epsl.2015.11.031.

Stadler, G., Gurnis, M., Burstedde, C., Wilcox, L.C., Alisic, L., and Ghattas, O., 2010, The Dynamics of Plate Tectonics and Mantle Flow: From Local to Global Scales: Science, v. 329, p. 1033–1038, doi:10.1126/science.1191223.

Stern, C.R., 1991, Role of subduction erosion in the generation of Andean magmas: Geology, v. 19, p. 78–81, doi:10.1130/0091-7613(1991)019<0078:ROSEIT>2.3.CO;2.

Stern, C.R., and Kilian, R., 1996, Role of the subducted slab, mantle wedge and continental crust in the generation of adakites from the Andean Austral Volcanic Zone: Contributions to Mineralogy and Petrology, v. 123, p. 263–281, doi:10.1007/s004100050155.

Sun, S.–., and McDonough, W.F., 1989, Chemical and isotopic systematics of oceanic basalts: implications for mantle composition and processes: Geological Society, London, Special Publications, v. 42, p. 313–345, doi:10.1144/GSL.SP.1989.042.01.19.

Syracuse, E.M., van Keken, P.E., and Abers, G.A., 2010, The global range of subduction zone thermal models: Physics of the Earth and Planetary Interiors, v. 183, p. 73–90, doi:10.1016/j.pepi.2010.02.004.

Syracuse, E.M., Maceira, M., Prieto, G.A., Zhang, H., and Ammon, C.J., 2016, Multiple plates subducting beneath Colombia, as illuminated by seismicity and velocity from the joint inversion of seismic and gravity data: Earth and Planetary Science Letters, v. 444, p. 139–149, doi:10.1016/j.epsl.2016.03.050.

Tackley, P.J., 2000, Mantle Convection and Plate Tectonics: Toward an Integrated Physical and Chemical Theory: Science, v. 288, p. 2002–2007, doi:10.1126/science.288.5473.2002.

Tao, W.C., and O'Connell, R.J., 1992, Ablative subduction: A two-sided alternative to the conventional subduction model: Journal of Geophysical Research: Solid Earth, v. 97, p. 8877–8904, doi:10.1029/91JB02422.

Tassara, A., and Echaurren, A., 2012, Anatomy of the Andean subduction zone: three-dimensional density model upgraded and compared against global-scale models: Geophysical Journal International, v. 189, p. 161–168, doi:10.1111/j.1365-246X.2012.05397.x.

Tilton, G.R., and Barreiro, B.A., 1980, Origin of Lead in Andean Calc-Alkaline Lavas, Southern Peru: Science, v. 210, p. 1245–1247, doi:10.1126/science.210.4475.1245.

Tormey, D.R., Hickey-Vargas, R., Frey, F.A., and Lopez-Escobar, L., 1991, Recent lavas from the Andean volcanic front (33 to 42 °S); Interpretations of along-arc compositional variations, *in* Andean Magmatism and its Tectonic Setting, Boulder, Colorado, Geological Society of America Special Paper, 265.

Tosdal, R.M., 1996, The Amazon-Laurentian connection as viewed from the Middle Proterozoic rocks in the central Andes, western Bolivia and northern Chile: Tectonics, v. 15, p. 827–842, doi:10.1029/95TC03248.

Trumbull, R.B., Riller, U., Oncken, O., Scheuber, E., Munier, K., and Hongn, F., 2006, The Time-Space Distribution of Cenozoic Volcanism in the South-Central Andes: a New Data Compilation and Some Tectonic Implications, *in* Oncken, O., Chong, G., Franz, G., Giese, P., Götze, H.-J., Ramos, V.A., Strecker, M.R., and Wigger, P. eds., The Andes, Springer Berlin Heidelberg, Frontiers in Earth Sciences, p. 29–43, doi:10.1007/978-3-540-48684-8_2.

Trumbull, R.B., Wittenbrink, R., Hahne, K., Emmermann, R., Büsch, W., Gerstenberger, H., and Siebel, W., 1999, Evidence for Late Miocene to Recent contamination of arc andesites by crustal melts in the Chilean Andes (25–26°S) and its geodynamic implications: Journal of South American Earth Sciences, v. 12, p. 135–155, doi:10.1016/S0895-9811(99)00011-5.

Turcotte, D.L., and Oxburgh, E.R., 1972, Mantle Convection and the New Global Tectonics: Annual Review of Fluid Mechanics, v. 4, p. 33–66, doi:10.1146/annurev.fl.04.010172.000341.

Turner, S.J., and Langmuir, C.H., 2015a, The global chemical systematics of arc front stratovolcanoes: Evaluating the role of crustal processes: Earth and Planetary Science Letters, v. 422, p. 182–193, doi:10.1016/j.epsl.2015.03.056.

Turner, S.J., and Langmuir, C.H., 2015b, What processes control the chemical compositions of arc front stratovolcanoes? Geochemistry, Geophysics, Geosystems, v. 16, p. 1865–1893, doi:10.1002/2014GC005633.

Turner, S.J., Langmuir, C.H., Dungan, M.A., and Escrig, S., 2017, The importance of mantle wedge heterogeneity to subduction zone magmatism and the origin of EM1: Earth and Planetary Science Letters, v. 472, p. 216–228, doi:10.1016/j.epsl.2017.04.051.

Turner, S.J., Langmuir, C.H., Katz, R.F., Dungan, M.A., and Escrig, S., 2016, Parental arc magma compositions dominantly controlled by mantle-wedge thermal structure: Nature Geoscience, v. 9, p. 772–776, doi:10.1038/ngeo2788.

Ulmer, P., and Trommsdorff, V., 1995, Serpentine Stability to Mantle Depths and Subduction-Related Magmatism: Science, v. 268, p. 858–861, doi:10.1126/science.268.5212.858.

US Geological Survey, 1996, GTOPO30 Global Digital Elevation Model: Sioux Falls, South Dakota, EROS Data Center, https://lta.cr.usgs.gov/GTOPO30.

Van Westrenen, W., Blundy, J., and Wood, B., 1999, Crystal-chemical controls on trace element partitioning between garnet and anhydrous silicate melt: American Mineralogist, v. 84, p. 838–847, doi:10.2138/am-1999-5-618.

Völker, D., Kutterolf, S., and Wehrmann, H., 2011, Comparative mass balance of volcanic edifices at the southern volcanic zone of the Andes between 33°S and 46°S: Journal of Volcanology and Geothermal Research, v. 205, p. 114–129, doi:10.1016/j.jvolgeores.2011.03.011.

Walker, B.A., Bergantz, G.W., Otamendi, J.E., Ducea, M.N., and Cristofolini, E.A., 2015, A MASH Zone Revealed: the Mafic Complex of the Sierra Valle Fértil: Journal of Petrology, v. 56, p. 1863–1896, doi:10.1093/petrology/egv057.

Ward, K.M., Zandt, G., Beck, S.L., Christensen, D.H., and McFarlin, H., 2014, Seismic imaging of the magmatic underpinnings beneath the Altiplano-Puna volcanic complex from the joint inversion of surface wave dispersion and receiver functions: Earth and Planetary Science Letters, v. 404, p. 43–53, doi:10.1016/j.epsl.2014.07.022.

Watts, A.B., 2001, Isostasy and Flexure of the Lithosphere: Cambridge University Press, 508 p.

Weertman, J., and Weertman, J.R., 1975, High Temperature Creep of Rock and Mantle Viscosity: Annual Review of Earth and Planetary Sciences, v. 3, p. 293–315, doi:10.1146/annurev.ea.03.050175.001453.

Weill, D.F., and Drake, M.J., 1973, Europium Anomaly in Plagioclase Feldspar: Experimental Results and Semiquantitative Model: Science, v. 180, p. 1059–1060, doi:10.1126/science.180.4090.1059.

Weis, D., Kieffer, B., Maerschalk, C., Pretorius, W., and Barling, J., 2005, High-precision Pb-Sr-Nd-Hf isotopic characterization of USGS BHVO-1 and BHVO-2 reference materials: Geochemistry, Geophysics, Geosystems, v. 6, doi:10.1029/2004GC000852.

Wieser, P.E., Turner, S.J., Mather, T.A., Pyle, D.M., Savov, I.P., and Orozco, G., in review, New constraints from Central Chile on the origins of enriched continental compositions in thick-crusted arc magmas: Geochimica et Cosmochimica Acta,.

Williams, W., 1992, Magmatic and structural controls on mineralization in the Paleocene magmatic arc between 22°40′ and 23°45′S, Antofagasta II Region, Chile [Unpubl. doctoral dissertation]: University of Arizona.

Workman, R.K., and Hart, S.R., 2005, Major and trace element composition of the depleted MORB mantle (DMM): Earth and Planetary Science Letters, v. 231, p. 53–72, doi:10.1016/j.epsl.2004.12.005.

Wörner, G., Lezaun, J., Beck, A., Heber, V., Lucassen, F., Zinngrebe, E., Rössling, R., and Wilke, H.G., 2000, Precambrian and Early Paleozoic evolution of the Andean basement at Belen (northern Chile) and Cerro Uyarani (western Bolivia Altiplano): Journal of South American Earth Sciences, v. 13, p. 717–737, doi:10.1016/S0895-9811(00)00056-0.

Wörner, G., Mamani, M., and Blum-Oeste, M., 2018, Magmatism in the Central Andes: Elements, v. 14, p. 237–244, doi:10.2138/gselements.14.4.237.

Wotzlaw, J.F., Decou, A., von Eynatten, H., Wörner, G., and Frei, D., 2011, Jurassic to Palaeogene tectono-magmatic evolution of northern Chile and adjacent Bolivia from detrital zircon U-Pb geochronology and heavy mineral provenance: Terra Nova, v. 23, p. 399–406, doi:10.1111/j.1365-3121.2011.01025.x.

Yoder, H.S., and Tilley, C.E., 1962, Origin of Basalt Magmas: An Experimental Study of Natural and Synthetic Rock Systems: Journal of Petrology, v. 3, p. 342–532, doi:10.1093/petrology/3.3.342.

Zentilli, M., Stark, A., Reynolds, P.H., Muija, T., Walker, J.A., and Ulriksen, C.E., 1991, Native sulphur deposits as the crown of epithermal systems? - isotopic and geochronological data on volcan Copiapó Complex, Maricunga, Northern Chile: VI Congreso Geológico Chileno, v. Resúmenes expandidos, p. 616–620.

Zhang, F., Lin, J., Zhou, Z., Yang, H., and Zhan, W., 2018, Intra- and intertrench variations in flexural bending of the Manila, Mariana and global trenches: implications on plate weakening in controlling trench dynamics: Geophysical Journal International, v. 212, p. 1429–1449, doi:10.1093/gji/ggx488.

Zhou, R., Schoenbohm, L.M., Sobel, E.R., Davis, D.W., and Glodny, J., 2017, New constraints on orogenic models of the southern Central Andean Plateau: Cenozoic basin evolution and bedrock exhumation: Geological Society of America Bulletin, v. 129, p. 152–170, doi:10.1130/B31384.1.

Zindler, A., and Hart, S., 1986, Chemical Geodynamics: Annual Review of Earth and Planetary Sciences, v. 14, p. 493–571, doi:10.1146/annurev.ea.14.050186.002425.

8 Appendix

8.1 Statistical methods used in Chapters 2, 3 and 4

8.1.1 Linear regression statistics

Residuals are the difference between observed or 'real' y values and y values predicted by a linear model (in the form: $y = mx + c$). A vector data set with n values marked $y_1,...,y_n$ (the 'real' values, shorthand: y_i), can each be associated with a predicted value $f_1,...,f_n$ (shorthand: f_i) from a linear model based on a relationship with $x_1,...,x_n$ (shorthand: x_i).

A vector of residuals (e_i) can be defined as follows:

Equation 2

$$e_i = y_i - f_i$$

Positive residual values show that the observed value of y is higher than would be predicted by the corresponding value of x. Negative residuals are when the observed y value is lower than would be predicted by the corresponding x value.

Correlation coefficient ('r') is a measure of the linear correlation between two variables (y_i and x_i) and has values ranging between 1 and -1. 'r' is calculated by dividing a measure of the covariance between two variables by the product of their standard deviations. For example:

Equation 3

$$r = \frac{\sum x_i\, y_i - n\bar{x}\bar{y}}{\sqrt{(\sum x_i^2 - n\bar{x}^2)}\sqrt{(\sum y_i^2 - n\bar{y}^2)}}$$

Where $\bar{x}$ and $\bar{y}$ are sample means.

Coefficient of Determination (R^2) describes what proportion of the variance in y_i that can be predicted by the corresponding value of x_i. Values of R^2 range between 0 and 1 (or 0 and 100%). If $R^2 = 0.85$, then 85% of variability in the observed values (y_i) can be predicted by the linear regression model. The remaining 15% of variability in y_i is termed the fraction of variance unexplained (FVU), which can be used as a judge of the model errors.

R^2 is calculated by taking the 'residual sum of squares' over the 'total sum of squares', subtracted from one:

Equation 4

$$R^2 = 1 - \frac{\sum_i (e_i)^2}{\sum_i (y_i - \bar{y})^2}$$

For simple linear least squares regression with only one independent and one dependent variable, R^2 is equal to the square of the correlation coefficient ('r'), and in such cases can be written as 'r^2'.

Significance (F Statistic and P-value) describes the probability of getting the same distribution of data using a random population where there is no dependent relationship between the two variables. A measure of significance of a correlation is the *P-value* which is determined by the F statistic. The *P-value* is the probability that the fit of the data to the statistical model is due to chance. For example, a *P-value* of 0.05 suggests that there is only a 5% chance that the data distribution observed would occur randomly and a 95% chance that the model predictions are accurate. This is specified as the 95% confidence level. For any given regression analysis here the null hypothesis is rejected if the p-value >0.05 as the model is deemed statistically insignificant.

8.2 Crustal thickness, elevation and isostasy (Chapters 3 & 4)

In Chapter 4, the interpretation of strong correlations between smoothed elevation and isotope signatures depend on the control of crustal thickness on arc front geochemistry (explored in Chapter 3). In this section, we explore the dependency of elevation on crustal thickness in the Andes, both along the volcanic arc (Figure 57) and within the South American continent (Figure 58 and Figure 59).

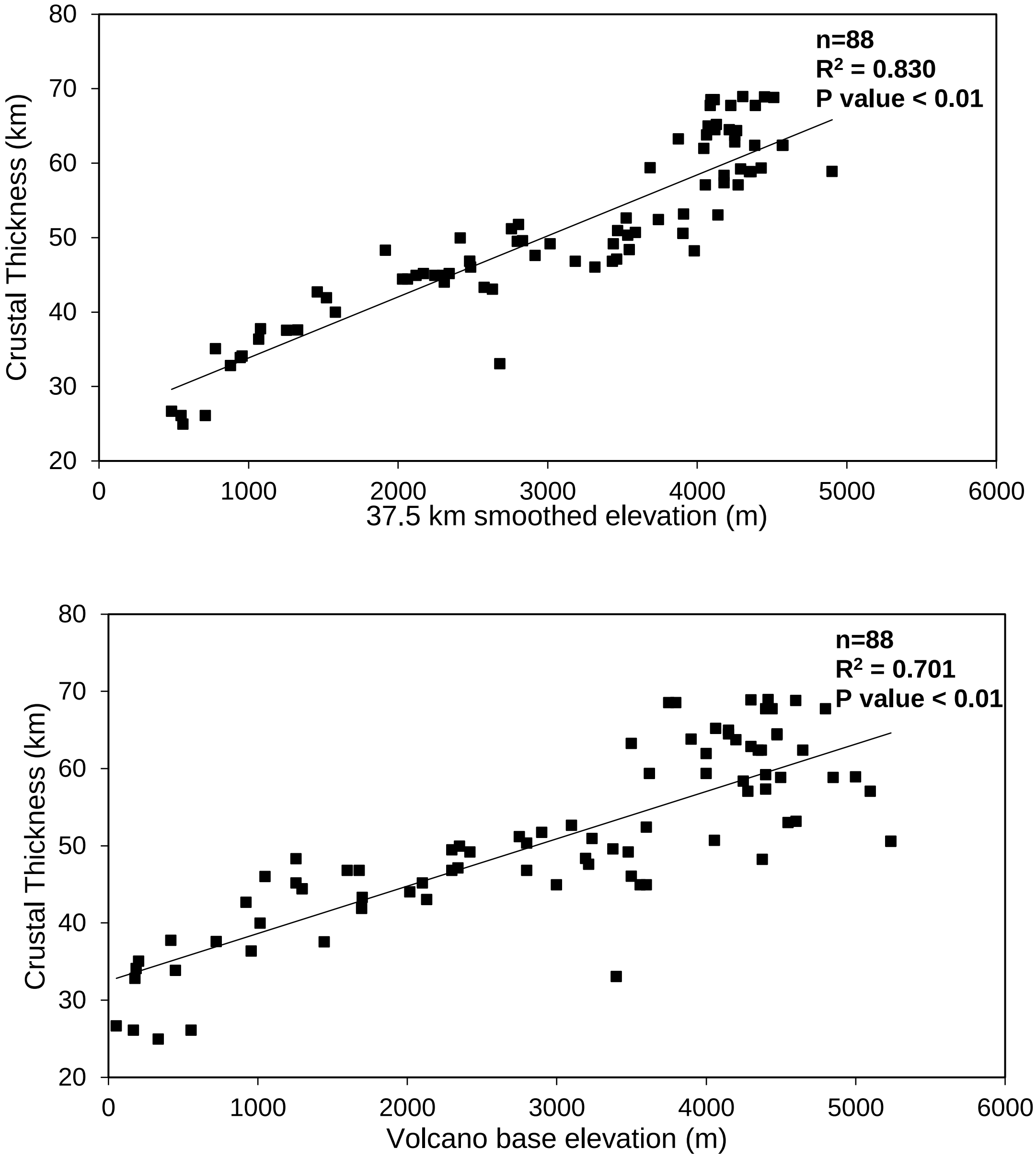

Figure 57: Statistical comparison of crustal thickness and elevation at Andean arc volcanoes. Crustal thickness (ref. Assumpção et al., 2013; RMS <3.5 km) and volcano base elevation (refs. de Silva and Francis, 1991; Völker et al., 2011) and Methods) data are the same as Figure 1. Smoothed elevation (same as Figure 3) was calculated using focal statistics on Shuttle Radar Topography Mission DEMs (SRTM, 90 m pixel resolution; ref. (Farr et al., 2007). A radius of 37.5 km was selected as this is half of the maximum crustal thickness in the Andean Plateau.

Linear regression analysis is performed between smoothed DEMs (Farr et al., 2007) and geophysical estimates of crustal thickness (Assumpção et al., 2013). The principle of isostasy states that areas of high elevation must be supported underneath by a buoyant crustal root. If this is the case in the Andes, it would be expected that elevation depends on crustal thickness by a linear relationship. For this analysis, crustal thickness data from the model of Assumpção et al. (2013) are used as this crustal thickness model is an updated version of the model of (Tassara and Echaurren, 2012), and is specific to crustal thickness only. The RMS (root mean squared) misfit quoted for crustal thickness estimates ranges between 1.7-4.7 km (Assumpção et al., 2013). The higher quoted error of 4.7 km is taken into account in the regression analysis of this study and displayed as error bars on Figure 58. Crustal thickness data are contained in a grid file of 1° latitude by 1° longitude spacing and loaded into ArcGIS™ along with the 37.5 km smoothed digital elevation model. Values of smoothed elevation are then extracted for each crustal thickness grid. Linear regression analysis is performed (Figure 58) and a statistically significant correlation found (P value < 0.05).

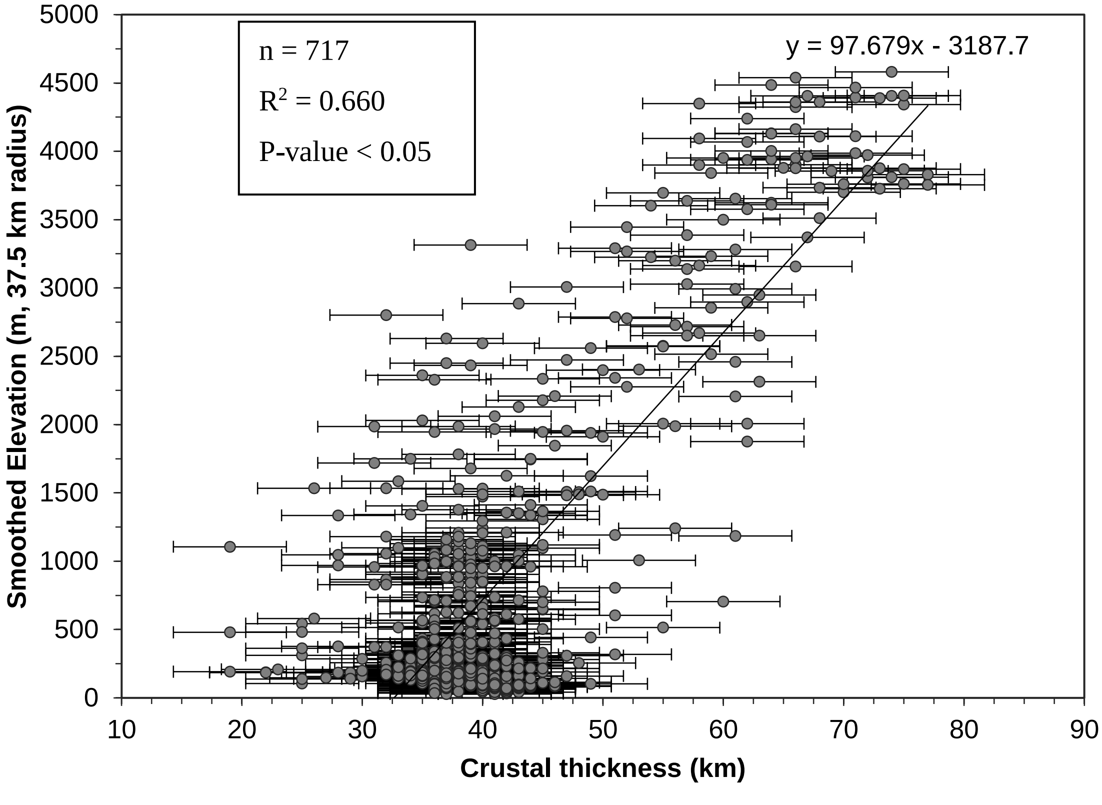

Figure 58: Linear regression model between crustal thickness and elevation for the South American Continent. Error bars on crustal thickness estimates are set as 4.7 km (the largest RMS error quoted by (Assumpção et al., 2013).

To find which locations in the Andes do not follow the principle of isostasy, residuals (e_i) from the linear regression line are calculated for each grid point. Residuals are plotted back on the topographic map and colour coded by their value (Figure 59). Sedimentary basins (including the Amazonian basin; the foreland basin to the west of the Columbian and Ecuadorian Andes; and the intramountain basin between the Western Cordillera and Sierras Pampeanas at ~30°

S) have elevations lower than would be predicted for their corresponding crustal thicknesses (green points; Figure 59). The majority of Andean Coastal Cordilleras have the high elevations relative to their crustal thickness (red points; Figure 59). Coastal dynamic topography at subduction zones are positive deflections at the front of the collision zone and have been related to elastic release after mega-thrust earthquakes at the plate interface. Maximum residual topography along the coast exceeds 2300 m in the areas adjacent to both the Peruvian flat slab and southern Puna Plateau.

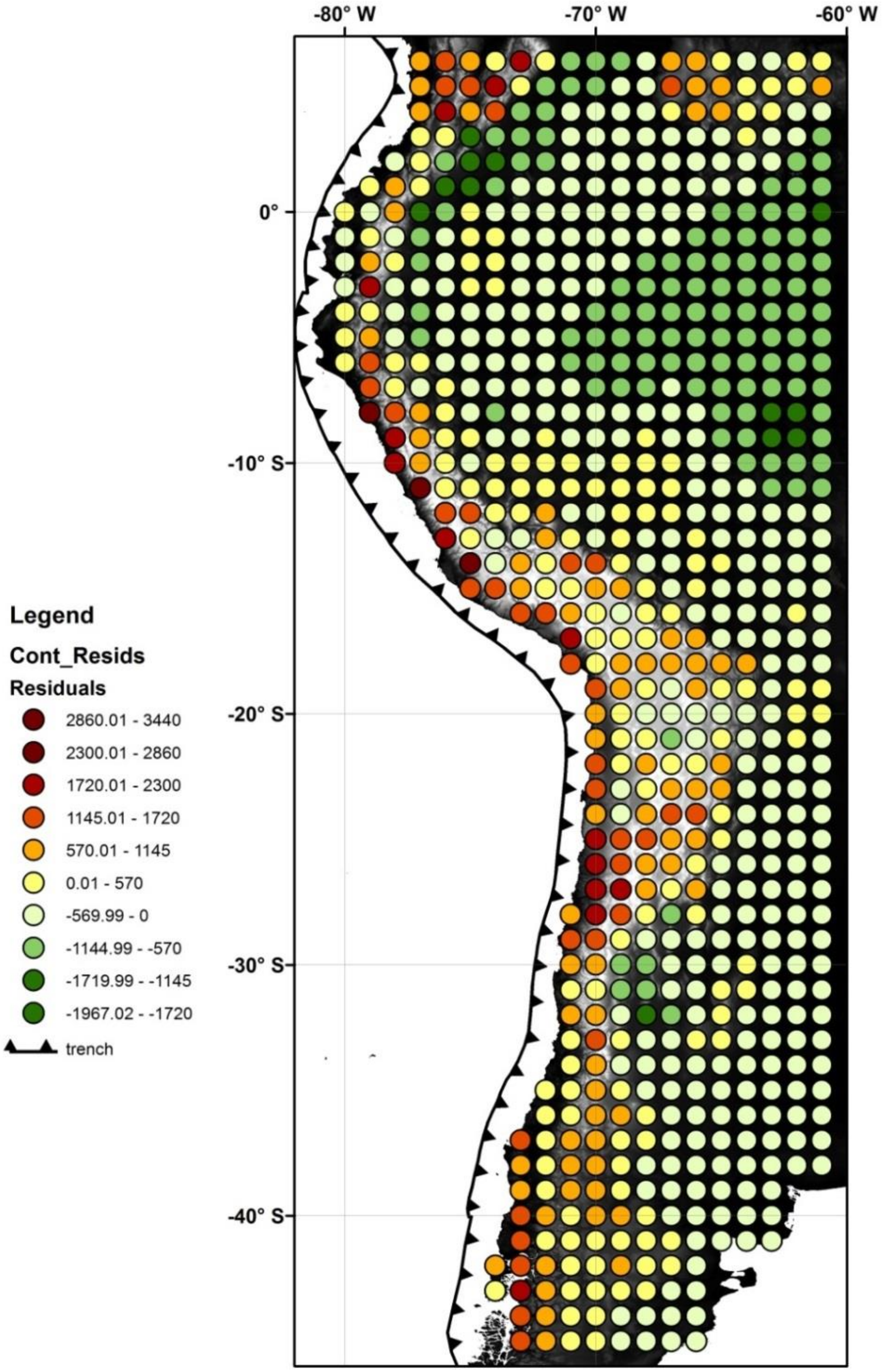

Figure 59: A map of the residuals from the linear relationship between crustal thickness and elevation in the South American continent. Yellow to orange colours are positive residuals related to elevations greater than would be predicted for their crustal thickness. Green shades are negative residuals.

8.3 Europium anomalies in Quaternary Andean lavas (Chapter 3)

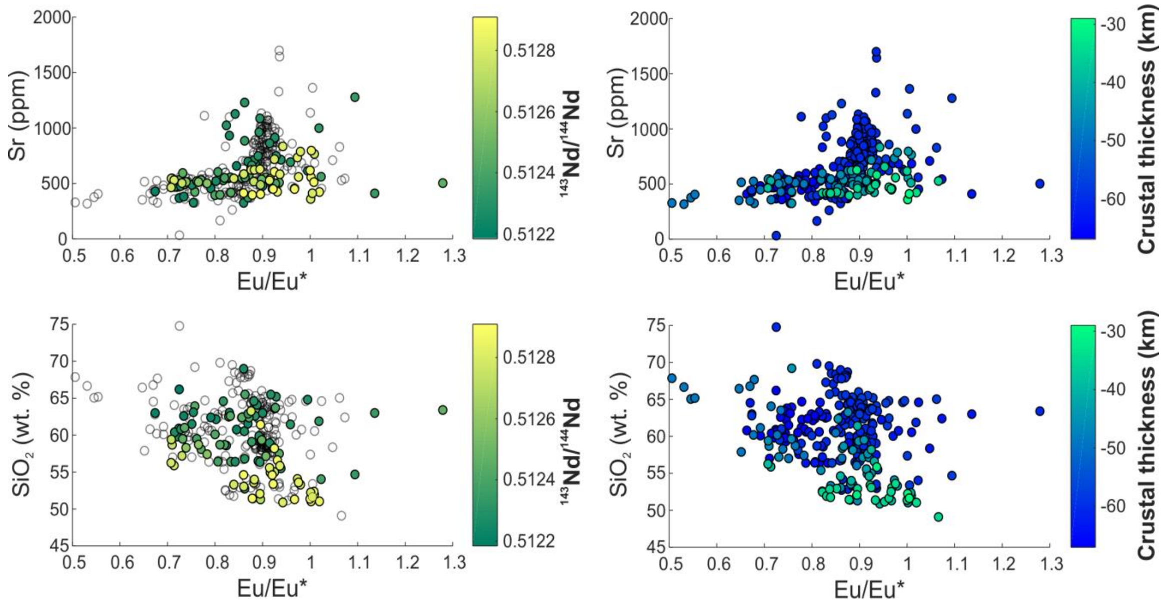

Figure 60: Eu/Eu* anomalies of SVZ and CVZ lavas plotted against Sr (ppm) and SiO$_2$ (wt. %), respectively. Eu/Eu* generally becomes more negative with increasing degrees of fractionation (higher SiO$_2$) and assimilation (lower ^{143}Nd/^{144}Nd). Samples from thin crust settings (<30 km) are relatively more mafic, with lower Sr concentrations and un-radiogenic ^{143}Nd/^{144}Nd ratios and a narrower range of Eu/Eu* (closer to 1), compared to thicker crust settings.

8.4 Sr-Sr isotope plot of Quaternary lavas (Chapters 3 & 5)

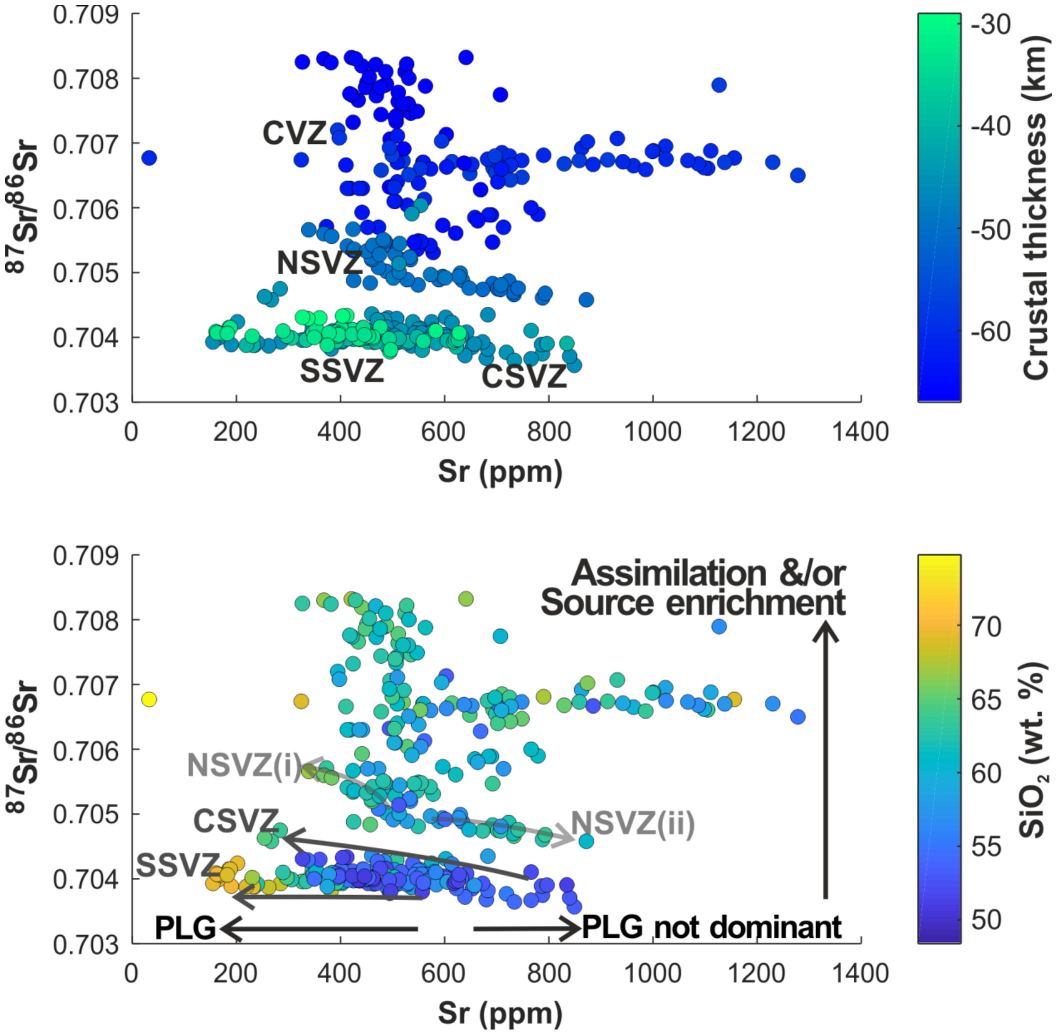

Figure 61: Sr (ppm) vs $^{87}Sr/^{86}Sr$, plotted as a function of crustal thickness and fractionation (SiO_2 content). Increasing $^{87}Sr/^{86}Sr$ ratios correspond to increasing crustal contamination or source enrichment. Decreasing Sr (ppm) contents with increasing SiO_2 indicate plagioclase dominant fractionation. Increasing Sr (ppm) with increasing SiO_2 content indicates Sr incompatibility and therefore a fractionating assemblage where plagioclase is not dominant. This plot is compared to assimilation and fractional crystallisation modelling of Central Andean Paleogene lavas and associated interpretations in Chapter 5.

8.5 References for SVZ geochemical compilation (Chapter 3)

Andersen, N.L., Singer, B.S., Jicha, B.R., Beard, B.L., Johnson, C.M., and Licciardi, J.M., 2017, Pleistocene to Holocene Growth of a Large Upper Crustal Rhyolitic Magma Reservoir beneath the Active Laguna del Maule Volcanic Field, Central Chile: Journal of Petrology, v. 58, p. 85–114, doi:10.1093/petrology/egx006.

Bouvet de Maisonneuve, C., Dungan, M.A., Bachmann, O., and Burgisser, A., 2012, Insights into shallow magma storage and crystallization at Volcán Llaima (Andean Southern Volcanic Zone, Chile): Journal of Volcanology and Geothermal Research, v. 211–212, p. 76–91, doi:10.1016/j.jvolgeores.2011.09.010.

Costa, F., and Singer, B., 2002, Evolution of Holocene Dacite and Compositionally Zoned Magma, Volcán San Pedro, Southern Volcanic Zone, Chile: Journal of Petrology, v. 43, p. 1571–1593, doi:10.1093/petrology/43.8.1571.

Davidson, J.P., Ferguson, K.M., Colucci, M.T., and Dungan, M.A., 1988, The origin and evolution of magmas from the San Pedro-Pellado volcanic complex, S. Chile: multicomponent sources and open system evolution: Contributions to Mineralogy and Petrology, v. 100, p. 429–445, doi:10.1007/BF00371373.

Deruelle, B., 1982, Petrology of the plio-quaternary volcanism of the South-Central and Meridional Andes: Journal of Volcanology and Geothermal Research, v. 14, p. 77–124, doi:10.1016/0377-0273(82)90044-0.

Deruelle, B., and Lopez-Escobar, L., 1999, Basalts, andesites, dacites and rhyolites from Nevados de Chillan and Antuco stratovolcanoes (southern Andes): a remarkable example of magmatic differentiation through crystal fractionation: Sciences de la Terre et des planetes, v. 329, p. 337–344.

Dixon, H.J., Murphy, M.D., Sparks, S.J., Chávez, R., Naranjo, J.A., Dunkley, P.N., Young, S.R., Gilbert, J.S., and Pringle, M.R., 1999, The geology of Nevados de Chillán volcano, Chile: Revista geológica de Chile, v. 26, p. 227–253, doi:10.4067/S0716-02081999000200006.

Dungan, M.A., Wulff, A., and Thompson, R., 2001, Eruptive Stratigraphy of the Tatara–San Pedro Complex, 36°S, Southern Volcanic Zone, Chilean Andes: Reconstruction Method and Implications for Magma Evolution at Long-lived Arc Volcanic Centers: Journal of Petrology, v. 42, p. 555–626, doi:10.1093/petrology/42.3.555.

Ferguson, K.M., Dungan, M.A., Davidson, J.P., and Colucci, M.T., 1992, The Tatara–San Pedro Volcano, 36 °S, Chile: A Chemically Variable, Dominantly Mafic Magmatic System: Journal of Petrology, v. 33, p. 1–43, doi:10.1093/petrology/33.1.1.

Futa, K., and Stern, C.R., 1988, Sr and Nd isotopic and trace element compositions of Quaternary volcanic centers of the Southern Andes: Earth and Planetary Science Letters, v. 88, p. 253–262, doi:10.1016/0012-821X(88)90082-9.

Gerlach, D.C., Frey, F.A., Moreno-Roa, H., and Lopez-Escobar, L., 1988, Recent Volcanism in the Puyehue—Cordon Caulle Region, Southern Andes, Chile (40·5°S): Petrogenesis of Evolved Lavas: Journal of Petrology, v. 29, p. 333–382, doi:10.1093/petrology/29.2.333.

Hickey, R.L., Frey, F.A., Gerlach, D.C., and Lopez-Escobar, L., 1986, Multiple sources for basaltic arc rocks from the southern volcanic zone of the Andes (34°–41°S): Trace element and isotopic evidence for contributions from subducted oceanic crust, mantle, and continental crust: Journal of Geophysical Research: Solid Earth, v. 91, p. 5963–5983, doi:10.1029/JB091iB06p05963.

Hickey -Vargas, R., Roa, H.M., Escobar, L.L., and Frey, F.A., 1989, Geochemical variations in Andean basaltic and silicic lavas from the Villarrica-Lanin volcanic chain (39.5° S): an evaluation of source heterogeneity, fractional crystallization and crustal assimilation: Contributions to Mineralogy and Petrology, v. 103, p. 361–386, doi:10.1007/BF00402922.

Hickey-Vargas, R., Holbik, S., Tormey, D., Frey, F.A., and Moreno Roa, H., 2016, Basaltic rocks from the Andean Southern Volcanic Zone: Insights from the comparison of along-strike and small-scale geochemical variations and their sources: Lithos, v. 258–259, p. 115–132, doi:10.1016/j.lithos.2016.04.014.

Hildreth, W., and Moorbath, S., 1988, Crustal contributions to arc magmatism in the Andes of Central Chile: Contributions to Mineralogy and Petrology, v. 98, p. 455–489, doi:10.1007/BF00372365.

Holm, P.M., Søager, N., Dyhr, C.T., and Nielsen, M.R., 2014, Enrichments of the mantle sources beneath the Southern Volcanic Zone (Andes) by fluids and melts derived from abraded upper continental crust: Contributions to Mineralogy and Petrology, v. 167, p. 1004, doi:10.1007/s00410-014-1004-8.

Jacques, G., Hoernle, K., Gill, J., Hauff, F., Wehrmann, H., Garbe-Schönberg, D., van den Bogaard, P., Bindeman, I., and Lara, L.E., 2013, Across-arc geochemical variations in the Southern Volcanic Zone, Chile (34.5–38.0°S): Constraints on mantle wedge and slab input compositions: Geochimica et Cosmochimica Acta, v. 123, p. 218–243, doi:10.1016/j.gca.2013.05.016.

Jacques, G., Hoernle, K., Gill, J., Wehrmann, H., Bindeman, I., and Lara, L.E., 2014, Geochemical variations in the Central Southern Volcanic Zone, Chile (38–43°S): The role of fluids in generating arc magmas: Chemical Geology, v. 371, p. 27–45, doi:10.1016/j.chemgeo.2014.01.015.

Lopez-Escobar, L., Cembrano, J., and Moreno, H., 1995, Geochemistry and tectonics of the Chilean Southern Andes basaltic Quaternary volcanism (37-46°S): Andean Geology, v. 22, p. 219–234, doi:10.5027/andgeoV22n2-a06.

Lopez-Escobar, L., Parada, M.A., Moreno, H., Frey, F.A., and Hickey-Vargas, R.L., 1992, A contribution to the petrogenesis of Osomo and Calbuco volcanoes, Southern Andes (41°00’-41°30’S): comparative study: Andean Geology, v. 19, p. 211–226, doi:10.5027/andgeoV19n2-a05.

Morgado, E., Parada, M.A., Contreras, C., Castruccio, A., Gutiérrez, F., and McGee, L.E., 2015, Contrasting records from mantle to surface of Holocene lavas of two nearby arc volcanic complexes: Caburgua-Huelemolle Small Eruptive Centers and Villarrica Volcano, Southern Chile: Journal of Volcanology and Geothermal Research, v. 306, p. 1–16, doi:10.1016/j.jvolgeores.2015.09.023.

Muñoz B., J., and Stern, C.R., 1988, The quaternary volcanic belt of the southern continental margin of South America: Transverse structural and petrochemical variations across the segment between 38°S and 39°S: Journal of South American Earth Sciences, v. 1, p. 147–161, doi:10.1016/0895-9811(88)90032-6.

Pioli, L., Scalisi, L., Costantini, L., Di Muro, A., Bonadonna, C., and Clavero, J., 2015, Explosive style, magma degassing and evolution in the Chaimilla eruption, Villarrica volcano, Southern Andes: Bulletin of Volcanology, v. 77, p. 93, doi:10.1007/s00445-015-0976-1.

Ruprecht, P., Bergantz, G.W., Cooper, K.M., and Hildreth, W., 2012, The Crustal Magma Storage System of Volcán Quizapu, Chile, and the Effects of Magma Mixing on Magma Diversity: Journal of Petrology, v. 53, p. 801–840, doi:10.1093/petrology/egs002.

Schindlbeck, J.C., Freundt, A., and Kutterolf, S., 2014, Major changes in the post-glacial evolution of magmatic compositions and pre-eruptive conditions of Llaima Volcano, Andean Southern Volcanic Zone, Chile: Bulletin of Volcanology, v. 76, p. 830, doi:10.1007/s00445-014-0830-x.

Sruoga, P., Llambías, E.J., Fauqué, L., Schonwandt, D., and Repol, D.G., 2005, Volcanological and geochemical evolution of the Diamante Caldera–Maipo volcano complex in the southern Andes of Argentina (34°10′S): Journal of South American Earth Sciences, v. 19, p. 399–414, doi:10.1016/j.jsames.2005.06.003.

Tormey, D.R., Frey, F.A., and Lopez-Escobar, L., 1995, Geochemistry of the Active Azufre—Planchon—Peteroa Volcanic Complex, Chile (35°15′S): Evidence for Multiple Sources and Processes in a Cordilleran Arc Magmatic System: Journal of Petrology, v. 36, p. 265–298, doi:10.1093/petrology/36.2.265.

Tormey, D.R., Hickey-Vargas, R., Frey, F.A., and Lopez-Escobar, L., 1991, Recent lavas from the Andean volcanic front (33 to 42 °S); Interpretations of along-arc compositional variations, in Andean Magmatism and its Tectonic Setting, Boulder, Colorado, Geological Society of America Special Paper, 265.

8.6 Volcano base elevation and isotopes (Chapter 4)

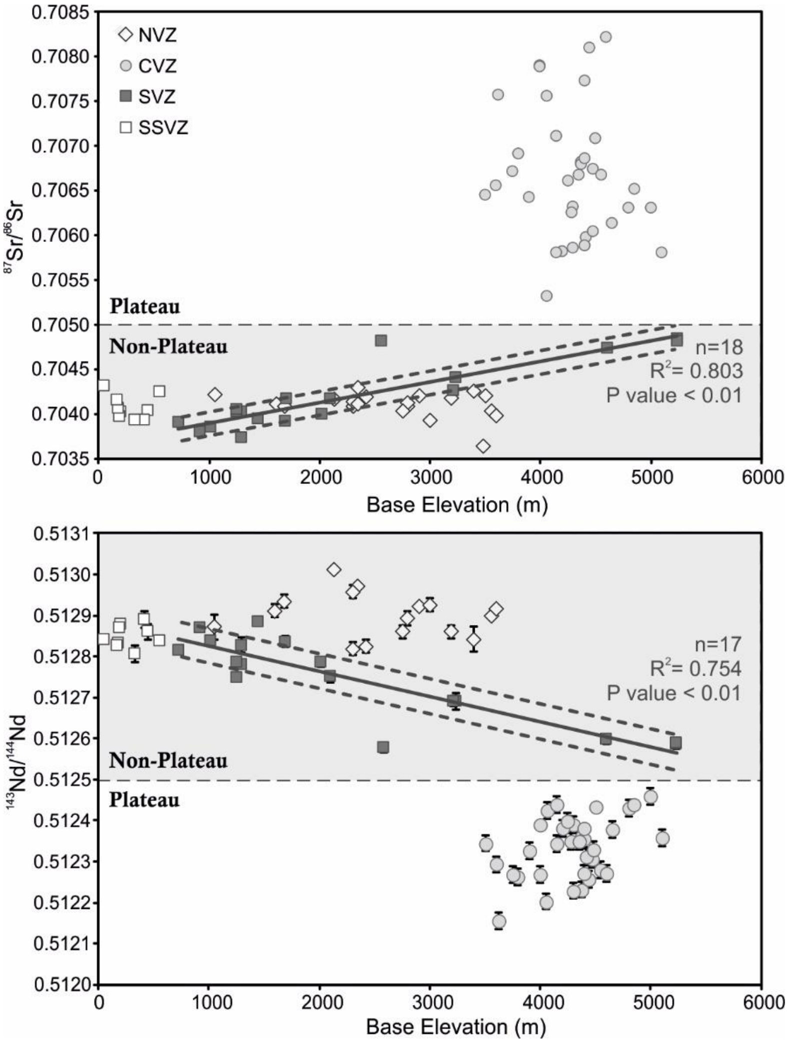

Figure 62: Baseline Sr- and Nd- isotopes as a plateau discriminant and paleoelevation proxy. Un-smoothed volcano base elevation data (refs. **de Silva and Francis, 1991; Völker et al., 2011)** and Methods) are the same as Figure 1. Baseline Sr- and Nd- data are the same as Figure 3. Linear correlations are still strong despite using different methods to obtain volcano elevations. Slopes identified using base elevation data produce paleo-base elevation estimates that are within error of smoothed elevation estimates using calibrations shown in Figure 3. The correlation between $^{143}Nd/^{144}Nd$ and volcano base elevation can be extended to include southern SVZ (south of 38.5°S, SSVZ) centres (n=27, R^2 = 0.825, P value < 0.01).

8.7 Central Andean Sr- and Nd-isotope compositions through time (Chapter 4)

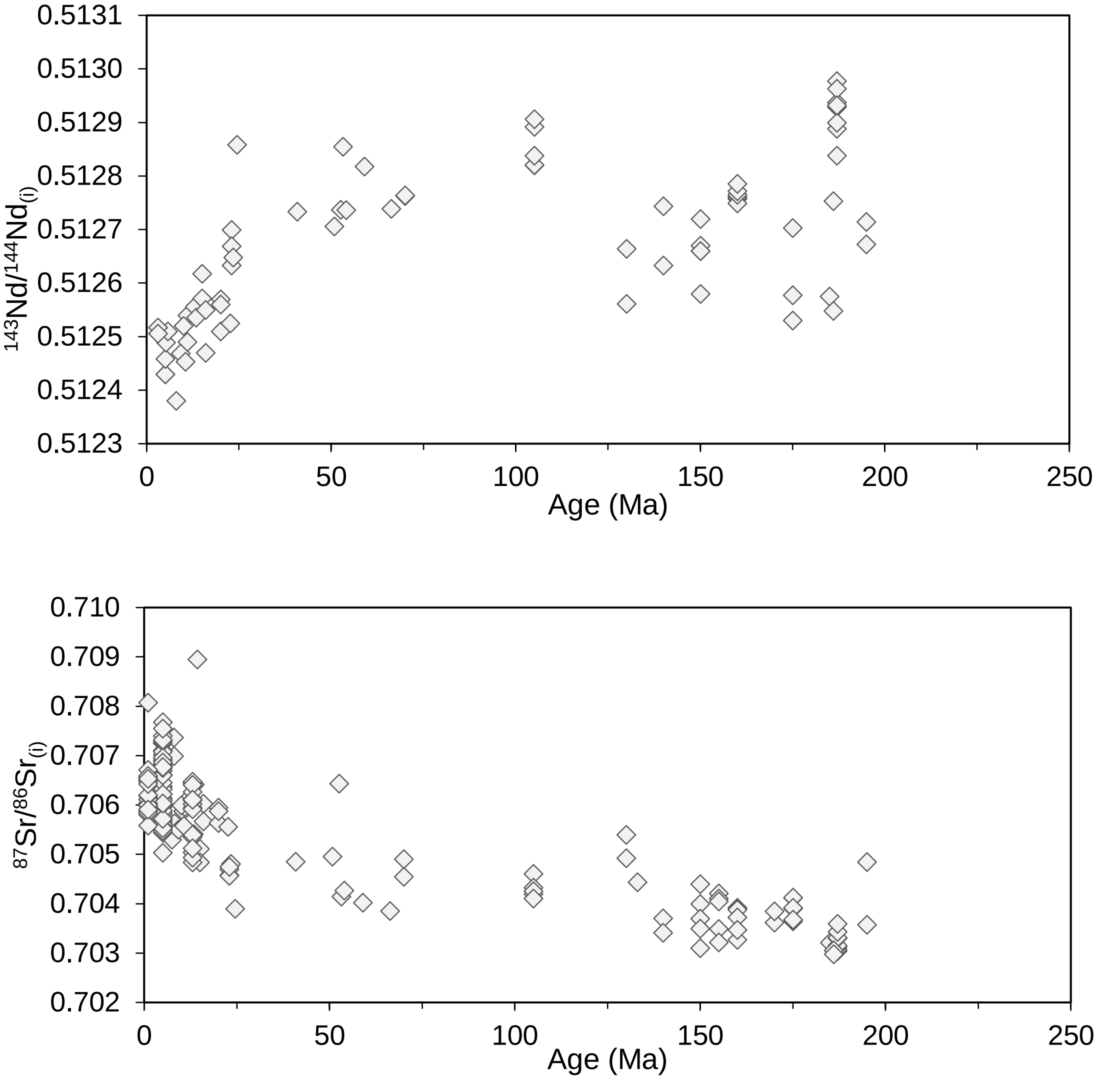

Figure 63: Evolution of age corrected Sr- (upper panel) and Nd- (lower panel) isotope ratios in Central Andean lavas through time. Data are the same as Figure 4 between 12-30° S (Electronic Appendix 3), excluding Quaternary data. This plot follows on from Haschke et al.(Haschke et al., 2002b) and the review of DeCelles et al.(DeCelles et al., 2009), including more recent analyses.

8.8 Dysprosium anomalies of Andean lavas (Chapter 5)

Mantle melting with amphibole or clinopyroxene in the residue or as a fractionating phase leads to more concave middle REE patterns, whereas garnet leads to heavy REE depletion relative to the middle REE (Davidson et al., 2013). Such trends can be shown on a plot of Dy/Dy* vs Dy/Yb (Figure 64; Davidson et al., 2013). The equation for calculating Dy/Dy* is expressed:

5

$$\frac{Dy}{Dy*} = \frac{Dy_N}{La_N^{4/13} \times Yb_N^{9/13}}$$

Some of the Segerstrom and Cachiyuyo lavas lie towards higher Dy/Yb ratios at similar range of Dy/Dy*, indicating relatively more involvement of garnet either in the source or residual mineralogy or mixing with a lower continental crust end-member (Figure 64). Quaternary CVZ lavas occupy a field spanning between mid- to upper-continental crust estimates (Rudnick and Fountain, 1995) and high pressure garnet-involvement. Jurassic and Cretaceous Central Andean lavas occupy a similar field as the Paleogene lavas, with one Jurassic sample plotting closer to the mantle end-members (Figure 64).

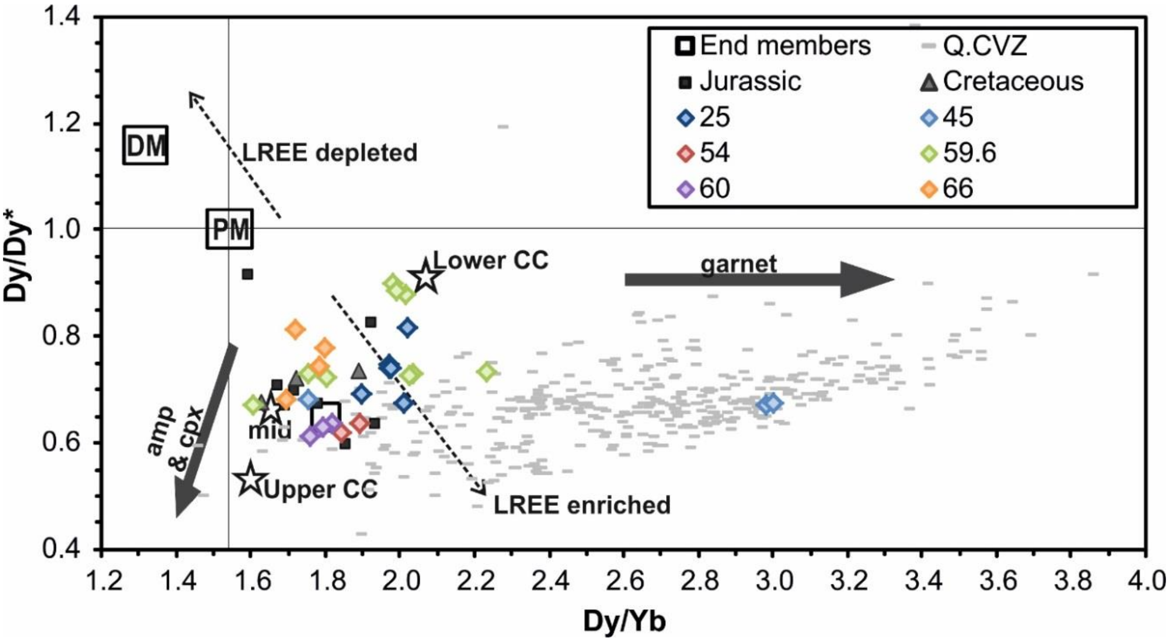

Figure 64: Plot of Dy/Dy* vs Dy/Yb after (Davidson et al., 2013), with vector arrows showing mineral controls on REE patterns. Garnet increases Dy/Yb over a limited range of Dy/Dy*, whereas amphibole and clinopyroxene decrease both Dy/Dy* and Dy/Yb (depending on choices of Kd values). The presence of presumed residual garnet in sediment melts could also increase Dy/Yb for Dy/Dy* values of ~0.6-0.7. Geochemical end-member compositions are shown for comparison: PM, primitive mantle (Sun and McDonough, 1989); DM, depleted mantle (Salters and Stracke, 2004); GLOSS, average global subducting sediment (Plank and Langmuir, 1998). Upper, mid and lower continental crust estimates (Rudnick and Fountain, 1995) are shown as stars.

8.9 Geochemical analyses of undated lavas (Chapter 5)

Supplementary Table 7: Major and trace element compositions of undated lavas

Name	**Qdebrada San Andres**					**Barrancas Blancas**	
Sample	**AT1.1**	**AT1.2**	**AT1.3a**	**AT1.3b**	**AT1.4**	**AT3.1**	**AT3.2**
SiO_2 (wt. %)	59.35	58.15	56.91	65.16	58.08	55.43	50.11
TiO_2	0.72	0.90	0.86	0.88	0.84	0.89	1.01
Al_2O_3	16.81	16.09	15.33	12.25	15.77	17.65	18.26
Fe_2O_3	5.62	6.70	6.70	6.01	6.54	6.69	7.55
MnO	0.09	0.11	0.12	0.05	0.13	0.11	0.11
MgO	3.62	3.84	4.27	2.71	4.32	3.52	4.37
CaO	5.55	6.94	7.17	5.79	7.65	6.54	7.72
Na_2O	3.16	3.07	3.18	1.94	2.94	3.33	2.78
K_2O	2.86	2.68	1.55	1.73	1.35	2.72	1.64
P_2O_5	0.30	0.36	0.34	0.36	0.34	0.29	0.23
SO_3	0.01	0.01	0.00	0.01	0.01	0.01	0.01
LOI	2.43	1.04	1.72	1.43	1.98	3.34	5.18
Total	100.54	99.87	98.15	98.33	99.94	100.53	98.96
$Na_2O + K_2O$	6.02	5.74	4.74	3.67	4.28	6.05	4.41
Sc (ppm)	17.44	20.27	19.99	23.00	19.94	17.68	20.64
V	151.00	182.60	172.70	156.50	168.30	158.30	201.20
Cr	170.70	85.89	122.70	121.70	116.30	32.80	51.28
Mn	0.09	0.11	0.13	0.05	0.14	0.12	0.12
Co	18.81	20.54	21.45	17.17	21.13	18.88	21.34
Ni	70.18	40.17	50.38	42.07	50.66	18.34	27.90
Cu	41.22	51.46	54.11	83.82	50.87	58.38	60.87
Zn	58.86	66.52	64.00	33.11	61.81	67.07	70.56
Ga	17.18	17.79	17.29	13.91	17.57	18.48	18.86
Rb	79.35	79.09	33.42	61.24	23.05	76.33	45.66
Sr	514.80	523.00	670.40	447.40	894.90	604.40	567.90
Y	15.36	18.11	17.79	14.93	17.70	19.23	19.08
Zr	106.50	114.60	115.20	82.53	117.30	160.60	115.40
Nb	6.26	6.20	6.34	4.35	6.38	7.55	6.35
Rh	0.94	0.95	0.95	0.98	0.96	0.91	0.96
Cs	3.72	6.89	57.00	5.54	55.70	2.27	11.55
Ba	889.50	760.70	809.30	569.10	850.30	561.00	458.30
La	14.90	14.35	14.48	11.44	14.61	22.18	18.06
Ce	30.79	30.54	31.11	24.66	31.07	48.54	39.50
Pr	4.04	4.17	4.17	3.40	4.15	6.61	5.51
Nd	15.80	16.85	16.83	14.07	16.74	26.19	22.63
Sm	3.30	3.63	3.61	3.10	3.60	5.15	4.70

Eu	0.98	1.09	1.05	0.88	1.05	1.41	1.37
Gd	3.14	3.58	3.56	3.06	3.51	4.47	4.25
Tb	0.47	0.54	0.54	0.47	0.53	0.63	0.62
Dy	2.67	3.14	3.08	2.66	3.06	3.44	3.41
Ho	0.53	0.64	0.62	0.54	0.61	0.67	0.68
Er	1.42	1.71	1.67	1.43	1.66	1.76	1.78
Tm	0.23	0.27	0.27	0.23	0.26	0.27	0.27
Yb	1.44	1.73	1.70	1.42	1.69	1.73	1.72
Lu	0.24	0.28	0.27	0.23	0.27	0.28	0.28
Hf	3.03	3.17	3.20	2.33	3.22	4.00	3.04
Ta	0.59	0.54	0.57	0.35	0.57	0.52	0.43
Re	0.99	1.00	1.01	1.04	1.02	0.97	1.02
Pb	11.66	10.45	10.89	8.22	10.95	8.21	6.99
Th	6.47	5.50	5.81	2.73	5.83	6.30	4.49
U	2.30	1.85	2.00	1.26	2.06	1.73	1.16

Supplementary Table 7 continued: Major and trace element compositions of undated lavas

Name	**Chépica**	**Peñón**	**Maricunga Dykes**		**Est. Quemada**	**Centinela**
Sample	**AT6.1**	**AT7.1**	**AT13.1**	**AT13.2**	**AT32.1**	**AT37.1**
SiO_2 (wt. %)	53.62	56.49	77.37	77.53	66.66	65.57
TiO_2	0.84	2.51	0.06	0.06	0.67	0.97
Al_2O_3	13.12	16.70	12.38	12.55	16.13	14.00
Fe_2O_3	9.25	8.14	1.04	1.11	3.99	5.59
MnO	0.80	0.17	0.02	0.02	0.01	0.16
MgO	6.91	3.54	0.06	0.14	1.03	0.23
CaO	2.91	6.40	0.49	0.45	1.75	2.10
Na_2O	0.19	4.13	3.83	3.80	9.02	2.20
K_2O	5.85	0.43	4.65	4.53	0.24	5.05
P_2O_5	0.40	0.39	0.00	0.00	0.13	0.29
SO_3	0.04	0.01	0.01	0.03	0.03	0.50
LOI	5.78	1.58	0.62	0.63	0.78	3.46
Total	99.72	100.48	100.54	100.86	100.45	100.11
$Na_2O + K_2O$	6.04	4.56	8.49	8.33	9.26	7.25
Sc (ppm)	21.85	27.54	3.368	2.42	13.35	14.77
V	176.40	265.00	0.77	1.38	103.50	20.21
Cr	432.40	16.06	5.22	2.28	33.91	0.91
Mn	0.80	0.18	0.02	0.02	0.01	0.15
Co	34.19	24.51	0.12	0.20	3.67	10.30
Ni	214.50	23.37	3.11	1.37	9.64	2.90
Cu	208.50	29.44	0.82	1.11	13.43	50.42
Zn	1094.00	77.41	36.38	38.27	10.53	106.10

Ga	19.80	19.78	17.50	18.03	15.11	17.80
Rb	251.10	7.29	213.20	234.50	3.43	229.40
Sr	152.40	473.60	40.82	44.28	84.73	122.70
Y	27.71	39.54	52.77	49.96	23.23	55.05
Zr	232.20	283.70	129.50	135.60	125.50	508.60
Nb	5.52	12.09	24.00	24.57	7.78	22.26
Rh	0.94	0.93	0.97	0.94	0.91	0.93
Cs	4.08	0.86	2.33	2.78	0.18	28.01
Ba	1905.00	277.20	77.95	89.78	84.15	591.20
La	35.11	16.61	12.96	11.31	8.08	41.91
Ce	88.45	41.81	35.16	32.32	22.03	98.14
Pr	12.55	6.36	5.49	5.10	4.07	12.65
Nd	51.57	28.52	24.02	22.11	17.55	50.21
Sm	9.98	6.83	7.47	6.61	3.86	10.51
Eu	2.26	2.17	0.25	0.22	1.07	1.58
Gd	7.35	7.31	7.94	6.92	3.70	9.83
Tb	0.92	1.17	1.36	1.20	0.58	1.58
Dy	4.45	6.85	8.20	7.53	3.45	9.22
Ho	0.83	1.38	1.70	1.61	0.75	1.91
Er	2.13	3.67	4.70	4.57	2.11	5.25
Tm	0.32	0.56	0.75	0.76	0.34	0.86
Yb	2.01	3.50	4.80	4.83	2.21	5.55
Lu	0.32	0.56	0.73	0.75	0.36	0.89
Hf	5.99	5.82	5.89	6.23	3.27	13.84
Ta	0.41	0.77	1.95	2.02	0.56	1.54
Re	0.99	0.99	0.96	0.98	0.92	0.93
Pb	233.70	4.46	4.24	4.30	3.80	21.10
Th	13.48	1.87	16.80	16.72	8.17	24.12
U	4.43	0.46	3.01	2.99	1.37	5.71